

University of Southampton Research Repository ePrints Soton

Copyright © and Moral Rights for this thesis are retained by the author and/or other copyright owners. A copy can be downloaded for personal non-commercial research or study, without prior permission or charge. This thesis cannot be reproduced or quoted extensively from without first obtaining permission in writing from the copyright holder/s. The content must not be changed in any way or sold commercially in any format or medium without the formal permission of the copyright holders.

When referring to this work, full bibliographic details including the author, title, awarding institution and date of the thesis must be given e.g.

AUTHOR (year of submission) "Full thesis title", University of Southampton, name of the University School or Department, PhD Thesis, pagination

UNIVERSITY OF SOUTHAMPTON

FACULTY OF PHYSICAL SCIENCES AND ENGINEERING

Optoelectronics Research Centre

Development of Optical Devices in a Flat-fibre Platform

by

Sumiaty Ambran

Thesis for the degree of Doctor of Philosophy

March 2013

UNIVERSITY OF SOUTHAMPTON

ABSTRACT

FACULTY OF PHYSICAL SCIENCES AND ENGINEERING

Doctor of Philosophy

DEVELOPMENT OF OPTICAL DEVICES IN A FLAT-FIBRE PLATFORM

Sumiaty Ambran

This thesis describes the development of optical devices in a novel flat-fibre platform. Device fabrication is achieved using direct grating writing and physical micromachining techniques.

A series of experimental studies have been undertaken in order to optimise the fabrication of UV-written waveguides and Bragg gratings in the flat-fibre geometry. The UV-writing parameters have been investigated including fluence and duty cycle, together with hydrogen loading and alignment factors. Loss measurements have been performed on a variety of passive and active structures using a novel distributed Bragg grating technique. The measured propagation loss of a channel waveguide based UV-written was $0.13 \text{ dB/cm} \pm 0.03 \text{ dB/cm}$.

Flat-fibre devices have been used as physical and refractive index sensors on a wedge flat-fibre structure. Through using UV-written Bragg gratings in series and parallel arrangement, it provides the capability of sensing two-dimensional bending and external refractive index variation in a single device.

Another passive device that has been developed in flat-fibre is the multimode interference (MMI) device. The concept of using two micro-machined trenches to fabricate the MMI device has also been discussed. In this work, a successful 1×3 MMI device has been fabricated by using a high precision dicing saw and the excess loss was measured as 1.89 dB.

Finally, the spectroscopy study of an erbium doped flat-fibre was performed. Absorption to about 0.32 dB/cm at 976 nm wavelength has been achieved in the erbium-doped flat-fibre. The first demonstration of signal amplification at wavelength of 1530 nm has been carried out where showing that the relative gain was 0.74 dB.

Contents

ABSTRACT	i
Contents	i
List of tables	vii
List of figures	ix
DECLARATION OF AUTHORSHIP	xvii
Acknowledgements	xix
Abbreviations	xxi
Chapter 1	1
Introduction	1
1.1 An Overview and Motivation	1
1.2 Aims of Research	4
1.3 Thesis Synopsis	5
Chapter 2	7
Optical Waveguide Background and Applications	7
2.1 Introduction	7
2.2 Theory of a Planar Optical Waveguide	9
2.2.1 Maxwell’s Equation	9
2.2.2 Marcatili Method	16
2.2.3 Film Mode Matching Method	18
2.2.4 Beam Propagation Method	19
2.3 Bragg Gratings	21
2.3.1 Bragg Grating Structure.....	22
2.3.2 Properties of Bragg gratings	24
2.3.3 Coupled-Mode Theory	25
2.4 Optical Passive and Active Devices	28
2.4.1 Splitters	28
2.4.2 Optical Sensors	29
2.4.2.1 Bragg Grating-Based Sensors	30

2.4.2.2	Waveguide-Based Sensors	31
2.4.3	Amplifiers	32
2.5	Conclusion	34

Chapter 3 35

Fabrication Techniques	35
3.1 Introduction	35
3.2 Standard Optical Fibre Fabrication	36
3.2.1 Preform Fabrication	38
3.2.1.1 MCVD	39
3.2.1.2 PCVD	41
3.2.1.3 OVD	42
3.2.1.4 VAD	43
3.2.2 Fibre Drawing	44
3.3 Fabrication Techniques of Planar Waveguide	45
3.3.1 Flame Hydrolysis Deposition	46
3.3.2 PECVD	47
3.4 Flat-fibre Platform Fabrication	48
3.4.1 Flat-fibre Preform Fabrication	50
3.4.2 Drawing the Flat-fibre Preform	53
3.5 Photosensitivity	54
3.6 Channel Waveguide Fabrication	55
3.6.1 Photolithography/Etching	56
3.6.2 Direct UV-Writing	58
3.6.3 Femtosecond Laser Direct Writing	59
3.6.4 Precision Dicing Saw Micromachining	59
3.7 Measurement Characterisation Set-up	60
3.8 Conclusion	62

Chapter 4 63

UV-Written Bragg Gratings in a Flat-fibre Substrate	63
4.1 Introduction	63
4.2 Direct Grating Writing	64
4.2.1 Amplitude Modulation Method	64
4.2.2 Phase Modulation Method	67
4.3 Interrogating Flat-fibre Performance via UV-written Bragg Gratings	68
4.3.1 Types of Flat-fibre	68

4.3.2	UV-Writing Parameters.....	70
4.3.3	Results and Discussion.....	71
4.4	UV-Writing Parameters Observation.....	74
4.4.1	Fluence	75
4.4.2	Duty Cycle	77
4.5	Flat-fibre Level of Planarisation	81
4.6	Birefringence in Flat-fibre	83
4.7	Conclusion	85
 Chapter 5		87
	Loss Measurement in Passive Flat-fibre Substrates	87
5.1	Introduction	87
5.2	Optical Loss Measurement Techniques	87
5.2.1	Cutback Technique.....	88
5.2.2	End-fire Coupling	89
5.2.3	Prism Coupling Technique	90
5.2.4	Scattered Light Collection	91
5.2.5	Fabry-Perot Cavity Technique	92
5.3	Novel Bragg Grating Loss Measurement.....	93
5.3.1	The Concept of Loss Measurement	93
5.3.2	Waveguide Definition.....	94
5.3.3	Characterisation.....	95
5.4	Results and Discussion	96
5.4.1	Channel Waveguide	96
5.4.2	S-Bend Loss Measurement	98
5.5	Optical Backscattered Reflectometer	102
5.6	Conclusion	104
 Chapter 6		105
	Physical and Refractive Index Sensors in Flat-fibre Platform	105
6.1	Introduction	105
6.2	Evanescent Field	107
6.3	Physical Bending Theory	109
6.3.1	Elasticity	109
6.3.1.1	Hooke's Law	109
6.3.2	Bending a Beam	112
6.3.3	Deflection of a Cantilever.....	114

6.3.4	Material Properties of Silica	114
6.4	Flat-fibre Sensor Device Concept	115
6.5	Refractive Index Sensor	117
6.6	Two-dimensional Bending and Refractive index Sensor	121
6.6.1	Concept and Device Design	122
6.6.2	Comsol Modelling.....	125
6.6.3	Characterisation	126
6.6.4	Results and Discussion	128
6.6.4.1	Refractive index sensing	129
6.6.4.2	Two-dimensional bending.....	131
6.6.4.3	Simultaneous Refractive index and two-dimensional bending	136
6.7	Conclusion	138

Chapter 7 139

Multimode Interference Device	139
7.1 Introduction	139
7.2 The Multimode Interference Device Concept	140
7.2.1 MMI Self-imaging Principle.....	141
7.3 Multimode Interference Device in Flat-fibre Platform	143
7.4 BeamPROP Modelling	146
7.5 Physical Micromachining of a Flat-fibre MMI device.....	149
7.6 Characterisation Setup.....	152
7.7 Result and Discussion.....	154
7.7.1 Propagation Loss	157
7.7.2 Scattering Loss	158
7.7.3 Coupling Loss	159
7.8 Conclusion.....	162

Chapter 8 163

Erbium-doped Flat-fibre.....	163
8.1 Introduction	163
8.2 Erbium-Doped Waveguide Amplifier	165
8.2.1 Energy level of Erbium doped ion	165
8.2.2 Limiting Factors of an Amplifier Efficiency.....	166
8.2.2.1 Host Glass	167
8.2.2.2 Ion-ion Interactions and Excited State Absorption (ESA)	168
8.2.2.3 Waveguide Loss	169

8.3	Erbium-Doped Flat-Fibre	170
8.3.1	Erbium-doped flat-fibre specification	170
8.3.2	Spectroscopy	171
8.3.2.1	Absorption Spectra	172
8.3.2.2	Fluorescence Lifetime	173
8.4	UV-Written Channel waveguide and Bragg Gratings in an Erbium-doped Flat-fibre	176
8.5	Flat-fibre Amplifier	180
8.6	Conclusion	184
Chapter 9	185
	Conclusions and Future Work	185
9.1	Conclusions	185
9.2	Future Work	188
9.2.1	Physical Twist and Bend Sensor.....	188
9.2.2	UV-written Multimode Interference (MMI) Device.....	188
9.2.3	Optical Hybrid Device	189
Appendix A	191
	List of Publications	191
List of References	193

List of tables

Table 1.1.1 Comparison of properties between standard single mode fibres, FHD and flat-fibre.	3
Table 3.4.1 Core layer composition of passive and active flat-fibre susbtrates.....	49
Table 4.3.1 The description of the four different recipes of flat-fibre substrates	69
Table 4.3.2 Peak spectral reflectivity of the Bragg grating about 1550 nm for the different substrates.	73
Table 5.4.1 The calculated values for the minimum radius of curvature, r , relative to the s -bend offset, s	99
Table 6.3.1 Mechanical properties of fused silica glass (taken from [108])......	115
Table 6.6.1 Summary of the function of each Bragg grating wavelength for bending and refractive index sensor	125
Table 7.5.1 Measured surface roughness of three different grit sizes of diamond blade saw.	152
Table 8.4.1 Summary of the erbium doped flat-fibre specification.....	179
Table 8.5.1 Summary of the measured output power from two different signal inputs before and after pumping the erbium-doped flat-fibre.	183

List of figures

Figure 2.1.1 An illustration of Snell's law showing the propagation of light through a boundary of two different media.....	8
Figure 2.1.2 The total internal reflection of light during propagation along a slab waveguide.	8
Figure 2.2.1 The structure of a slab waveguide comprising a sandwich structure of an upper and an under cladding. The left of the figure illustrates the refractive index of the structure.	9
Figure 2.2.2 Symmetric and anti-symmetric modes excitation within a slab waveguide.	15
Figure 2.2.3 Two different channel waveguide geometries (a) stripe and (b) buried, where n_1 and n_2 are the core and cladding refractive index, respectively.	16
Figure 2.2.4 The Marcatili rectangular cross section of the core and cladding layers.	17
Figure 2.2.5 The simple structure of a uniform waveguide showing the layers and slices section used in the FMM method.	18
Figure 2.2.6 Schematic diagram of BPM analysis for (a) light propagation within a tapered waveguide and (b) light propagation in free space within a thin waveguide in the middle of the distance, h	20
Figure 2.3.1 Propagation of an incident light into a Bragg grating structure where the light is reflected (red line) by the grating structure and the rest of the light are transmitted.	21
Figure 2.3.2 (a) Illustration of a uniform Bragg grating structure with uniform grating pitch, induced index modulation for (b) uniform Bragg grating and (c) Gaussian-apodised Bragg grating.....	23
Figure 2.3.3 The reflectivity versus wavelength for (a) uniform and (b) Gaussian apodised Bragg grating structures.	23
Figure 2.3.4 Spectral reflectivity against normalised wavelength for (a) grating length and (b) amplitude index modulation variation.....	27
Figure 2.4.1 Optical splitter in a planar substrate combining several y-splitters in a single component.	29
Figure 2.4.2 Planar Bragg grating sensor with a window etched on top of the substrate surface to allow direct contact between the analyte and the Bragg grating structure.	31
Figure 2.4.3 Illustration of the basic structure of Mach-Zehnder configuration.	31

Figure 2.4.4 Fabry-Perot interferometer (FPI) for (a) external and (b) internal cavity structure.....	32
Figure 2.4.5 Illustration of population inversion in the three level transition system of an erbium-doped laser.	33
Figure 3.2.1 The basic configuration of an optical fibre. The core has higher refractive index than its surrounding cladding layer.	37
Figure 3.2.2 The tree diagram of vapour phase processes where including two different techniques of vapour phase oxidation (VPO) namely inside-VPO and outside-VPO.....	38
Figure 3.2.3 A configuration process of a modified chemical vapour deposition (MCVD) technique.	39
Figure 3.2.4 Making a preform using the MCVD technique where (a) shows the deposition process and (b) the consolidation process.	40
Figure 3.2.5 A plasma CVD process using a microwave cavity to make a preform.	41
Figure 3.2.6 Outside vapour deposition (OVD) for making a preform, where soot particles are deposited outside a rotating rod.	42
Figure 3.2.7 Vapour axial deposition (VAD) process for making a preform.	43
Figure 3.2.8 A standard fibre drawing tower that is used for drawing a conventional optical fibre.....	44
Figure 3.3.1 An image of the silica-on-silicon platform where the core layer is sandwiched between the upper and under cladding. The base of the device is silicon.....	45
Figure 3.3.2 Flame hydrolysis deposition technique to deposit a planar substrate.....	46
Figure 3.3.3 Illustration of a plasma enhanced chemical vapour deposition process to produce a planar substrate.....	48
Figure 3.4.1 Flat-fibre geometry showing (a) cross section and (b) flexibility of a length of the flat-fibre substrate.	49
Figure 3.4.2 The flow chart of flat-fibre fabrication for passive and active device.....	51
Figure 3.4.3 Illustration of combination between soot particles and solution doping after the solution doping process is taken placed.	52
Figure 3.4.4 Illustration of drawing a flat-fibre platform by applying a vacuum to the upper end of the preform.	53
Figure 3.6.1 The process of photolithography and etching technique, which involve several steps.	57
Figure 3.6.2 Illustration of integrated UV-written buried channel waveguide on a flat-fibre substrate.	58

Figure 3.6.3 Micromachined trenches images from (a) end facet and (b) top view.	60
Figure 3.7.1 The characterisation setup for UV-written channel waveguides and Bragg gratings in flat-fibre substrates.	61
Figure 4.2.1 UV-writing configuration for the amplitude modulation technique. A two-crossed UV-beam is tightly focused onto a photosensitivity sample.	65
Figure 4.2.2 The cross section of the interference pattern at certain angle to determine an inherent grating pitch of a Bragg grating wavelength.	66
Figure 4.2.3 UV-writing configuration setup using the phase control method.	68
Figure 4.3.1 Illustration of four different recipes of flat-fibre substrates namely Substrate A, Substrate B, Substrate C and Substrate D.	70
Figure 4.3.2 The flat-fibre cross-section for (a) substrate A and B and (b) substrate C and D.	70
Figure 4.3.3 A 3D schematic diagram of the flat-fibre with three UV-written Bragg gratings	71
Figure 4.3.4 Spectral reflectivity of three different Bragg gratings in (a) Substrate A, (b) Substrate B, (c) Substrate C and (d) Substrate D.	73
Figure 4.4.1 The calculated translation speed against fluence.	75
Figure 4.4.2 Illustration of the effective refractive index level of a UV-written Bragg grating.	76
Figure 4.4.3 A plot of effective refractive index of the waveguide mode against the UV writing fluence, points are experimental data and also shows a fitted linear trend line.	77
Figure 4.4.4 An illustration showing how duty cycle changes the refractive index contrast, shows a duty cycle of (a) 0.5 and (b) 0.9. The blue square wave represents the control signal to the AOM, high level denotes the laser is on. The red sine wave represents an equivalent sinusoidal modulation in the induced refractive index.	78
Figure 4.4.5 Spectral reflectivity of a waveguide containing six Bragg gratings written with a duty cycle of 0.5.	79
Figure 4.4.6 Spectral peak reflectivity plotted with respect to duty cycle for the Bragg grating written at 1545 nm.	80
Figure 4.4.7 The effective refractive index against the duty cycle variation.	80
Figure 4.5.1 The schematic diagram of a series of UV-written channel waveguides each containing two Bragg gratings.	81
Figure 4.5.2 Plot showing peak reflectivity of Bragg grating wavelength at 1560 nm against 15 channel waveguides number.	82

Figure 4.5.3 Plot showing the effective refractive index of the 15 waveguides, at 1560 nm, against the channel waveguide number.	83
Figure 4.6.1 Plot showing the birefringence of 15 waveguides at a wavelength 1560nm as a function of channel waveguide number.	84
Figure 4.6.2 Illustration of guide mode field within a channel waveguide modelled in FIMMWAVE software for TM mode.	85
Figure 5.2.1 A cutback loss measurement technique that measures the output power from the optical fibre with long and short lengths.	88
Figure 5.2.2 A loss measurement of a planar waveguide using end-fire coupling.	90
Figure 5.2.3 Prism coupling loss measurements on a planar waveguide.	90
Figure 5.2.4 Loss measurement of a planar waveguide via scattered light method.	91
Figure 5.2.5 A Fabry-Perot cavity loss measurement technique for channel waveguide.	92
Figure 5.3.1 Waveguide structure schematic for the Bragg grating loss measurement technique.	94
Figure 5.3.2 A schematic diagram of a channel waveguide with ten Bragg gratings along a 40 mm length of flat-fibre substrate.	95
Figure 5.3.3 A schematic diagram for an s-bend configuration where five Bragg gratings before and after the s-bend were defined in the flat-fibre substrate.	95
Figure 5.3.4 Characterisation setup for loss measurement in forward and backward configuration.	96
Figure 5.4.1 Reflectivity of the straight channel waveguide against wavelength. The UV-written channel waveguide containing ten Bragg gratings distributed along the length of the sample.	97
Figure 5.4.2 The ratio of peak power from forward, P and backward direction, P' against the grating position in the waveguide.	97
Figure 5.4.3 The spectral reflectivity of forward and backward direction for the four different offsets.	99
Figure 5.4.4 The offset difference for s-bend with offset (a) 50 μm and (b) 100 μm	101
Figure 5.5.1 OBR graphical window to show the reflected signal from the endfacet of the flat-fibre substrate.	103
Figure 5.5.2 Propagation loss measurement using OBR technique.	103
Figure 6.1.1 Schematic diagram of Rosette configuration with three FBGs.	106

Figure 6.2.1 Illustration of evanescent tail of a guided mode in a planar waveguide where (a) without analyte and (b) with analyte.	108
Figure 6.2.2 Spectral reflectivity showing a wavelength shifting from λ_1 to λ_2 due to sense of different refractive index oils.	108
Figure 6.3.1 Illustration of stretching a rectangular beam where showing the original beam (dash yellow line) and the stretched beam (solid line).	110
Figure 6.3.2 Illustration of bending of a rectangular beam, where tensile stress and compression occur at the same time. The amount of the stress along the y-axis is symmetric to the neutral axis of the beam.	112
Figure 6.3.3 Illustration of bent beam and showing the neutral axis of the beam (green line).	113
Figure 6.3.4 A cantilever beam with a concentrated weight, W applied at the free end of the beam with deflection of z(L).	114
Figure 6.5.1 The Illustration of refractive index sensor using a series of Bragg grating structure.	117
Figure 6.5.2 Normalised spectral reflectivity against the Bragg grating wavelength.	118
Figure 6.5.3 A centre wavelength shifting at 1525 nm against the refractive index oil variation.	119
Figure 6.5.4 The centre wavelength of the 1545nm grating shifting against the refractive index oil.	120
Figure 6.5.5 The sensitivity of the refractive index sensing against the refractive index oil.	120
Figure 6.6.1 A bending configuration at the free end point displacement in x and y-axis direction.	121
Figure 6.6.2 3D schematic of the top polished wedge cladding for the flat-fibre sensor device.	123
Figure 6.6.3 Schematic diagram of flat-fibre substrate sensor from the (a) top view including grating positioning (see Table 6.6.1), (B) side view of the sample.	124
Figure 6.6.4 Modelling structure diagram of top-polished flat-fibre substrate using Comsol software.	126
Figure 6.6.5 Flat-fibre substrate pigtailed with a two-port SMF pigtail and clamped with several small substrate glasses to secure the fixed point of the sample.	127
Figure 6.6.6 The characterisation setup for a two-port SMF pigtailed to the flat-fibre sample.	127

Figure 6.6.7 Schematic diagram for bending characterisation. One end of the flat-fibre substrate is clamped and the end is deflected to represent bending configuration.	128
Figure 6.6.8 The normalised spectral reflectivity against the range of wavelength for the waveguide 1 (blue line) and waveguide 2 (green line).	129
Figure 6.6.9 Spectral reflectivity of Bragg grating wavelength about (a) 1505 nm and (b) 1575 nm.	130
Figure 6.6.10 Centre wavelength shift against different refractive index oils for Bragg grating about 1575 nm.	131
Figure 6.6.11 Absolute centre wavelength shift of Bragg gratings along the length of the flat-fibre due to bending in positive y-axis.	132
Figure 6.6.12 Gradient of the centre wavelength shift against the grating positions along the length of the flat-fibre against deflection in x-axis.	133
Figure 6.6.13 Centre wavelength shift of Bragg gratings against the deflection in y-axis for wavelength about (a) 1614nm and (b) 1541nm.	134
Figure 6.6.14 Centre wavelength shift against the deflection in x-axis direction for wavelength about (a) 1614 nm and (b) 1541 nm.	135
Figure 6.6.15 Centre wavelength shift against deflection in (a) y-axis and (b) x-axis for the Bragg grating at 1575 nm. A positive centre wavelength shift can be seen, indicated on the graphs, when exposing the sample to a refractive index oil.	137
Figure 7.2.1 A principle multimode interference device with one input channel and one output channel known as 1x1 MMI device.	141
Figure 7.3.1 3D image of MMI flat-fibre device with two micromachining trenches. The MMI section is parallel to the trenches.	145
Figure 7.3.2 Illustration of high- and low-index contrast from the end facet of the flat-fibre due to air-trenches micromachining.	146
Figure 7.4.1 An MMI modelling structure built in BeamPROP RSoft software. Three pathways have been set to monitor the power that travel through the MMI section.	147
Figure 7.4.2 Illustration of BeamPROP modelling of the propagation light within the MMI section. (a) From top view and (b) 3D image.	148
Figure 7.5.1 Dicing a trench using a rotating blade saw in opposite direction of the translation stage that the flat-fibre substrate is placed.	149
Figure 7.5.2 (a) A microscope image of the end facet of the MMI section with two trenches and (b) A top view of the SEM image showing the parallel characteristics part of the MMI length. Two trenches were cut allowing the core layer being exposed to the air, providing a	

high index contrast between the refractive index of the core layer and the air-trenches.	151
Figure 7.6.1 A butt coupling between the PM fibre and the MMI section with index matching gel.	152
Figure 7.6.2 Characterisation setup for (a) monitoring the output mode pattern observed from monitor, (b) output power measurement by scanning the PM fibre across the MMI cross section and (c) monitoring of wavelength scanning.	154
Figure 7.7.1 The modal image pattern of the 1x3 MMI device recorded by the NIR camera at 1641 nm.	155
Figure 7.7.2 A distribution output power of the modal image through scanning measurement technique at the end facet of the MMI region using a PM fibre. The scanning is implemented horizontally along the width of the MMI section.	155
Figure 7.7.3 The insertion loss from each of the three output spots against the wavelength. The total excess loss is also calculated by summing all three output powers at each respective wavelength.	156
Figure 7.7.4 The solid line represents the normalised transmission from the modelling, showing good agreement to the experimental data. The optimum wavelength of the maximum point is 1652nm.	157
Figure 7.7.5 The normalised output power against the wavelength for trenches with and without index oil.	159
Figure 7.7.6 Normalised mode output profile for optical PM fibre. The measured data is fitted with Gaussian profile.	160
Figure 7.7.7 Normalised output mode profile from spot 1 in (a) vertical and (b) horizontal axes.	161
Figure 8.2.1 Illustration of a three transition energy level of an erbium-doped waveguide to produce amplified stimulated emission.	166
Figure 8.2.2 Cross-section data from three fibres with different host compositions, taken from [139].	168
Figure 8.2.3 Illustration of co-operative upconversion process which occurs in erbium doped waveguides. (a) An energy exchange between two erbium ions and (b) shows the location of the erbium ion resulted from energy exchange process.	169
Figure 8.3.1 An image of the cross section of an erbium-doped flat-fibre platform.	171
Figure 8.3.2 Characterisation setup of absorption spectra measurement for erbium-doped flat-fibre substrate.	172
Figure 8.3.3 Absorption spectra of erbium-doped flat-fibre along 18.8 cm planar slab waveguide.	173

Figure 8.3.4 Characterisation of fluorescence lifetime measurement of an erbium-doped flat-fibre substrate where using laser diode as a pump light source.....	174
Figure 8.3.5 The fluorescence lifetime measurement showing the fluorescence exponentially decreases after the LD power laser is off.	175
Figure 8.3.6 Fluorescence lifetime of the erbium-doped fibre where fitting with single exponential equation.....	175
Figure 8.4.1 Schematic diagram of distributed Bragg gratings along the erbium-doped flat-fibre substrate.....	176
Figure 8.4.2 Normalised spectral reflectivity against wavelength for the erbium-doped flat-fibre.	177
Figure 8.4.3 Spectral reflectivity against wavelength for TE and TM polarisation.	177
Figure 8.4.4 Effective refractive index against wavelength for TM and TE polarisation.....	178
Figure 8.4.5 The ratio of peak power from forward, P and backward, P' direction against the grating position for the erbium-doped flat-fibre.	179
Figure 8.5.1 Characterisation setup for signal amplification, where using the wavelength division multiplexing (WDM) to couple the light from laser diode and tunable light source.....	180
Figure 8.5.2 Amplified spontaneous emission observed from the erbium-doped flat-fibre when launching a laser diode at 980 nm.	181
Figure 8.5.3 Output power from the erbium-doped flat-fibre substrate against wavelength with and without pump power for 1530 nm signal wavelength and signal output of -23 dBm. The resolution of the OSA was set to 0.5 nm to allow an accurate power measurement.	182
Figure 9.2.1 A schematic of flat-fibre laser using a rare-earth doped flat-fibre and MMI device combination.	190

DECLARATION OF AUTHORSHIP

I, **Sumiaty Ambran** declare that the thesis entitled **Development of Optical Devices in a Flat-fibre Platform** and the work presented in the thesis are both my own, and have been generated by me as the result of my own original research.

I confirm that:

- this work was done wholly or mainly while in candidature for a research degree at this University;
- where any part of this thesis has previously been submitted for a degree or any other qualification at this University or any other institution, this has been clearly stated;
- where I have consulted the published work of others, this is always clearly attributed;
- where I have quoted from the work of others, the source is always given. With the exception of such quotations, this thesis is entirely my own work;
- I have acknowledged all main sources of help;
- where the thesis is based on work done by myself jointly with others, I have made clear exactly what was done by others and what I have contributed myself;
- parts of this work have been published as listed in references.

Signed:

Date:.....

Acknowledgements

First and foremost, I would like to express my sincere gratitude to my supervisors, Professor Jayanta Sahu and Professor Peter Smith, for their support, encouragement and tolerance during my studies here in the ORC. I am also extremely thankful to Dr. James Gates and Dr. Christopher Holmes for their knowledge, motivation and the time they spent to help me when I came across challenges.

Honestly, working within the group of Engineered Photonics Devices and Application and Silica Fibre Fabrication is fantastic experience that I will never forget. Special thanks go to Dr. Andrew Webb and Helen Rogers, who have helped me throughout my studies. Many thanks to all my group members, both past and present for their help and support, Chaotan Sima, Lewis Carpenter, Paolo Mennea, Peter Cooper, Saurabh Jain, Dr. Mohammad Belal, Dr. Richard Parker, Dr. Benjamin Snow, Dominic, Francesca Mountford, Deepak Jain, Robert Standish, Martin Nunez Velazques, and Dr. Timothy May-Smith.

I would also like to thank my colleagues and staffs within the ORC, Seyed Reza Sandoghchi, Neil Session, Ming Ding, Rand Ismael, Jessica, Eve Smith, Deanna Standan, Mark Lessey, Sonali Dasgupta, Kannan Pradeesh, Ehab Saleh, Jiangfa Zhang, Paul Allwood, Peh Siong, and others who have helped me directly or indirectly for their endlessly helpful and supportive.

My special gratefulness goes to all my family members and friends especially my beloved husband Ahmad Shahrir Rafei, my mother Patimah Kuis, my father Ambran Aziz, my siblings Patmawati, Ratmawati, Jefry, and also all my lovely daughters Humaira Arfa, Nadhirah Arfa, and Khayyirah Arfa for being infinitely supportive and understanding, thank you very much for being my strength too.

I am indebted to Dr. Rafiq Adikan who encouraged and supported me to further my studies here in the ORC. Last but not least, thanks to my scholarship Ministry of Higher Education (MOHE) and University Technology of Malaysia (UTM) for giving me opportunity to study abroad. Not to forget the Malaysian society in Southampton for their kindness and their organisation of many valued activities.

Abbreviations

2D	Two Dimensional
AOM	Acousto-Optic Modulator
ASE	Amplified Spontaneous Emission
BPM	Beam Propagation Method
CNC	Computer Numerical Control
DBR	Distributed Bragg Reflector
DGW	Direct Grating Writing
EDFA	Erbium Doped Fibre Amplifier
EDWA	Erbium Doped Waveguide Amplifier
EOM	Electro-Optic Modulator
ESA	Excited State Absorption
FBG	Fibre Bragg Grating
FFT	Fast Fourier Transform
FHD	Flame Hydrolysis Deposition
FPI	Fabry-Perot Interferometer
FTTH	Fibre To The Home
GODCs	Germanium Oxygen Deficient Centres
LED	Light Emitting Diode
MCVD	Modified Chemical Vapour Deposition
MMI	Multimode Interference
NIR	Near Infrared
OBR	Optical Backscattered Reflectometer

OSA	Optical Spectrum Analyser
OVD	Outside Vapour Deposition
PCF	Photonic Crystal Fibre
PCVD	Plasma Chemical Vapour Deposition
PECVD	Plasma Enhanced Chemical Vapour Deposition
PM	Polarisation Maintaining
SLED	Spontaneous Light Emitting Diode
SMF	Single Mode Fibre
TE	Transverse Electric
TIR	Total Internal Reflection
TM	Transverse Magnetic
UV	Ultra Violet
VAD	Vapour Axial Deposition

Chapter 1

Introduction

1.1 An Overview and Motivation

The evolution of optical technology has revolutionised the modern lifestyle. The technology has been applied in many fields such as telecommunications, medicine and structural monitoring. The main benefit of optical technology compared to electronic and radio communication alternatives is the high bandwidth capacity [1]. High bandwidth has allowed high-speed optical telecommunications, which is in increasing demand by businesses and individuals. This, amongst other reasons, has resulted in a growing demand for optical technology in the communication sector. Today's internet network uses optical fibre technology as a transmission medium, providing high data transmission rates and yielding a more efficient and higher performance system than ever before. This is highlighted by the UK Government's National Infrastructure Plan 2011 included a budget allocation of £100 million for superfast broadband (up to 100 Mbps) in ten "super-connected cities" across the country [2].

The success of the technology derives from the small cross-section dimension, low loss, low fabrication cost, lightweight, and flexibility of the optical fibre, which has also made it attractive for other applications. The optical technology has been widely used in medical applications such as endoscopy, where it is used to image organs within the human body [3]. In addition, there are a large number of optical technology applications in the area of structural monitoring, where buildings and bridges can be embedded with fibre optic sensors to observe structural faults [4].

Optical fibres, while ideal for point-to-point communications, are not suitable for the branching and splitting of light signals. Thus, it is noteworthy to mention that the field of integrated planar optics also plays an essential and indispensable role in the development of an all-optical signal processing system [5]. *Miller* was the first to highlight the concept of integrated optics in 1969 [6]. Ideally, the structure of the integrated optic device consists of a light source, waveguide and detector components, which are all integrated on a single substrate, and thus offers a dense and compact structure as well as a well-designed optical system. Such devices are known as monolithic optical integrated circuits. However, in integrated optics, it is not necessary to have all the components in a single substrate, and bulk components may be used as well.

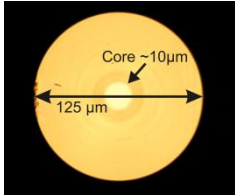

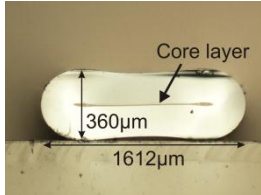
Following *Miller's* proposal, several types of material systems have been used as a substrate for integrated circuits, including silica (e.g. silica-on-silicon), silicon (e.g. silicon-on-insulator), polymer, sol-gels, lithium niobate and gallium arsenide [7]. Nevertheless, the most favourable material system that has been used in passive integrated optical devices is silica-on-silicon due to its low propagation loss and excellent mode matching with standard optical fibres [8]. Flame hydrolysis deposition (FHD) [9] and plasma enhanced chemical vapour deposition (PECVD) [10] are the most common deposition techniques for fabricating silica-on-silicon substrates. Both deposition techniques typically use flat silicon wafers as a substrate to support the thin silica layers, and thereby limit the maximum size of the substrate to around 30 cm in length. Besides that, silicon wafers are expensive and also require expensive growth of thick layers of thermal oxide to form the underclad and stress reducing layers.

As a consequence to the constraints mentioned above, a joint venture between the Silica Fibre and Engineered Photonics Devices and Application groups in the Optoelectronics Research Centre has invented a novel platform for fabricating planar integrated optical devices, called 'Flat-fibre' [11]. As mentioned before, the silica glass based fibre platform is clearly recognised as the material of choice for communications, offering low cost, long device lifetimes, and environmental stability. Thus, the flat-fibre technology made by a silica glass is used as a platform to develop an integrated planar optical device. The benefits offered by flat-fibre compared to conventional planar waveguides (and standard optical fibres) are presented in Table 1.1.1 [12]. Most of the advantages listed in the Table 1.1.1 overcome many of weaknesses of conventional planar waveguides. The distinct advantage offered by the flat-fibre platform is the way in which it is fabricated. It uses modified chemical vapour deposition (MCVD) and a standard fibre drawing tower, techniques used to fabricate conventional optical fibres, and thereby presents a low cost route to fabricate integrated planar de-

VICES. The MCVD technique is a mature optical technology and has the capability of producing low-loss silica based materials. The deposited preform fabricated via the MCVD process is then collapsed by applying a vacuum during fibre drawing to shape the fibre into a planar cross section.

Table 1.1.1 Comparison of properties between standard single mode fibres, FHD and flat-fibre.

Properties Comparison

	Optical fibre	Planar waveguide	Flat-fibre
			
Low Loss	Yes	No	Yes
Low Cost	Yes	No	Yes
Multi-functional	No	Yes	Yes
Long Length	Yes	No	Yes
Mechanically Flexible	Yes	No	Yes
High Uniformity	Yes	No	Yes

In conjunction with a direct ultraviolet writing (DUW) technique, optical circuitry can be designed in the flat-fibre, presenting more compact passive devices for light signal manipulation [13]. The technique offers a simple and quick fabrication and involves the scanning of a focused UV-laser beam into the core layer of a photosensitive planar substrate. The positive refractive index change induced can be as much as 10^{-2} [14], more than sufficient to form a channel waveguide. An adaption of the DUW technique is the direct grating writing (DGW) technique [15]. Here two crossed UV-beams form an interference pattern which can be used to define a Bragg grating structure. The DGW technique opens up the possibility of fabricating integrated planar circuits in the flat-fibre substrate. To improve the passive device performance, efforts have been

made to improve the photosensitivity of the flat-fibre sample and thereby reduce fabrication time. To date this has been achieved by adding dopants such as germanium (Ge) and boron (B) into the core layer of the flat-fibre. Most of the flat-fibre devices presented in this thesis have employed the DGW technique, making use of a Bragg grating structure as a tool for device characterisation and optimisation. Accordingly, the thesis discusses research investigating the composition of flat-fibre and the development of optical components such as γ -splitters, Bragg gratings with improved strength and sensor designs. Apart from the UV-writing technique, one of the fabricated flat-fibre devices uses an ultra-precision dicing machine to produce a multimode interference device for light splitting. A planar waveguide can be produced within the core layer via micromachining the substrate. This consequently induces interference between guided modes, and thus splitting of the light occurs according to the dimensions of the device.

In order to fabricate an active device, one can consider doping the fibre with rare-earth ions and hence inducing light amplification. Thus, an erbium doped flat-fibre has been fabricated by Dr. *Andrew Webb* (one of member in the Silica Fibre Fabrication group) using the same technique as used to fabricate a passive flat-fibre substrate. The compositional difference is obtained during the MCVD process where in-situ solution doping is applied, adding erbium rare-earth ions into the preform of the flat-fibre glass. A series of experimental works has been carried out to characterise the fibre including spectroscopy of the erbium doped flat-fibre and the first demonstration of light amplification within the flat-fibre.

The motivation of this research is the development of high quality and increased performance of integrated optical components compatible with the existing optical transmission line of standard single mode fibre (e.g. SMF-28). Flat-fibre provides the field of optics with a low-cost optical transmission system that can be fully integrated into the standard optical fibre network.

1.2 Aims of Research

The aims of this research are listed as follows:

- i. To develop a series of planar integrated devices with high performance and low optical loss in a flexible long length of flat-fibre platform.
- ii. To demonstrate the capability of the flat-fibre substrate to be implemented as a physical and refractive index sensor.

- iii. To fabricate a multimode interference device for light splitting using an alternative method of making use two-micromachined trenches to induce interference between guided modes within the core of the flat-fibre.
- iv. To characterise an erbium doped flat-fibre and demonstrate light amplification within such a device.

1.3 Thesis Synopsis

This thesis consists of nine chapters describing theoretical background and experimental work.

Chapter 1 provides an introduction to the subject area and the aims of the research. The advantages of flat-fibre substrate against conventional standard single mode fibre and planar waveguide are described in this chapter. The aims of the research are also listed here.

Chapter 2 explains the theoretical background of the research which is presented in this thesis. Starting with the theoretical analysis of planar optical waveguides, the chapter includes description of the Marcatili, film mode matching and beam propagation methods. These methods have been used in the experimental work. The concept of the Bragg grating and a series of optical devices such as splitters, sensors and amplifiers are also described in this chapter. This is to develop an understanding of the operational principle of these optical devices.

Chapter 3 describes several fabrication techniques including the fabrication of standard optical fibre and also planar materials. This includes the fabrication of the basic flat-fibre device. The UV-writing method for defining a channel waveguide is also introduced in this chapter. The general characterisation setup used to characterise the fabricated devices is also provided.

Chapter 4 presents two different appearances of the direct grating writing technique, namely amplitude modulation and phase modulation. Experimental work that has been carried out for UV-writing parameter optimisation is described here. The planarisation of the flat-fibre cross section, and also the birefringence of the flat-fibre are discussed in this chapter.

Chapter 5 presents a novel technique for measuring the propagation loss of a planar waveguide. The technique requires a series of Bragg gratings distributed along

the length of the flat-fibre substrate in order to quantify waveguide loss in the substrate. Conventional techniques used for the loss measurement of planar waveguides are also described. For comparison purposes, an optical backscattered reflectometer is used to measure the propagation loss in the flat-fibre.

Chapter 6 discusses the sensitivity of the flat-fibre substrate as a sensor device. The background theory of bending a beam and the concept of evanescent fields are given in the early section of the chapter. Following this, the concept of the flat-fibre sensor is described. The capability of the device to sense multiple parameters, namely two-dimensional bending as well as refractive index sensing is briefly described.

Chapter 7 introduces an alternative fabrication technique to develop a multimode interference device in the flat-fibre platform. This technique uses a high precision micromachining tool which is employed to fabricate a multimode interference (MMI) device in the flat-fibre platform. Two micromachined trenches are fabricated parallel to the MMI section in order to confine light within the core layer of the flat-fibre substrate. A 1x3 MMI splitter device is presented in this chapter.

Chapter 8 discusses results from an investigation into the erbium-doped flat-fibre. The absorption spectra and the lifetime of the flat-fibre are performed. The chapter includes results from the first demonstration of light amplification within the flat-fibre substrate.

Chapter 9 summarises the key results and outcomes from the thesis and also highlights the future work of this research work.

Chapter 2

Optical Waveguide Background and Applications

2.1 Introduction

This chapter introduces the theoretical background of the optical waveguides that are used in this thesis and covers slab and channel waveguide structures. The first section introduces the fundamental analysis for describing a slab waveguide mode, which is derived from Maxwell's equations. In the following section the Marcatili method is presented which provides an analytical tool for the modelling of channel waveguide. A film mode matching method that is implemented in the FIMMWAVE software is also explained. This is followed by explaining the principle of the beam propagation method that is used in developing a multimode interference device. Many of the experiments reported here have used Bragg grating structures fabricated via a direct grating writing (DGW) technique. Therefore, the chapter also provides the theoretical concept of Bragg grating and several types of Bragg grating structures. The chapter concludes with a brief background of several optical devices namely optical splitter device, optical sensors and amplifiers.

Before discussing the theory of planar optical waveguide, it is worth describing the fundamentals of light propagation in a waveguide. The concept of total internal reflection (TIR) is the basis of light propagation in any waveguide [16]. Starting with the understanding of Snell's law where the propagation of an incident light ray with angle θ_1 will be refracted at the angle of θ_2 as the light propagates through a boundary of two different materials with dissimilar refractive index, n (in this case $n_1 > n_2$) as depicted in Figure 2.1.1. The relationship between the angles and the refractive indices is

expressed in equation (2.1). In the situation when θ_2 is equal to 90° , then θ_1 is known as a critical angle, θ_c and at any angle of θ_1 that exceeds the critical angle TIR will occur. Figure 2.1.2 shows a slab waveguide substrate where a layer of higher refractive index material (n_1) is sandwiched between two layers of lower refractive index (n_2) material. With the correct conditions TIR will occur, confining the light to the central core layer as indicated by the arrows. This is a basic structure of a slab waveguide.

$$n_1 \sin \theta_1 = n_2 \sin \theta_2 \tag{2.1}$$

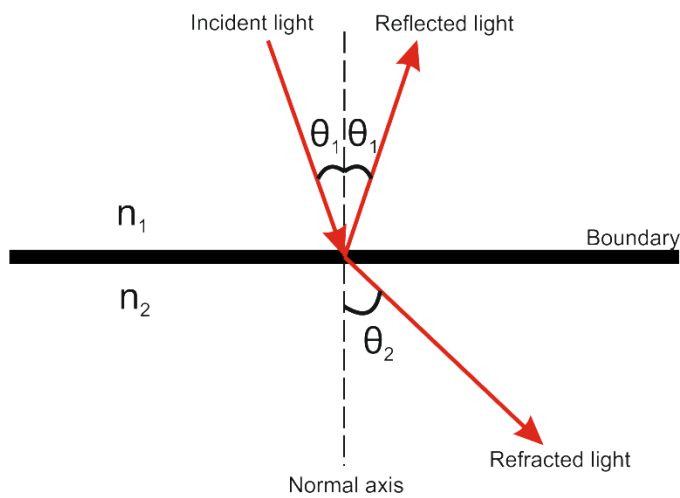


Figure 2.1.1 An illustration of Snell’s law showing the propagation of light through a boundary of two different media.

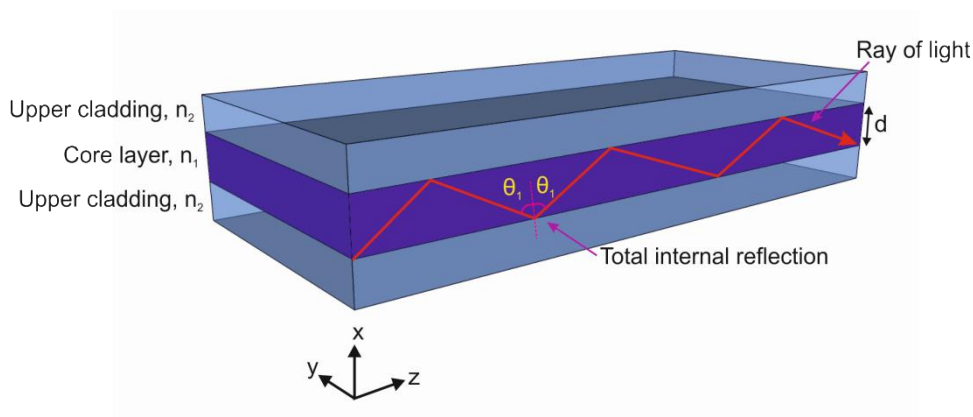


Figure 2.1.2 The total internal reflection of light during propagation along a slab waveguide.

2.2 Theory of a Planar Optical Waveguide

This section explores a number of methods for theoretically modelling waveguide structures. The modal analysis of a planar waveguide starts with Maxwell's equations which are generally used to analyse a planar waveguide. Further analysis is carried out into a particular channel waveguide where the Marcatili method is introduced. The principle of the film mode matching method is used in the FIMMWAVE software which is later used in defining the effective refractive index of a channel waveguide. Finally, the concept of the split step is described which is used in the beam propagation method for describing the operation of multimode interference.

2.2.1 Maxwell's Equation

The structure of a slab waveguide is shown in Figure 2.2.1, it consists of a core layer that has a refractive index slightly higher than the over cladding and under cladding layers to allow total internal reflection. Firstly, Maxwell's equations are considered in layered media. The simplified expressions below describe the electromagnetic fields in an isotropic, linear, nonconducting and nonmagnetic medium. The mode analysis approach in this section is taken from *An Introduction to Fiber Optics* by Ghatak and Thyagarajan and provides a fundamental insight into the operation of an optical waveguide [16].

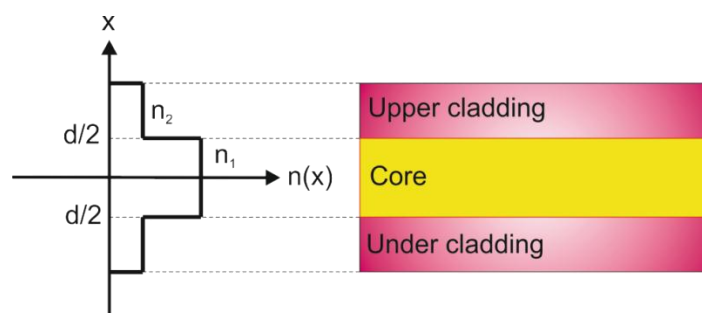


Figure 2.2.1 The structure of a slab waveguide comprising a sandwich structure of an upper and an under cladding. The left of the figure illustrates the refractive index of the structure.

Starting with Maxwell's equations:

$$\nabla \times \bar{E} = -\frac{\partial \bar{B}}{\partial t} = -\mu_0 \frac{\partial \bar{H}}{\partial t} \quad (2.2)$$

$$\nabla \times \bar{H} = \frac{\partial \bar{D}}{\partial t} = \epsilon_0 n^2 \frac{\partial \bar{E}}{\partial t} \quad (2.3)$$

$$\nabla \cdot \bar{D} = 0 \quad (2.4)$$

$$\nabla \cdot \bar{B} = 0 \quad (2.5)$$

Where \bar{E} , \bar{D} , \bar{B} and \bar{H} are the electric field, electric displacement, magnetic induction, and magnetic intensity, respectively. The constitutive relations of those parameters are

$$\bar{B} = \mu_0 \bar{H} \quad (2.6)$$

$$\bar{D} = \epsilon \bar{E} = \epsilon_0 n^2 \bar{E} \quad (2.7)$$

Where $\mu_0 = (4\pi \times 10^{-7} \text{Ns}^2/\text{C}^2)$ is the free space magnetic permeability, ϵ is the dielectric permittivity of the medium with refractive index of n , and $\epsilon_0 = (8.854 \times 10^{-12} \text{C}^2/\text{Nm}^2)$ represents the permittivity of free space. By solving the equations above and assuming that the refractive index varies only in the x axis gives

$$n^2 = n^2(x) \quad (2.8)$$

Then, the electric and magnetic fields expressions may be written as below

$$\bar{E}_j = E_j(x)e^{i(\omega t - \beta z)}; \quad j = x, y, z \quad (2.9)$$

$$\bar{H}_j = H_j(x)e^{i(\omega t - \beta z)}; \quad j = x, y, z \quad (2.10)$$

By substituting the above expressions into equation (2.2) and (2.3), then Maxwell's equations are reduced to two sets of independent equations which are expressed as

$$i\beta E_y = -i\omega\mu_0 H_x \quad (2.11)$$

$$\frac{\partial E_y}{\partial x} = -i\omega\mu_0 H_z \quad (2.12)$$

$$-i\beta H_x - \frac{\partial H_z}{\partial x} = i\omega\varepsilon_0 n^2(x) E_y \quad (2.13)$$

and

$$i\beta H_y = i\omega\varepsilon_0 n^2(x) E_x \quad (2.14)$$

$$\frac{\partial H_y}{\partial x} = -i\omega\varepsilon_0 n^2(x) E_z \quad (2.15)$$

$$-i\beta E_x - \frac{\partial E_z}{\partial x} = i\omega\mu_0 H_y \quad (2.16)$$

The first three equations above (2.11) - (2.13) are known as transverse electric (TE) modes since the electric field has only a transverse E_y component. While, the last three equations (2.14) - (2.16) describe the mode known as transverse magnetic (TM) as the solution contains only the H_y component.

Expressions (2.11) - (2.13) may be now be used to analyse the TE modes of a symmetric, step index planar waveguide. By substituting H_x and H_z from equations (2.11) and (2.12) respectively into equation (2.13) gives the following expression

$$\frac{d^2 E_y}{dx^2} + [k_0^2 n^2(x) - \beta^2] E_y = 0 \quad (2.17)$$

where $k_0 = \omega(\varepsilon_0\mu_0)^{\frac{1}{2}} = \frac{\omega}{c}$ and $c (3 \times 10^8 \text{ ms}^{-1})$ represents the speed of light in free space.

Aforementioned, the analysis detailed here considers the x -dependent profile where the refractive index profile is represented by (also see Figure 2.2.1)

$$n(x) = \begin{cases} n_1; & |x| < \frac{d}{2} \\ n_2; & |x| > \frac{d}{2} \end{cases} \quad (2.18)$$

By satisfying the boundary conditions of E_y and ensuring $\frac{dE_y}{dx}$ is continuous at $x = \pm \frac{d}{2}$, then substituting the $n(x)$ in equation (2.17), expressions (2.19) and (2.20) can be obtained.

$$\frac{d^2 E_y}{dx^2} + (k_0^2 n_1^2 - \beta^2) E_y = 0, \quad |x| < \frac{d}{2} \quad \text{core layer} \quad (2.19)$$

$$\frac{d^2 E_y}{dx^2} + (k_0^2 n_2^2 - \beta^2) E_y = 0, \quad |x| > \frac{d}{2} \quad \text{cladding layer} \quad (2.20)$$

In order to have guided modes which are mainly confined within the film, the condition below must be satisfied.

$$\left(n_2^2 < \frac{\beta^2}{k_0^2} < n_1^2 \right), \quad (2.21)$$

When $\beta^2 > k_0^2 n_2^2$ is satisfied, the modes will be confined and guided within the core layer with a small penetration into the cladding region. However, when this condition is not satisfied, the modes that are excited at the boundary will tend to leak away from the core region which is known as radiation modes.

Equations (2.19) and (2.20) may be simplified into the form

$$\frac{d^2 E_y}{dx^2} + (\kappa^2) E_y = 0; \quad |x| < \frac{d}{2} \quad \text{core layer} \quad (2.22)$$

$$\frac{d^2 E_y}{dx^2} - (\gamma^2) E_y = 0; \quad |x| > \frac{d}{2} \quad \text{cladding layer} \quad (2.23)$$

where

$$\kappa^2 = k_0^2 n_1^2 - \beta^2 \quad (2.24)$$

$$\gamma^2 = \beta^2 - k_0^2 n_2^2 \quad (2.25)$$

Equations (2.22) and (2.23) can be satisfied by solutions in the form of (2.26) and (2.27) respectively, where A, B, C and D are constants.

$$E_y(x) = A \cos \kappa x + B \sin \kappa x; |x| < d/2; \quad (2.26)$$

$$E_y(x) = \begin{cases} C e^{\gamma x}; & x < -\frac{d}{2} \\ D e^{-\gamma x}; & x > \frac{d}{2} \end{cases} \quad (2.27)$$

The refractive index distribution is symmetric, when

$$n^2(-x) = n^2(x) \quad (2.28)$$

Therefore, the solutions can be interpreted as either symmetric or anti-symmetric modes which can be expressed as

$$E_y(-x) = E_y(x) \quad \text{symmetric modes} \quad (2.29)$$

$$E_y(-x) = -E_y(x) \quad \text{anti-symmetric modes} \quad (2.30)$$

Equation (2.31) represents the symmetric modes of the slab waveguide. Equation (2.32) and (2.33) ensures continuity of both $E_y(x)$ and $\frac{dE_y(x)}{dx}$ at the boundaries, $x = \pm \frac{d}{2}$ respectively.

$$E_y(x) = \begin{cases} A \cos \kappa x; & |x| < \frac{d}{2} \\ C e^{-\gamma|x|}; & |x| > \frac{d}{2} \end{cases} \quad (2.31)$$

$$A \cos\left(\frac{\kappa d}{2}\right) = C e^{-\frac{\gamma d}{2}} \quad (2.32)$$

$$-\kappa A \sin\left(\frac{\kappa d}{2}\right) = -\gamma C e^{-\frac{\gamma d}{2}} \quad (2.33)$$

Dividing equation (2.33) by equation (2.32) yields

$$\xi \tan \xi = \frac{\gamma d}{2} \quad (2.34)$$

where

$$\xi = \frac{\kappa d}{2} = \left(k_0^2 n_1^2 - \beta^2\right)^{\frac{1}{2}} \frac{d}{2} \quad (2.35)$$

Introducing the dimensionless waveguide parameter V-number, as expressed in equation (2.37) provides the relation;

$$\xi \tan \xi = \left(\frac{1}{4}V^2 - \xi^2\right)^{\frac{1}{2}} \quad (2.36)$$

$$V = k_0 d \left(n_1^2 - n_2^2\right)^{\frac{1}{2}} \quad (2.37)$$

Also, using the same procedure as the symmetric mode, the anti-symmetric mode can be obtained as the form,

$$-\xi \cot \xi = \left(\frac{1}{4}V^2 - \xi^2\right)^{\frac{1}{2}} \quad (2.38)$$

where,

$$E_y(x) = \begin{cases} B \sin \kappa x; & |x| < \frac{d}{2} \\ \frac{x}{|x|} D e^{-\gamma|x|}; & |x| > \frac{d}{2} \end{cases} \quad (2.39)$$

Therefore, the symmetric modes and the anti-symmetric modes can be concluded as,

$$\xi \tan \xi = \left(\frac{1}{4}V^2 - \xi^2\right)^{\frac{1}{2}}; \quad \text{Symmetric modes} \quad (2.40)$$

$$-\xi \cot \xi = \left(\frac{1}{4}V^2 - \xi^2\right)^{\frac{1}{2}}; \quad \text{Anti-symmetric modes} \quad (2.41)$$

Figure 2.2.2 shows a plot of symmetric and anti-symmetric modes against the parameter ξ . This graph illustrates the symmetric and anti-symmetric modes that are excited within the slab waveguide. It can be seen that, the intersection of the $\xi \tan \xi$ (red line) and $-\xi \cot \xi$ (blue line) with the V parameter of $V = 4$ (black line) determines the number of symmetric and anti-symmetric modes propagating within the waveguide

with a V parameter of $V = 4$. In the case of $V = 4$, the waveguide supports one symmetric and one anti-symmetric modes. The graph also shows that this planar case waveguides with V -numbers less than π support only a single symmetrical mode.

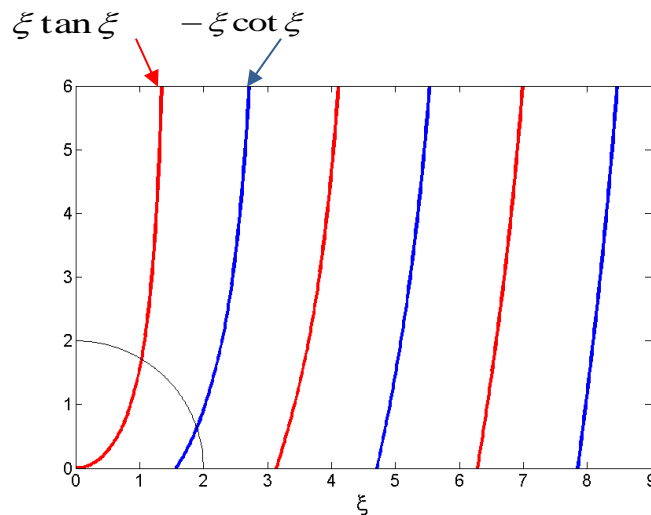


Figure 2.2.2 Symmetric and anti-symmetric modes excitation within a slab waveguide.

The analysis that is described in this section only considers the propagation supported by a slab waveguide. In this structure, the propagating light is only confined in a vertical axis, and typically has high loss due to the lack of lateral confinement. In contrast a channel waveguide has the capability of guiding light in two dimensions. This structure is more useful for integrated optical devices. There are several geometries of channel waveguides, two of the most common are the stripe and buried channel waveguides and are illustrated in Figure 2.2.3 (a) and (b), respectively [17]. Stripe channel waveguides are commonly applied in semiconductor based-optical devices. However this structure tends to have high loss due to the high index contrast and surface roughness of the surrounding wall of the channel waveguide. The buried channel waveguide is surrounded by a cladding region and typically has lower index contrast, is less affected by the environmental and thus can exhibit lower loss. In this thesis, most of the devices use a buried channel waveguide fabricated via the direct UV-writing grating technique. In the next section, a numerical technique known as the Marcattili method to analyse a channel waveguide structure will be described.

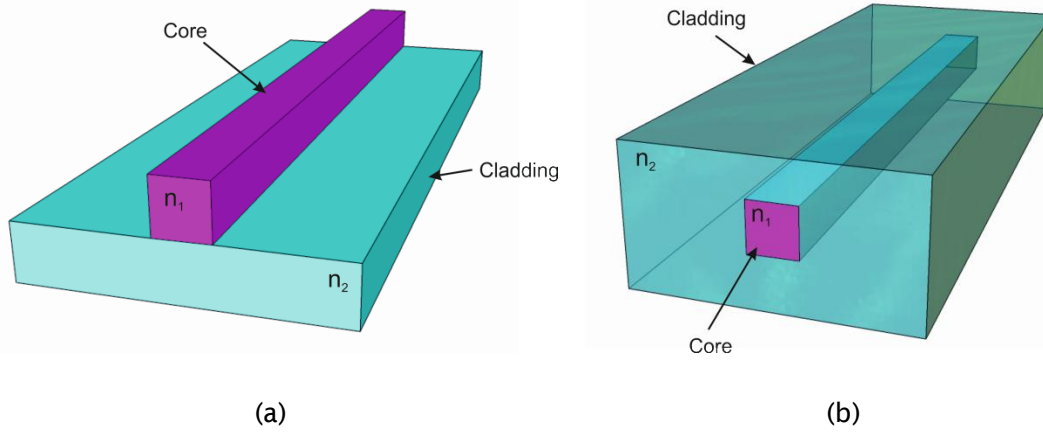


Figure 2.2.3 Two different channel waveguide geometries (a) stripe and (b) buried, where n_1 and n_2 are the core and cladding refractive index, respectively.

2.2.2 Marcatili Method

In this section, the Marcatili method is introduced to show how the technique can analyse the modes of a channel waveguide structure. The Marcatili method offers a high precision and uncomplicated approach to estimate the effective refractive index of a waveguide [18]. Figure 2.2.4 shows the rectangular cross section of refractive index core and cladding layers defined by Marcatili method. The cross section is divided by nine regions which are $n_1, n_2, n_3, n_4, n_5, n_6, n_7, n_8$ and n_9 . The method assumes that areas n_1, n_3, n_7 and n_9 are neglected due to the small proportion of light that propagates in these regions. Yet, the light is strongly confined in the core region, n_5 , with a slight penetration into the n_2, n_4, n_6 and n_8 regions. Accordingly, from such an assumption, Marcatili has defined two independent index profiles; regions A and B, yielding to effective refractive index calculation. The propagation constant, k_z along the propagation axis z is determined by equation (2.42), where $k_s = (2\pi/\lambda)n_s$ ($s = 5, 2, 4, 6, 8$), k_x and k_y are the transverse propagation constants in the x and y directions respectively. The parameters k_x and k_y can be determined by equation (2.43) and (2.44) respectively.

$$k_z = \left(k_5^2 - k_x^2 - k_y^2\right)^{\frac{1}{2}} \quad (2.42)$$

$$k_x = \frac{p\pi}{d_w} \left(1 + \frac{A_4 + A_6}{\pi d_w}\right)^{-1} \quad (2.43)$$

$$k_y = \frac{q\pi}{d_h} \left(1 + \frac{n_2^2 A_2 + n_8^2 A_8}{\pi_1 d_h} \right)^{-1} \quad (2.44)$$

The variable of p and q are the number of local electric field peaks in the x - and y -axis directions. Where A is defined by

$$A_{(2,4,6,8)} = \frac{\lambda}{2(n_s^2 - n_c^2)^{\frac{1}{2}}} \quad (2.45)$$

The effective index, n_{eff} is then calculated by

$$n_{eff} = \frac{k_z \lambda}{2\pi} \quad (2.46)$$

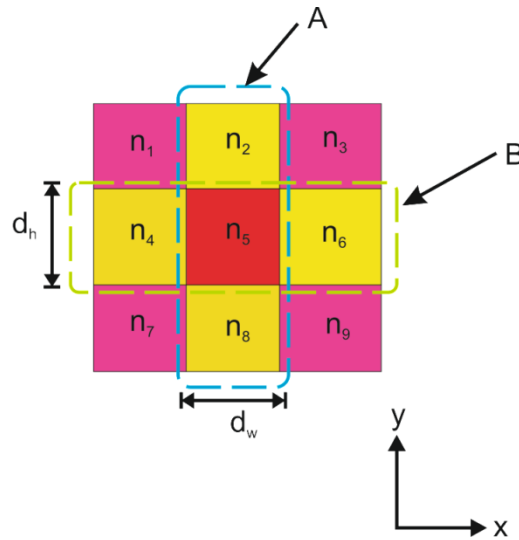


Figure 2.2.4 The Marcatili rectangular cross section of the core and cladding layers.

Although the Marcatili method is not used to model waveguides in this work, the principle of this technique is similar to that used in the FIMMWAVE software tool which will be used to model some of fabricated devices described in this thesis. Thus, the next section briefly presents the principle of the method used in the FIMMWAVE software which is a film mode matching method.

2.2.3 Film Mode Matching Method

FIMMWAVE is a commercial mode solver which uses a fully vectorial mode finder for waveguide structures. It offers a rapid and very accurate solution even for complex and challenging to model waveguide structures, for instance, devices with that have both high index layers and large weakly guided structures. It uses a film mode matching (FMM) method to calculate the mode fields in a waveguide structure [19]. The method yields an accurate mode field calculation over the entire cross section of the waveguide. Moreover, the method offers efficient and straightforward analysis where a simple uniform waveguide structure is simply divided into several slices and layers as depicted in Figure 2.2.5. Due to the symmetric structure, the left side section is not considered in the calculation and hence offers rapid analysis. In the FMM operation, the TE and TM modes for each film are achieved by accumulating the modes that have similar wavevector along the propagation direction and by altering the modal amplitudes in each film, the field distributions at the slice interfaces can be matched.

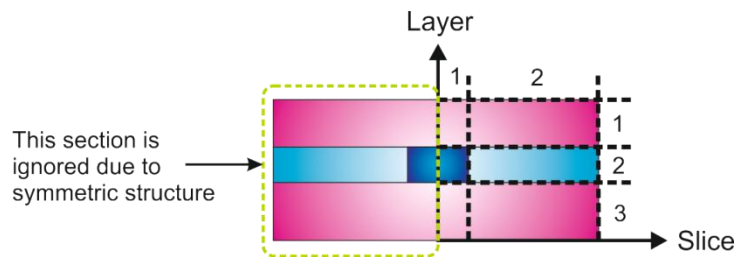


Figure 2.2.5 The simple structure of a uniform waveguide showing the layers and slices section used in the FMM method.

Another method that is used in modal calculation is the beam propagation method. The method has been extensively applied in describing the operation of the propagation mode for particular multimode interference pattern.

2.2.4 Beam Propagation Method

The concept of beam propagation method (BPM) as the name implies, can be used to explore the nature of wave propagation. It may be applied to both linear and nonlinear lightwave propagation. It is a simple numerical algorithm method that uses the slowly varying envelope approximation. The fundamental operation of BPM uses a split-step technique to determine the evolution of the light along a waveguide. The split-step method uses the repeating of an axially small separation distance, z . The details of which are given below.

The foundation of the BPM method is based on the scalar Helmholtz equation as expressed in equation (2.47), where the electric field consists of an axially slowly varying envelope term and rapidly varying term as labelled in equation (2.48).

$$\frac{\partial^2 E}{\partial x^2} + \frac{\partial^2 E}{\partial y^2} + \frac{\partial^2 E}{\partial z^2} + k^2 n^2(x, y, z)E = 0 \quad (2.47)$$

$$E(x, y, z) = \underbrace{\phi(x, y, z)}_{\text{Axially slowly varying envelope}} \underbrace{\exp(-ikn_0 z)}_{\text{Rapidly varying envelope}} \quad (2.48)$$

In the BPM method, these two terms can be considered independently as they affect the light propagation separately in the small distance, z . Figure 2.2.6 (a) shows the beam propagation within the visible tapered waveguide with distance, h and (b) shows the beam propagation within free-space with a thin waveguide in the middle of the distance, h [20]. The phase retardation within the thin waveguide shown in Figure 2.2.6 (b) is treated as the same as the tapered waveguide depicted in Figure 2.2.6 (a).

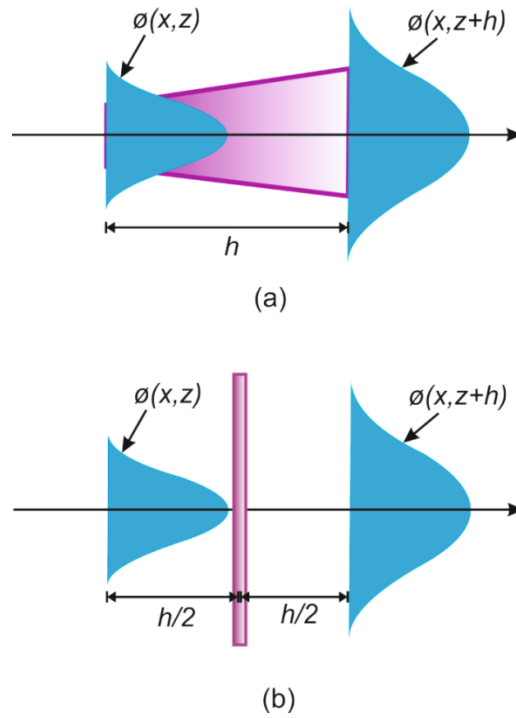


Figure 2.2.6 Schematic diagram of BPM analysis for (a) light propagation within a tapered waveguide and (b) light propagation in free space within a thin waveguide in the middle of the distance, h .

Generally, in BPM analysis, the electric field $\phi(x, z)$ is first propagated through the half way free space distance of $h/2$ before it has phase retardation due to the waveguide distance, h and is then propagated again with another distance $h/2$ in order to attain $\phi = (x, z + h)$. The formal solution of the Fast Fourier Transform (FFT) of the BPM is expressed in equation (2.49) and uses the two operators of A and B.

$$\phi(x, z + h) = \exp\left(\frac{hA}{2}\right) \exp(hB) \exp\left(\frac{hA}{2}\right) \phi(x, z) \tag{2.49}$$

Where,

$$A = -i \frac{1}{2kn_0} \nabla^2, \tag{2.50}$$

$$B = -\alpha(x, z) - ik[n(x, z) - n_0] \tag{2.51}$$

The operator A represents the free space propagation effect, whereas, operator B represents the waveguide effect of loss or gain and phase retardation within the wave-

guide. Where, $-\alpha\phi$ term represents the loss or gain happens in the propagation and $\nabla^2 = \partial^2/\partial x^2$. The method explained in this section is the basis of a multimode interference device operation that will be further explained in Chapter 7.

In the previous section, two different optical structures including slab and channel waveguides have been discussed. This analysis has not considered any other optical functions other than light confinement. Thus, in the following section, the basic concept of the Bragg grating structure is discussed.

2.3 Bragg Gratings

A simple Bragg grating structure is a series of refractive index perturbations along a channel waveguide where the guided light is scattered by each grating plane. Each perturbation results in a small reflection of the propagating light. In the case where the incident light has a similar wavelength to the so called Bragg grating wavelength, reflections from multiple interfaces will constructively add in the counter-propagating direction to form a reflected Bragg grating signal. Whereas, incident light that does not satisfy the Bragg condition will result in the numerous reflected components to be out of phase and will ultimately cancel out. Therefore, the spectral reflectivity will only correspond to the assigned Bragg grating wavelength and other wavelengths will be transmitted through the waveguide as shown in Figure 2.3.1 .

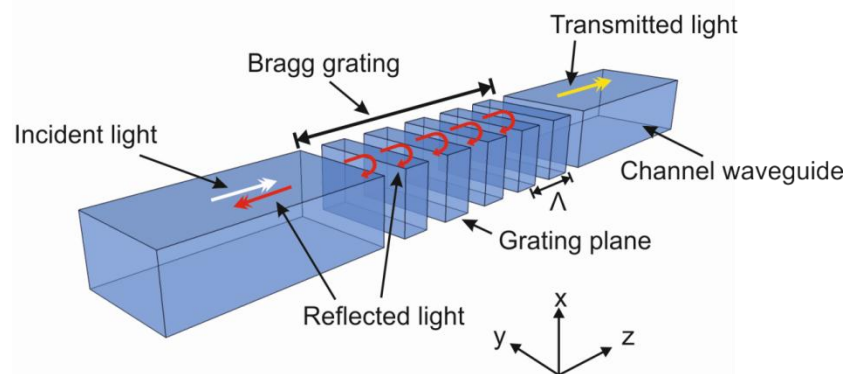


Figure 2.3.1 Propagation of an incident light into a Bragg grating structure where the light is reflected (red line) by the grating structure and the rest of the light are transmitted.

2.3.1 Bragg Grating Structure

The properties of Bragg gratings can be varied depending on its application. This can be done by changing the structure of the Bragg grating through altering the refractive index (i.e. refractive index profile and offset) and grating period. The simplest structure of a Bragg grating is a uniform Bragg grating. It has uniform index modulation where the refractive index profile can be expressed as equation (2.52)

$$n(z) = n_0 + \Delta n \cos\left(\frac{2\pi z}{\Lambda}\right) \quad (2.52)$$

where n_0 is the average refractive index and Δn represents the induced refractive-index perturbation. The parameter z is the distance along the propagation axis. Figure 2.3.2 (a) illustrates the uniform Bragg grating structure with a constant grating pitch. This structure has a uniform refractive index profile as shown in Figure 2.3.2 (b). For low reflectivity gratings, the spectrum can be calculated from the Bragg grating structure via a Fourier transform. The spectral reflectivity of the uniform Bragg grating structure has significant side lobes which can be unwanted feature as shown in Figure 2.3.3 (a) [21]. The existence of the side lobes can yield problems when considering a particular filter and in sensing applications. These side lobes can be suppressed by apodisation technique. The apodisation here means that the magnitude of the refractive index perturbation of the Bragg grating structure is gradually decreased towards a zero value at both ends of the grating length as depicted in Figure 2.3.2 (c). Typical devices implement Gaussian apodisation, a modelled reflection spectrum can be seen in Figure 2.3.3 (b). In this thesis, most of the fabricated devices, which involve Bragg grating structures, have employed Gaussian apodisation. In the following section, the properties of the Bragg grating are described.

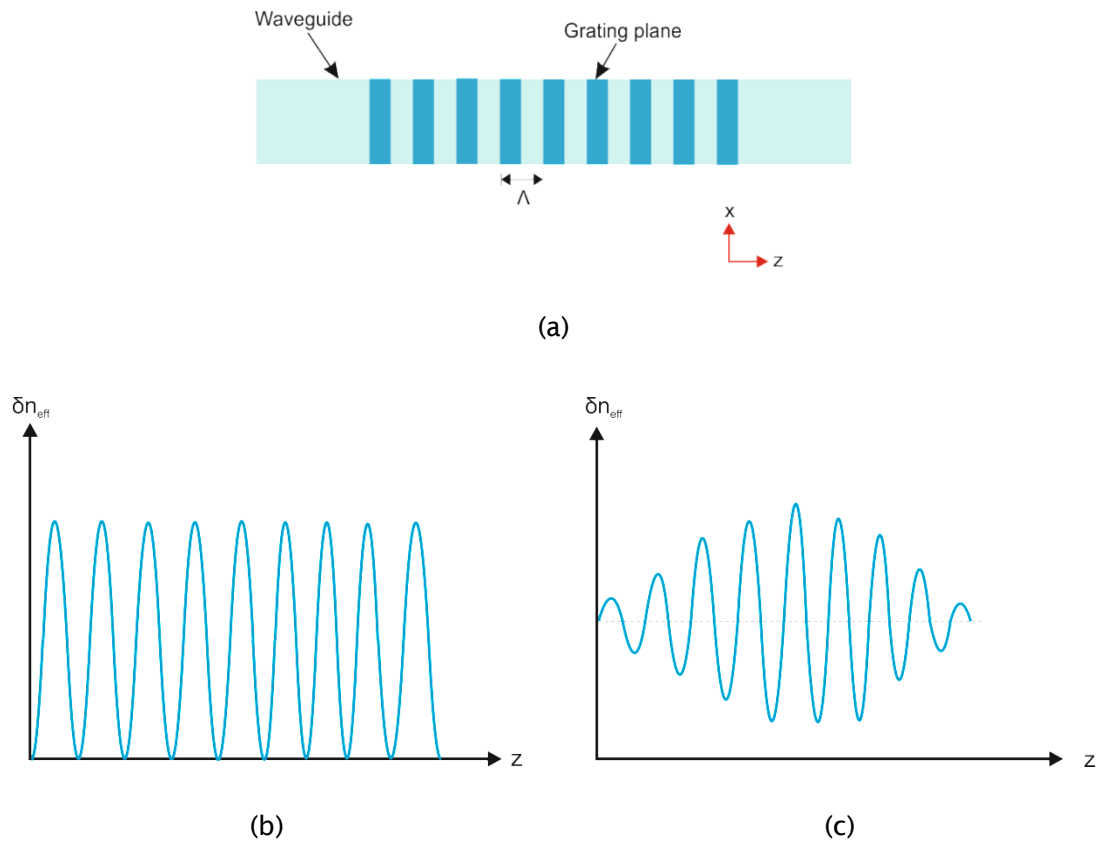


Figure 2.3.2 (a) Illustration of a uniform Bragg grating structure with uniform grating pitch, induced index modulation for (b) uniform Bragg grating and (c) Gaussian-apodised Bragg grating.

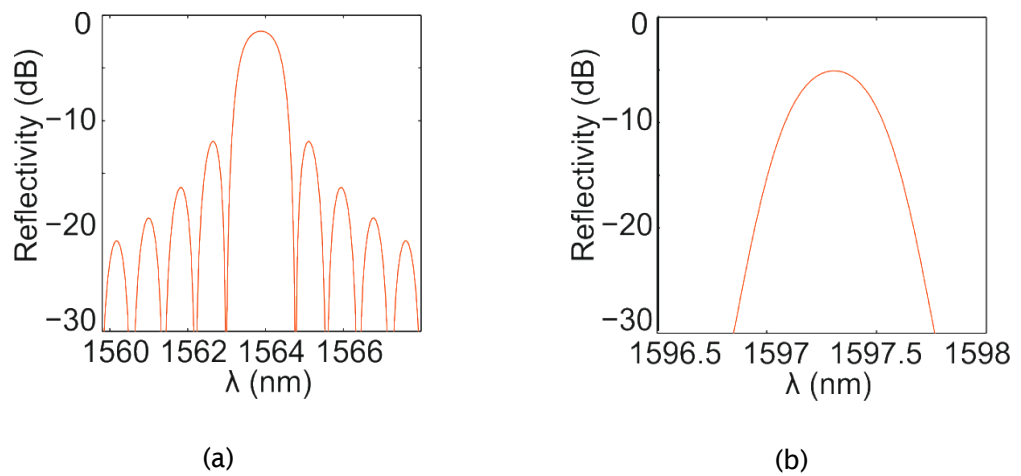


Figure 2.3.3 The reflectivity versus wavelength for (a) uniform and (b) Gaussian apodised Bragg grating structures.

2.3.2 Properties of Bragg gratings

The mathematical analysis of the Bragg grating properties can be presented by using the principles of energy and momentum conservation of the Bragg grating structures. This analysis considers a uniform fibre Bragg grating structure where the grating planes are perpendicular to the direction of light propagation. In the Bragg grating structure, the energy of both transmitted and reflected light must be conserved. In order to conserve the momentum, the wavevector of the reflected wave k_r must be equal to the total of the incident wavevector k_i and the grating wavevector K as expressed by

$$k_r = k_i + K \quad (2.53)$$

If the Bragg grating condition is satisfied, the incident wavevector is equal to the reflected wavevector ($k_i = -k_r$) and $k = \frac{2\pi n_{eff}}{\lambda}$. Therefore,

$$-\frac{2\pi n_{eff}}{\lambda} = \frac{2\pi n_{eff}}{\lambda} + \frac{2\pi}{\Lambda} \quad (2.54)$$

Rearrangement of equation (2.54) leaves to the expression

$$\lambda_B = 2n_{eff} \Lambda \quad (2.55)$$

This simple equation defines the centre Bragg wavelength, λ_B , that is reflected at the Bragg grating structure. This wavelength depends on the effective refractive index, n_{eff} of the optical mode and the grating period, Λ [22].

The mathematical analysis above does not provide any information regarding the strength of the Bragg grating reflectivity and the spectral bandwidth. The following analysis will use coupled-mode theory in order to predict the grating strength and the spectral bandwidth of Bragg grating structure.

2.3.3 Coupled-Mode Theory

The analysis described here is extracted from Erdogan's work [23]. The reflectivity of the grating can be expressed as

$$r = \frac{\sinh^2 \left(\sqrt{\kappa^2 - \hat{\sigma}^2} L \right)}{\cosh^2 \left(\sqrt{\kappa^2 - \hat{\sigma}^2} L \right) - \frac{\hat{\sigma}^2}{\kappa^2}} \quad (2.56)$$

Where L is the grating length, κ is the AC coupling coefficient and $\hat{\sigma}$ is the DC self-coupling coefficient which can be defined as

$$\kappa = \frac{\pi \overline{\delta n_{eff}}}{\lambda} \quad (2.57)$$

$$\hat{\sigma} = \delta + \sigma \quad (2.58)$$

where

$$\sigma = \frac{2\pi \overline{\delta n_{eff}}}{\lambda} \quad (2.59)$$

and

$$\delta = 2\pi n_{eff} \left(\frac{1}{\lambda} - \frac{1}{\lambda_D} \right) \quad (2.60)$$

Where $\overline{\delta n_{eff}}$ is the amplitude of the refractive index perturbation. The difference between the inverse of the propagating wavelength, λ , and the inverse design wavelength, λ_D ($\lambda_D \equiv 2n_{eff}\Lambda$) is known as the detuning, δ . Figure 2.3.4 (a) and (b) show the spectral reflectivity against the normalised wavelength. Different values of grating length are displayed in Figure 2.3.4 (a), where the $\overline{\delta n_{eff}}$ was kept constant at 1×10^{-3} . It can be seen that, the longer the grating length, the stronger the reflectivity. In Figure 2.3.4 (b), the grating length was held constant at 2.0 mm and varied the $\overline{\delta n_{eff}}$ value. It shows that the higher the amplitude index perturbation the stronger the reflectivity. Both parameters affect the strength of the grating reflectivity and the bandwidth.

The spectral bandwidth of grating can be measured from the first zero of both sides of the spectral reflectivity graph. The spectral bandwidth analysis of the grating structure can be calculated by

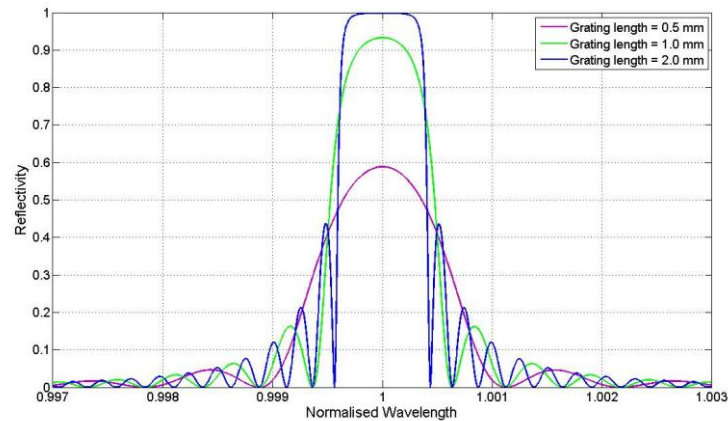
$$\frac{\Delta\lambda_0}{\lambda} = \frac{\overline{\delta n_{eff}}}{n_{eff}} \sqrt{1 + \left(\frac{\lambda_D}{\overline{\delta n_{eff}} L} \right)^2} \quad (2.61)$$

Equation (2.61) shows that there are two key factors that determine the bandwidth of the grating. The first situation is if the grating has a low index contrast, ($\overline{\delta n_{eff}} \ll \frac{\lambda_D}{L}$), then the spectral bandwidth is dependent on the grating length, L , expressed by

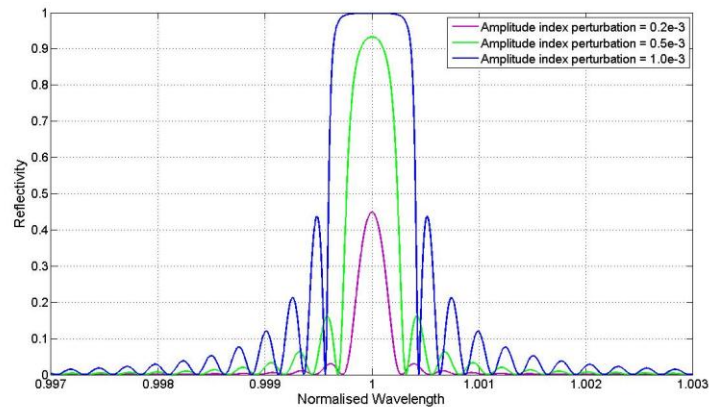
$$\frac{\Delta\lambda_0}{\lambda} = \frac{\lambda_D}{n_{eff} L} \quad (2.62)$$

In the second situation, the spectral bandwidth is dependent on the index contrast of the grating, where the condition $\overline{\delta n_{eff}} \gg \frac{\lambda_D}{L}$ is fulfilled. The spectral bandwidth can then be expressed by

$$\frac{\Delta\lambda_0}{\lambda} = \frac{\overline{\delta n_{eff}}}{n_{eff}} \quad (2.63)$$



(a)



(b)

Figure 2.3.4 Spectral reflectivity against normalised wavelength for (a) grating length and (b) amplitude index modulation variation.

Therefore, it can be understood that a particular bandwidth spectral reflectivity can be achieved by either increasing the grating length or increasing the refractive index modulation amplitude. The Bragg grating structure has been widely used in many applications, especially in optical telecommunications and sensing. In the following section, several optical devices are introduced to give general knowledge regarding their applications.

2.4 Optical Passive and Active Devices

In this section, the operating concept of several optical devices is briefly described to give an overview about the device functionality. This includes optical splitters, sensors and amplifiers. Central to the entire discipline of optical telecommunication is the employment of silica optical fibre technology used as an optical transmission line, yet planar integrated optical devices have also played an important role in the field. Recent developments in optical integrated planar devices have heightened the need for these optical components that are used for light manipulation. There are numerous types of planar material systems that have been demonstrated such as silica-on-silicon, silica-on-insulator, polymer and other semiconductor materials (i.e. Indium gallium arsenide (InGaAr)).

2.4.1 Splitters

Optical splitters are one of the key important components for high-density optical integrated circuit development. The optical splitter is a passive device used to split light into two or more channels with a specific ratio. The operation strongly depends on the design of the splitter itself. The device can be made directly from fibre where several fibres are fused together in a single component to split or combine light into several outputs [24]. However, this is only suitable for a large scale optical-based system. Thus, for a small scale device on chip, typically a waveguide splitter on a planar-based platform is a device of interest as illustrated in Figure 2.4.1 [25]. A number of splitter designs have been fabricated such as y-junction [26], x-coupler [27] and multimode interference devices [28]. In the planar geometry, the conventional route to fabricate these devices is photolithography and etching techniques. The technique provides high quality components but the need for clean-room facilities which is high-cost facilities requirements.

Another alternative that offers low-cost fabrication of integrated waveguide components including splitters has been introduced and demonstrated [29]. In this technique, a splitter can be designed by scanning a UV-spot light on a photosensitivity planar substrate. The device size of the UV-written splitter design is limited by the bend loss of the waveguide and the number of outputs.

A more compact splitter device with many outputs can be realised using the concept of multimode interference. These devices have a small footprint, stable power splitting and large spectral bandwidth. The device has a large width dimension com-

pared to the height of the waveguide to induce multimode interference within the waveguide which will be further discuss in Chapter 7.

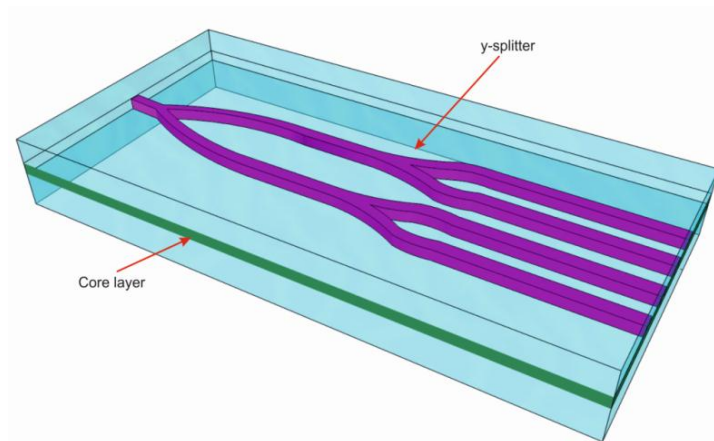


Figure 2.4.1 Optical splitter in a planar substrate combining several y-splitters in a single component.

2.4.2 Optical Sensors

Recently, optical sensors have achieved extensive recognition in fields including civil engineering, medicine and industry [30]. This is due to the inherent advantages offered by optical sensors, which can overcome some of the drawbacks of conventional electrical sensors. These drawbacks include intrinsic limitations of high transmission loss and vulnerability to electromagnetic interference. Other benefits associated with optical sensors include high sensitivity, long-lifetime and the ability to operate in flammable environments. The most common optical sensor is an optical fibre sensor, which have been demonstrated in many fields [31]. Optical fibre sensors can be categorised into two types of sensor namely intrinsic and extrinsic. In an intrinsic sensor the waveguide sensor itself is the sensing element. An evanescent-wave sensor is an example of an intrinsic sensor. In the case of an extrinsic sensor, an optical transducer is attached to the waveguide to sense the measurand. There are many types of optical sensor device using a variety of different physical phenomenon, an extensive review can be found elsewhere [30], [32]. The following section looks at a few optical waveguide sensors.

2.4.2.1 Bragg Grating-Based Sensors

A Bragg grating-based sensor is an optical device sensor that uses a grating structure, such as Bragg gratings as a tool to sense physical or chemical parameters. The technology of an optical fibre Bragg grating (FBG) sensor is well established and has been employed in many applications [33]. The Bragg grating structure is directly interacted upon by the measurand (i.e. physical or chemical parameters) changes in the Bragg grating spectral, such as Bragg grating wavelength shift, can be monitored to provide the signal. This occurs due to the interaction of the measurand with the evanescent component of the guided mode which changes the effective refractive index of the mode and results in a shift of the centre Bragg grating wavelength.

There are numerous techniques which use Bragg grating structures to sense physical and chemical parameters. One of the techniques is using a tilted fibre Bragg grating (TFBG) has been performed for bending sensor [34]. The technique manipulates the transmission power from the cladding modes of the TFBG. Any changes of the TFBG curvature will change the transmission power. Another technique for making a bending sensor implements an erbium (Er^{3+}) doped distributed-Bragg-reflector (DBR) fibre laser [35]. It makes use of a short cavity Er^{3+} DBR fibre laser with a low polarisation beat frequency. The system is highly sensitive to small changes of curvature as small as $1.8 \times 10^{-2} \text{ m}^{-1}$.

In the case of refractive index sensors, a thinned fibre Bragg gratings has been demonstrated to sense a range of different refractive index oils [36]. It manipulates the thickness of the etched cladding in order to expose the Bragg grating structure to the surrounding area and measurand. A recent demonstration extends this work by using a microfiber based Bragg grating sensor [37]. This particular structure offers great benefits such as larger evanescent fields and ultra-small device sizes.

Planar integrated Bragg grating sensors have also shown important role in optical sensor device due to its capability for integration [38]. In the planar Bragg grating sensor, one way of sensing chemical parameters is by using an etched window which exposes the Bragg grating structure to the analyte (i.e. refractive index oil) as shown in Figure 2.4.2.

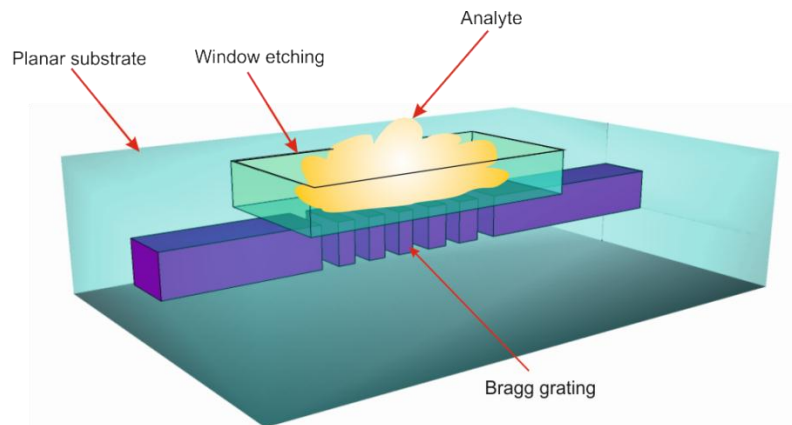


Figure 2.4.2 Planar Bragg grating sensor with a window etched on top of the substrate surface to allow direct contact between the analyte and the Bragg grating structure.

2.4.2.2 Waveguide-Based Sensors

The waveguide based-sensor uses particular configuration to sense chemical or physical parameters where no Bragg gratings are involved in the sensor device. The Mach-Zehnder configuration is one of the most well-recognised waveguide-based sensor geometries [39]. Figure 2.4.3 shows the basic arrangement of the Mach-Zehnder interferometer, where input light is split into two channels via coupler 1. One of the channels is exposed to a measurand while the other is used as a reference. The light in the two channels are recombined using coupler 2 and output light is measured. The interference signal produced by the superimposed light is monitored to sense the measurand.

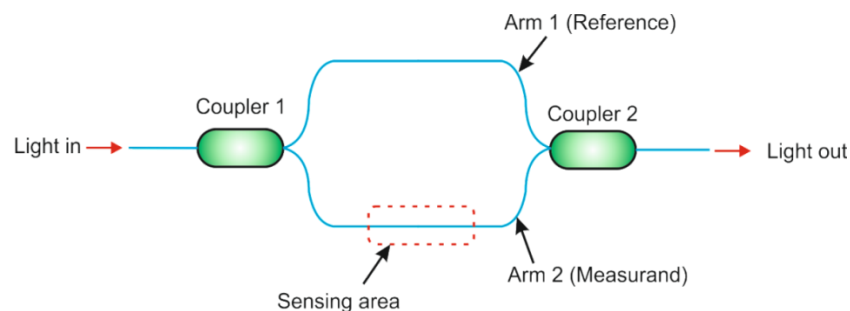


Figure 2.4.3 Illustration of the basic structure of Mach-Zehnder configuration.

Another common technique for waveguide based-sensors uses a Fabry-Perot interferometer (FPI). This multiple-beam interferometer uses a resonant cavity which is exposed to the measurand for sensing purposes. There are two types of FPI configuration namely extrinsic and intrinsic FPI sensors [40]. Figure 2.4.4 shows the configuration of both structures. In the extrinsic FPI sensor, the cavity is located outside the optical waveguide which forms an air cavity, whilst the intrinsic FPI structure has the cavity along the inside of the optical waveguide. The extrinsic FPI is more preferable in a refractive index sensor because the measurand can easily access to the air cavity. In terms of physical parameters, the intrinsic FPI is more desirable due to high coupling efficiency and finesse.

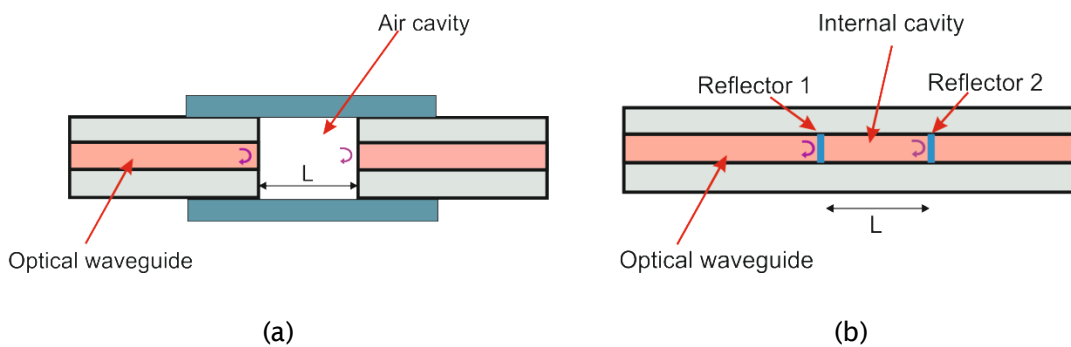


Figure 2.4.4 Fabry-Perot interferometer (FPI) for (a) external and (b) internal cavity structure.

2.4.3 Amplifiers

Optical amplifiers are important component in generating a high-quality optical-based system and are typically used to overcome the losses within it. As the name implies, optical amplifiers are optical devices that amplify transmissions signal to a higher optical power within an active medium. The active medium refers to the medium which contains some active component such as rare-earth ions that are doped into a waveguide. The active waveguide is then pumped using an external light source to excite the active ions into higher energy level and consequently produces population inversion as illustrated in Figure 2.4.5 [41].

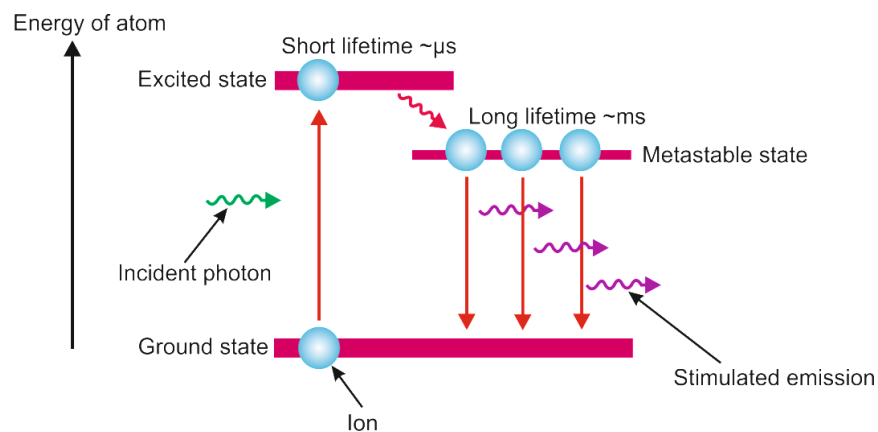


Figure 2.4.5 Illustration of population inversion in the three level transition system of an erbium-doped laser.

Population inversion is the critical process in signal amplification. The population inversion is formed when more excited ions exist in the higher energy level compared to the ground energy level. In a three level transition system for instance, this occurs due to the excited ion that stays in the highest excited state where it can only last around microseconds. After that, it can decay to the metastable state where it stays for a longer time of around milliseconds. Therefore, more ions can be populated at the metastable state which consequently induces the population inversion. The active ions that exist at the metastable state can decay to the ground state by stimulated emission at the same wavelength to the signal that needs to be amplified to generate more optical signal power. Apart from stimulated emission, there is another decay process known as a spontaneous emission. However, in the spontaneous emission, photons are emitted in all directions with no light amplification involved in this process. The photons emitted from this process do not necessarily have the same frequency, phase and direction to the desired signal, thus has a potential to degrade the efficiency of the light amplification.

The most common type of optical fibre amplifier is known as an erbium doped fibre amplifier (EDFA) [42]. The core of the fibre is doped with trivalent erbium ions that can be pumped using 980 nm light for instance and used to amplify a signal about the 1550 nm wavelength range. The properties of the amplifier make it suitable for use in optical telecommunication systems. Basically, the EDFA works by multiplexing the information signal and the pump laser into the erbium-doped fibre and consequently the information signal can be amplified when the pumped signal interacts with the er-

bium-doped ions. The pioneering of this concept has significantly improved optical telecommunication and other optical technology systems.

2.5 Conclusion

As a conclusion, the basic theory regarding planar optical waveguides has been briefly discussed. This includes the mode analysis using Maxwell's equations, Marcatili method, film mode matching and lastly beam propagation methods. The chapter also discusses the operation of the very useful waveguide structure, Bragg gratings. Several important components such as splitters, optical sensors and amplifiers are introduced to give an understanding of the applications of optical waveguides. In the next chapter, several fabrication techniques that are used to fabricate conventional optical fibres and planar waveguides are reviewed.

Chapter 3

Fabrication Techniques

3.1 Introduction

Nowadays, industry is heading towards low-cost fabrication techniques for optical device manufacturing. The development of the flat-fibre approach targets this same aim. As mentioned earlier in Chapter 1, one of the main advantages of the flat-fibre platform is its low-cost fabrication technique. The fabrication of flat-fibre uses conventional silica optical fibre fabrication facilities which leads to low-cost fabrication [11]. That is one of the reasons why the flat-fibre substrate was developed in 2007 [43]. It is also expected that by using the same fabrication technique as standard optical fibre, it will consequently produce a low loss optical waveguide due to the high uniformity of the core layer after being pulled out by the drawing process. From this, it can provide potentially lower loss compared to the typical higher losses in other types of planar platform [44].

In this chapter, a brief description of the process of the flat-fibre fabrication and optical waveguide definition in the core layer of the flat-fibre is explained. The introduction of various alternative techniques that are used to fabricate conventional optical fibre is firstly presented. This includes the making of a so-called preform by various methods. The focus will be on a modified chemical vapour deposition (MCVD) technique, which is the technique has been used to produce the preforms for the flat-fibre platform. However, other common preform fabrication techniques such as plasma chemical vapour deposition (PCVD), outside vapour deposition (OVD) and vapour axial deposition (VAD) are also described for comparison purposes. This is followed by a

description of the fibre drawing process which is implemented to produce long-lengths of commercial optical fibre. Various fabrication techniques for planar waveguide manufacturing are also presented. These will be also covered in this chapter to compare the technique used to fabricate the flat-fibre platform and the other commercial fabrication techniques for different planar substrates.

Optical waveguides are required in order to confine light within the planar substrate for an integrated optical device. There are several techniques that can be used to produce the waveguide [45], [13]. One of the options is to use photolithography and an etching technique [46]. This method is well-established for fabricating complex integrated semiconductor components. It can be cost-effective for mass production. However, the photolithography and etching technique requires a flat surface to begin with, thus it is not suitable for creating waveguides in the flat-fibre substrate as the surface is not entirely flat. Accordingly, the technique of a direct UV-writing is utilised for producing a channel waveguide in the flat-fibre platform [47]. The technique will be briefly discussed as most of the work presented in this thesis has implemented this technique for channel waveguide fabrication. Other alternative techniques for channel waveguide fabrication are also described namely femtosecond laser direct writing and precision dicing saw micromachining. Finally, the characterisation setup that is used to measure the fabricated flat-fibre device is discussed.

3.2 Standard Optical Fibre Fabrication

The technology of an optical fibre is a well-known invention that has been widely implemented in numerous fields [16]. It uses the concept of total internal reflection to transmit light within an optical waveguide. The structure of the optical fibre consists of two basic layers which are the core layer that is surrounded by a layer known as a cladding layer as shown in Figure 3.2.1. In particular, for silica optical fibre, the cladding is often made from a pure silica glass. Whilst the core of the fibre is doped with other dopant elements such as germanium, boron and phosphorus, such that the core layer has a higher refractive index than the cladding layer in order to allow total internal reflection within the core. The addition of dopant elements into the core layer will determine the characteristics of the optical fibre such as refractive index, numerical aperture and the mode profile. The diameter of the core is normally around $\sim 5 - 8 \mu\text{m}$ depending on its applications for a single mode fibre.

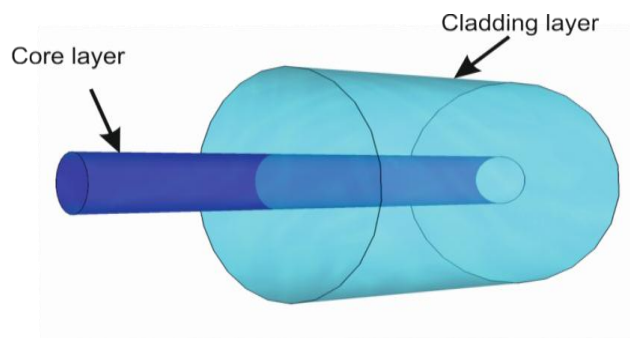


Figure 3.2.1 The basic configuration of an optical fibre. The core has higher refractive index than its surrounding cladding layer.

Much standard optical fibre is doped with germanium to increase the refractive index of the core layer [48]. In addition, by adding the germanium composition, it has been found that the dopant element can increase the photosensitivity of the core layer and this is the basic requirement for UV-written Bragg grating production. Preform fabrication allows the composition of the fibre to be controlled which indirectly determines the specification of the optical fibre. There are various routes for making the preform which are based on vapour phase processes that can be summarized into a large tree diagram shown in Figure 3.2.2 [49]. The vapour phase processes are well-known preform fabrication techniques that use the principle of chemical vapour deposition. They can be categorised into two major sections, namely inside vapour phase oxidation and outside vapour phase oxidation. The technique of inside vapour phase oxidation involves depositing layers on the inside of a substrate tube. In contrast, the outside vapour phase oxidation employs deposition from outside a rod. In this section, we will discuss the common techniques only for preform production namely modified chemical vapour deposition, plasma chemical vapour deposition, outside vapour deposition and vapour axial deposition.

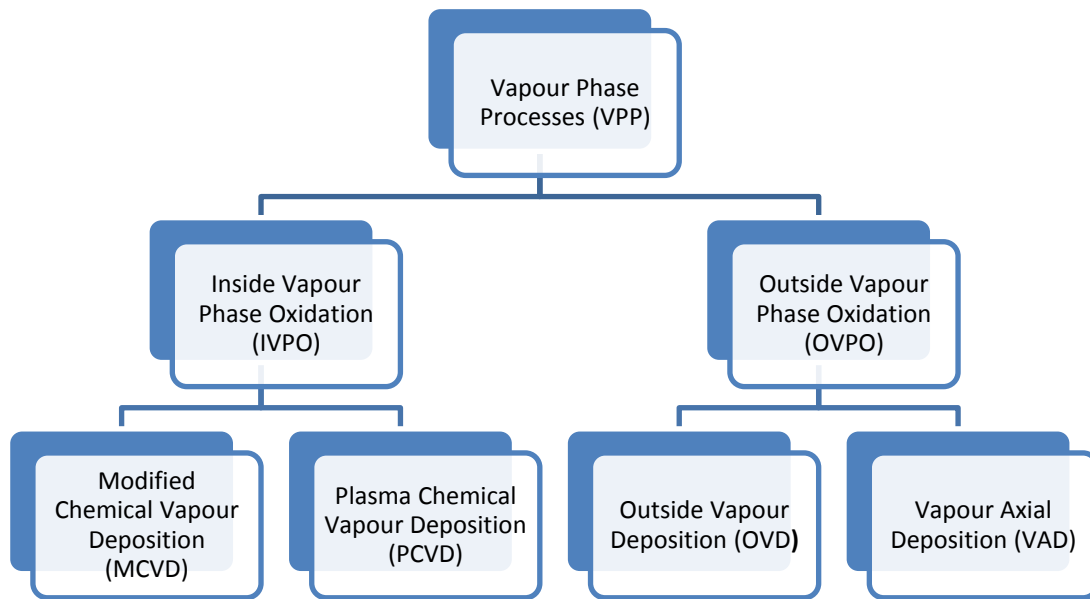


Figure 3.2.2 The tree diagram of vapour phase processes where including two different techniques of vapour phase oxidation (VPO) namely inside-VPO and outside-VPO.

3.2.1 Preform Fabrication

The most common technique that is used to fabricate a preform is using modified chemical vapour deposition (MCVD) [50]. The MCVD technique is compatible with high vapour pressure precursors. The technique also offers clean deposition process due to the preform being prepared from inside the glass tube which can avoid contamination from outside factors. Another technique that fabricates the preform from inside is known as a plasma chemical vapour deposition (PCVD). The main difference between those techniques is the heating process where the MCVD uses flame torches while the PCVD employs a plasma torch. The primary reason of using the plasma torch is to reduce the hydroxyl (OH) element in the preform when using the flame torch. In contrast to the MCVD and PCVD, a deposition technique that is prepared from outside a target rod known as outside vapour deposition (OVD) will also be discussed. This is followed by a vapour axial deposition (VAD) which is a very similar technique to OVD but is performed with an axial fabrication direction.

3.2.1.1 MCVD

Modified chemical vapour deposition is a well-known technique to fabricate a specialty fibre such as rare-earth doped optical fibres for fibre amplifiers. It has been reported that using the technique, the propagation loss of an optical fibre can be reduced to less than 0.2 dB/km [51]. The technique is based on the deposition of the reagents on the inside surface of the rotating substrate tube via a high temperature [50]. Figure 3.2.3 shows the configuration of the MCVD preform fabrication process. The process involves passing through a carrier gas such as oxygen into a liquid precursor to evaporate the chemical reagent which is directed into the rotating substrate tube. The liquid precursors are typically from chemicals that have high vapour pressure at room temperature such as silicon tetrachloride (SiCl_4) and germanium tetrachloride (GeCl_4). The amount of the chemical reagent flows into the tube is controlled by the flow of the carrier gas. As the reactant agents flow through the rotating substrate tube, the heating process is applied to the outside of the tube via a flame torch burner. The burner is moved in the same direction as the flow.

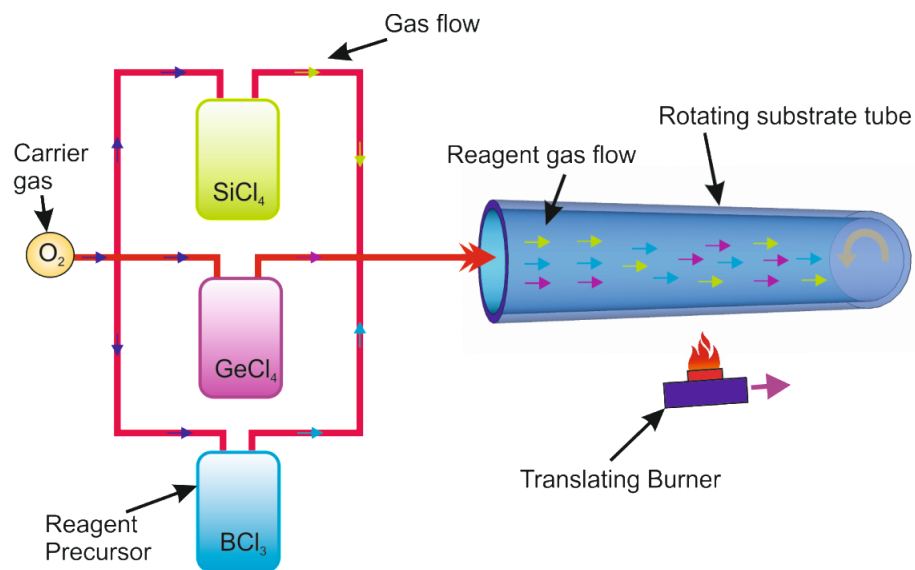


Figure 3.2.3 A configuration process of a modified chemical vapour deposition (MCVD) technique.

At high-temperatures (e.g. in excess of 1200°C), the oxidised reactant agents will transform into particles soot that are then deposited downstream from the hot zone. This phenomenon is known as a thermophoresis process and is illustrated in Fig-

Figure 3.2.4 (a). At this stage, the process is known as deposition process. The deposited soot is then fused together to form a thin glassy layer when the burner reaches the section where the particle soot being deposited as shown in Figure 3.2.4 (b). At this stage the process is called as consolidation process where a higher temperature is supplied onto the rotating substrate tube. The refractive index of the deposited layer is determined by the doping concentration used and the flow rate. Finally, the substrate tube is then collapsed into a solid preform using a high burner temperature and is drawn into optical fibre in the next step of drawing process which will be discussed later. In the next section, the process of plasma chemical vapour deposition is explained.

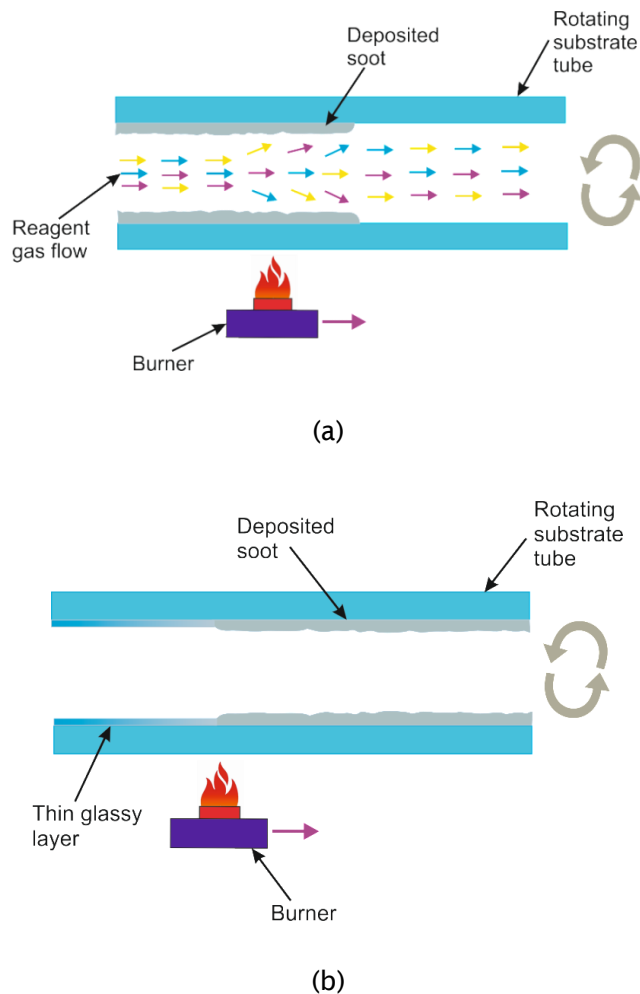


Figure 3.2.4 Making a preform using the MCVD technique where (a) shows the deposition process and (b) the consolidation process.

3.2.1.2 PCVD

The principle of plasma chemical vapour deposition (PCVD) is similar to the MCVD technique with key differences in the heating system. Also, in the PCVD method, the process of deposition and consolidation of the preform is prepared at the same stage [52]. A plasma process is used to induce a chemical reaction between the reactant agents, which ultimately creates the oxidation process within the rotating substrate tube. The plasma is produced using a microwave cavity resonator which is exposed to the inside of the tube and traversed as shown in Figure 3.2.5. From this process, a few micrometres of a glassy layer can be achieved compared to the MCVD technique. Other techniques that are modified from this concept are plasma enhanced CVD, plasma impulse CVD and surface plasma CVD. The most common technique that is used to fabricate a thin planar substrate is the plasma enhanced CVD which will be discussed later.

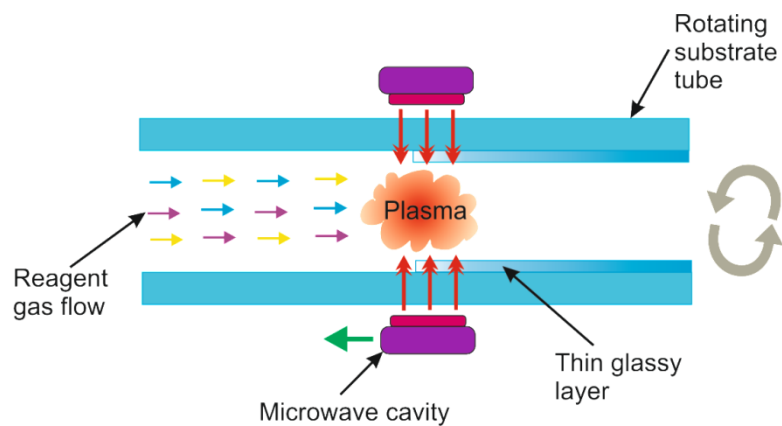


Figure 3.2.5 A plasma CVD process using a microwave cavity to make a preform.

3.2.1.3 OVD

The outside vapour deposition (OVD) fabrication technique involves soot deposition on the surface of a target rod [53]. The technique has been employed to fabricate a single mode and multimode fibre with improved optical specification such as numerical aperture and reduced hydroxyl effects [54]. A torch burner with mixed reactant agents and carrier gas is directed onto the target rod which traverses in both forward and backward directions to create a soot body as shown in Figure 3.2.6. The reactant agents that are fed to the torch are vaporised and controlled to alter the refractive index of the preform. The core layer is deposited first and followed by the cladding layer. After the soot deposition is completed, a process known as dehydration and consolidation procedure is taken placed in a furnace. At this stage, the soot body is dried to make sure no contamination appears in the preform and also to remove hydroxyl. Then, a high temperature is used to form a solid transparent glass preform. The solid preform is then transferred to the fibre drawing tower for finished optical silica fibre.

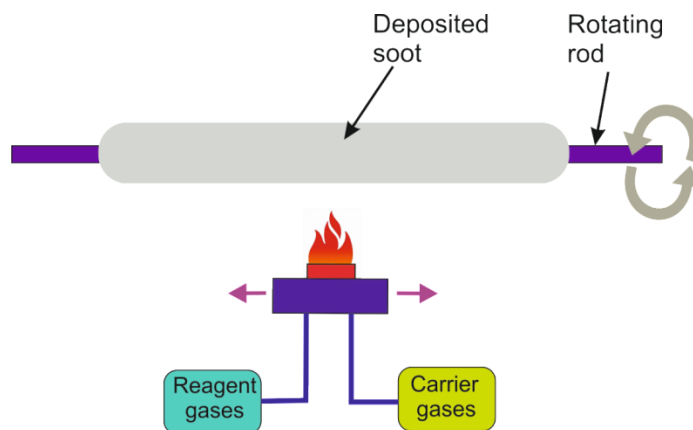


Figure 3.2.6 Outside vapour deposition (OVD) for making a preform, where soot particles are deposited outside a rotating rod.

3.2.1.4 VAD

The vapour axial deposition (VAD) technique has similar process with OVD where deposition is prepared from outside a target rod. The key difference of this technique is the continuity of the deposition and consolidation process in a single axial direction for preform fabrication as shown in Figure 3.2.7 [55]. Flame torches are firstly directed onto the bottom of the target rod to create a deposited soot body. Then, the deposited rod is pulled upward so that the torches do not need to move. The process is continued with sintering process where the deposited rod is exposed with other torches that are placed further up the preform. The preform is then drawn for final optical fibre. The technique is commonly used to fabricate a commercial standard single mode fibre due to the capability of the method to produce large preforms that can be drawn into 100's kilometres length. It has been reported that by using the VAD technique, a low loss single mode fibre with 0.2 dB/km was achieved [56].

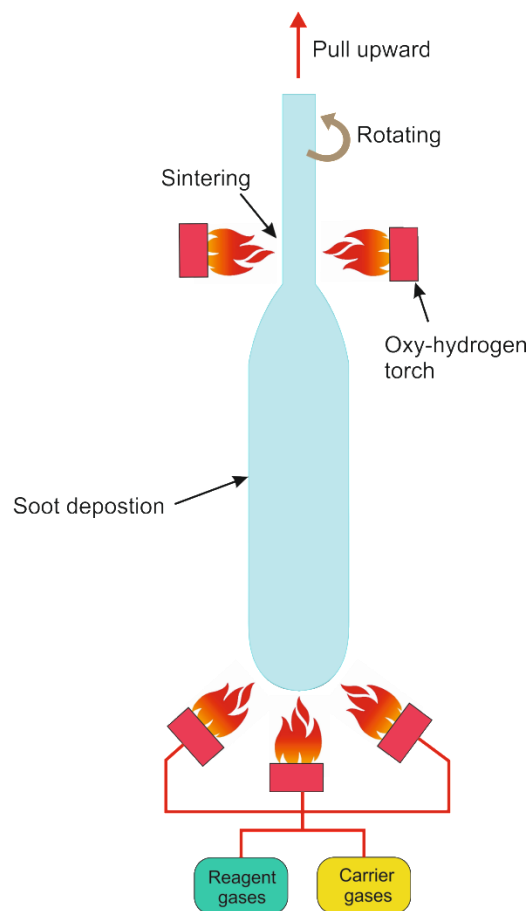


Figure 3.2.7 Vapour axial deposition (VAD) process for making a preform.

3.2.2 Fibre Drawing

Fibre drawing is the final process of producing an optical fibre. The preform that has been collapsed into a solid glass form at the preform glass lathe is mounted vertically into the furnace of the fibre drawing tower. To start with, a short length of the preform tip is heated at a high temperature until a small piece of molten glass drops under gravity. Then, a thin glass tail of the preform is drawn to a capstan and pulled it towards a drum winder. The diameter of the pulled fibre is computer-controlled where considering the feed rate and the capstan speeds of the process. The fibre is coated on-line using polymer in order to protect the fibre whilst pulling it. The process of the standard fibre drawing tower is shown in Figure 3.2.8. Next, the fabrication of flat-fibre platform will be briefly described. In advance, other conventional techniques that are used to fabricate a planar substrate will be firstly introduced in the next section.

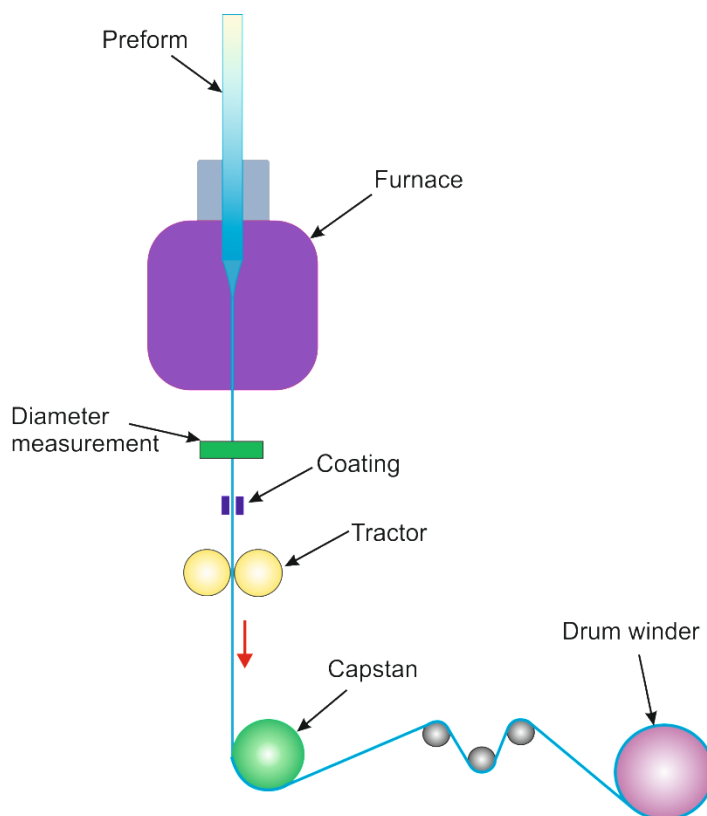


Figure 3.2.8 A standard fibre drawing tower that is used for drawing a conventional optical fibre.

3.3 Fabrication Techniques of Planar Waveguide

It is worth comparing planar waveguide fabrication processes to that used for making the flat-fibre planar platform. There are many types of planar substrate systems that have been demonstrated using various techniques of fabrication. In this section, the planar substrate of silica-on-silicon is reviewed due to the similarity of the structure to the flat-fibre platform. Figure 3.3.1 shows the structure of the silica-on-silicon which consists of three silica layers upon a silicon wafer. The core layer is sandwiched with upper cladding and under cladding layers. The three silica layers are made to have well-matched refractive index to produce zero-delta configuration. The zero-delta configuration means zero difference in refractive index between those three layers. This is done by altering the dopant composition of each silica layer. Normally, dopants such as germanium, boron and phosphorus are added to the silica layer. Apart from altering the refractive index, the dopants also used to adjust the photosensitivity of the layer. In particular, the core layer contains more germanium and boron to increase the photosensitivity of the layer for the next channel waveguide developing via UV-writing technique. Two common techniques used to fabricate the silica-on-silicon substrate are flame hydrolysis deposition (FHD) and plasma enhanced chemical vapour deposition (PECVD). Both techniques are introduced in this section along with their advantages and disadvantages.

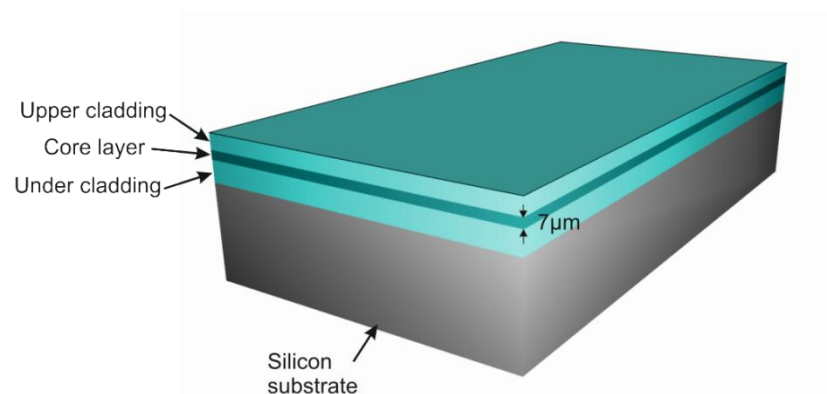


Figure 3.3.1 An image of the silica-on-silicon platform where the core layer is sandwiched between the upper and under cladding. The base of the device is silicon.

3.3.1 Flame Hydrolysis Deposition

Flame hydrolysis deposition (FHD), as the name suggests, uses a flame hydrolysis reaction to produce a thin film layer on a planar substrate [57]. The FHD fabrication process described in this section is referring to a production of a silica-on-silicon substrate as noted earlier. Before the FHD process commences, the silicon wafer must be treated first by placing the wafer into a furnace with temperature around 1100°C. This is to allow a thin thermal oxide growth on the wafer surface to support bonding between the silicon wafer and the deposited silica layers on top of it. The technique used in the FHD method is a similar process to the OVD deposition where the reactant agents are supplied directly to the burner. FHD uses an oxy-hydrogen flame to induce an oxidation of the reactant agents which ultimately produces particles of soot which are deposited on the oxidised silicon wafer as illustrated in Figure 3.3.2. The surface of the wafer is directly exposed to the flame and traversed forwards and backwards until all the area of the silicon is covered. It must be noted that the different thermal expansion between the silicon substrate and the silica layers will induced stress in the core layer and this results a stress induced birefringence. However, the stress induced birefringence can be reduced by using an appropriate thermal expansion of the overcladding of the core layer [58].

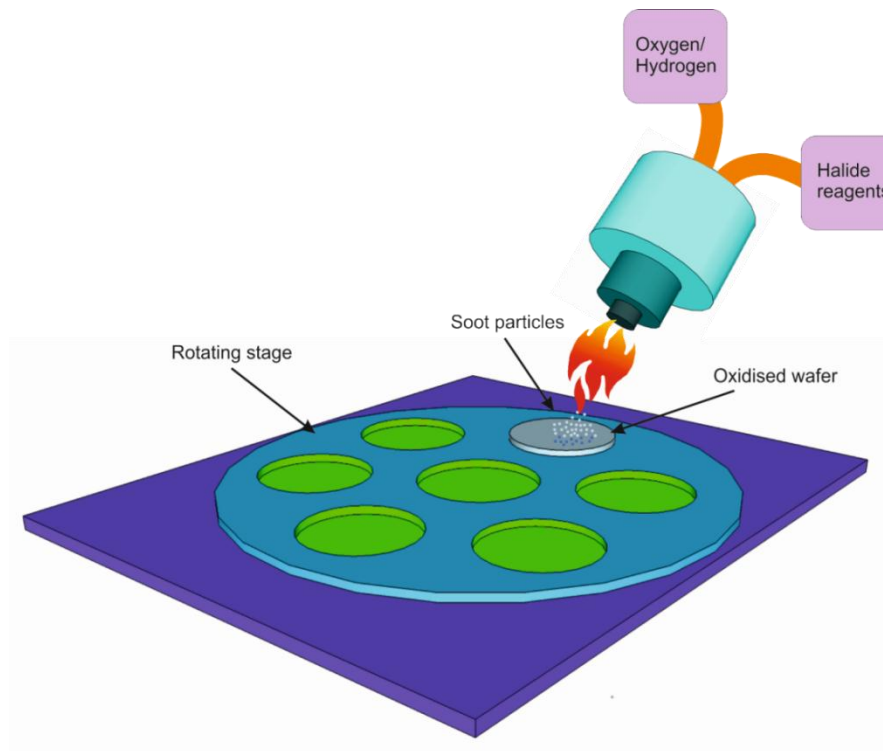


Figure 3.3.2 Flame hydrolysis deposition technique to deposit a planar substrate.

Silicon tetrachloride (SiCl_4) is used as the reactant agent to produce silica layer and added with some other precursors such as germanium tetrachloride (GeCl_4), boron trichloride (BCl_3) and phosphorus trichloride (PCl_3) for adjusting the refractive index and level of photosensitivity of each layers. Adding the germanium and phosphorus to the silica layer will increase the refractive index of the layer, yet, decreased refractive index is obtained when adding the boron. Following this, the refractive index and the level of photosensitivity of each layer can be adjusted. The deposition process is followed by a consolidation stage to form a solid dense glassy layer, where the finished deposited layer is transferred to the furnace with temperature around 1400°C [59]. It has been reported that the propagation loss of 0.01 dB/cm in a channel waveguide fabricated by FHD is achievable [9]. Another deposition technique used to produce the silica-on-silicon substrate is known as plasma enhanced chemical vapour deposition (PECVD). This technique will be briefly discussed in the next section.

3.3.2 PECVD

Plasma enhanced chemical vapour deposition (PECVD) is a derivative technique from chemical vapour deposition (CVD). It offers better performance compared to the standard plasma CVD techniques. The major advantages provided by the PECVD technique are the high deposition level and also the capability of the technique to produce a good quality of a thin film [60]. In addition the technique also benefits from flexibility to develop different types of planar substrate layers. The PECVD technique is routinely implemented in microelectronics fabrication. A key factor in its uptake is the ability of PECVD to work at lower temperatures [61]. Figure 3.3.3 shows the configuration of plasma enhanced vapour deposition for planar deposition. In general, the technique uses plasma energy induced by supplying an external radio frequency (RF) electric field to accelerate charged particles into a vacuum chamber to ionize the supplied reactant gases. From this, a very thin layer of material is deposited on top surface of a planar substrate placed in the vacuum chamber. In the case of silica deposition, normally the reactant gases silane (SiH_4) and nitrous oxide (N_2O) are used. The applied RF power and also the amount of the reactants gases are important parameters to ensure the deposition of low loss glass layers. It has been reported that using the PECVD technique, silica glass layers with propagation losses as low as 0.2 dB/cm can be achieved [62].

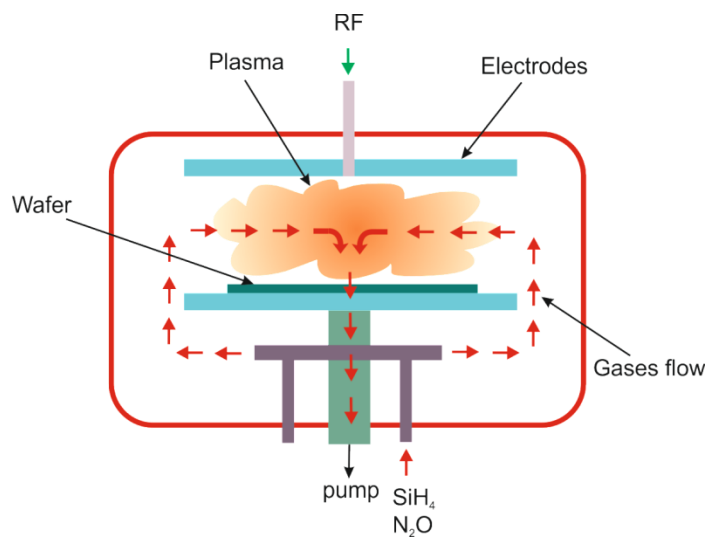


Figure 3.3.3 Illustration of a plasma enhanced chemical vapour deposition process to produce a planar substrate.

3.4 Flat-fibre Platform Fabrication

The industrial demand for a cost effective device fabrication has motivated many researchers and it was this motivation which led to the innovation of the flat-fibre platform noted earlier. Two different fabrication techniques for conventional optical fibre and planar platform substrate have been introduced in the previous sections to give an overview of how both structures are developed. Here, the particular processes and parameters used to fabricate a flat-fibre platform are described. The flat-fibre fabrication was prepared by Dr. *Andrew Webb*. The flat-fibre platform is fabricated based on the fabrication technique of conventional optical fibre using MCVD and fibre drawing. The technique differs from conventional optical fibre manufacture as the substrate tube is collapsed during the fibre drawing where the flat-fibre is shaped into a planar geometry. This is facilitated by applying a vacuum to the top of the preform end tip.

The geometry of the flat-fibre platform shown in Figure 3.4.1 (a) and (b) represents the cross section of the substrate and the flexibility of the flat-fibre in long lengths, respectively. The flat-fibre is made from silica material, the same material used in the conventional low loss optical fibre. The characteristics of the flat-fibre become more interesting due to the well-matched coupling between the flat-fibre and the existing standard optical fibre. The core section has a higher refractive index than the

surrounding cladding section through the manipulation of dopant composition of the core section.

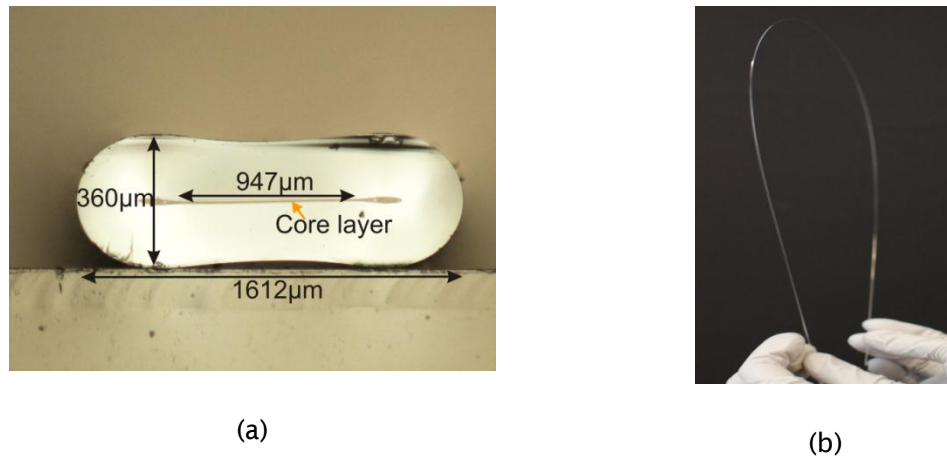


Figure 3.4.1 Flat-fibre geometry showing (a) cross section and (b) flexibility of a length of the flat-fibre substrate.

There are two types of flat-fibre substrate namely passive and active flat-fibre. The composition of both flat-fibre platforms is summarised in the Table 3.4.1. The passive flat-fibre refers to the composition of the core section where no rare-earth ions have been doped in the core. Only dopants that can increase the refractive index and the photosensitivity are added into the core layer of the passive flat-fibre. Whilst the erbium doped flat-fibre, as the name implies, is the active substrate that has erbium in its core layer composition. Despite the two platforms having different core compositions, the fabrication technique is the same other than the addition of the erbium dopant to the preform.

Table 3.4.1 Core layer composition of passive and active flat-fibre substrates.

Flat-fibre types	Composition			
	Germanium (Ge)	Boron (B)	Erbium (Er)	Aluminium (Al)
Passive	✓	✓	X	X
Active	✓	X	✓	✓

3.4.1 Flat-fibre Preform Fabrication

In this section, the particular process of fabricating the passive and active flat-fibre preform is explained. A modified chemical vapour deposition (MCVD) technique is used to make the preform of the flat-fibre. The principle of the technique has been introduced in previous section; here more details of the process in terms of making the flat-fibre preform will be given. Figure 3.4.2 shows the flow chart of fabricating the flat-fibre. This is to give a clear explanation about the process of passive and active device fabrication.

The process starts by preparing a glass tube (Heraeus Suprasil F300) with gas phase etching and flame polishing for surface roughness removal. Next, several silica cladding layers are deposited on the inside of the substrate glass tube to provide a low loss barrier. This is followed by a soot deposition on top of the cladding layer for the core layer preparation. During these processes, the glass soot, primarily silica (SiO_2), is deposited on the surface of the glass tube whilst a torch burner is traversed in the same direction of the gas flow. This is done by passing the reagent gas, such as SiCl_4 , into the substrate glass tube. Other additional dopants can be included by adding reagents such as germanium tetrachloride (GeCl_4) and boron trichloride (BCl_3) to the gas stream.

For the passive flat-fibre platform, the MCVD process is undergone at high temperature allowing the consolidation process to be performed immediately after the soot deposition and is done so by a single pass of the flame torch. However, in the case of active flat-fibre platform, the soot deposition process is prepared at lower temperature. This is to allow solution doping of the soot particles as illustrated in Figure 3.4.3. For the active flat-fibre used in this work, a solution doping of 0.67 g of erbium chloride (ErCl_3) and 35.0 g of aluminium chloride (AlCl_3) in 175 ml of methanol (MeOH) has been used. The solution doping liquid is fed and distributed gently into the rotating substrate glass tube containing soot body using an in-situ solution doping technique [63]. Following this, the deposited soot is consolidated using the flame torch of the MCVD lathe.

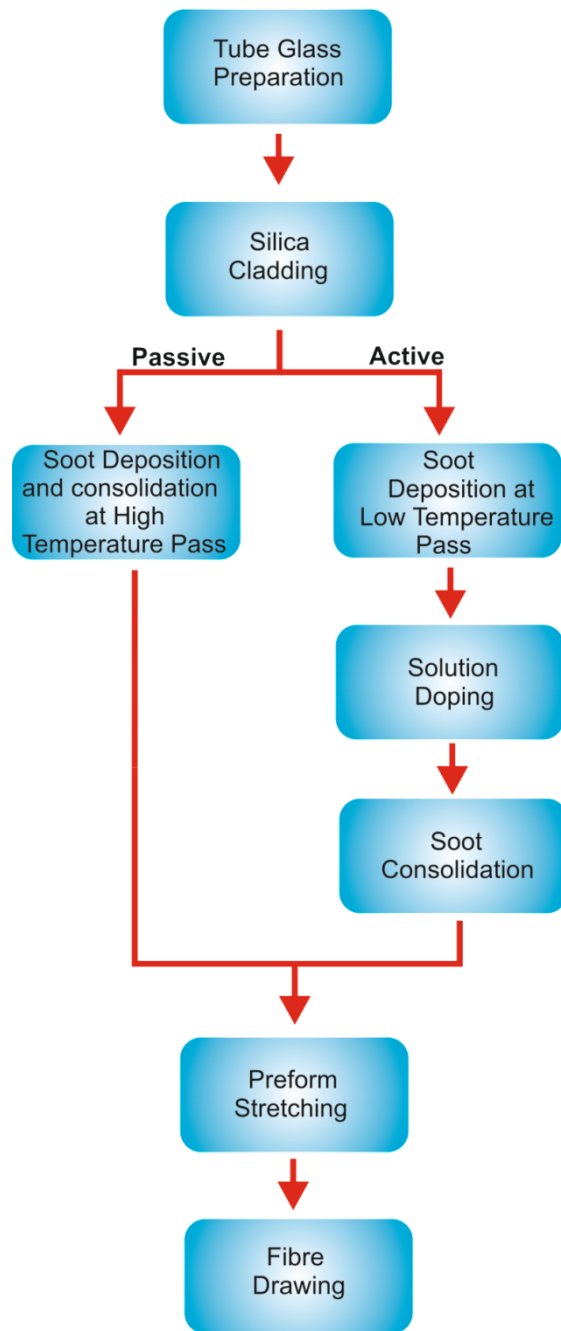


Figure 3.4.2 The flow chart of flat-fibre fabrication for passive and active device.

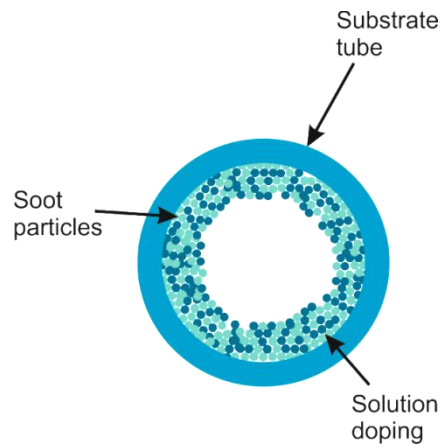


Figure 3.4.3 Illustration of combination between soot particles and solution doping after the solution doping process is taken placed.

In the final stage of making the flat-fibre preform is a stretching process to alter the dimension of the substrate glass tube. Once the process of making the preform is completed, a fibre drawing process is taken place, where corresponding process is described in the next section.

3.4.2 Drawing the Flat-fibre Preform

Drawing flat-fibre is achieved via a fibre drawing tower and was implemented in a very similar process as conventional optical fibre as previously discussed. However, in drawing the flat-fibre, the conventional process is altered whereby the upper end of the flat-fibre substrate is connected to a vacuum as illustrated in Figure 3.4.4. This is to aid the collapsing process of the flat-fibre substrate, into a planar geometry, in the furnace chamber of the draw tower. Tractors act as a driving force to pull down the flat-fibre. Two important parameters in controlling the geometry of the flat-fibre are the vacuum pressure and the temperature of the furnace chamber. In this particular work, the vacuum pressure was set to 5 millibar and the furnace temperature was around 2100 °C. Once the right geometry is achieved, at certain value of pressure and temperature, the fibre is drawn into a long length of several meters.

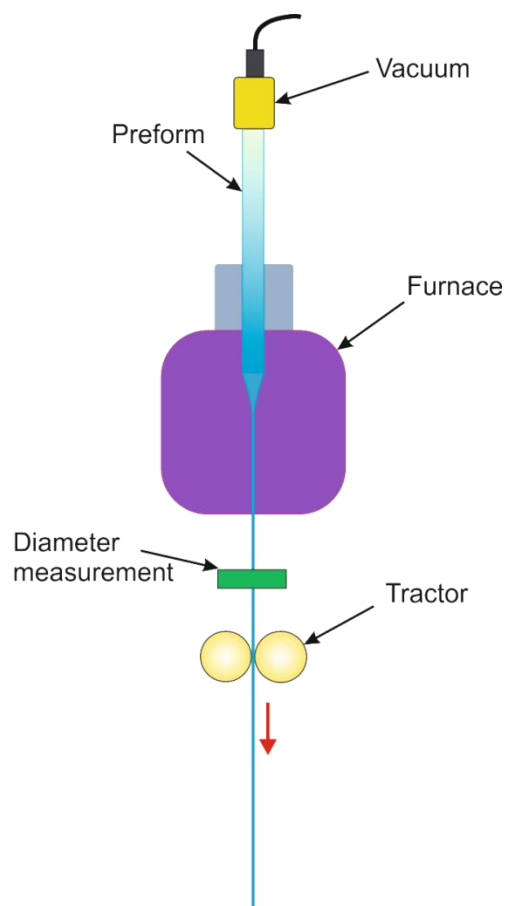


Figure 3.4.4 Illustration of drawing a flat-fibre platform by applying a vacuum to the upper end of the preform.

For waveguide defining, the flat-fibre is cleaved into small lengths depending on the requirements of the optical device. The method for waveguide defining is described later. Beforehand, the photosensitivity of material will be discussed first in order to understand the physical mechanisms involved in the UV-writing technique.

3.5 Photosensitivity

Photosensitivity is a critical parameter that must be understood in order to produce an optical device using UV-writing. By definition, the photosensitivity of a material is the level of response to the exposure of a specific light. Normally, the material response is a localised refractive index change that is permanently altered [64]. It has been found that the addition of germanium (Ge) for instance into a silica-based material will increase the photosensitivity of the material. The first demonstration showing the photosensitivity of Ge-doped optical fibre by *Hill et al* has had a high impact on development of various optical waveguide devices based on UV-writing technique [65]. They used an argon (Ar) ion laser at 488 nm launched into a fibre and overtime observed the generation of a Bragg grating. They revealed the level of fibre photosensitivity through assessing the refractive index changes of the fibre due to the Ar-ion laser exposure.

Considerable effort has been made to investigate the ability of Ge doping of silica to increase the material photosensitivity [66]. Despite the fact that Ge-doped silica fibre shows photosensitivity, it has been discovered that the photosensitivity can be further enhanced through a hydrogen loading process [67]. This approach has significantly improved the refractive index change when exposed to a UV-light without the need for increasing the germanium composition, refractive index changes of around 5.9×10^{-3} have been achieved [67]. Hydrogen loading is performed by diffusing hydrogen (H_2) into a fibre, with the Ge-dopant, at low temperatures and high pressures. Principally, the H_2 molecules that diffuse into the Ge-doped silica fibre will react at the Si-O-Ge sites, which results to the formation of Si-OH and oxygen deficient germanium defects [68]. The formation of oxygen deficient germanium defects ultimately contributes to the improvement of refractive index change when exposing the UV-light. This is due to the absorption peak of the germanium oxygen deficient centres (GODCs) occurs at approximately 240 nm when exposed to UV-light. Using this technique an index contrast of ~ 0.0096 has been reported [14]. However, it must be noted that hydrogen loading may also increase the hydroxyl (OH) content of the glass which results in an absorption at about 1400 nm wavelength. However, this is not a problem when the working wavelength is not in that region and most of the fabricated devices presented

here uses wavelength around 1550 nm. Nevertheless, another technique known as deuterium loading can also be used to increase the photosensitivity of the fibre instead of hydrogen loading. This process yields lower propagation loss due to the presence of oxygen-deuterium bonds which do not have absorption near to the wavelength of interest (i.e. 1550 nm). In practice the hydroxyl absorption is negligible in the short propagation lengths of planar waveguides. Moreover, adding other dopants such as boron (B) and tin (Sn) into the core layer of the fibre can be also applied to further increase the photosensitivity of the material.

3.6 Channel Waveguide Fabrication

Development of integrated optical devices in flat fibre requires channel waveguide defining for light manipulation. The earlier section of this chapter only covers the fabrication of a planar slab waveguide. There are several techniques of waveguide definition that have been demonstrated to produce integrated optical devices. The common technique that is normally used for channel waveguide formation is through using a photolithography and an etching technique [69], [70]. This technique originates from the fabrication of microelectronic chips and with some modification of the process it is currently the preferable route for the development of integrated optical devices. The advantages and disadvantages of using this technique are mentioned in the next section. However, it must be noted that a requirement of using the photolithography and etching technique is that the substrate must be flat. Therefore, the technique is not well-suited to the flat-fibre platform with an uneven surface.

Accordingly, an alternative technique for waveguide defining in the flat-fibre platform is a direct UV-writing technique. In the direct UV-writing technique, the material of the planar substrate has to be photosensitive to a UV-light in order to increase the refractive index of the core layer which subsequently forms the channel waveguide. Most of the work presented in this thesis has implemented the UV-writing technique for optical device definition. For comparison purposes, a femtosecond laser direct writing technique is also described in this chapter. Apart from these techniques, there is another alternative method to develop a channel waveguide via a micromachining technique. The micromachining technique has been used in fabricating a multimode interference device (MMI) which is discussed later in this chapter.

3.6.1 Photolithography/Etching

Photolithography and etching methods have the ability to produce a complex integrated device which does not require a photosensitive planar layer. It is suitable for a large quantity production which leads to a low cost fabrication. However, for a prototype device fabrication, the technique is not desirable as different designs require a different photo-mask which makes the technique time consuming and costly. To understand the process of the technique, the principle steps of producing a channel waveguide is explained, although, such methods have not been used to fabricate any optical devices presented in this thesis.

Figure 3.6.1 shows the basic procedure of fabrication via photolithography and etching. It starts with a planar substrate with core and under cladding layer. The process of photolithography begins by depositing a photoresist coating on top of the core layer. This is followed by placing a photo-mask on top of the photoresist layer which subsequently covers the desired sections thereby creating the waveguides. The mask and sample are exposed to UV-light and the photoresist is developed to remove the unwanted photoresist. Once photolithography is complete, an etching process will be taken place. There are two common techniques for the etching process either wet [71] or dry etching [72]. The etching process will etch away the core layer section which is not covered by the photoresist area. Finally, the uncovered waveguide channels are deposited with upper cladding layer to create the final optical devices.

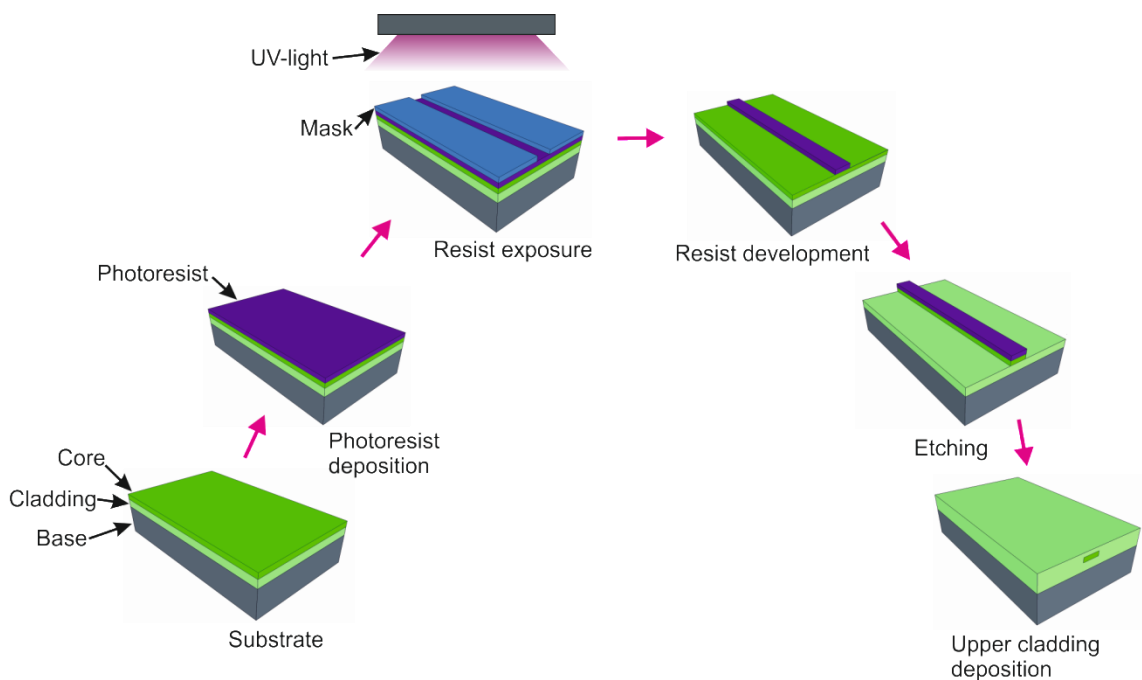


Figure 3.6.1 The process of photolithography and etching technique, which involve several steps.

From the process steps explained above, it demonstrates that the technique involves several steps to achieve a final optical device and this is time consuming. Apart from this, the process of photolithography and etching technique needs to be done in a cleanroom facility, a requirement that is not necessary for direct UV-writing technique. In which a waveguide can be directly produced from single step only and do not need for the cleanroom environment. In addition, the main reason why the photolithography and etching technique is not suitable for waveguide defining in the flat-fibre platform is due to surface of the flat-fibre is not flat as addressed before. The next section will briefly explain the direct UV-writing technique for defining channel waveguides.

3.6.2 Direct UV-Writing

Direct UV-Writing (DUW) is a technique which can define buried channel waveguides within a layer of photosensitive material as illustrated in Figure 3.6.2. The technique was first applied to a Ge-doped silica film by *Svalgaard et al* in 1994 [73]. The reported substrate contained germanium and yielded a refractive index change of order 10^{-3} . They used a point-to-point technique to UV-write a channel waveguide. In this work the direct UV-writing technique was performed in a plasma enhanced chemical vapour deposited (PECVD) silica-on-silicon substrate where the measured propagation loss of less than 0.2 dB/cm was achieved [74]. The UV source was generated by a frequency doubled argon ion laser to achieve a continuous wave UV-light at a wavelength of 244 nm. The light is focussed onto a photosensitive core layer and moved on a translation stage that is computer controlled. At the position where the UV-light is focused the local refractive index increases, this increase defines a channel waveguide. The technique offers fast fabrication times and no need for expensive masks associated with alternative fabrication techniques such as photolithography.

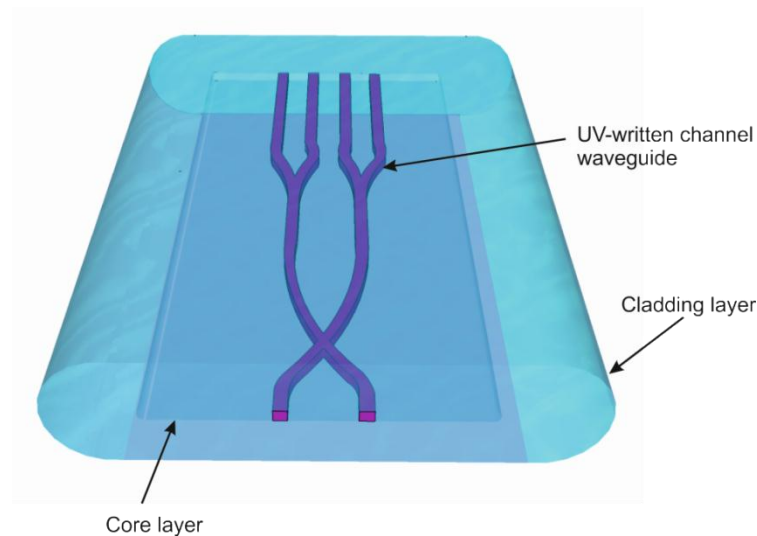


Figure 3.6.2 Illustration of integrated UV-written buried channel waveguide on a flat-fibre substrate.

The parameters of the waveguide are determined by the photosensitivity of the material and the power used during the translation of the sample. A material with higher photosensitivity will provide better waveguide confinement due to high refrac-

tive index contrast. It has been shown that photosensitivity of sample doped with germanium and boron can be enhanced by hydrogen loading prior to a UV-writing of the waveguide as discussed earlier. Another technique for waveguide fabrication known as a femtosecond laser writing is described in the following section.

3.6.3 Femtosecond Laser Direct Writing

The femtosecond laser direct writing technique is an alternative route to fabricate channel waveguides. The process is achieved by scanning a tightly focused beam from a femtosecond laser into a bulk transparent material. A main advantage of this technique is that it does not require a sample with photosensitivity and as such has the capability of producing waveguides in three dimensions compared to the direct UV-writing technique within a two-dimensional plane. The technique is capable of defining channel waveguides with high refractive index contrast, a waveguide with $\Delta n = \sim 0.035$ has been demonstrated in a glass substrate [75]. The induced refractive index change depends on the translation speed of the sample and also the pulse energy of the laser. A waveguide propagation loss of 0.86 dB/cm has been demonstrated in a fused silica glass [76]. The femtosecond laser direct writing technique has been extensively performed in many passive and active optical devices [77]. The following section describes another method of fabricating a waveguide using physical micromachining.

3.6.4 Precision Dicing Saw Micromachining

An alternative technique for defining channel waveguides is proposed and investigated in Chapter 7 of this thesis. The technique uses physical micromachining of the flat-fibre to form the lateral boundaries of the channel waveguide. This technique has previously been used to fabricate a cantilever structure on a silica-on-silicon substrate [78]. The technique uses a precision dicing saw and a diamond bonded blade and is suitable for rapid-prototyping and potentially scalable for mass production. The saw is used to create a trench by a single saw pass. Figure 3.6.3 (a) and (b) show the image of the diced trenches from the end facet and the top of the substrate, respectively. Before the cut is made, the blade is dressed to ensure good 'optical' quality of the cut trenches is achieved. This can be done by dressing the blade on a silicon wafer with multiple cuts, the translation speed of which is varied to correctly dress the blade. Once the dressing step is done, the following process is cutting trenches on a real sample. Be-

forehand, the sample is attached onto an adhesive plastic layer and placed onto a translation stage. The method described here is primarily used in the fabrication of the multimode interference (MMI) device presented in Chapter 7. The next section will explain the principle characterisation setup that has been used for fabricated optical devices presented in this thesis.

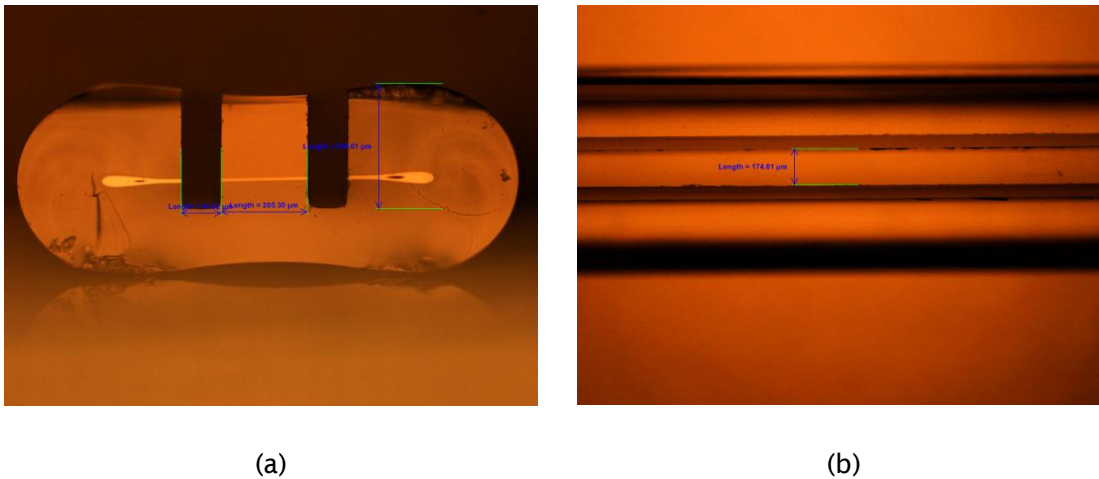


Figure 3.6.3 Micromachined trenches images from (a) end facet and (b) top view.

3.7 Measurement Characterisation Set-up

Figure 3.7.1 shows a schematic of the primary characterisation setups used to observe the performance of fabricated optical devices. A superluminescent diode (SLED) based broadband light source is connected to a 3-dB coupler via a polariser and polarisation controller. One of the ports of the 3-dB coupler is connected to a single mode fibre (SMF). The SMF is then butt-coupled to the waveguide under investigation and the reflectivity of the Bragg gratings is measured by an optical spectrum analyser (OSA) (AN-DO AQ 6317B) that is connected via the 3-dB coupler. All the fibre components are single mode at interrogation wavelengths. The alignment between the fibre and the channel waveguide is optimised by adjusting the translation stage and observing the output mode from the waveguide via a near infrared (NIR) camera. For the measurement to be accurate the correct polarisation state must be launched i.e. TE or TM. This can be done by observing the output mode pattern of the waveguide on the NIR camera. The polarisation controller is adjusted until none light is transmitted through a

polariser that is placed in front of the NIR camera. The optical spectra were collected in a LabVIEW program and the Gaussian apodised grating spectra were fitted with a Gaussian curve providing an accurate value of the peak reflectivity and central wavelength.

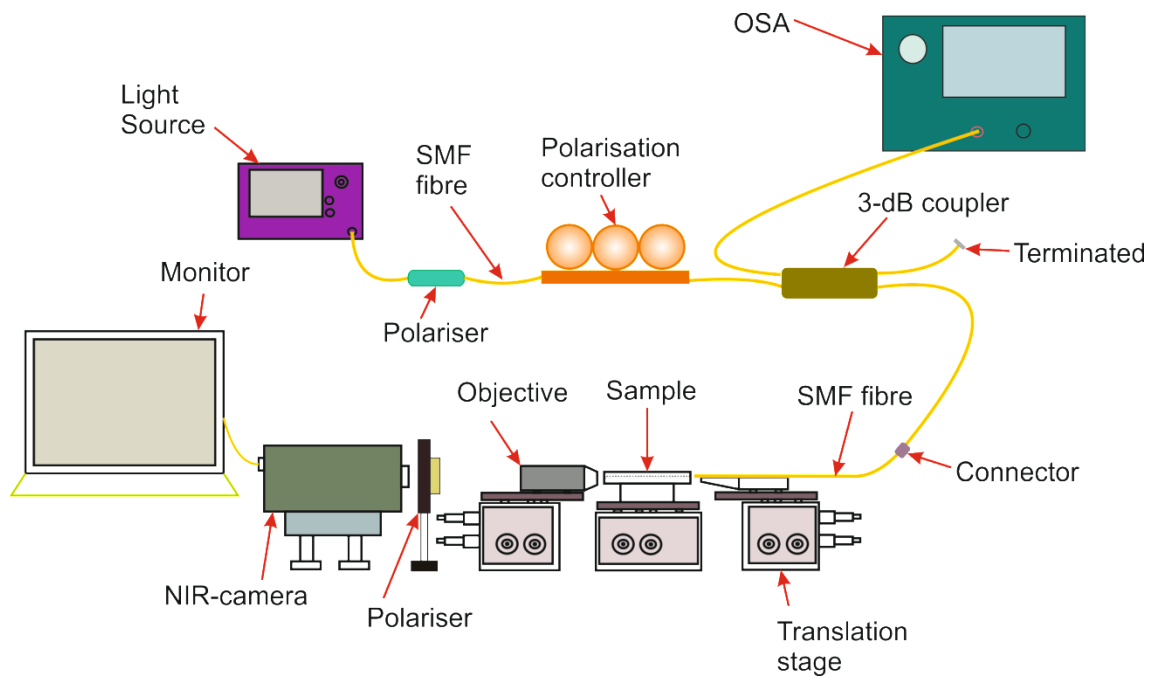


Figure 3.7.1 The characterisation setup for UV-written channel waveguides and Bragg gratings in flat-fibre substrates.

3.8 Conclusion

In conclusion, this chapter has provided an introduction to fabricating conventional optical fibre using different techniques. This includes the main methods of making optical fibre preforms namely MCVD, PCVD, OVD and VAD. This was followed by an explanation of the process of drawing the preform into a final optical fibre. The common techniques for planar waveguide fabrication have also been explained to give an overview of conventional processing. The fabrication of silica-on-silicon is a common substrate of interest as the optical structure is similar to that of flat-fibre. The fabrication process of flat-fibre is described, the MCVD technique for producing the preform and the modified drawing process. The photosensitivity of a planar substrate is also explained as most of the fabricated optical devices presented in this thesis have used a UV-writing technique for defining the waveguide. The chapter also gives details of alternative methods used to define channel waveguide namely femtosecond writing and precision micromachining. Finally, the chapter covers one of the main characterisation setups used to measure the performance of the fabricated flat-fibre devices. In the next chapter, the development of UV-written Bragg grating in a flat-fibre platform is discussed.

Chapter 4

UV-Written Bragg Gratings in a Flat-fibre Substrate

4.1 Introduction

This chapter briefly describes the concept of the direct grating writing (DGW) technique used to produce the Bragg grating structures within the planar core layer on a flat-fibre substrate. The technique has the ability to produce a channel waveguide and Bragg grating structures simultaneously. There are two operating modes of the DGW process that are used in our UV-writing setup namely amplitude modulation [15] and phase modulation control [21]. In much of this work the UV-written Bragg grating structures are used as a probe to measure the flat-fibre specifications. One of the specifications refers to the performance of the different flat-fibre compositions, of which four different forms are investigated in this thesis. The performance of the Bragg grating is observed via spectral reflectivity. The Bragg grating reflectivity is used to optimise two important key parameters of the DGW process, namely fluence and duty cycle. The Bragg gratings have also been used to measure the uniformity of the flat-fibre core layer in order to obtain information about the capability to support multiple parallel waveguides. Lastly, the birefringence of the flat-fibre substrate is calculated by subtracting the effective index of two different polarisations (i.e. transverse electric (TE) and transverse magnetic (TM)).

4.2 Direct Grating Writing

A simple Bragg grating structure consists of a series of refractive index perturbations along a channel waveguide [22]. This is normally fabricated by using a UV laser light to form an interference pattern which when exposed to a core of the waveguide generates a refractive index modulation to create the grating planes [79]. The system used in this thesis uses the same physical mechanisms as that used in fibre Bragg grating fabrication, i.e. UV illumination increases the local refractive index of an appropriately doped glass. However, the technique used in this thesis employs an interferometer to generate the interference pattern which in turn creates the index perturbation to form both the channel waveguide and Bragg gratings. The technique is called direct grating writing (DGW) [15]. It is an extension of the process of the direct UV-writing technique that is described in Chapter 3. This non-cleanroom technique offers flexibility in designing an integrated waveguide without the need for phase-masks and photolithography. The technique uses a single 244 nm UV-laser and an interferometer based system to produce an interference pattern within the overlap between two tightly focused laser beams. Gratings can be formed by modulation of the amplitude or phase of the inscribing light.

The formation of a channel waveguide can be achieved by averaging out the effect of the interference pattern by not modulating the beams while translating the sample. In the case of defining the Bragg gratings, two different methods have been demonstrated to control the grating inscription. The first method is an amplitude modulation that was developed by *Emmerson et al* in 2002 [13] and later this system was modified by adding phase control demonstrated by *Sima et al* [21]. The two methods use a similar configuration setup. The only difference between them is the way in which it modulates the UV-laser to produce the Bragg grating structures. The next section gives a brief explanation of the two techniques.

4.2.1 Amplitude Modulation Method

An amplitude modulation method uses an acousto-optic modulator (AOM) to modulate the intensity of the UV-laser beam. The fabrication process is implemented by using a computer numerical control (CNC) system that communicates with a high precision 3-axis air bearing translation stage. Figure 4.2.1 shows the UV-writing setup configuration using the amplitude modulation technique. Firstly, an Argon ion laser of 488 nm wavelength is frequency doubled in order to yield an ultraviolet wavelength at 244 nm.

The UV-laser is then modulated via the AOM. The output light from the AOM is aligned to ensure that only the first order diffracted beam is coupled into the beam expander. The beam is then split into two beams via a splitter. Two UV-beams are focused and crossed with the same path length arms to create the interference pattern within the 6 μm diameter spot as illustrated in Figure 4.2.2. The two beams are each focused into the photosensitive core layer of the planar slab waveguide.

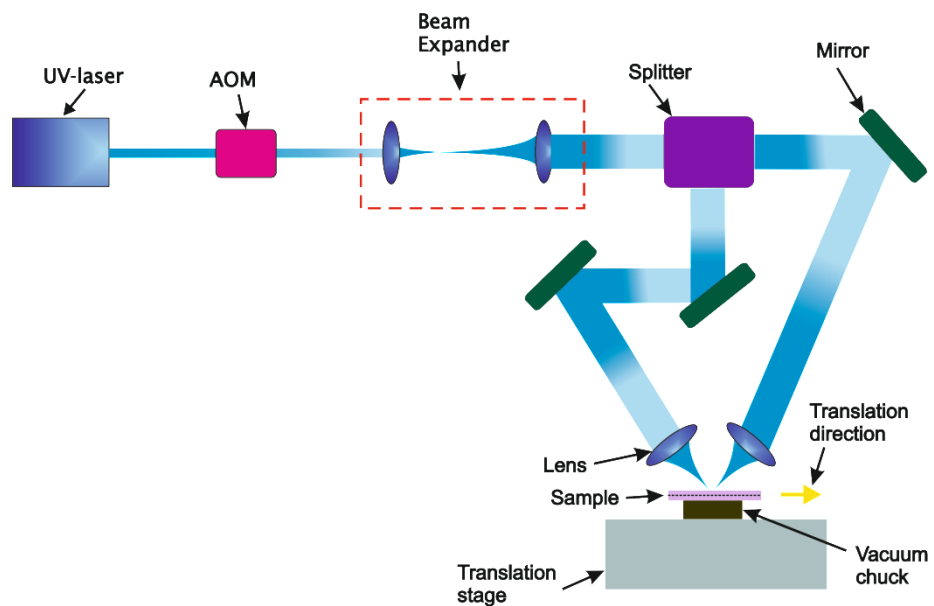


Figure 4.2.1 UV-writing configuration for the amplitude modulation technique. A two-crossed UV-beam is tightly focused onto a photosensitivity sample.

The interference pattern within the focused beam has several grating planes. The period of grating planes, Λ , can be determined by the intersection angle, θ of the crossed beams. The relationship of the parameters is defined in equation (4.1), where the λ_{uv} is the UV-laser wavelength. The period of the grating will determine the Bragg grating wavelength. The DGW system is primarily used to fabricate Bragg gratings at wavelengths around 1550 nm, which correlates to an intersection angle of $\sim 13^\circ$. The setup has the flexibility to write a range of wavelength varied around that defined by the intersection angle. Exact control of the grating wavelength is determined by the software control. The ability of the system to write a wide wavelength band originates from the small spot used to define the waveguide.

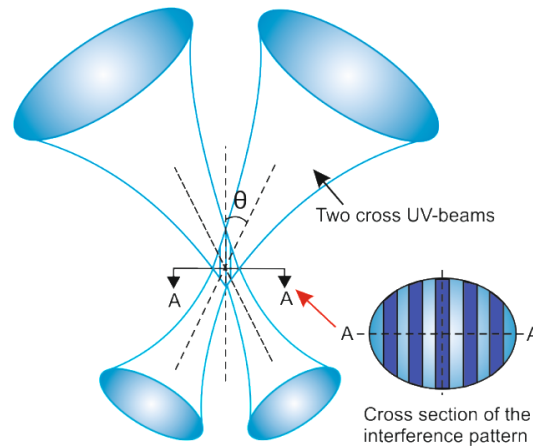


Figure 4.2.2 The cross section of the interference pattern at certain angle to determine an inherent grating pitch of a Bragg grating wavelength.

$$\Lambda = \frac{\lambda_{uv}}{2\sin\theta} \quad (4.1)$$

Wavelength detuning is used to alter the centre wavelength of Bragg gratings. This is implemented by manipulating the magnitude of the distance between each UV-spot exposure. This will subsequently change the period of the grating without need to change the inherent period of the interference pattern via the crossing angle. This detuning process has been extensively discussed in Emmerson's thesis [13]. Particularly, the detuning process involves an additional displacement, δ , to the inherent grating pitch, Λ . The displacement is either added or subtracted to the grating pitch ($\Lambda \pm \delta$) in order to modify the centre wavelength of the Bragg grating, which results in a spectral window spanning from 1400 nm to 1700 nm. The maximum displacement, Δ can be quantified by taking the ratio between the grating pitch and the number of the inherent interference periods within the beam spot, N . The relationship of those parameters can be expressed as in equation (4.2). It shows that the detuning bandwidth is inversely proportional to the spot size.

$$\Delta = \frac{\Lambda}{N} \quad (4.2)$$

It must be noted that the technique has a limitation in terms of the grating reflectivity, where the larger the detuning of the inherent grating pitch, the weaker the grating strength. However, within the wavelength band of 1425 nm - 1675 nm, a variation of ~3 dB is observed. Most of the fabricated Bragg gratings in the flat-fibre substrate used the amplitude modulation technique because of the time during the fabri-

cation; the phase modulation technique was still under development. However, some of the more recent samples have implemented the phase controlled technique. This is because the phase modulation technique provides faster fabrication speeds and stronger Bragg gratings. A brief overview of the phase modulation technique is described in the next section, and a detailed description of the technique can be found in [21].

4.2.2 Phase Modulation Method

A phase modulation method is implemented by using an electro-optic modulator (EOM) in one arm of UV interferometer. The technique manipulates the fringes of the interference pattern by controlling the relative optical phase of the crossed-beams. This changes the position of the fringes within the writing spot. The writing speed of the technique is faster than the previous amplitude modulation method due to the removal of the AOM, removing loss from the path, and also because of the writing speed for the channel waveguide and Bragg grating is kept constant. Figure 4.2.3 shows the set-up applied in the phase modulation technique. It shows that the UV-laser of 244 nm wavelength is directly launched into the beam expander via a shutter and split into two beams. One beam is phased controlled by using the EOM. The EOM is driven by a high voltage amplifier with a sawtooth signal; the duty cycle of this signal again controls the refractive index contrast of the Bragg grating. As with the AOM system all the fabrication operation is controlled by computer system.

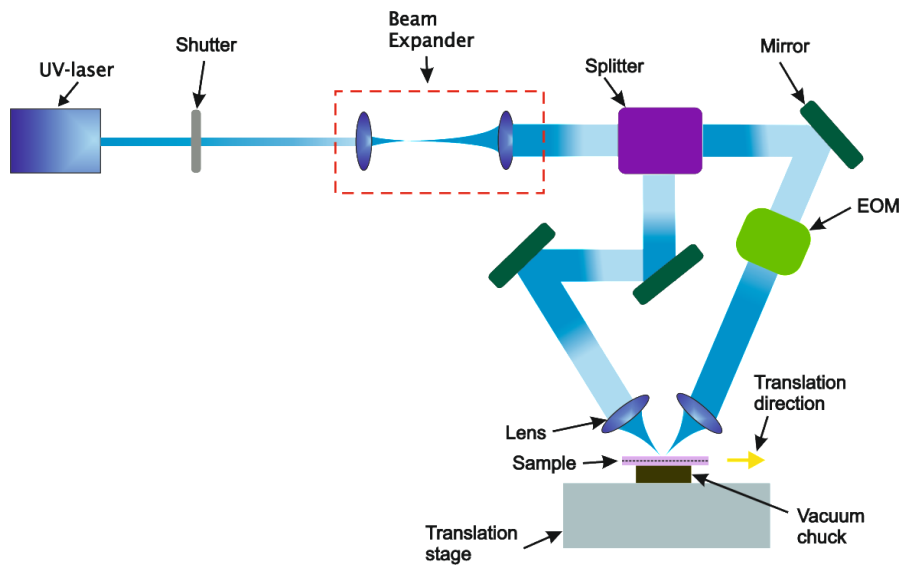


Figure 4.2.3 UV-writing configuration setup using the phase control method.

The experimental works described in the following are implemented with the amplitude modulation technique. The Bragg grating, fabricated using the amplitude modulation technique, is sufficient for device optimisation.

4.3 Interrogating Flat-fibre Performance via UV-written Bragg Gratings

4.3.1 Types of Flat-fibre

A series of experiments has been performed to investigate the performance of flat-fibre samples with different compositions. Fabrication of flat-fibre samples has different number of batches, which has altered composition prepared by Dr. *Andrew Webb* (member of the Silica Fibre group). In this chapter, four different flat-fibre samples are considered, by which the samples have different recipes, as detailed in Table 4.3.1. The effective index, n_{eff} presented in the Table 4.3.1 was measured via the spectral interrogation of UV writing of Bragg gratings.

The material composition for a UV-written waveguide substrate is a vital element that determines the performance of the device. Two different doping concentrations have been given in the Table 4.3.1. The doping concentration was calculated from mo-

lar refractivity of a silica glass, which was estimated from the precursor flow rates of the flat-fibre fabrication. A sample with higher photosensitivity would in general improve the performance of the UV-written channel waveguide and Bragg gratings [80], and as such much of this thesis investigates routes to enhance the photosensitivity. These investigations started by looking at germanium only doped flat-fibre and were followed by samples containing the elements of germanium and boron (Ge - B). These samples were loaded in a hydrogen chamber to increase the photosensitivity. Figure 4.3.1 shows the illustration of the four different samples with different recipes. The sample with germanium composition only is labelled as Substrate A, whereas Substrate C has two elements of germanium and boron. From these two types of substrates, the process of hydrogen loading yielded Substrate B and Substrate D. Figure 4.3.2 (a) and (b) show the flat-fibre cross-section showing the dimensions of Substrate A and C, respectively.

Table 4.3.1 The description of the four different recipes of flat-fibre substrates

Substrate	Fibre No.	Doping Concentration	Recipe	Effective index, n_{eff} @ ~1550 nm	Core Thickness
A	T0059-G30021/D	5.4 mol% (Ge)	Ge	1.4596	7.8 $\mu\text{m} \pm 0.3 \mu\text{m}$
B	T0059-G30021/D	5.4 mol% (Ge)	Ge and hydrogen loaded	1.4614	7.8 $\mu\text{m} \pm 0.3 \mu\text{m}$
C	T0384-G30168/D	5.4 mol% (Ge) 13.3 mol% (B)	Ge-B	1.4505	7.1 $\mu\text{m} \pm 0.3 \mu\text{m}$
D	T0384-G30168/D	5.4 mol% (Ge) 13.3 mol% (B)	Ge-B and hydrogen loaded	1.4519	7.1 $\mu\text{m} \pm 0.3 \mu\text{m}$

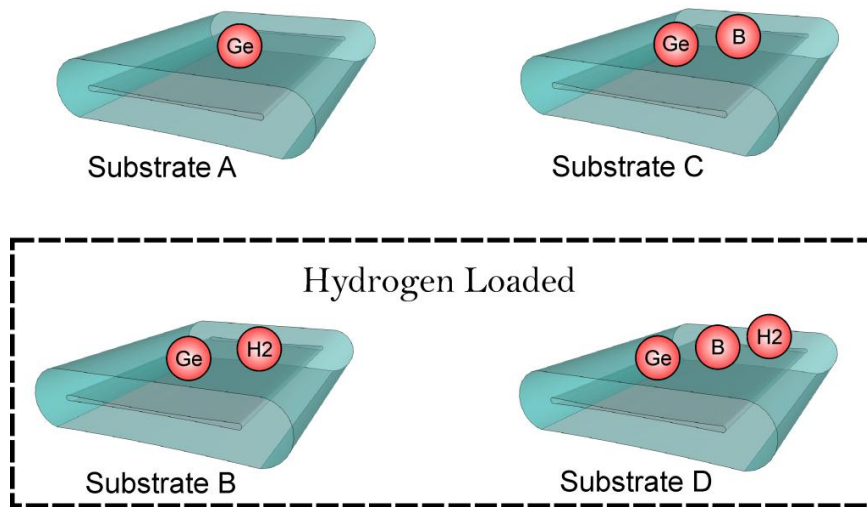


Figure 4.3.1 Illustration of four different recipes of flat-fibre substrates namely Substrate A, Substrate B, Substrate C and Substrate D.

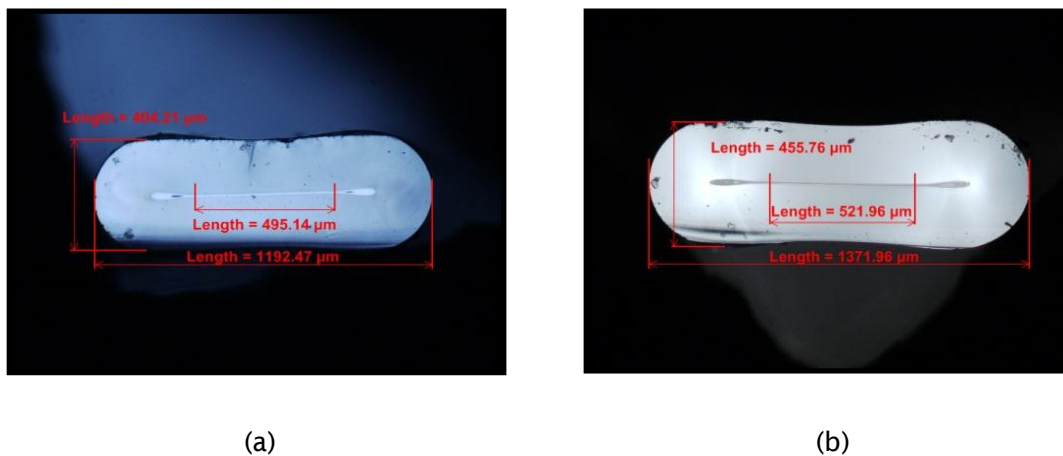


Figure 4.3.2 The flat-fibre cross-section for (a) substrate A and B and (b) substrate C and D.

4.3.2 UV-Writing Parameters

The same UV-writing parameters have been used for comparative purposes. Each type of fibre was UV-written with a single waveguide containing three Bragg gratings with the Bragg wavelength 1540 nm, 1550 nm and 1560 nm. The 3D-schematic diagram of the UV-written Bragg grating is depicted in Figure 4.3.3. The fluence and duty cycle

chosen were 50 kJcm^{-2} and 0.5, respectively. These values were selected in this preliminary experiment, although neither parameter had been optimised at this stage. A description of these parameters and the optimisation is discussed in Section 4.4. The characterisation setup, similar to the configuration shown in Section 3.7, was used to measure the spectral reflectivities of the UV-written Bragg grating channel waveguides.

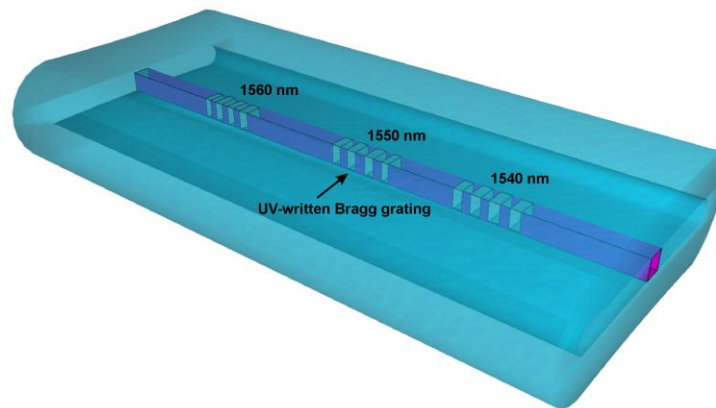


Figure 4.3.3 A 3D schematic diagram of the flat-fibre with three UV-written Bragg gratings

4.3.3 Results and Discussion

Table 4.3.1 summarises some of the key characteristics of the four different substrates which includes the series number of different batches of fabrication. Included in this table is the effective index of the UV written channel waveguides and were measured from the reflection spectrum of the Bragg grating about 1550 nm. It can be seen that the Substrate A has higher effective refractive index than the Substrate C. This is expected because the composition of Substrate A contains germanium only which increases the refractive index of the core layer. However, in Substrate C the addition of boron decreases the effective index. The effect of the hydrogen loading process on the effective index was to increase Substrate B by about 0.12 % from the Substrate A. A similar trend is observed for Substrate D.

Figure 4.3.4 shows the spectral reflectivity against wavelength for the three Bragg gratings in the four different substrates as previously described. In the Figure 4.3.4 (a) and (b), the resolution of the spectral data, taken from the OSA, were

measured with a resolution of 0.5 nm, while the graphs shown in the Figure 4.3.4 (c) and (d) were at 0.2 nm. This explains the lower noise of (a) and (b) observed on the data. The plots show three primary peaks produced by the three distinct Bragg gratings and are produced by interaction with the fundamental mode. In addition, to the left side of each fundamental peak, smaller peaks can be observed, most evidence in the results from Substrate C and D. These side peaks are caused by the reflection from a higher order mode and coupling of this mode with the fundamental mode. This clearly shows that substrates B, C and D exhibit multimode behaviour. It is also likely that Substrate A would demonstrate multimode behaviour; however the grating strength is so weak that the side peak would not be visible above the noise floor.

The performance of the substrates can be measured by comparing the strength of the spectral reflectivity of the Bragg gratings. The peak reflectivity of the second Bragg grating, about 1550 nm, is summarised in Table 4.3.2. The optical power launched into the device is determined by using the ~3.4 % reflection from the end facet of the launch fibre when not coupled to the device. With this data the reflectivity of the gratings can be determined and takes into account the spectral characteristics of the source and the fibre components. The approach does not take into account the coupling loss into the flat-fibre and thus assumes that the coupling loss is similar for each case. As the Bragg gratings were all weak (i.e. the reflectivity was not saturated) the peak reflectivity is proportional to the refractive modulation and photosensitivity. Two key results can be observed in this data;

- i) Adding boron (B) into the core layer of flat-fibre has significantly improved the performance of the Bragg gratings.
- ii) The hydrogen loading process has also significantly increased the photosensitivity producing a much stronger response.

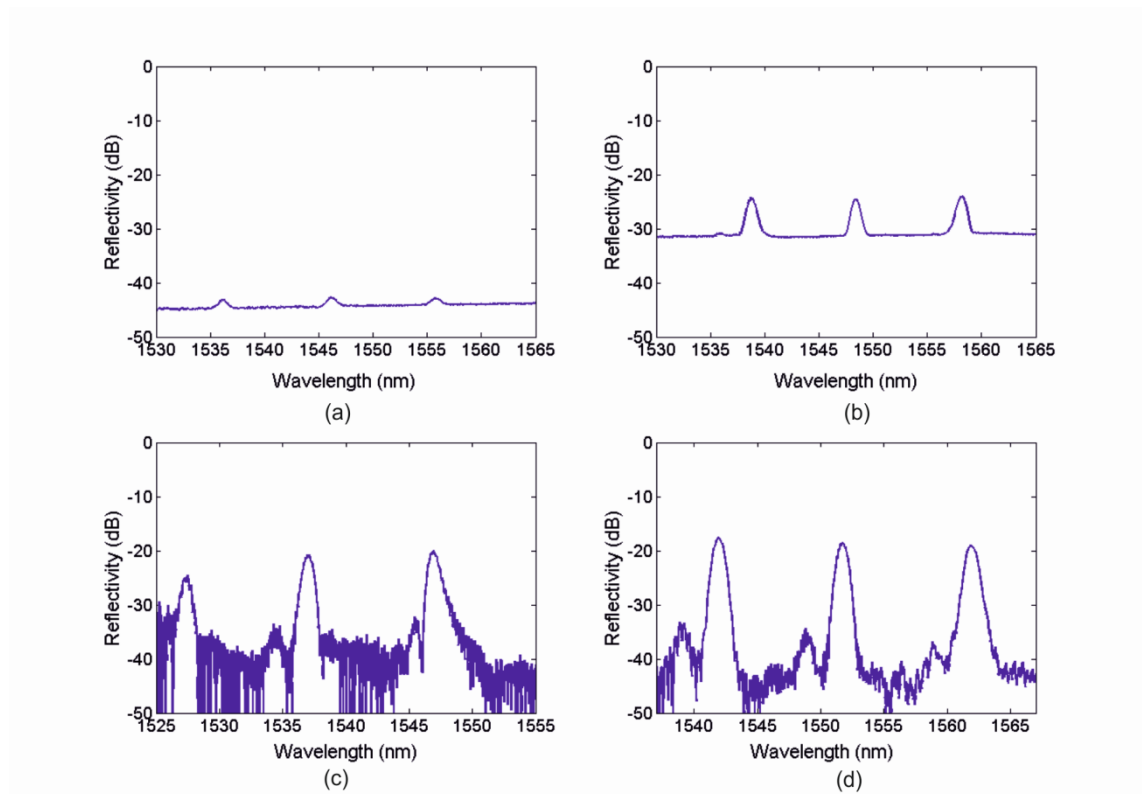


Figure 4.3.4 Spectral reflectivity of three different Bragg gratings in (a) Substrate A, (b) Substrate B, (c) Substrate C and (d) Substrate D.

Table 4.3.2 Peak spectral reflectivity of the Bragg grating about 1550 nm for the different substrates.

Flat-fibre type	Peak Reflectivity (dB)
Substrate A	-42.74
Substrate B	-24.55
Substrate C	-21.25
Substrate D	-18.7

It can be seen that, the hydrogen loading process has obviously increased the grating strength of the Substrate B compared to the Substrate A. The grating strength is further increased when the fibre was co-doped with boron as demonstrated by the Substrate C. This is due to the capability of boron to increase the photosensitivity of the core fibre [81]. In addition, boron is one of the few elements that reduce the refractive index of the glass. Again hydrogen loading of Substrate C gave some improvement, ~2.5dB increased reflectivity, somewhat lower than that seen for Substrate B. This is likely to be a result of the ability of the hydrogen to reach the core layer. The Substrate B was hydrogen loaded with two grooves on the top of the fibre and thus decreased the thickness of the cladding to around 10 μm opposed to the actual cladding layer of ~200 μm . This thin cladding layer of the Substrate B allowed the hydrogen gas to diffuse into the core layer of the flat-fibre. As a result Substrate B showed a significant increase in grating strength compared to Substrate A. And is again a much greater increase than that seen between Substrate C and D where no grooves were used. Only small improvement can be seen between Substrate C and D even after hydrogen loading for ~ 2 months. This improvement is probably largely due to the experimental variation and improvement of the UV-writing procedure and characterisation and not as consequence of hydrogen loading. With the normal cladding thickness of the flat-fibre, it is expected very little hydrogen gas reaches the core layer, even in 2 months, due to the exponential relationship of gas diffusion [13]. It should also be noted that increasing the UV induced refractive index change not only increases the grating strength but also reduces potential waveguide propagation loss and hence both of these mechanisms would improve grating reflectivity.

4.4 UV-Writing Parameters Observation

The quality of the UV-writing channel waveguide and Bragg grating structures is influenced by the characteristics of the sample's material and also the UV-writing parameters. As previously discussed the Bragg grating wavelength is determined by the effective refractive index and the grating pitch of the Bragg grating structure. The primary method of modifying Bragg wavelength is through altering the grating pitch. The precise value for effective refractive index is determined by the fluence parameter; in addition, the duty cycle parameter will affect the grating plane index contrast of the index perturbation. Both parameters, fluence and duty cycle, significantly determine the features of the UV-written Bragg grating, the next section will further discuss these relationships.

4.4.1 Fluence

Fluence is the energy density of UV-light exposed to the sample measured in units of kJcm^{-2} and can be calculated by equation (4.3), where I_{UV} is the average intensity (in kWcm^{-2}), a is the spot size diameter (in cm) and v_{trans} is the translation speed (cms^{-1}). The average intensity is the ratio between the UV-power (kW) and the cross section of the UV-beam spot with r is the Gaussian beam spot radius. This can be calculated by using the equation (4.4). The calculated relationship of fluence and translation speed of UV-writing is plotted in Figure 4.4.1 and shows that the fabrication speeds, and hence time, is strongly affected by the fluence. In this plot the assumed UV-light power is 100 mW with a UV-spot beam diameter of $5 \mu\text{m}$. The fluence parameter manipulates the translation velocity of the writing process and the exposed power to the particular region of a photosensitive sample. This will determine the level of the effective refractive index (n_{eff}) as illustrated in Figure 4.4.2, which shows the UV induced refractive index change relative to the native core refractive index (n_{core}). In planar UV written waveguides the UV induced change is normally in the order of 10^{-3} [73].

$$F = \frac{I_{UV} \times a}{v_{trans}} \quad (4.3)$$

$$I_{UV} = \frac{P_{UV}}{\pi r^2} \quad (4.4)$$

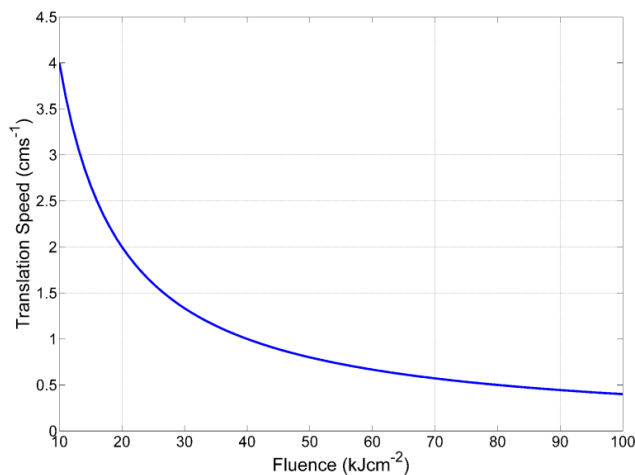


Figure 4.4.1 The calculated translation speed against fluence.

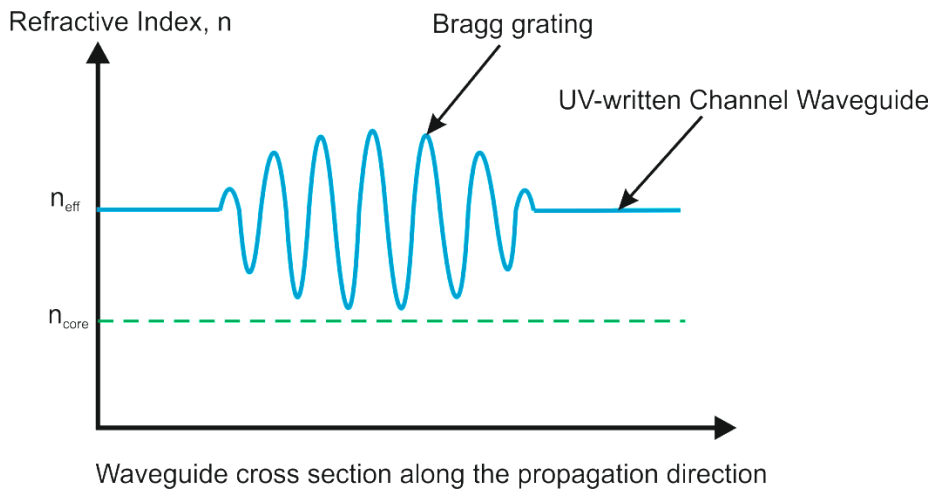


Figure 4.4.2 Illustration of the effective refractive index level of a UV-written Bragg grating.

Experimentally, the effect of fluence was investigated in Substrate C by fabricating several waveguides each containing eight different Bragg gratings with wavelengths varying from 1540 nm to 1575 nm distributed along the waveguide. The fluence of the individual waveguides, including the gratings, was varied from 10 to 140 kJcm^{-2} with a duty cycle of 0.5. The duty cycle was kept constant and the wavelength of 1550 nm was chosen for comparison purposes. Figure 4.4.3 shows the effective refractive index of the waveguides as a function of fluence. The graph shows an approximate linear increase with the gradient of $(4.62 \pm 0.78) \times 10^{-6} (\text{kJ}^{-1}\text{cm}^2)$ of effective index with fluence.

This data shows a few key points; the data suggests that even at high fluence (i.e. 140 kJcm^{-2}) the effective refractive index is still increasing and has not saturated this is in stark contrast to standard FHD samples where saturation is obvious at and above 25 kJcm^{-2} [13]. The second point is that the fitted trend line shows a maximum UV induced change in n_{eff} of $\sim 0.65 \times 10^{-3}$ which is slightly lower than that achieved in hydrogen loaded FHD samples; however the flat-fibre requires a much higher fluence. It can also be observed that the higher the fluence the stronger the spectral reflectivity of the grating. Yet, it is worth noting that higher fluences require longer writing times to complete a single waveguide as shown in Figure 4.4.1. In this experiment longer writing times are not detrimental to the consistency of the waveguide parameters. However longer writing times would be of concern if the sample was hydrogen loaded, which would experience out-gassing during the writing or process. This highlights the trade-off between enhanced photosensitivity and consistent writing conditions. In the

next section, the effect of duty cycle is investigated to optimise the performance of the UV-writing process.

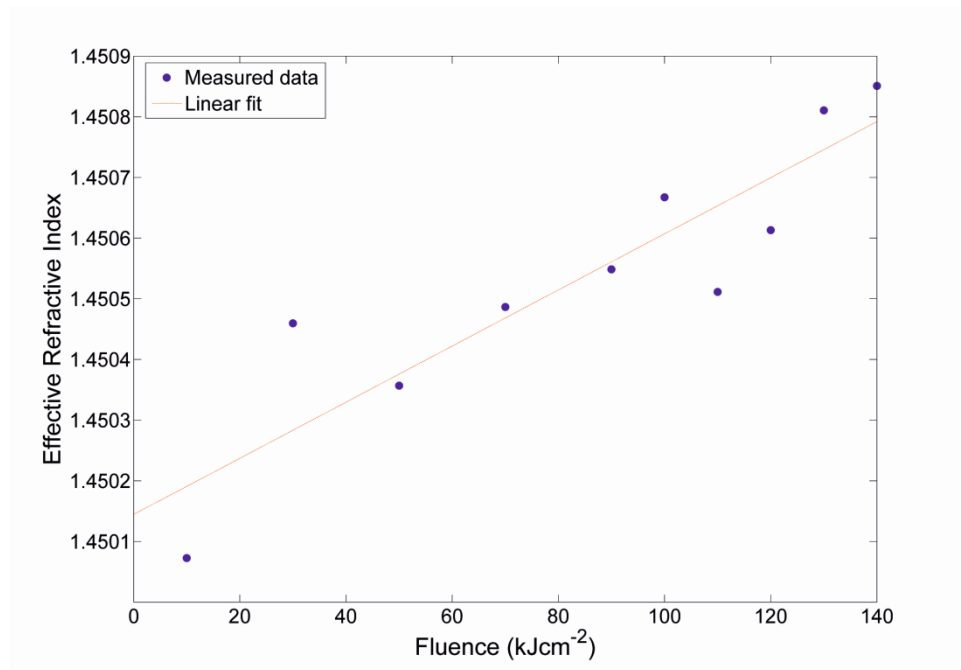


Figure 4.4.3 A plot of effective refractive index of the waveguide mode against the UV writing fluence, points are experimental data and also shows a fitted linear trend line.

4.4.2 Duty Cycle

A duty cycle parameter used in the UV-writing process can be defined as a ratio of the distance the UV-laser is on with respect to the total grating period as illustrated in Figure 4.4.4. The duty cycle has a range of 0 and 1, where 0 signifies no UV-laser is exposed, while 1 represents the laser is always on and thus produces a channel waveguide. For instance for a duty cycle of 0.6 the laser will be on 60% of the period and off 40%. The duty cycle parameter actually defines the index contrast of the grating plane, by which the lower the duty cycle, the higher the index contrast becomes. Modulation of the UV-laser is achieved via an acousto-optic modulator (AOM) as the translation stage moves.

In the UV-writing system, a technique that is termed as ‘fluence matching’ is used to control the average effective index of the Bragg grating and waveguide, so to

ensure they have a similar value. This is to avoid the Bragg grating structure experiencing unwanted additional reflections due to the dissimilarity of the effective refractive index between the channel waveguide and Bragg grating. The technique manipulates the translation speed of the UV-writing process which controls the fluence parameter. The relationship of these parameters is expressed in equation (4.5), where the translation speed of writing the Bragg grating, v_{BG} is controlled by the duty cycle and the translation speed (mm/minute) of the channel waveguide, v_w .

$$v_{BG} = \text{duty cycle} \times v_w \quad (4.5)$$

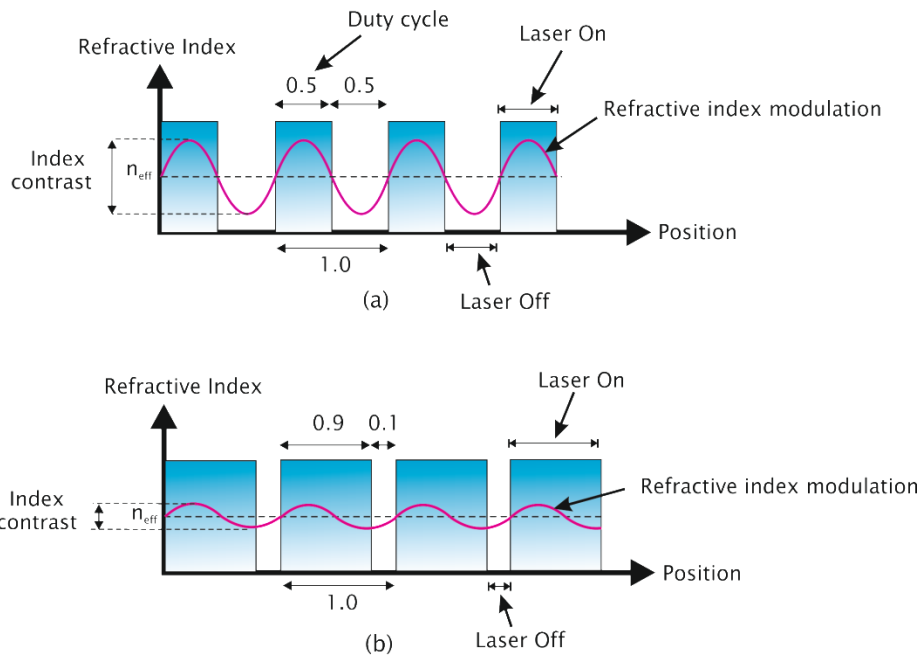


Figure 4.4.4 An illustration showing how duty cycle changes the refractive index contrast, shows a duty cycle of (a) 0.5 and (b) 0.9. The blue square wave represents the control signal to the AOM, high level denotes the laser is on. The red sine wave represents an equivalent sinusoidal modulation in the induced refractive index.

For the duty cycle investigation, a range of duty cycles between 0.1 to 0.8 was observed. A number of waveguides in Substrate C with six different Bragg gratings was written with a fluence of 50 kJcm^{-2} . The spectral reflectivity of these Bragg gratings can be seen in Figure 4.4.5, where for this particular graph the duty cycle was 0.5. The peak spectral reflectivity of the first Bragg grating from each waveguide is plotted in Figure 4.4.6, and provides a trend of grating strength versus duty cycle. This shows

that the greatest reflectivity can be achieved by using a duty cycle of 0.1. However, it must be noted that a small duty cycle results in a much longer fabrication time as a consequence of the fluence matching. The effective refractive index of the 1550 nm Bragg grating with respect to the duty cycle is plotted in Figure 4.4.7. It shows that the effective refractive index for the duty cycle variation is similar for the all duty cycle values and confirms that the fluence matching (i.e. control of the translation speed of stage system) is correct. In this experiment, the average effective refractive index was 1.45035 with a standard deviation of 1.2×10^{-4} .

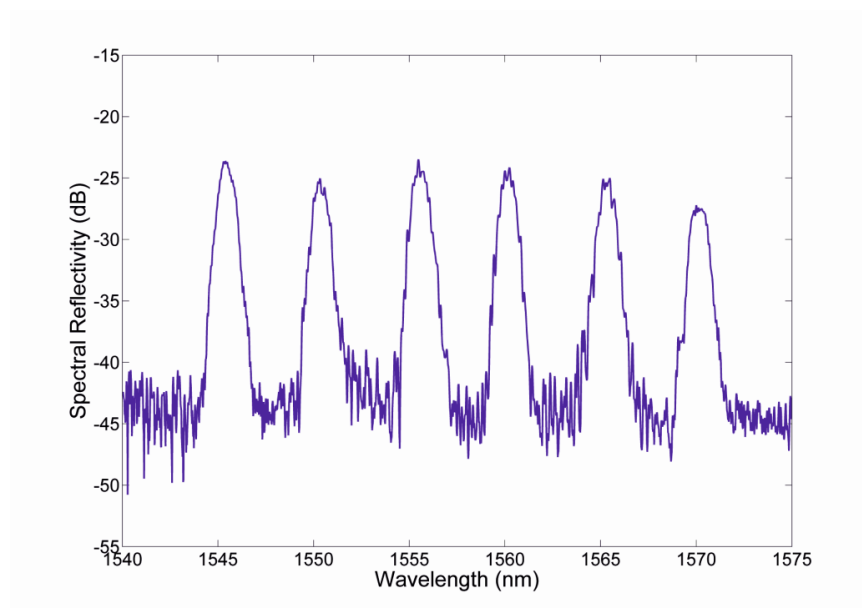


Figure 4.4.5 Spectral reflectivity of a waveguide containing six Bragg gratings written with a duty cycle of 0.5.

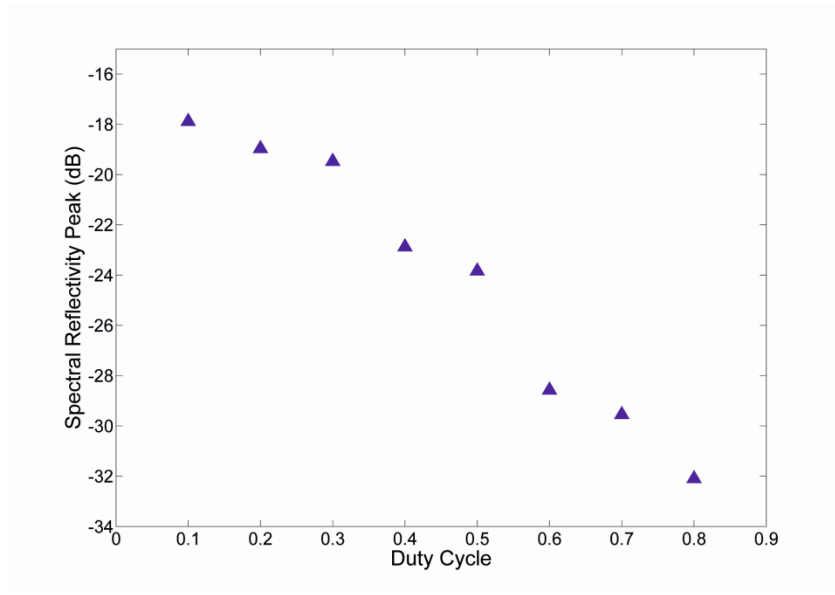


Figure 4.4.6 Spectral peak reflectivity plotted with respect to duty cycle for the Bragg grating written at 1545 nm.

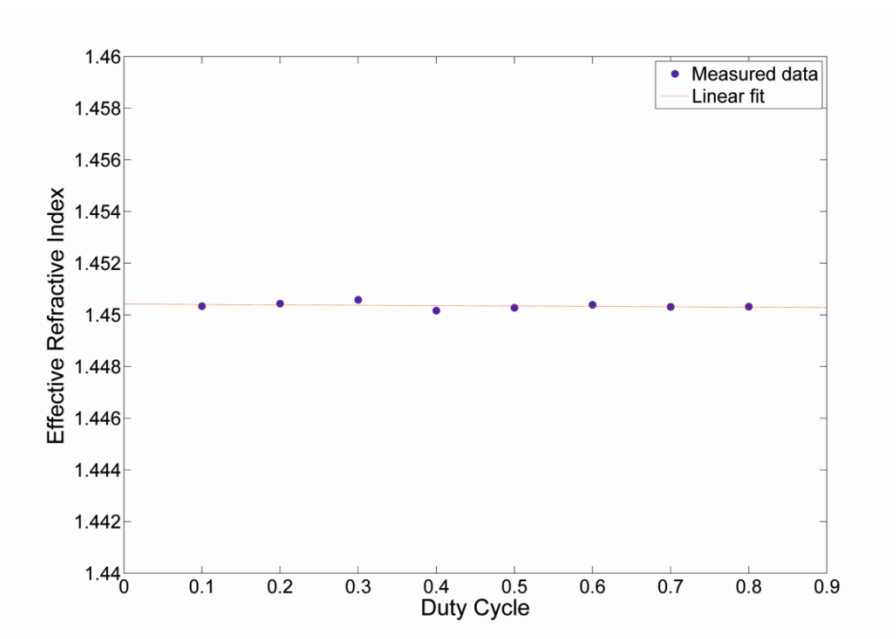


Figure 4.4.7 The effective refractive index against the duty cycle variation.

4.5 Flat-fibre Level of Planarisation

The ability of the flat-fibre structure to support multiple waveguides in a single substrate is the main advantage of flat-fibre. However, due to the fibre actually having a 'bow-tie' shape, it is difficult for the flat-fibre to have UV-written waveguides at every position within the core layer of the fibre. An important parameter of the substrate is the planarity i.e. the flatness and uniformity. To experimentally investigate this parameter fifteen UV-written waveguides, distributed along the cross-section of the core layer, were UV written. Each waveguide contained two Bragg gratings with the design wavelengths of 1550 nm and 1560 nm, as shown in Figure 4.5.1. The waveguides were laterally separated by 50 μm and the total sample length was 6 mm. The grating length was 2 mm and each grating separated by 0.5 mm.

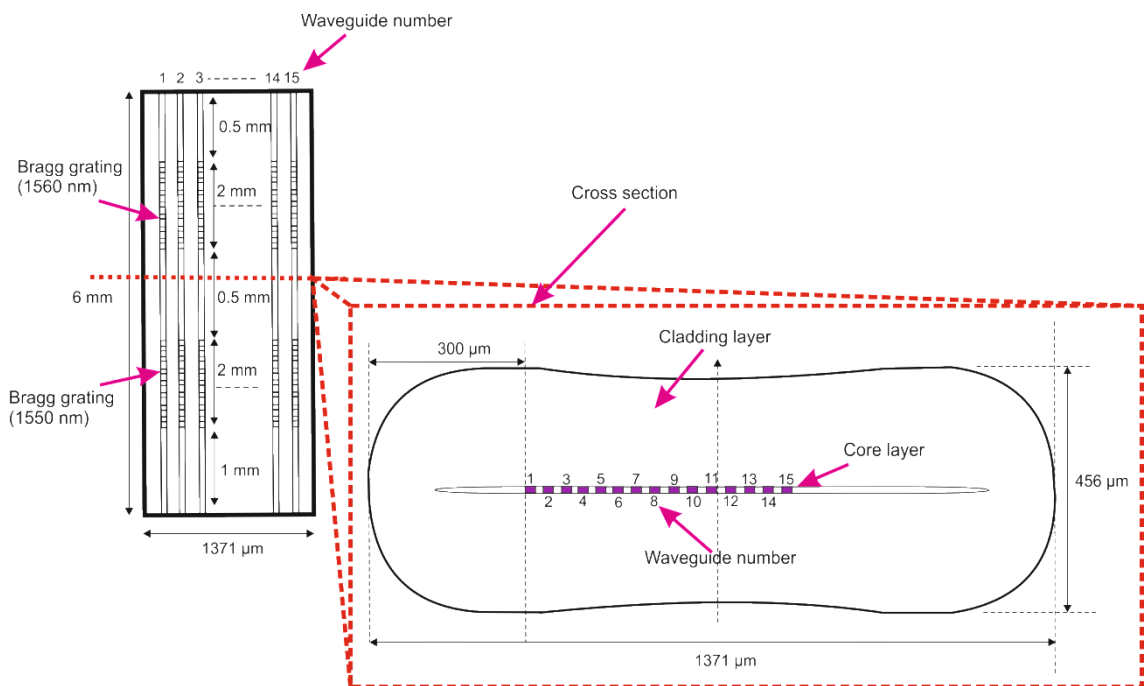


Figure 4.5.1 The schematic diagram of a series of UV-written channel waveguides each containing two Bragg gratings.

As before the Bragg gratings act as a probe to interrogate the properties of the waveguide. Figure 4.5.2 shows a plot of the peak reflectivity of the 1560 nm Bragg grating versus the channel waveguide number. It shows that the peak reflectivity of the gratings (1560 nm Bragg wavelength) located at the waveguide number 6 to 15 display

similar reflectivities. The error in this region is mainly due to coupling uncertainty. This leads to an approximate ± 1 dB variation in measured reflectivity. Therefore, it can be concluded that the core layer and the cladding layer (that the UV laser propagates through) is approximately flat and uniform. However, it can be observed that for the first five waveguides, the peak reflectivity varies widely; this is thought to be attributed to thickness or surface variation of the cladding. These variations distort the two beams, altering the focus and more importantly the overlap of the two UV beams yielding weaker Bragg gratings as seen at positions 3 and 4. Interestingly the strength of the gratings and waveguides is restored in channel waveguides 1 and 2 corresponding to a location where the cladding again becomes approximately flat, see Figure 4.5.2. This illustrates that in this case the form of the cladding (i.e. shape) is more important than the thickness uniformity.

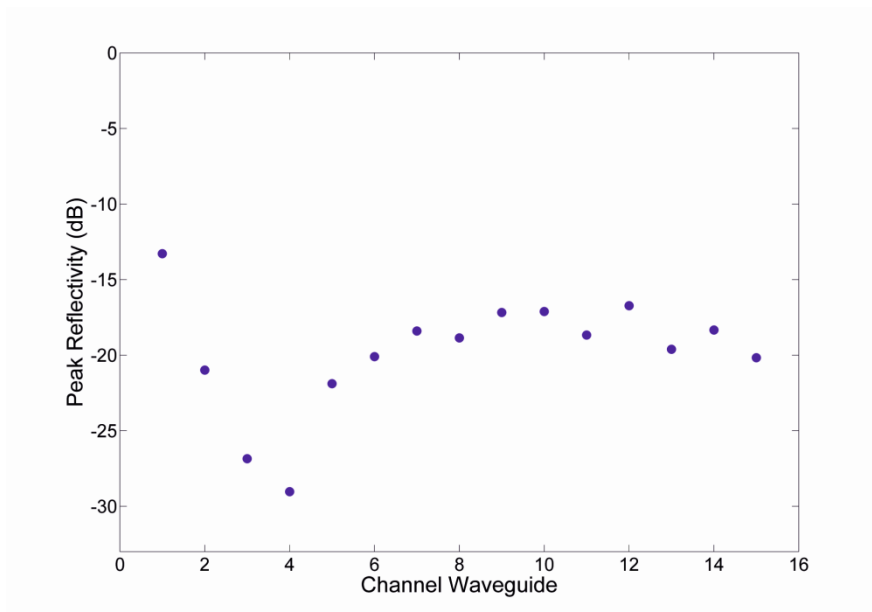


Figure 4.5.2 Plot showing peak reflectivity of Bragg grating wavelength at 1560 nm against 15 channel waveguides number.

Other than the cladding thickness uniformity the same Bragg grating data can provide information regarding the uniformity of the core layer. The effective refractive index of the 1560 nm Bragg grating at TE polarization is plotted in Figure 4.5.3. It shows that the effective index of the gratings placed within waveguides 8 to 15 are very similar with the average effective index of 1.45034 and with a standard deviation

of 6×10^{-5} . This depicts that the region where the waveguides 8 to 15 are located is flat and have uniform thickness. Thus, a more integrated planar waveguide can be defined within this area. Yet, the effective index of waveguides 1 to 7 shows an increasing trend towards the edge of the sample. This is due to the increased thickness of the core layer, and also results in an increased number of supported modes.

These measurements show that the flatness and the uniformity of the flat-fibre platform are of key importance in order to develop an integrated optical planar device especially for complex integrated circuits. Future work would include the fabrication of a flat-fibre with a flatter cladding surface. This can be achieved by dicing both edges along the length of the flat-fibre preform before drawing. Birefringence of the flat-fibre will be discussed in the next section.

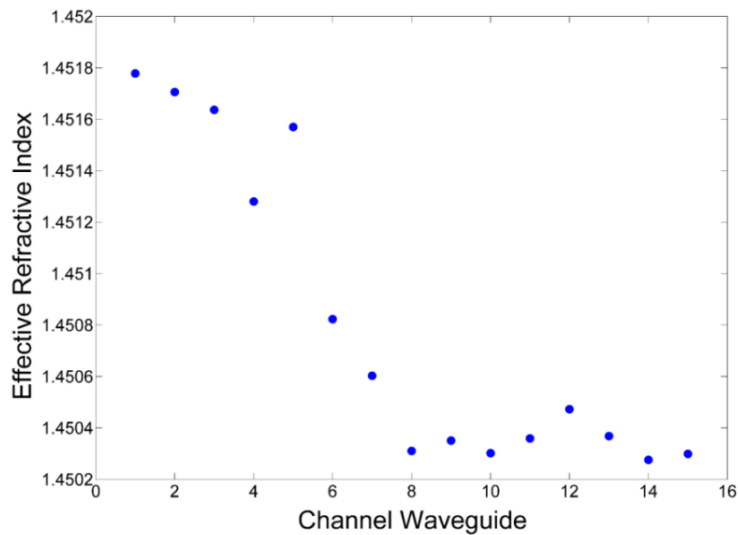


Figure 4.5.3 Plot showing the effective refractive index of the 15 waveguides, at 1560 nm, against the channel waveguide number.

4.6 Birefringence in Flat-fibre

Birefringence is a material property where the refractive index of the material depends on the polarisation of the propagating light. Birefringence can originate from two physical mechanisms, categorized as geometrical birefringence [82] or stress-induced birefringence [83]. With geometrical birefringence, it is the asymmetrical geometry of the

waveguide that influences the birefringence of the waveguide. While stress-induced birefringence, as the name suggests, is induced due to the effect of the stress on the optical waveguide from internal and external sources. In the case of the current flat-fibre devices there is an obvious geometrical birefringence caused by the dimensional differences between the UV-written channel waveguide width and core layer thickness. The birefringence of a sample can be calculated by taking the difference between the effective refractive index of the TM, n_{TM} and TE, n_{TE} modes as expressed in equation (4.6).

$$\text{Birefringence} = n_{TM} - n_{TE} \quad (4.6)$$

To observe the birefringence of the flat-fibre, the same sample used in the planarisation experiment was investigated. This data can be seen in Figure 4.6.1. This data again illustrates the uniformity of the channel waveguides 8 to 15 where the birefringence of the waveguides is very similar. From the graph, it shows that the mean birefringence of the UV-written waveguides in this region (waveguides 8 to 15) was 4.00×10^{-4} with a standard deviation of 0.04×10^{-4} .

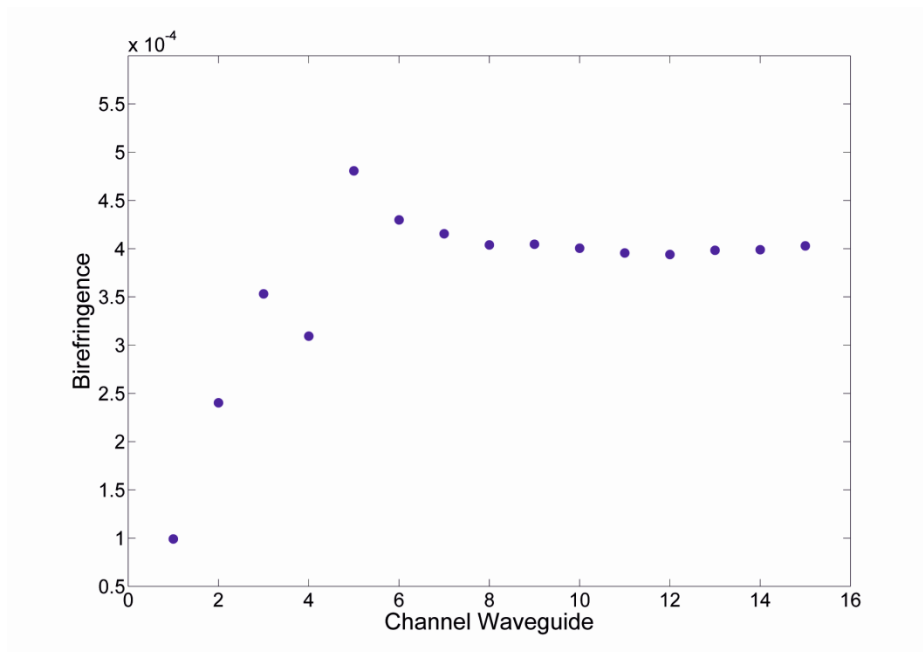


Figure 4.6.1 Plot showing the birefringence of 15 waveguides at a wavelength 1560nm as a function of channel waveguide number.

In order to estimate the magnitude of the geometrical birefringence of the flat-fibre, a channel waveguide was modelled using FIMMWAVE software. The model does not take into account any stress induced birefringence that generated by the waveguide geometry. The flat-fibre modelling parameters were taken from Table 4.3.1; the UV written waveguide width and refractive index contrast were taken to be $6\ \mu\text{m}$ and 0.001 respectively. This results in the effective refractive index of 1.451417 and 1.451403 for respective TM and TE modes, resulting in a birefringence of 1.4×10^{-5} . False colour image of the guided polarisation mode generated by the FIMMWAVE modelling for TM mode is shown in Figure 4.6.2.

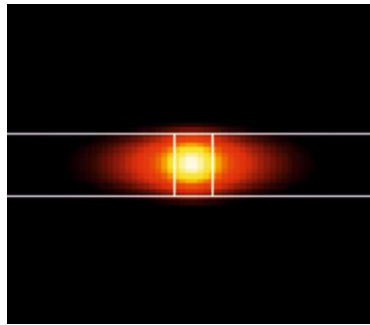


Figure 4.6.2 Illustration of guide mode field within a channel waveguide modelled in FIMMWAVE software for TM mode.

The measured birefringence achieved in this work is higher than the modelled birefringence. This is likely due to the stress induced birefringence within the flat-fibre generated during the fabrication process. However, the experimental data within the channel waveguide 1 to 7 shows that the birefringence varies largely and is shown to decrease towards the edge of the core section. This is likely due to the region having lower residual stress. In addition the UV writing parameters are unknown in this region i.e. spot size due to aberrations and that may also contribute to the reduction.

4.7 Conclusion

In this chapter, a brief description of direct UV-writing configuration has been given. A series of UV-written flat-fibre samples with Bragg gratings have been characterised and used to investigate two of the main UV-writing parameters, fluence and duty cycle. In

addition the Bragg grating structures have also provided some initial data on the effect of boron doping and hydrogen loading on the flat-fibre's photosensitivity. Such data is significantly useful in order to optimize the performance of UV-written waveguides and Bragg gratings. The flatness of the core layer of the flat-fibre substrate has also been investigated to look at the suitability of the platform for more complex integrated devices. The chapter finishes by looking at the birefringence of the flat-fibre. The next chapter discusses the loss measurement of the flat-fibre substrate using different optical methods.

Chapter 5

Loss Measurement in Passive Flat-fibre Substrates

5.1 Introduction

One of the main parameters requiring measurement when fabricating integrated optical devices is insertion loss. In fact, characterising waveguide propagation loss provides useful information for optimising and enhancing device performance. Thus, in this chapter, an innovative loss measurement technique demonstrated in a UV written optical waveguide is described. The technique uses the reflected power from Bragg grating structures to evaluate the propagation loss of the waveguide [84]. Alternative techniques that are used for waveguide loss measurement are reviewed as a comparison to our technique. The technique used in this work is a non-destructive technique where no destructive changes to the waveguide are involved, so long as Bragg grating structures exist within the waveguide. The technique is suitable for short waveguide samples with low propagation loss. In addition, the method allows simple and effective measurement that is independent of coupling loss and grating variation. Loss measurement of various waveguide structures has been undertaken, including straight channel waveguide and s-bends in the flat-fibre platform.

5.2 Optical Loss Measurement Techniques

Waveguide propagation loss can in principle, be simply measured by launching an identified input power into a waveguide and measuring the output power [85]. However, it is not as simple as that, as several losses contribute to the measurement. Thus, it

is important to use a measurement technique that can distinguish between the attenuation loss and other additional losses occurring within a channel waveguide. Additional losses, including modal mismatch between facet couplings, Fresnel reflection, and surface roughness of the waveguide end facet, which can cause light scattering, must be considered when measuring the device loss. There are several techniques which have been developed for device loss measurement for characterisation purposes [86], [87] and [88]. The techniques use either a destructive or non-destructive experimental procedure. The following section describes some common techniques used to measure propagation loss in optical fibre and planar optical waveguides.

5.2.1 Cutback Technique

The cutback technique is a destructive method of measuring attenuation in a channel waveguide. Attenuation is the power loss in the channel waveguide due to absorption, scattering and from other contributing losses. The technique involves comparing the output power from two different measurements which have different length of devices [89]. Figure 5.2.1 shows the procedure of the cutback loss measurement. The length of the measured device in measurement 1 is labelled in the figure as L_{long} , the length of the sample in measurement 2 is L_{short} , whilst the output power from the shorter and longer device are P_s and P_L , respectively. In order to calculate the attenuation of the device, the expression shown in equation (5.1) can be used, where the L is the difference in length between L_{long} and L_{short} as indicated in the figure below.

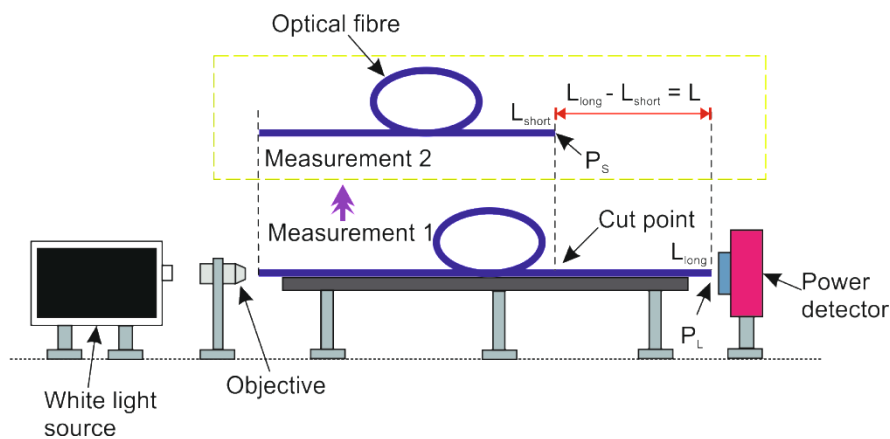


Figure 5.2.1 A cutback loss measurement technique that measures the output power from the optical fibre with long and short lengths.

$$\alpha \left(\frac{dB}{m} \right) = \frac{10 \log_{10} \left(\frac{P_L}{P_S} \right)}{L} \quad (5.1)$$

The technique is suitable for loss measurement in an optical fibre which involves cutting a length of the device under test, so that two different outputs of different lengths can be compared. Cleaving the optical fibre is simple and easy by using a commercial fibre cleaver. Hence, there is little issue with possible imperfection or inconsistency on the fibre end facet in subsequent measurements. In the case of a planar waveguide device, a variation in coupling efficiency results from cutting and polishing the end facet of the device. The cutback technique is dependent on the coupling efficiency of the measurement setup, thus is not so readily suitable for planar device. Another way of measuring the propagation loss of a planar device is via an end-fire coupling technique which is described in the next section.

5.2.2 End-fire Coupling

Another destructive loss measurement, known as the end-fire coupling technique, is introduced to characterise a planar device. The technique has similar procedure to the cutback method where a number of identical planar samples with different lengths are measured. Figure 5.2.2 shows the setup of the end-fire coupling loss measurement. Focused light is launched onto the input of the sample and the transmitted light measured from the output section using an optical detector. The procedure is simple and straight forward, but complications can exist. As with the cutback technique, the issues relate to the need to physically cut the samples into different lengths which can cause different coupling efficiency for different sample lengths. Therefore, a non-destructive loss measurement technique is more attractive where no physical change in planar device is required. Accordingly, it has been reported for the first time that the optimum end-fire technique has employed a non-destructive procedure through using self-pumped phase conjugation [90]. This method uses the second pass of the laser light to measure the waveguide propagation loss. The first pass of the laser beam is adjusted to the waveguide mode profile and automatically coupled back the phase-conjugated beam into the waveguide and thus yields the optimum coupling efficiency. From this technique, the modal mismatch can be neglected. The following section will describe other non-destructive loss measurement techniques particularly suited to planar waveguides.

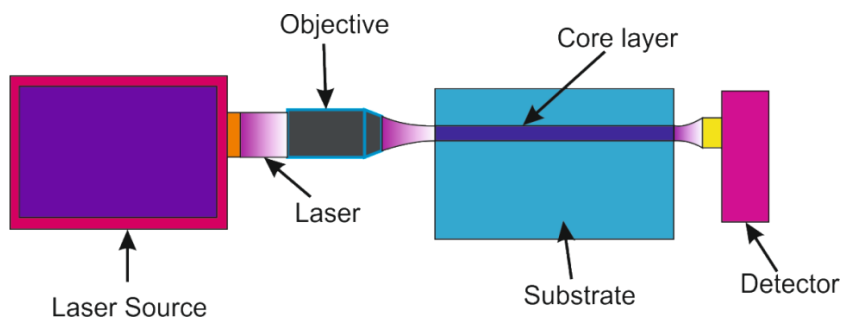


Figure 5.2.2 A loss measurement of a planar waveguide using end-fire coupling

5.2.3 Prism Coupling Technique

A prism coupling technique offers convenient loss measurement, where no physical changes to the device are needed [91], [92]. The basic configuration of the prism coupling loss measurement is shown in Figure 5.2.3. At least two prisms are required for the technique; one prism at the input section is kept fixed at one position and the other prism where the light is collected will be moved along the waveguide. Normally, the technique uses two or three prisms located on top of the sample in order to couple light in and out of the planar waveguide. The light is coupled to the planar waveguide through the evanescent field. The out-coupled lights from two different prism positions are compared to obtain the waveguide loss.

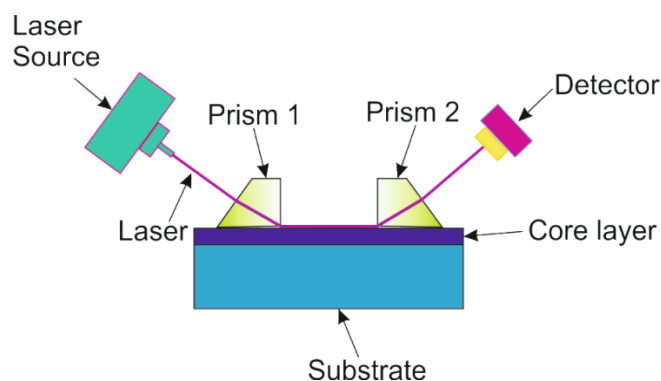


Figure 5.2.3 Prism coupling loss measurements on a planar waveguide.

Conventionally, the out-coupling prism is located as close as possible to the planar waveguide in order to optimise the out-coupling efficiency. However the out-

coupled power is typically quite low for a buried channel waveguide. Therefore, one way to optimise the out-coupling efficiency is by using a plastic prism which has been demonstrated by *Zhou et al* [93]. They applied heat to a plastic prism so that the prism is softened and thus an extremely close contact between the prism and the waveguide surface can be achieved. Even though the prism coupling technique is more adaptable than end-fire coupling, the technique still suffers from inconsistency in coupling loss every time the position of the out-coupling prism is changed. Therefore, a scattered light collection technique is more favourable, and is described in the next section.

5.2.4 Scattered Light Collection

In a scattered light collection technique, waveguide loss is measured by launching laser radiation into the waveguide and collecting the scattered light along the length of the waveguide using a fibre bundle [94] or a camera [95], [96]. In [95], the light is launched forward and backward into waveguide and the scattered light collected. The loss is obtained by taking the ratio between the total power distributions in each direction. Figure 5.2.4 shows the basic configuration for the scattered light collection technique. The technique provides a convenient way to measure the propagation loss, with no mechanical operation involved, and is independent of the coupling efficiency and facet reflectivities. However, the technique is only suitable for waveguides with losses around 1 dB/cm or even higher. Thus, accurately measuring propagation loss in a low-loss planar waveguide would be a challenge for the technique.

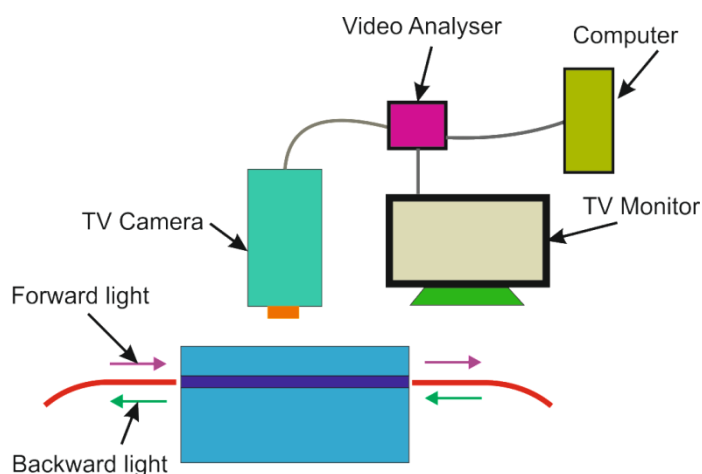


Figure 5.2.4 Loss measurement of a planar waveguide via scattered light method

5.2.5 Fabry-Perot Cavity Technique

The Fabry-Perot cavity technique is a loss measurement that has the ability of quantifying a propagation loss for low loss waveguides (<1 dB/cm). It compares the contrast of the Fabry-Perot cavity to measure the propagation loss of a planar waveguide. Figure 5.2.5 shows the basic configuration of the Fabry-Perot cavity loss measurement technique. Two dielectric coated mirrors are placed at both end facets of the waveguide to produce a cavity. The cavity can be adjusted by extending the cavity length via two optical fibres butt-coupled in and out of the waveguide [97]. This technique is somewhat independent of coupling efficiency and is a non-destructive loss measurement. However, in the case of Fabry-Perot cavity technique, prior knowledge of the mirror reflectivity is required to attain appropriate accuracy.

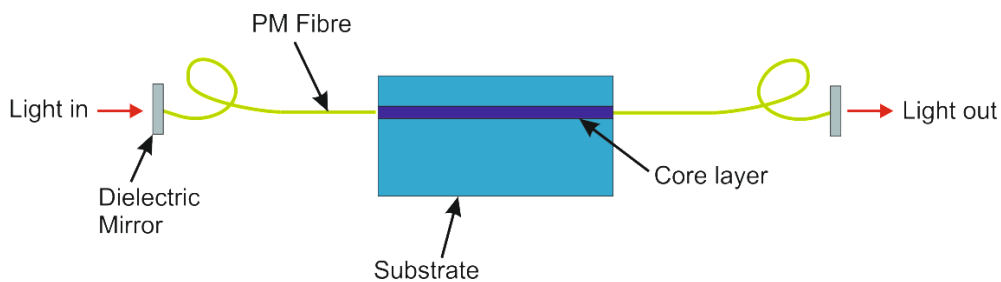


Figure 5.2.5 A Fabry-Perot cavity loss measurement technique for channel waveguide.

The technique used in this work is a non-destructive technique where no physical changes to the waveguide are involved. The technique is suitable for short waveguide samples with low propagation loss. In addition, the method allows simple and effective measurement that is independent of coupling loss and grating variation. The propagation loss in a flat-fibre substrate has been characterised and the measured loss for the sample was found to be 0.12 dB/cm. In comparison, the propagation loss in a flame hydrolysis deposition (FHD) substrate was found to be 0.235 dB/cm, showing that flat-fibre substrate has a lower loss compared to standard FHD substrates. In the next section, the concept of the novel Bragg grating loss measurement will be briefly discussed.

5.3 Novel Bragg Grating Loss Measurement

5.3.1 The Concept of Loss Measurement

This technique involves a series of integrated Bragg grating structures distributed along a length of waveguide. By observing the reflected power of each Bragg grating in two opposing directions, forward and backward, as depicted in Figure 5.3.1, propagation loss can be quantified. The direct measurement can be obtained by taking the ratio between the forward and backward reflected spectral power to obtain the propagation loss of the waveguide. The propagation loss measurement via this technique is not influenced by the coupling loss variation where two different measurements of opposing launch power directions are involved. Furthermore, the measurement is also independent of the grating spectral strength variation for different measurements. The relationship for loss, L (dB/cm) is calculated in equation (5.2), where P_n and P'_n (n represents the Bragg grating number) are the peak reflectivities in the forward and reverse directions respectively, measured in dB, and d is the separation of the gratings in cm. When plotting a graph of reflected power ratio against the position of the Bragg grating, the loss can be easily observed by taking the gradient of the line graph which is in units of dB/cm.

$$L = \frac{(P_1 - P_2) + (P'_2 - P'_1)}{4d} \quad (5.2)$$

The measurement adopts several assumptions about the waveguide and Bragg gratings. Firstly, the loss is not wavelength dependent over the spectral range of the Bragg gratings. Secondly the Bragg gratings have the same reflectivity when observed from opposing directions. This second assumption is generally true for weak Bragg gratings with small grating plane tilt. A further assumption is that the UV-written waveguides are sufficiently good enough to support the Bragg grating structures. It is also assumed that the waveguide losses are constant throughout the length of the waveguide.

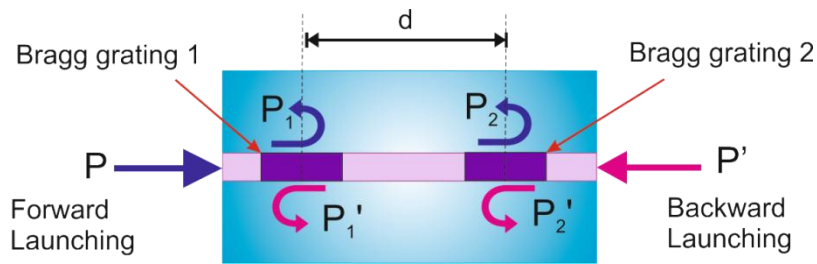


Figure 5.3.1 Waveguide structure schematic for the Bragg grating loss measurement technique.

5.3.2 Waveguide Definition

To measure the propagation loss using the Bragg grating loss measurement technique, a channel waveguide with a series of Bragg gratings along the length of the device must be defined using a direct grating writing technique. The direct grating writing technique has been described in Chapter 4, where two tightly focused UV-beams are used to produce the channel waveguide and Bragg gratings simultaneously. The propagation loss for a straight channel waveguide in Substrate C (as described in Chapter 4) of flat-fibre platform has been measured, where ten different Bragg gratings, with different central wavelengths, were distributed along the 40 mm long channel waveguide using 50 kJcm^{-2} fluence and a duty cycle of 0.5. The waveguide structure schematic is shown in Figure 5.3.2. The grating length was 1.5 mm with a waveguide spacing of 2 mm between each Bragg grating. It must be noted that to ensure the Bragg grating structures does not influence the waveguide loss, fluence-matching between the gratings and waveguides is employed during the UV-writing process. In addition to measuring the propagation loss of a channel waveguide, the technique is also useful for device optimisation where an s-bend configuration has been produced in the flat-fibre platform. Figure 5.3.3 show the configuration schematic for the s-bend.

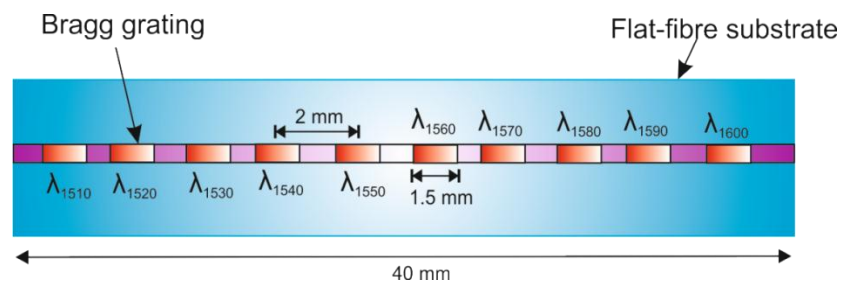


Figure 5.3.2 A schematic diagram of a channel waveguide with ten Bragg gratings along a 40 mm length of flat-fibre substrate.

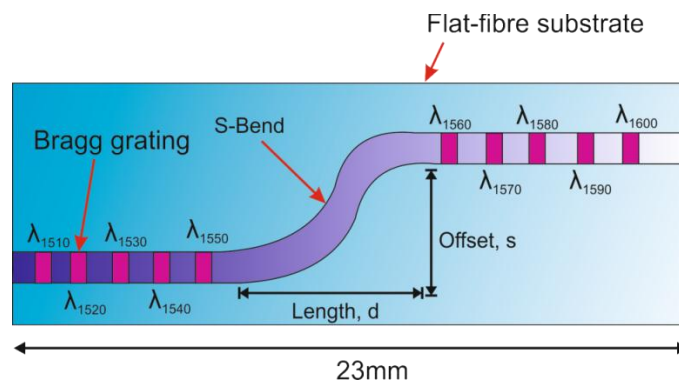


Figure 5.3.3 A schematic diagram for an s-bend configuration where five Bragg gratings before and after the s-bend were defined in the flat-fibre substrate.

5.3.3 Characterisation

A similar characterisation setup as previously shown in Chapter 3 has been used for measuring the propagation loss of a UV-written Bragg grating channel waveguide. Figure 5.3.4 shows the setup configuration used to characterise the waveguide in a forward and backward direction. The reflected spectrum in each direction was measured. In the forward direction, the light source is launched into the waveguide via facet A, whereas in the backward direction, the light is launched into the waveguide via facet B. In the next section, the results for the channel waveguide and s-bend configuration are discussed.

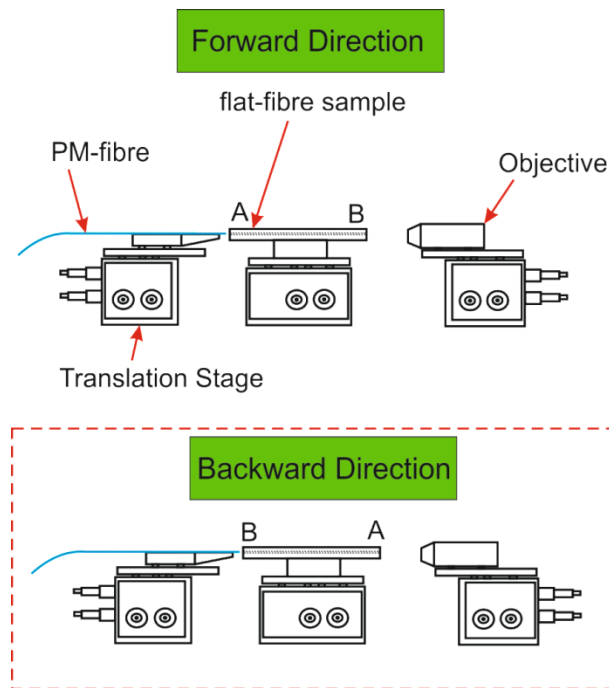


Figure 5.3.4 Characterisation setup for loss measurement in forward and backward configuration.

5.4 Results and Discussion

5.4.1 Channel Waveguide

Figure 5.4.1 shows the reflectivity of the UV-written Bragg gratings within the channel waveguide. The reflected spectra of ten Gaussian apodised Bragg gratings, where the central wavelength varied from 1510 nm to 1600 nm can be observed from the graph. The position of each grating along the waveguide has been shown in Figure 5.3.2. In the forward direction, the launched light was first incident on the Bragg grating of 1510 nm, whereas for the opposite direction, the Bragg grating of 1600 nm was the first illuminated. Figure 5.4.2 shows the ratio of the peak reflectivities in dB as a function of grating location. Using regression analysis, the gradient of the straight line fit provides a propagation loss for a straight channel waveguide of $0.13 \text{ dB/cm} \pm 0.03 \text{ dB/cm}$. This error is higher than that observed in FHD samples and is attributed to the slightly multimode nature of the flat fibre substrate.

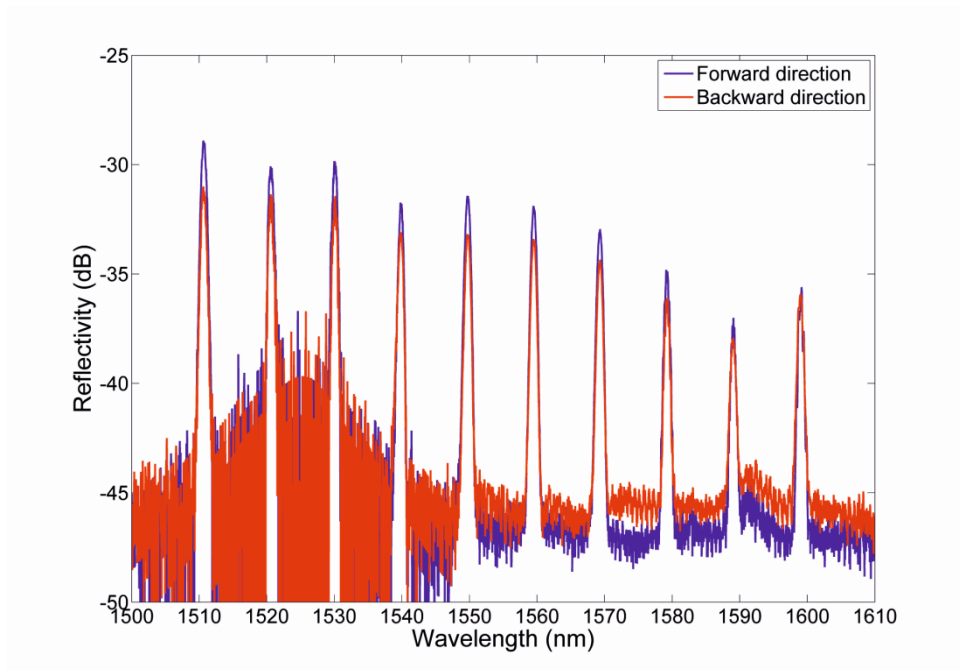


Figure 5.4.1 Reflectivity of the straight channel waveguide against wavelength. The UV-written channel waveguide containing ten Bragg gratings distributed along the length of the sample.

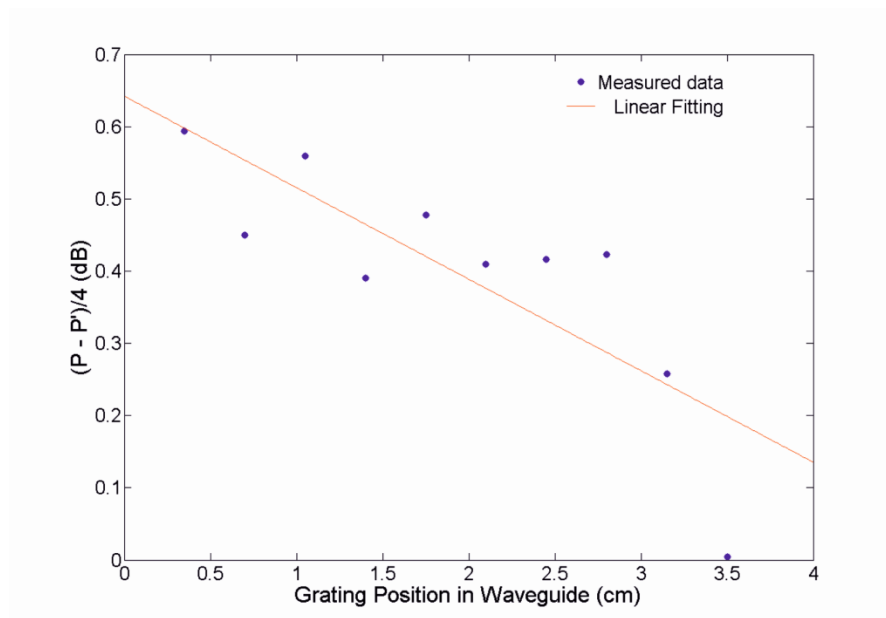


Figure 5.4.2 The ratio of peak power from forward, P and backward direction, P' against the grating position in the waveguide.

Owing to the simple and effective approach offered by the Bragg grating loss measurement technique, it was also used to interrogate UV-written s-bend waveguide components. The propagation losses of the device are observed by varying the related parameters contributing to device optimisation. This will be further discussed in the following section.

5.4.2 S-Bend Loss Measurement

The s-bend structure is the basis for constructing a y-splitter. The following experiment investigates the optimum value of the offset, s (see Figure 5.3.3) to minimise the bend loss within the s-bend structure. The s-bend structure was designed via a cosine bend, which can be modelled by [98]

$$f(x) = \left(\frac{s}{2}\right) \left(1 - \cos\left(\frac{\pi x}{d}\right)\right) \quad (5.3)$$

Where s is the s-bend offset and d is the s-bend length as illustrated in Figure 5.3.3.

The minimum radius of curvature, r can be expressed by

$$r = \frac{s^2 + d^2}{4s} \quad (5.4)$$

From equation (5.4), the calculated minimum radius for each offset is revealed in Table 5.4.1, where the bend length of 5.5 mm is the same for all the offsets. It can be seen that the higher the offset, the lower the minimum radius.

Table 5.4.1 The calculated values for the minimum radius of curvature, r , relative to the s-bend offset, s .

<i>Offset, s</i>	<i>Minimum Radius, r</i>
50 μm	150 mm
100 μm	76 mm
150 μm	50 mm
200 μm	38 mm

In order to observe the loss of the s-bends, ten different Bragg gratings were distributed in two straight channel waveguides before and after the s-bend, as illustrated in Figure 5.3.3. Four different offsets were investigated, 50, 100, 150 and 200 μm using a fluence of 90 kJcm^{-2} , a duty cycle of 0.5 and with an s-bend length, d of 5.5 mm. Figure 5.4.3 shows the reflected spectra of the Bragg gratings in forward and reverse directions for each different offset.

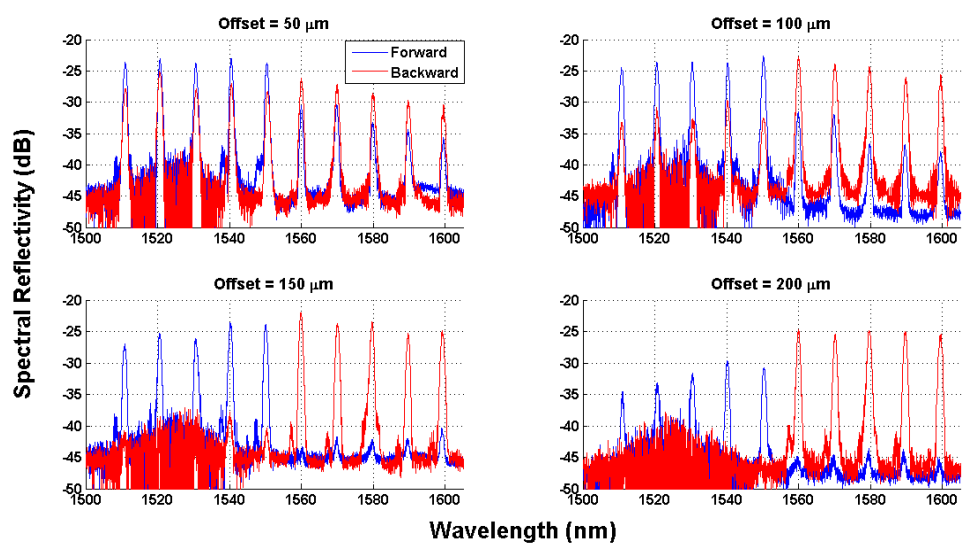
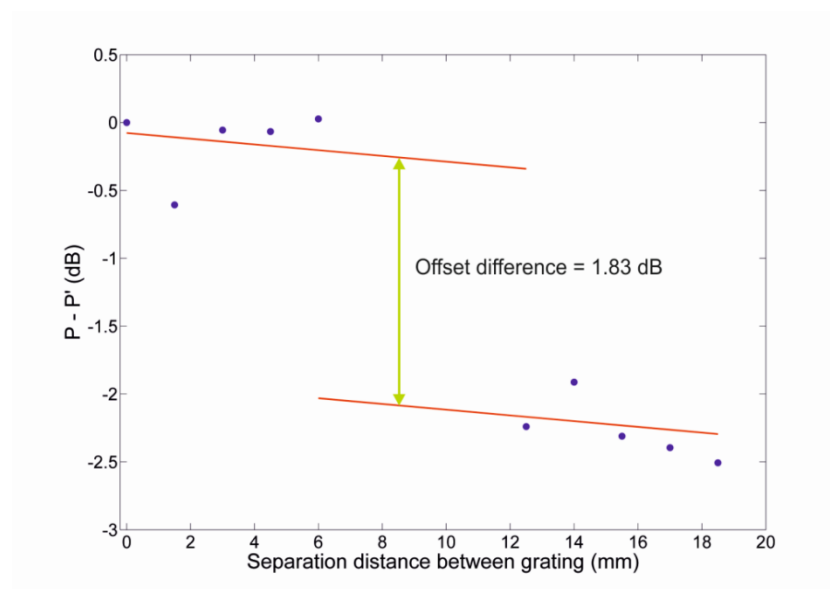


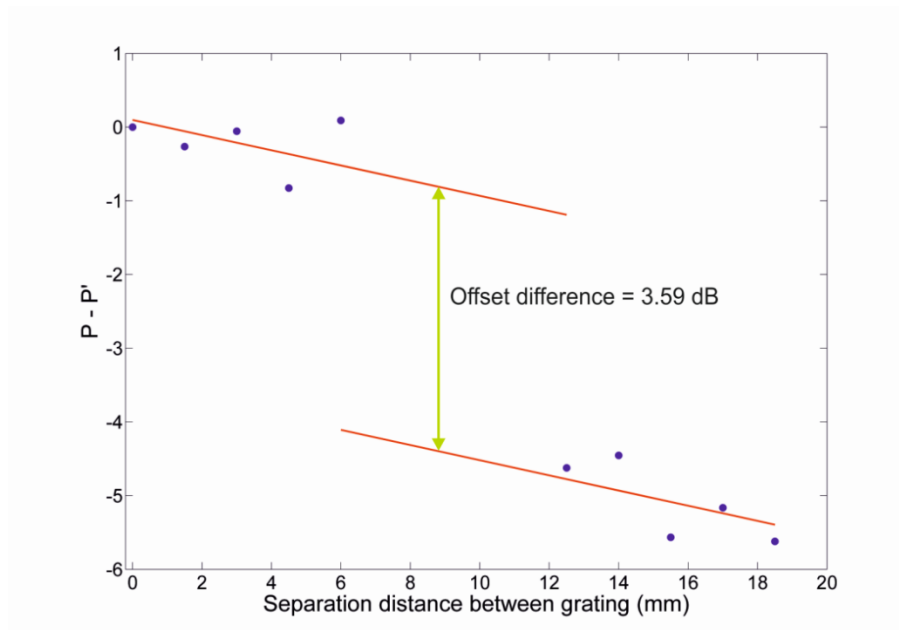
Figure 5.4.3 The spectral reflectivity of forward and backward direction for the four different offsets.

It can be observed from Figure 5.4.3 that the larger s-bends, those with offsets 150 and 200 μm , show very weak reflected signals after the s-bend region. In contrast, the s-bends with 50 and 100 μm offset present reflected signals such that an accurate Gaussian fit can be obtained. This agrees with previous experiments which have shown that higher offset values, which correspond to smaller bend radii, display exponentially increasing bend loss [99]. Physically, this is due to the bend radius significantly affecting the mode propagation, especially at the outer edge of the bend structure. In a straight channel waveguide the mode field distribution of light is symmetric in shape and centred at the middle of the waveguide. However, as it travels through a bending structure, the optical mode laterally shifts away from the centre of the bent waveguide. As the result, a portion of the light at the outer edge will be weakly guided and will tend to radiate away from the waveguide. This phenomenon is known as radiation loss [100].

As a result of the poor signal strength, only the loss of the 50 and 100 μm s-bend offsets can be analysed from this experiment, since the technique requires comparison of the peak spectral reflectivities from both directions. The spectral reflectivity ratio (difference in dB) for both s-bend offsets is plotted in Figure 5.4.4 where (a) and (b) represent 50 μm and 100 μm offset, respectively.



(a)



(b)

Figure 5.4.4 The offset difference for s-bend with offset (a) 50 μm and (b) 100 μm .

The measured data is fitted by using regression analysis in order to obtain the gradient of the propagation loss in the channel waveguide. The fitted data represents the linear line (red line) which has the same gradient before and after the s-bend struc-

ture and assumes that the propagation loss in the straight waveguide is constant. Following this, the s-bend loss can be evaluated by taking the difference between the two fitted lines, as shown Figure 5.4.4 (a) and (b). From this data the loss was 1.83 dB and 3.59 dB for 50 μm and 100 μm s-bend offsets, respectively. This data shows that smaller s-bend offset will tend to have smaller bend loss. This is due to the relationship of s-bend offset with the radius of curvature where the bend loss is exponentially increased with the reduced radius.

This measurement technique offers straightforward and effective measurement for s-bend loss. This observation shows that the Bragg grating loss measurement technique can be used for device optimisation and not only for loss propagation observation. In order to make a comparison, the flat-fibre sample was also measured using an optical backscattered reflectometer (OBR) system by launching light into a channel waveguide without any UV-written Bragg grating and waveguide structures.

5.5 Optical Backscattered Reflectometer

A commercial optical backscattered reflectometer (OBR) was used to measure the propagation loss of the flat-fibre sample. The commercial OBR 4400 series from Luna technologies has been used to measure the propagation loss of the flat-fibre. The OBR system offers ultra-high spatial resolution down to 40 μm scale which has the capability to quantify waveguide losses in a short device length. The principle of the OBR system is based on monitoring reflected signal induced by device splice, connection, end facet and even faults such as bend, breaks, or deformation. The OBR system is connected to the computer and from its intuitive graphical interface, it can show the location along the length of a device under test that causes reflections, as depicted in Figure 5.5.1. This provides a convenient way to directly access the measurement results. The reflected power from a length of flat fibre is shown in Figure 5.5.2. Assuming the material composition of the waveguide is the same within this region, the gradient provides a measurement of the propagation loss. The measured loss was $0.09 \text{ dB/cm} \pm 0.01 \text{ dB/cm}$, which is in good agreement with the Bragg grating loss measurement technique with a difference of 0.04 dB/cm.

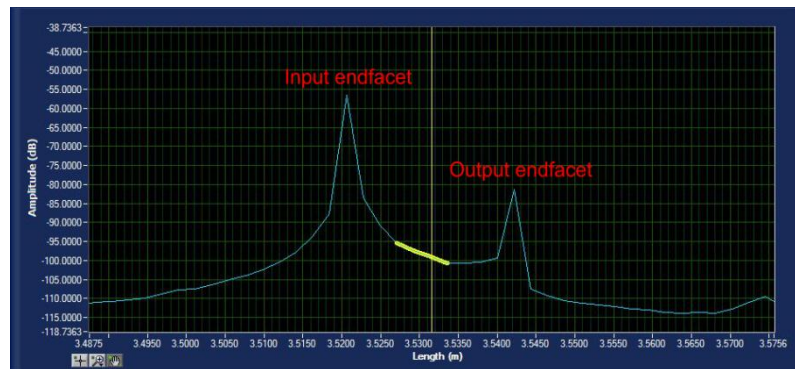


Figure 5.5.1 OBR graphical window to show the reflected signal from the endfacet of the flat-fibre substrate.

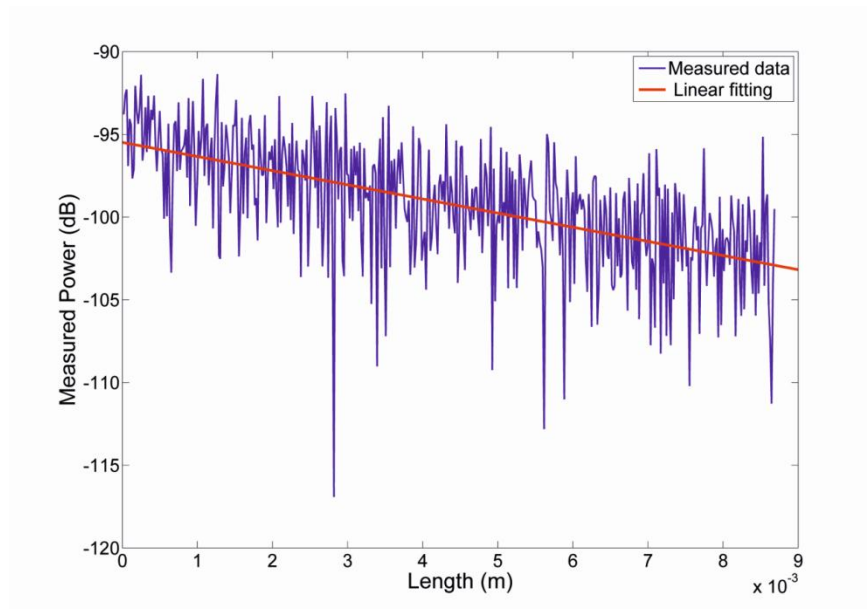


Figure 5.5.2 Propagation loss measurement using OBR technique.

5.6 Conclusion

In summary, the concept of a novel Bragg grating loss measurement technique has been explained and used to measure the propagation loss in a channel waveguide. This technique has been compared to the optical backscattered reflectometer (OBR) and shows good agreement. Furthermore, the technique has been further used to measure the bend loss of s-bend structure. In the next chapter, the capability of the flat-fibre substrate to be used as a physical and refractive index sensor will be revealed.

Chapter 6

Physical and Refractive Index Sensors in Flat-fibre Platform

6.1 Introduction

A brief description about optical sensors has been given in Chapter 2. In this chapter, the focus is on Bragg grating based physical and refractive index sensors. Owing to the numerous advantages offered by optical sensors, they have seen a wide range of applications in refractive index [101] and physical [102] detection. Several techniques have been demonstrated, but the most common technique implements a Bragg grating structure which is widely employed in a fibre Bragg grating (FBG) sensor. This is due to the benefits offered by the Bragg grating which has low loss, multiplexing capability, and by measuring wavelength relies on a signal largely independent of intensity variations. Despite all the listed advantages, the technique is generally limited to a single sensing parameter. This is probably due to the difficulties in realising integrated capability in a standard fibre design. In some applications, it is desirable to have multiple parameter sensors in a single compact detection platform which can provide enhanced localized information for a system.

A single fibre is not ideal for measuring two dimensional bending and refractive index. One of the reasons for this is due to in a fibre Bragg grating, for instance, the sensing regions are distributed at separate positions. In fact, the packing of a standard single fibre is limited by associated bend loss. Therefore, there is no such single optical FBG sensor that can sense two dimensional bending and refractive index in a compact volume. Nevertheless, there are several numbers of configurations that have been designed in order to allow the FBG structures to be used for sensing multiple parame-

ters in a single package. One of the techniques, for measuring two-dimensional deflection attaches a single FBG onto a cantilever-mount [103]. However, this configuration has no inherent temperature reference available. A Rosette configuration makes use of three FBGs in a triangle pattern as shown in Figure 6.1.1, each forming a side of a triangle, and offers better performance as vectorial strain can be monitored [104]. However, the minimum size of the device is limited because of bend loss associated with the side of the triangle loops.

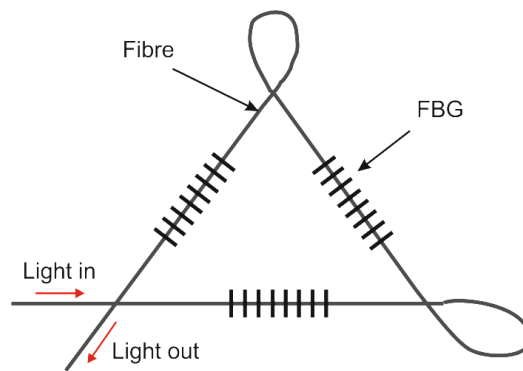


Figure 6.1.1 Schematic diagram of Rosette configuration with three FBGs.

Whilst FBGs traditionally require complicated packaging to achieve 2D bend sensing, alternative non-FBG approaches exist that do not require such packaging. A multi-core photonic crystal fibre (PCF) has been demonstrated in order to sense 2D bending [105]. The sensor offers compact detection because it contains only one single fibre. It has three cores in a single fibre. The sensing measurement manipulates the differential strain that is related to an optical phase from each core. Yet, in the case of multi-parameter sensing, for instance bending and refractive index sensors in a single fibre, Bragg grating elements are still less suited. Using a planar platform can be a good choice for that particular purpose. Though, it is worth noting that planar structures are typically rigid, thus have a limited range and in some circumstances the rigidity could interfere with what is to be measured.

In this work, a compact multi-parameter sensor is presented, which combines the benefits offered by a standard optical fibre with integrated planar optics. The Bragg grating structures are used as a tool for quantifying the sensitivity of the sensor device. A series of experimental studies has been performed, involving fabrication and characterisation of optical sensor devices in flat-fibre. Three parameters have been

considered in these experiments namely refractive index, bending and temperature. The Bragg grating structure is produced by using the direct grating writing technique. In a preliminary experiment, a series of refractive index oils were used to measure the sensitivity of the flat-fibre substrate to sense external refractive index. The sensitivity of the optical flat-fibre sensor device to about 95 nm per refractive index unit has been obtained. Following this, a two-dimensional bending and refractive index oil sensors is demonstrated in a single flat-fibre substrate.

This chapter is organised by firstly explaining the principle of evanescent field sensing and the bending theory and also how it relates to the Bragg grating structure. The fabrication and characterisation procedure of the sensor device is described. Finally, the result for the refractive index and two-dimensional bending sensor is revealed and discussed.

6.2 Evanescent Field

In this work, refractive index sensors have been developed by exposing the evanescent field of the waveguide mode. An evanescent field is a near-field wave with an exponential decay pattern that is exposed near to the boundary of a waveguide. Principally, evanescent fields are formed when there is a total internal reflection occurring at the boundary of the waveguide. From this, the way that the refractive index sensor device operates is by exposing the evanescent tail of the guided mode to the analyte. The guided mode will be dependent on the external refractive index, if the evanescent field is supported in that medium. Commonly, the principle of exposing the waveguide's evanescent mode field to the analyte is used for a chemical and refractive index sensors [106].

The work presented in this chapter uses a Bragg grating structure to monitor refractive index oil. The mode of the Bragg grating structure is exposed to a series of refractive index oils, the effect of this is to change the propagation of the guided mode. Bragg grating based-sensors that use this effect generally do so via the perturbation of the evanescent field of the guided mode. The mode's evanescent tail is exposed to the different refractive indices which will change the effective refractive index of the guided mode as depicted in Figure 6.2.1, where (a) and (b) represent sample with and without analyte, respectively. The change of the effective refractive index of the guided mode will consequently shift the centre wavelength of the Bragg grating as

shown in Figure 6.2.2. The concept explained here will be the principle used in this work for the refractive index sensor.

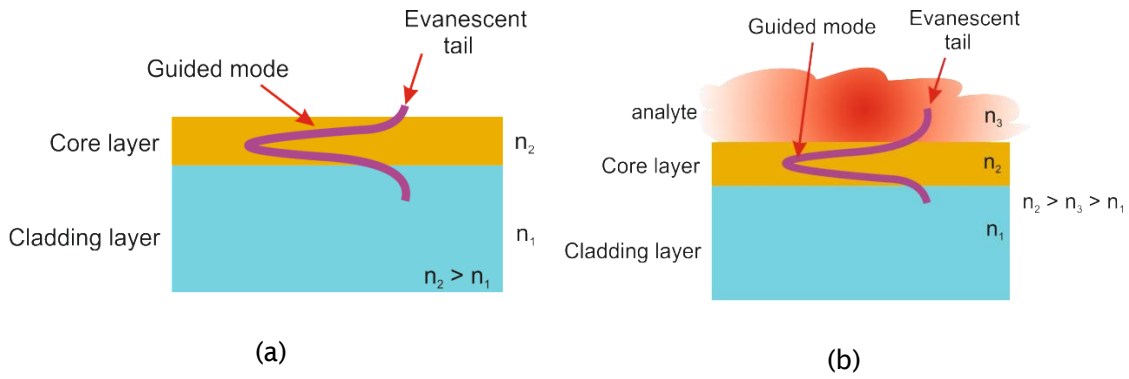


Figure 6.2.1 Illustration of evanescent tail of a guided mode in a planar waveguide where (a) without analyte and (b) with analyte.

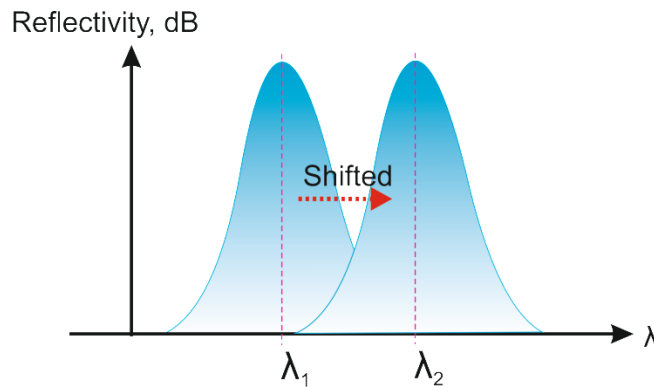


Figure 6.2.2 Spectral reflectivity showing a wavelength shifting from λ_1 to λ_2 due to sense of different refractive index oils.

6.3 Physical Bending Theory

6.3.1 Elasticity

Elasticity is a material property which indicates the behaviour of physical body; for instance, when force is applied to a body, at some points the shape of the body will deform and return to its original shape when the force is removed [107]. This kind of behaviour is essential for the substance to be used as a physical sensor. If the physical sensor is exposed to some forces it will cause a physical deformation. In this section, the principle of elastic behaviour is described, firstly explaining Hooke's Law and followed by the principle of bending a beam and lastly about the Bragg grating response and its strain relationship. This theory is essential to understand the response and routes for optimisation of the flat-fibre bending sensor.

6.3.1.1 Hooke's Law

In general, when considering an elastic solid substance, for instance a rectangular beam, as shown in Figure 6.3.1, an applied force in a uniaxial direction will cause the beam to change in length in all dimensions. The change in length along the direction of applied force is labelled as Δl . This is proportional to the applied force as expressed in equation (6.1) known as Hooke's law. The expansion of Δl is also correlated to the original length, l and the cross-sectional area of the beam, A on which the force is applied and this condition can be expressed as in equation (6.2). Combining equation (6.1) and (6.2), presents a constant of proportionality that is a material property known as a Young's modulus, E . From equation (6.2), it can be rewritten as equation (6.3) to represent the Hooke's law.

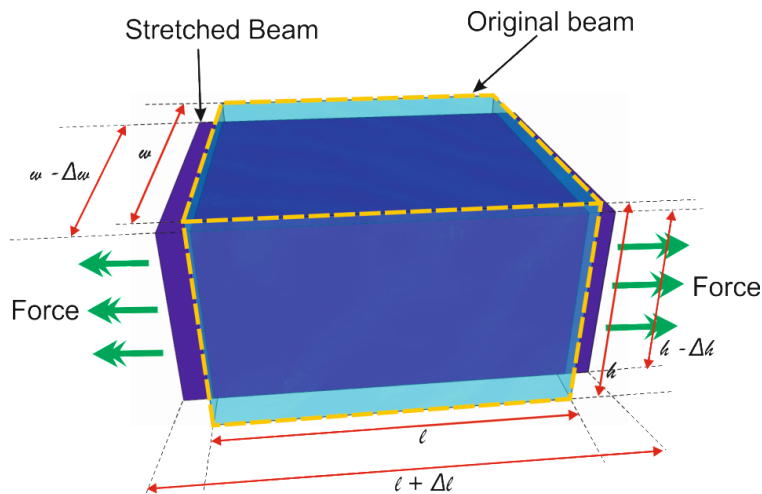


Figure 6.3.1 Illustration of stretching a rectangular beam where showing the original beam (dash yellow line) and the stretched beam (solid line).

$$F \propto \Delta l \quad (6.1)$$

$$F = EA \frac{\Delta l}{l} \quad (6.2)$$

$$\frac{F}{A} = E \times \frac{\Delta l}{l} \quad (6.3)$$

Stress, $\sigma = \text{Young's modulus, } (E) \times \text{strain, } (\varepsilon)$

An internal stress within a beam is induced when force acting on a certain area of the beam, which can be defined as a ratio between the force and the area that it contacts. This can be seen at the left hand-side of the equation (6.3). The induced strain is dependent on the nature of the material it interacts with. In addition, according to the Hooke's law, the stress has a linear relationship to the strain with certain proportionality depending on the material that is used. The strain effect is defined as a ratio between a length expansion caused by a force and its original length as stated in the right-hand-side of the equation (6.3). The Young's modulus represents the slope of the linear portion of a stress-strain curve. From the stress-strain curve, it shows that at some point the material will reach its elastic limit beyond which the linear proportionality of the stress and strain breaks down. At this point, Hooke's law is no longer

obeyed. By knowing the value of the Young's modulus of certain material, it gives the information about the material's stiffness.

Apart from the Young's modulus, there is another property that specifies the elasticity of a substrate which is known as Poisson's ratio. As described above, there is a change in length in the same direction of the applied force, this introduces some changes in length in the other directions perpendicular to the applied force namely the width, w and height, h of the beam. Poisson's ratio, ν , is a constant that relates the ratio of changes in width, Δw to the original width, w and the strain of the beam when stretching it as expressed in equation (6.4).

$$\frac{\Delta w}{w} = \frac{\Delta h}{h} = -\nu \frac{\Delta l}{l} \quad (6.4)$$

Normally, the value for the Poisson's ratio is within 0.0 to 0.5. Both parameters of Young's modulus and also the Poisson's ratio are used to determine the elastic properties of a specific homogeneous isotropic material. In the next section, the principle of bending a beam will be briefly explained.

6.3.2 Bending a Beam

In this section, the principle theory of bending a beam is described in order to give an overview of how the beam deforms subject to a bending. Considering a rectangular beam, when bending the beam in vertical direction, the beam will deform as shown in Figure 6.3.2. It can be seen that the length of the top surface is increased while the bottom surface decreased. This means that the top and the bottom surface of the beam experienced tensile stress and compression, respectively. There is a plane within the beam which has no extension or compression. This position is known as the neutral plane or neutral axis when referring to the cross-section of the beam as labelled in Figure 6.3.2. The length of the beam at the neutral axis is not changed. The location of the neutral axis depends on the shape of the structure and materials from which it is made.

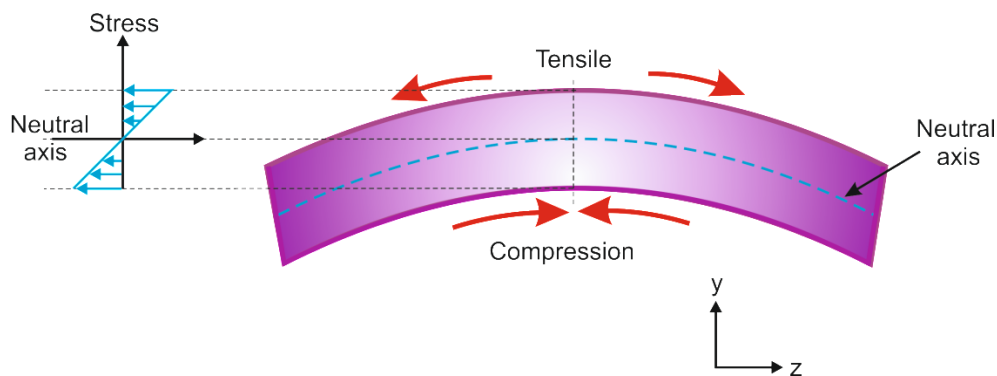


Figure 6.3.2 Illustration of bending of a rectangular beam, where tensile stress and compression occur at the same time. The amount of the stress along the y -axis is symmetric to the neutral axis of the beam.

The strain occurring at any one point in the beam is proportional to the distance from the neutral axis and inversely proportional to the radius of curvature of the bending. This can be expressed as in equation (6.5), where the distance, y and the radius of curvature, R can be illustrated as in Figure 6.3.3 [107]. This relationship is further expanded by applying Hooke's law into equation (6.5) and yields the expression in equation (6.6). This shows that the stress is also proportional to the distance, y . The act of bending is actually caused by a bending moment, M . The bending moment can be quantified by integrating the force multiplied by the distance, y in particular cross-sectional area as expressed in equation (6.7). By substituting the equation (6.6) into

(6.7), the expression of equation (6.8) can be derived, where I is the moment of inertia of the device. For a particular condition the deflection of a cantilever will be described in the next section.

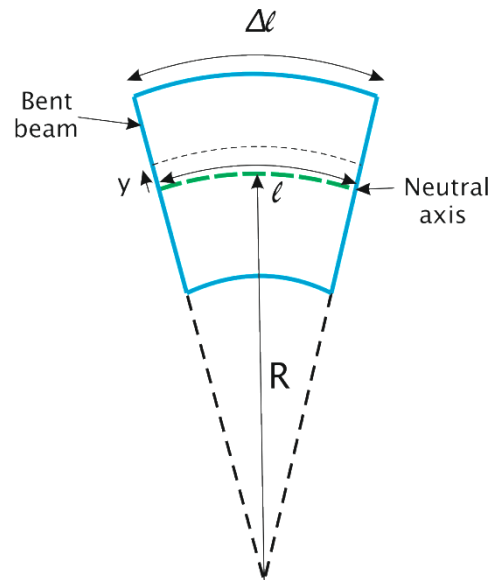


Figure 6.3.3 Illustration of bent beam and showing the neutral axis of the beam (green line).

$$\frac{\Delta l}{l} = \frac{y}{R} \quad (6.5)$$

$$\frac{\Delta F}{\Delta A} = E \frac{y}{R} \quad (6.6)$$

$$M = \int_{cross\ section} y dF \quad (6.7)$$

$$M = \frac{EI}{R} \quad (6.8)$$

$$I = \int y^2 dA \quad (6.9)$$

6.3.3 Deflection of a Cantilever

Considering a cantilever beam structure, where one end is fixed and which is deflected by the free end of the beam with an applied force, W as shown in Figure 6.3.4. The beam is deflected as $z(L)$ where the length of the beam is L . The maximum deflection at the end tip of the beam can be defined as in equation (6.10).

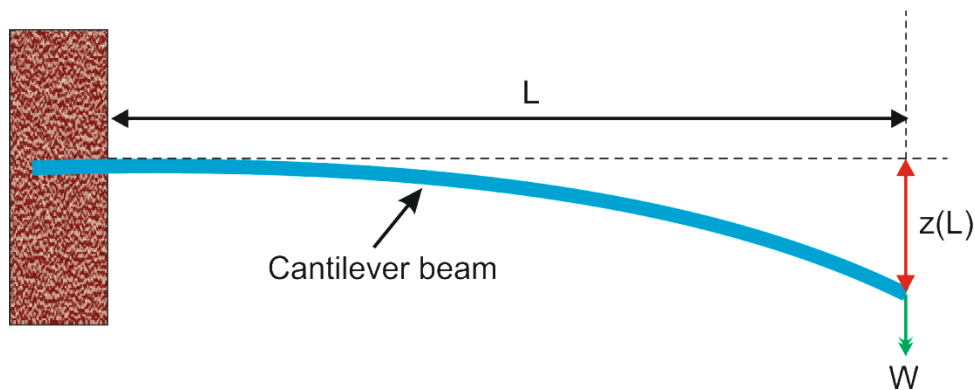


Figure 6.3.4 A cantilever beam with a concentrated weight, W applied at the free end of the beam with deflection of $z(L)$.

$$z(L) = \frac{WL^3}{3EI} \quad (6.10)$$

6.3.4 Material Properties of Silica

It is important to understand the material properties of the sample that is used for a physical sensor. This is because the physical sensor is directly correlated to the material properties of the sample. In this work, a flat-fibre substrate made from silica is used as a sensor platform. Generally, silica is a high purity non-crystalline silicon dioxide (SiO_2), which is typically a brittle and transparent glass. Also, it is a type of isotropic structure by which at every point along the substrate the elastic properties of the flat-fibre are similar in all directions. The cladding of the flat-fibre is made by pure silica without any other additional composition and thus has a refractive index of 1.444 at 1550 nm. The core of the flat-fibre has been doped with germanium (Ge) which makes the refractive index higher than the cladding layer about 1.46. Table 6.3.1 shows the

standard mechanical properties of fused silica glass [108]. Typical Poisson's ratio for silica is 0.17.

Table 6.3.1 Mechanical properties of fused silica glass (taken from [108]).

Parameter	Standard
Density	2.201 g/cm ³
Shear Modulus	31 GPa at 25 °C
Young's Modulus	73 GPa at 25 °C
Tensile Strength	50 MPa
Compressive Strength	1.1 GPa

6.4 Flat-fibre Sensor Device Concept

The refractive index and bending sensor components have been integrated into a single multiplexed device. The device contains a series of Bragg gratings that each has a dependency on strain and external refractive index. As previously discussed in Chapter 4, the Bragg grating structures are a periodic refractive index modulation that are created by focusing two crossed beams of ultraviolet (UV) light on the photosensitive sample. Light that is launched into the Bragg grating structure will be reflected back if the wavelength satisfies the Bragg condition. The reflected signal of the Bragg wavelength will shift due to changes in the effective refractive index or grating pitch. The centre Bragg wavelength has a proportional relationship to the effective refractive index and grating pitch of the device as expressed in equation (2.55).

When considering a refractive index sensor, one can think of changes in the effective refractive index of the guided mode that will occur when exposing the sensor to different refractive index oils. The concept is also applicable to a physical sensor, where bending of the waveguide alters the material stress and the refractive index of the waveguide and again affects the centre wavelength of the reflected signal. However, it must be noted that, when the structure of the sample is changed, it will also

change the pitch of the Bragg grating. The relative Bragg wavelength shift occurring in the Bragg grating structure can be expressed by equation (6.11).

$$\frac{\Delta\lambda_B}{\lambda_B} = \frac{\Delta n_{eff}}{n_{eff}} + \frac{\Delta\Lambda}{\Lambda} \quad (6.11)$$

Thermal changes induce strain via thermal expansion, thus the surrounding temperature changes are an influence to parameter sensing. It has been observed that the temperature sensitivity of optical fibre and FHD Bragg gratings is ~ 10 pm/°C. Even though this change is very small, temperature variations during the experiment can significantly affect the measurement data. The complete wavelength shift ($\Delta\lambda_{x,y}$) of a Bragg grating to a given strain, including temperature, T effects, can be expressed as equation (6.12) [109].

$$\frac{\Delta\lambda_{x,y}}{\lambda_B} = \varepsilon_z - \frac{n_{x,y}^2}{2} [P_{11}\varepsilon_{x,y} + P_{12}(\varepsilon_z + \varepsilon_{y,x})] + \eta\Delta T \quad (6.12)$$

where, ε_x , ε_y and ε_z are the applied strain for x, y and z axes, P_{11} and P_{12} are the photo-elastic constants of the waveguide, $n_{x,y}$ is the effective refractive index of the guided mode and η is the temperature coefficient.

6.5 Refractive Index Sensor

In a preliminary experiment, a UV-written Bragg grating structure was used to observe the ability of the flat-fibre to sense different refractive index oils. The schematic diagram of the flat-fibre substrate sensor is shown in Figure 6.5.1 (a). In order to expose the Bragg grating field mode to an external refractive index, part of the cladding layer was lapped and polished by using a Logitech model LP50 polishing machine. The flat-fibre substrate was made to have a tilted structure as shown in Figure 6.5.1 (b). Thereby, the Bragg grating mode, in the core layer, can be easily exposed to the refractive index oil. After polishing the spectra from gratings at 1550 and 1555 nm were no longer detectable as they were removed during the polishing process.

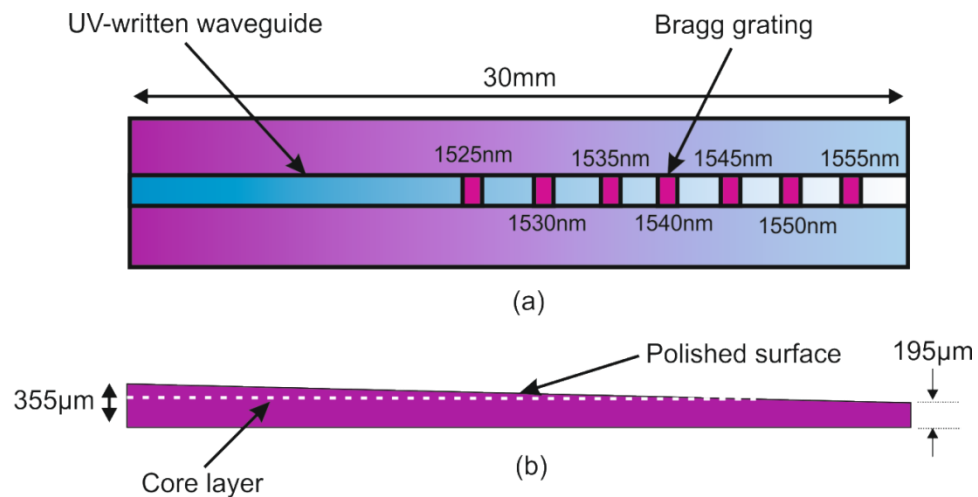


Figure 6.5.1 The Illustration of refractive index sensor using a series of Bragg grating structure.

To experimentally investigate the refractive index sensitivity, the flat-fibre is first pigtailed with polarisation maintaining (PM) fibre to ensure a constant intensity and single polarisation optical source was coupled into the flat-fibre substrate. An erbium fibre based ASE light source was launched into the sample, the light was polarised such that the transverse electric (TE) polarisation was coupled into the device. The reflection spectrum of the device was analysed with an optical spectrum analyser via a circulator and the individual grating peaks were fitted using a LabVIEW program which accurately determined the central Bragg wavelength.

On applying several different refractive index oils to the flat-fibre surface only the centre wavelength of 1545 nm was seen to shift significantly. The reason for this was that due to the wedge form of the flat-fibre, this was the only Bragg grating with sufficient cladding removed that the mode was exposed to the refractive index oils. Figure 6.5.2 shows the spectral reflectivity power against the Bragg grating wavelength. The data shows that the centre wavelength of the 1545 nm grating shifts when exposed to the refractive index oil of 1.39. The data also indicates that the four other Bragg gratings were not spectrally shifted and thus not affected by the index oil. The effect of different refractive index oils on the Bragg grating structure at 1525 nm was also observed and is shown in Figure 6.5.3. This small variation is probably due to the temperature variation during the experiment. The maximum centre wavelength shift was 34 pm which would correspond to a temperature change of $\sim 3.4^\circ\text{C}$ which is quite likely in the laboratory environment.

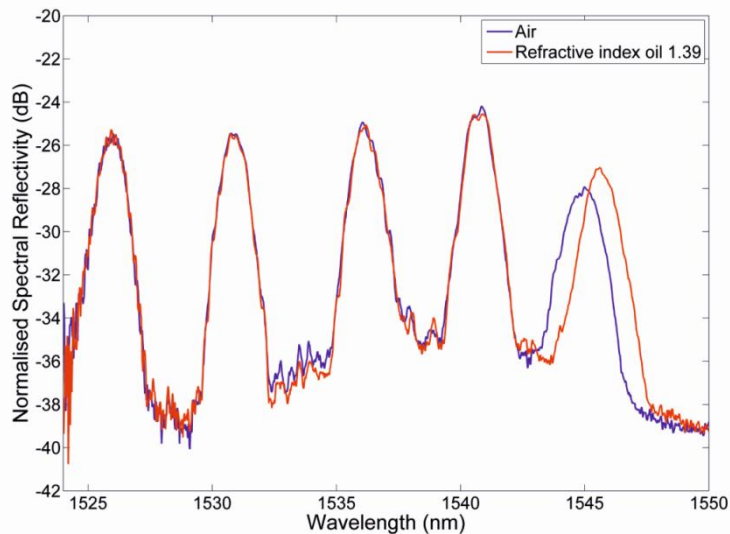


Figure 6.5.2 Normalised spectral reflectivity against the Bragg grating wavelength.

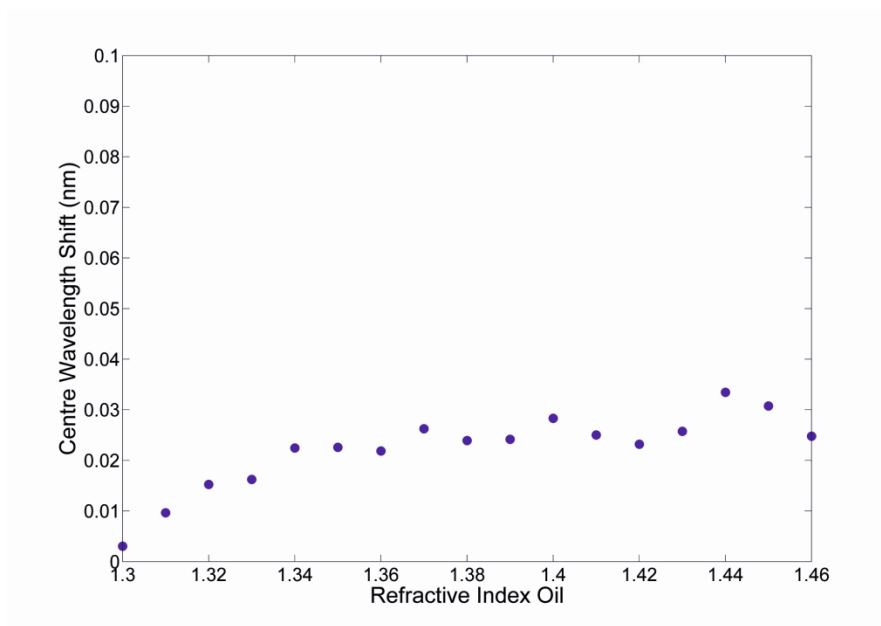


Figure 6.5.3 A centre wavelength shifting at 1525 nm against the refractive index oil variation.

Figure 6.5.4 shows the Bragg grating centre wavelength shifting against the refractive index oil. The temperature variation has been considered in this graph. From the graph, the maximum shift of the centre wavelength is 3.16 nm for the 1.46 refractive index oil. The gradient of the data provides the sensitivity to refractive index change as a function of refractive index analyte and is plotted in Figure 6.5.5. This data shows that the highest sensitivity of the device is ~ 95 nm per refractive index unit which results at the highest refractive index of 1.46. This is expected as the high refractive index oil shifts the waveguide mode into the analyte (i.e. refractive index oil) and thus exposes more of the evanescent field to the analyte thereby increasing the sensitivity.

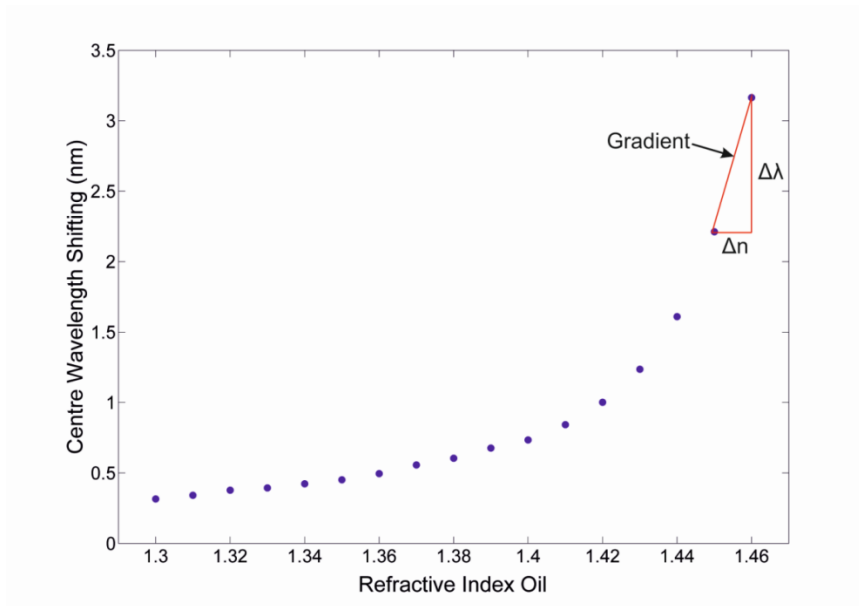


Figure 6.5.4 The centre wavelength of the 1545nm grating shifting against the refractive index oil.

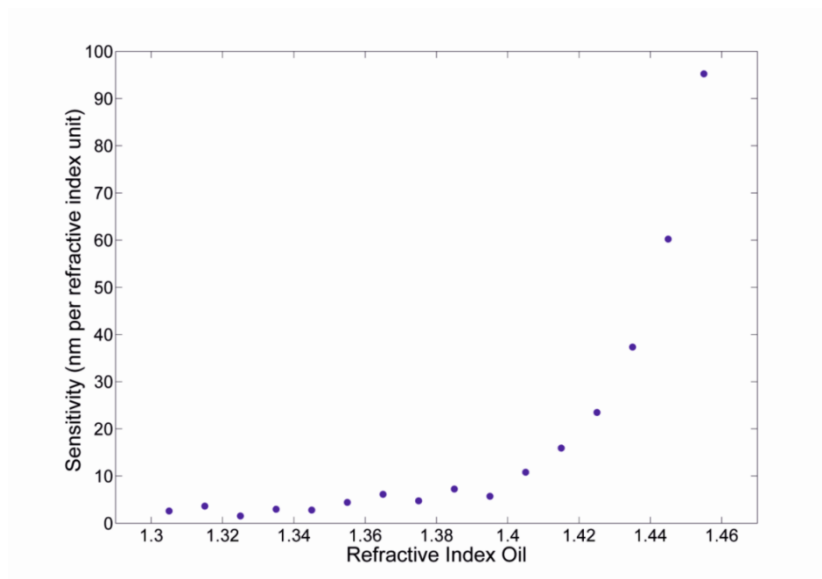


Figure 6.5.5 The sensitivity of the refractive index sensing against the refractive index oil.

From the measurement it is clear that the flat-fibre substrate has the ability to sense different refractive index oils with a maximum shift of 3.16 nm. It is expected that a sensor device in flat-fibre could be further improved by placing a thin film of high refractive index material on the surface of the device. This technique has been used in the past to enhance sensitivity and uses the high index layer to displace the optical mode so that higher proportion of the mode propagates within the analyte [110]. The device presented in this section was not designed for a two-dimensional bending. In order to distinguish two directions of bending, a new geometry is proposed that uses two separate waveguides parallel to each other. The following section shall describe this concept in further detail and also combine operation of bend sensing with refractive index monitoring using the principles outlined in this section. This new device offers improved function over the simple single channel device.

6.6 Two-dimensional Bending and Refractive index Sensor

In this section, a multifunctional sensor device which has the capability of sensing two-dimensional bending and refractive index simultaneously in a single planar platform of flat-fibre substrate is presented. For two-dimensional deflections, the flat-fibre is clamped such that it forms a cantilever. The displacements of the cantilever tip in the x and y axis directions are manipulated as illustrated in Figure 6.6.1.

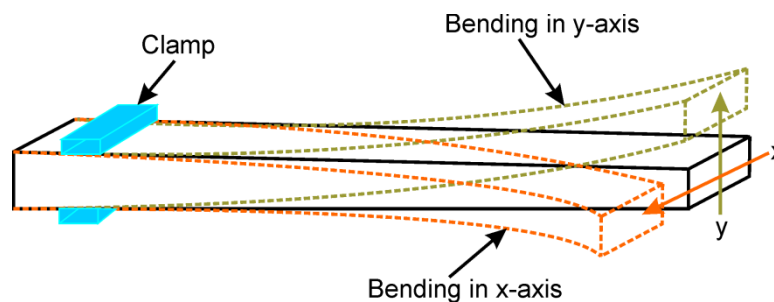


Figure 6.6.1 A bending configuration at the free end point displacement in x and y-axis direction.

6.6.1 Concept and Device Design

In this particular work, the design of the flat-fibre platform is similar to the previous device described in Section 6.5, where the flat-fibre has a wedged top cladding that is lapped and polished using a Logitech model LP50 polishing machine as illustrated in 3D image shown in Figure 6.6.2. The difference between those devices is only in the waveguide design where involving two UV-written channel waveguides with Bragg gratings are used. A flat-fibre substrate with germanium and boron co-doped has been used in this work. The substrate was cleaved into a 30 mm length. Part of the cladding of the sample was removed, resulting in a wedge of about 0.27° . By removing material, the neutral axis was shifted relative to the core layer of the flat-fibre. This meant that Bragg gratings existing in the core layer were more sensitive to induced strain.

The measurement of two-dimensional bending is achieved by clamping the flat-fibre in a cantilever arrangement. In particular, the tip of fibre free end is then displaced to represent the bending configuration. In order to distinguish bending effect in horizontal or lateral displacement, the mapping configuration of the Bragg grating is a significant characteristic that must be considered for two-dimensional bending sensor. This is to allow different gratings to experience different responses to environmental refractive index and induced strain, which affects their respective spectral response. Apart from that, the mode of the UV-written Bragg grating in the core layer can be exposed to an external refractive index, via an evanescent field interaction. A range of refractive index oil was applied to the device in order to calibrate the sensitivity of the flat-fibre sensor. The index oils are placed on top of the flat-fibre substrate, thus, exposing the external refractive index oils to certain gratings.

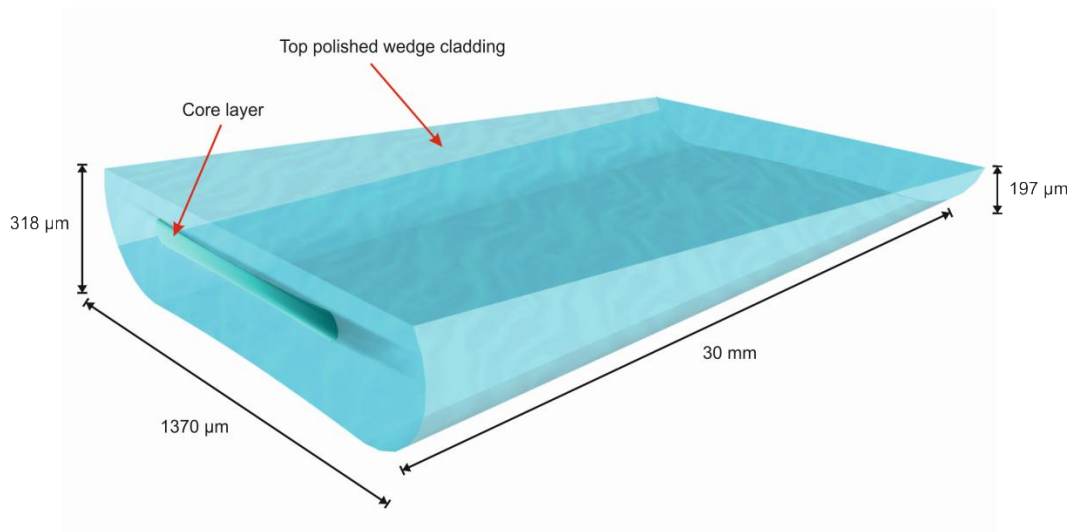


Figure 6.6.2 3D schematic of the top polished wedge cladding for the flat-fibre sensor device.

Figure 6.6.3 (a) shows the schematic diagram of the flat-fibre sensor containing two UV-written waveguides labelled as a UV-written waveguide 1 and 2. Each waveguide is located 125 μm away from the neutral axis of the device in x-axis. In the waveguide 1, it consists of a series of multiplexed Bragg gratings, while the waveguide 2 has only one Bragg grating wavelength (1541 nm) which is located parallel to the Bragg grating wavelength of 1575 nm. Through physically machining flat-fibre into a wedge as illustrated in Figure 6.6.3 (b) allowing the parameters of strain bending and refractive index oil to be sensed in a single monitoring.

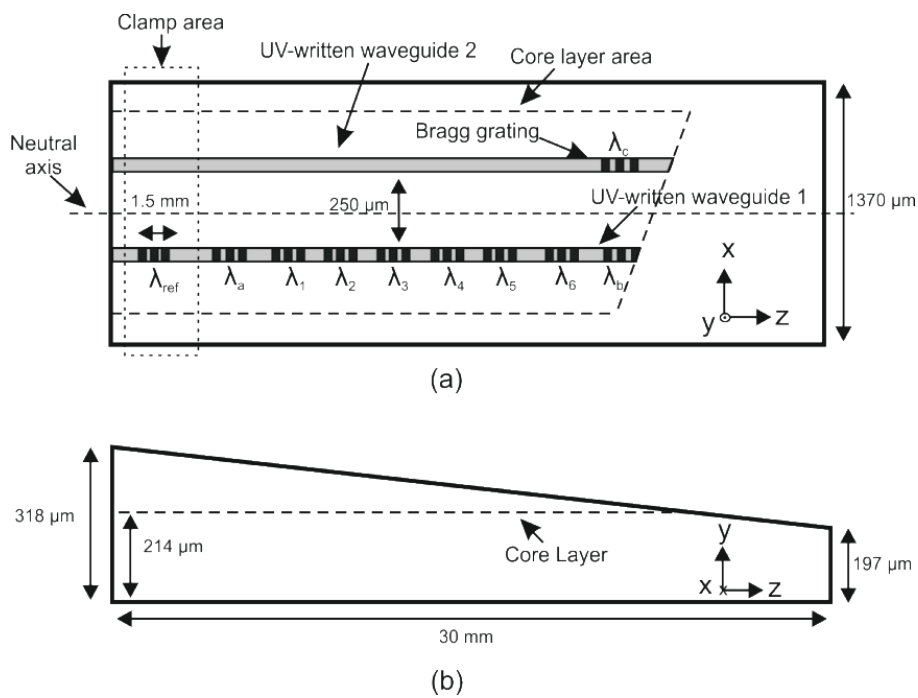


Figure 6.6.3 Schematic diagram of flat-fibre substrate sensor from the (a) top view including grating positioning (see Table 6.6.1), (B) side view of the sample.

Table 6.6.1 describes the function of each Bragg gratings along the core of the flat-fibre in order to sense refractive index oil and two-dimensional bending. Basically, ten Bragg gratings were UV-written into the substrate but only those at the wavelengths 1614 nm, 1575 nm and 1541 nm are used to monitor the bending effect in two-dimensional deflections. While for the refractive index sensor, the Bragg grating at 1575 nm is used because of the design structure. The Bragg grating of 1505 nm was not subject to bending, and so is used as a temperature reference. To measure the bending strength at different locations along the z-axis, the Bragg gratings of 1609 nm, 1604 nm, 1555 nm, 1560 nm, 1565 nm and 1570 nm are observed in x and y-axis deflections.

Table 6.6.1 Summary of the function of each Bragg grating wavelength for bending and refractive index sensor

Label	Wavelength (nm)	Waveguide	Purpose
λ_{ref}	1505	1	Temperature Reference
λ_a	1614	1	Bending sensor
λ_b	1575	1	Refractive index and bending sensor
λ_c	1541	2	Bending sensor
$\lambda_{(n=1,2..6)}$	1609, 1604, 1555, 1560, 1565, 1570	1	Bending strength along the length of the substrate

6.6.2 Comsol Modelling

To understand the behaviour of a cantilever beam structure with respect to the bending strain effect, a finite element simulation using the commercial software Comsol Multiphysics is developed. A cantilever beam with a wedge angle of 0.27 degrees on the top surface was modelled by *Peter Cooper* (one of member in the Engineered Photonics Devices and Application group) to represent the fabricated flat-fibre sensor device. From this modelling, the strain response of the fabricated device can be predicted as the beam structure is bent in different directions. One end of the beam is a fixed constraint to simulate effect of being clamped. The other end is deflected in x and y axis direction.

Figure 6.6.4 illustrates the modelled flat-fibre sensor being deflected in y-axis direction. To calculate the strain effect within the flat-fibre substrate, the Comsol Solid Mechanics interface is used. The Bragg wavelength shifts in response to bending of the flat-fibre at various locations are approximated by computing the calculated three linear strains at their respective locations using equation (6.12). The simulated results of the modelled flat-fibre substrate were compared to the experimental data and will be discussed in the following sections.

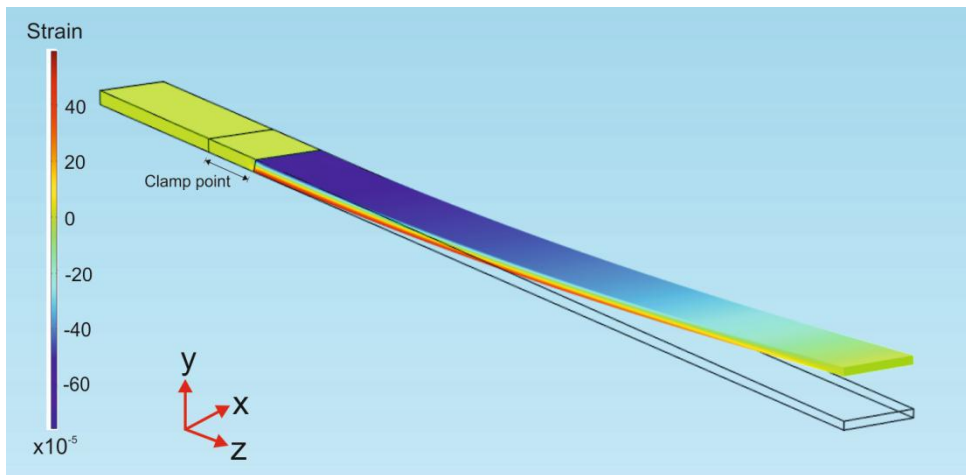


Figure 6.6.4 Modelling structure diagram of top-polished flat-fibre substrate using Comsol software.

6.6.3 Characterisation

The fabricated flat-fibre substrate is firstly pigtailed with a two-port single mode fibre (SMF) pigtail and secured with UV-cure glue for a physically robust connection as shown in Figure 6.6.5. The two-port SMF fibre pigtail is used as the substrate has two UV-written waveguides. The configuration of the characterisation setup shown in Figure 6.6.6 is implemented, where a polarised broadband light source (SLED) is split into two channels via a 3-dB coupler for simultaneous measurement from two channel waveguides. The polarisation of each channel is maintained using a polarisation controller. Two optical spectrum analysers (OSA) are used to monitor the spectral response of the Bragg gratings due to the bending effect and refractive index oil variation.

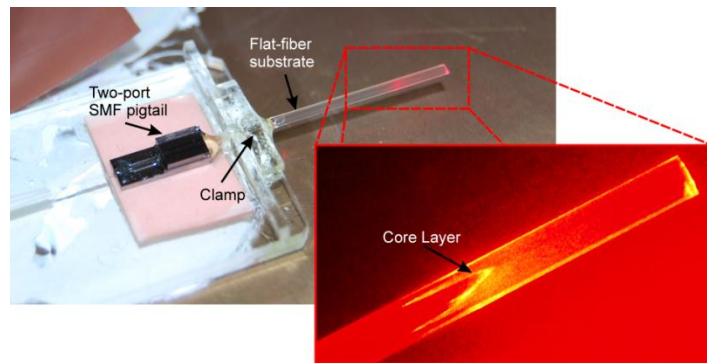


Figure 6.6.5 Flat-fiber substrate pigtailed with a two-port SMF pigtail and clamped with several small substrate glasses to secure the fixed point of the sample.

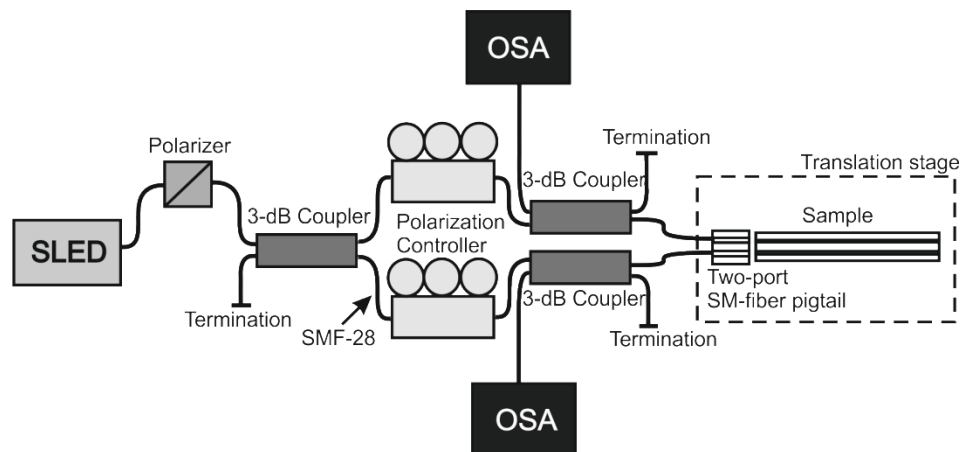


Figure 6.6.6 The characterisation setup for a two-port SMF pigtailed to the flat-fibre sample.

In calibrating the sensitivity of the flat-fiber substrate device to an external refractive index, a range of different refractive index oils (Cargille) spanning from 1.3 to 1.46 has been measured by placing the index oil on top of the polished surface of the device. Following this, the spectral response of the Bragg grating at 1575 nm is monitored from the OSA and beforehand the reflected spectrum of each Bragg grating is fitted by a Gaussian fitting algorithm. This step is also implemented in characterising the two-dimensional bending. Figure 6.6.7 shows the schematic diagram of the two-dimensional bending characterisation. One end of the flat-fibre which is near to the pigtailed point is clamped using four small rectangular glass substrates and secured with UV-curing adhesive. It is possible to control the displacement of the cantilever's

tip of the flat-fibre device via the translation stage. One translation stage is used to provide positive and negative displacement in the x and y direction. The differentials between each grating are performed to infer the deformation occurred to the flat-fibre substrate.

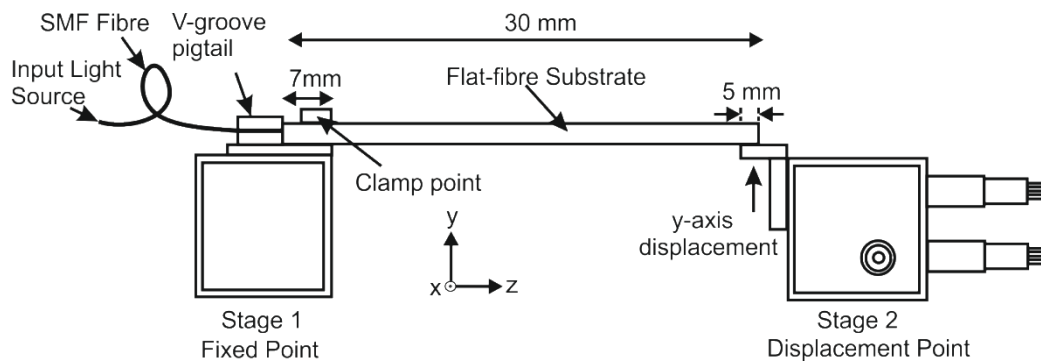


Figure 6.6.7 Schematic diagram for bending characterisation. One end of the flat-fibre substrate is clamped and the end is deflected to represent bending configuration.

6.6.4 Results and Discussion

Ten Bragg gratings are monitored, shown in Figure 6.6.8. The blue line is the reflection spectrum from waveguide 1; the green line is the reflection spectrum from waveguide 2. The Bragg grating wavelength about 1505 nm is observed in order to provide information about temperature variation during the experimental session. The grating centred about 1575 nm is calibrated for changes in external refractive index. Following this, bending the flat-fibre substrate in two different directions namely x and y -axis deflections is discussed. Two Bragg gratings from the 10 written were used to distinguish two-dimensional bending. These had wavelengths about 1614 nm and 1541 nm. The capability of the device to sense multiple parameters is demonstrated by monitoring the four multiplexed wavelengths about 1541 nm, 1575 nm, 1614 nm and 1505 nm. From this multiple parameter monitoring, a matrix is constructed. In summation, it distinguishes two-dimensional bending in x -axis deflection, x and y -axis deflection, y , refractive index, n and temperature, T , parameters and the involved Bragg grating wavelengths, expressed in equation (6.13). The temperature variation of Bragg grating wavelength about 1505 nm, 1541 nm, 1575 nm and 1614 nm have been observed and result with a linear correlation between centre wavelength shifts against the temperature variation with approximately 9 pm/°C.

$$\begin{pmatrix} \Delta\lambda_{1541} \\ \Delta\lambda_{1575} \\ \Delta\lambda_{1614} \\ \Delta\lambda_{1505} \end{pmatrix} = \begin{pmatrix} A_{11} & A_{12} & A_{13} & A_{14} \\ A_{21} & A_{22} & A_{23} & A_{24} \\ A_{31} & A_{32} & A_{33} & A_{34} \\ A_{41} & A_{42} & A_{43} & A_{44} \end{pmatrix} \begin{pmatrix} x \\ y \\ n \\ T \end{pmatrix} \quad (6.13)$$

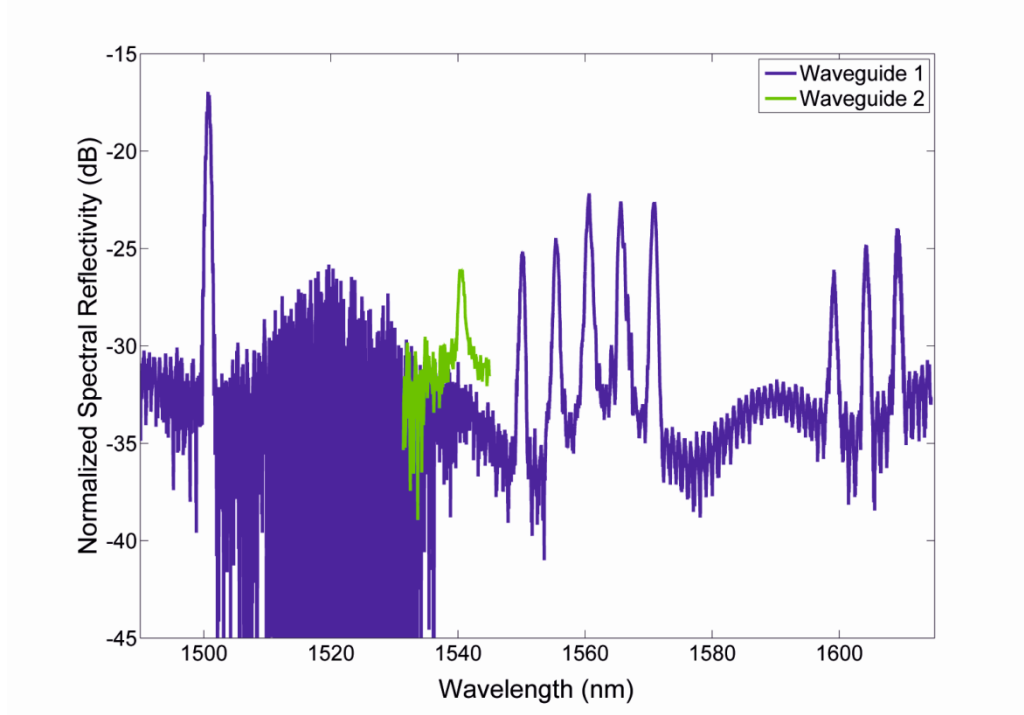


Figure 6.6.8 The normalised spectral reflectivity against the range of wavelength for the waveguide 1 (blue line) and waveguide 2 (green line).

6.6.4.1 Refractive index sensing

The sensitivity of the flat-fibre sensor device has been discussed earlier in the Section 6.5. However, the fabricated device described in the Section 6.5 is not designed for two-dimensional bending as clearly stated earlier. Thus, in this section, the sensitivity of this flat-fibre sensor device is measured in order to calibrate the sensor device for this particular work. Figure 6.6.9 shows the spectral reflectivity of Bragg grating wavelength about 1505 nm and 1575 nm before and after placing the index oil of 1.46 onto the flat-fibre device. It can be seen from Figure 6.6.9 (a), that the centre wavelength of the Bragg grating about 1505 nm is not changed due to the fact that no interaction occurred between the guided mode and the external refractive index at that particular position. However, there is a significant centre wavelength shift from Bragg grating

wavelength about 1575 nm which can be observed in the Figure 6.6.9 (b). This indicates that the Bragg grating has sufficient cladding removed, such to make its evanescent field sensitive to external refractive index.

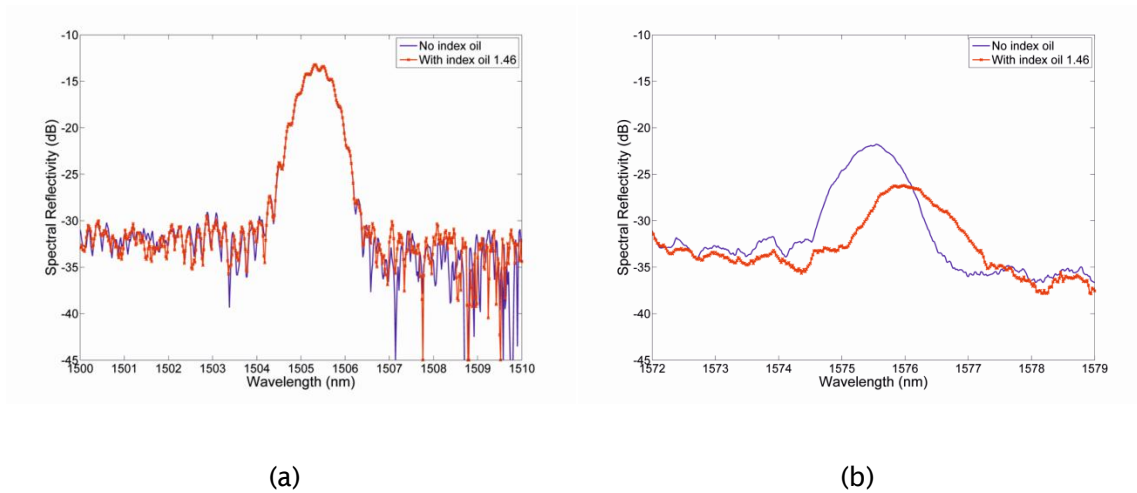


Figure 6.6.9 Spectral reflectivity of Bragg grating wavelength about (a) 1505 nm and (b) 1575 nm.

Figure 6.6.10 shows the Bragg grating wavelength shift with respect to different refractive index oils. The refractive index oils varied from 1.33 to 1.46. It can be seen that the maximum wavelength shift is 0.50 nm occurred when placing the index oil of 1.46 on top of the flat-fibre substrate. This yielded a maximum sensitivity of the refractive index to around 22.6 nm per refractive index unit. In the following section, the two-dimensional bending where considering deflection in x and y axis direction is discussed.

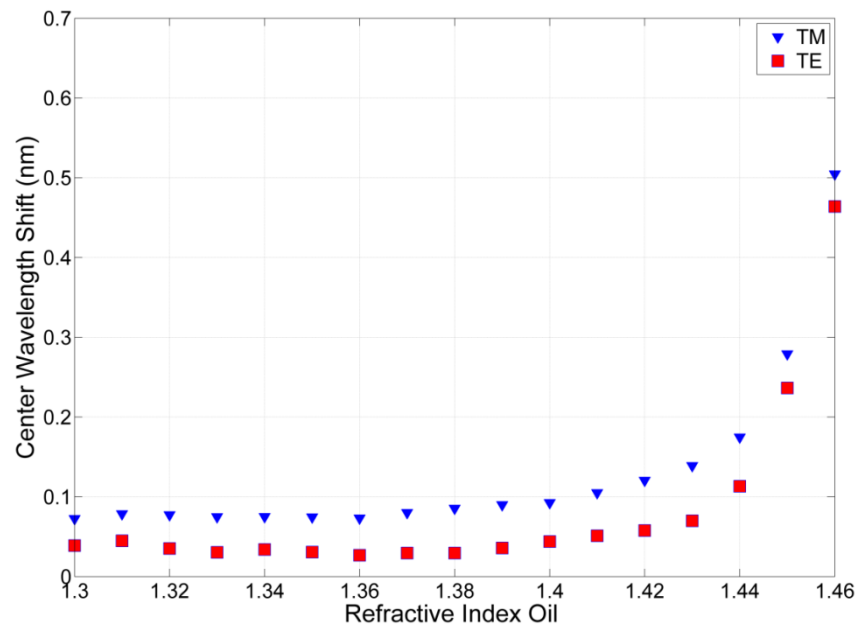


Figure 6.6.10 Centre wavelength shift against different refractive index oils for Bragg grating about 1575 nm.

6.6.4.2 Two-dimensional bending

In this section, the capability of the flat-fibre substrate to sense bending in two dimensions is described. Positive and negative deflections in each axis were performed. Each of these waveguides is located either side of the neutral axis of the x-axis as depicted in Figure 6.6.3 (a). This means that they will each show responses of different sign (positive or negative) when bent in the x-axis and the same sign when bend in the y-axis. These two Bragg grating wavelengths are about 1614 nm and 1541 nm. Beforehand, the response of the ten UV-written Bragg gratings along the flat-fibre substrate due to the bending in each direction is first observed. Figure 6.6.11 shows the absolute centre wavelength shift for each grating located along the length of the channel waveguide 1. The response trend of the centre wavelength shift agrees with the simulation result where the maximum strain occurred close to the grating position of λ_4 . The graph is obtained by bending the flat-fibre substrate in the positive y-axis deflection up by 1.0 mm. It showed a non-linear relationship between the centre wavelength shift with respect to the grating position. This is due to the fabricated device structure has a wedge profile in y-axis, where the neutral axis along its length is varied as illus-

trated in Figure 6.6.3 (b). Therefore, the strain effect of each position along the z-axis demonstrated a non-linear relationship.

However, in a normal rectangular geometry where the neutral axis is constant along its length, it is expected that the centre wavelength shift of the gratings along the z-axis reduces as the distance of the grating from the root point is increased. This can be seen when bending the substrate in x-axis deflection as depicted in Figure 6.6.12. It shows the gradient of wavelength shift with respect to different grating position for each different deflection in positive x-direction. It can be seen that the smaller deflections display a positive gradient. This is thought to be dominated by noise as the strain effect is small. However for greater deflections the experimental data follows the simulation results.

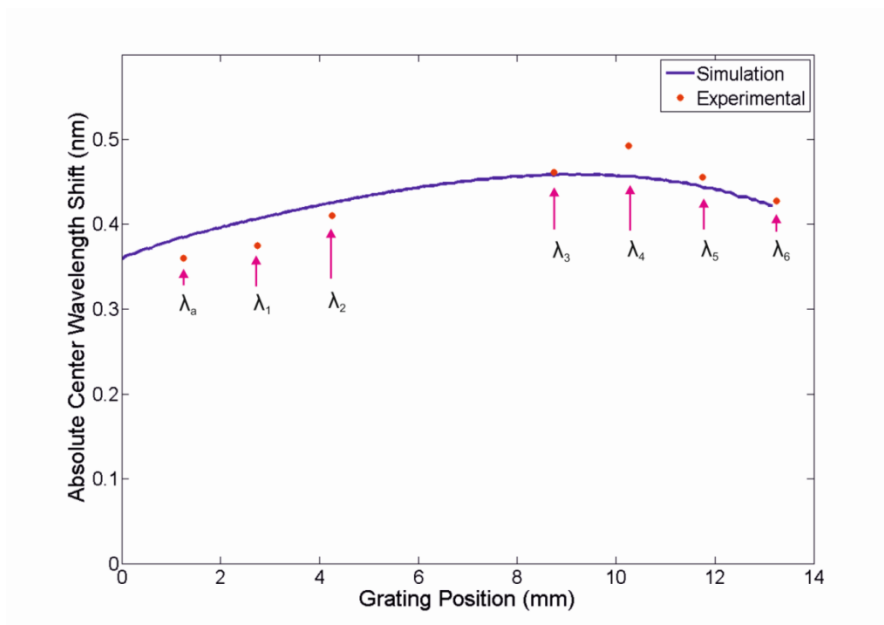


Figure 6.6.11 Absolute centre wavelength shift of Bragg gratings along the length of the flat-fibre due to bending in positive y-axis.

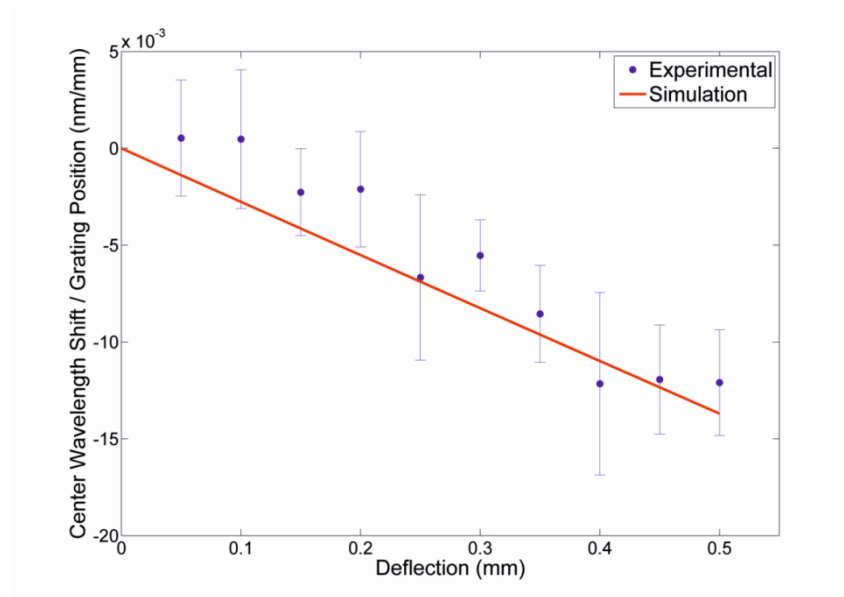


Figure 6.6.12 Gradient of the centre wavelength shift against the grating positions along the length of the flat-fibre against deflection in x-axis.

Figure 6.6.13 shows the centre wavelength shift against the y-axis of positive and negative displacements for Bragg grating wavelength about 1614 nm and 1541 nm. Both gratings depict a similar trend when bending the flat-fibre substrate either in positive or negative position. This is expected as both gratings are located in the same plane which is the core of the flat-fibre substrate and also due to the wedge form of the flat-fibre. The experimental data has good correlation to the simulated result when bending the fibre up to positive 1 mm. The gradient and the associated errors for both grating represent the matrix elements A_{12} and A_{32} which are -0.40 ± 0.01 and -0.41 ± 0.01 , respectively. The associated errors are the standard deviation from the linear regression of the data. In particular, for positive y-axis deflection, the gratings have a negative shift due to compressive strain. Whereas bending the fibre to the negative y-axis deflection, a positive shift can be seen due to tensile strain.

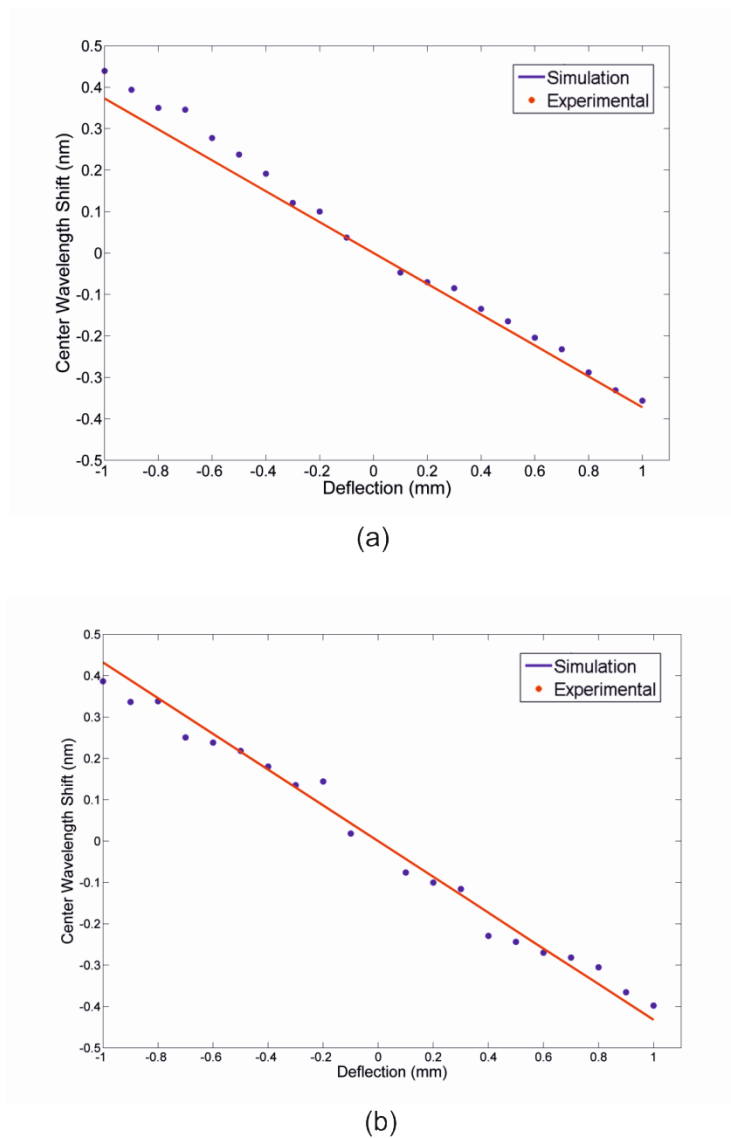


Figure 6.6.13 Centre wavelength shift of Bragg gratings against the deflection in y-axis for wavelength about (a) 1614nm and (b) 1541nm.

In the case of bending the flat-fibre in the x-axis, both of the gratings demonstrate opposite sign of gradient as shown in Figure 6.6.14. The wavelength shift of about 1614 nm has positive gradient whereas the 1541 nm has negative gradient. The fact that the Bragg gratings are being located at different position of x-axis, one experiences stretching (1614 nm) and the other compression (1541 nm) for particular positive deflection. For this measurement, the matrix element of A_{11} and A_{31} are 0.54 ± 0.01 and -0.21 ± 0.01 for the wavelength about 1614 nm and 1541 nm, respectively. The gradient of the Bragg grating wavelength about 1614 nm is higher than the wave-

length about 1541 nm and has less noise. This is anticipated due to the variation of bending stress for different distances from the clamped point of the flat-fibre substrate configuration. In this assessment, the larger the Bragg grating wavelength shift, the greater the magnitude of stress in the structure becomes. It is worth noting that the location of the Bragg grating about 1614 nm is close to the cantilever root, therefore it can be observed that the matrix elements of 1541 nm has a higher error compared to that of the 1614 nm grating because of the small bending effect, thus a larger signal to noise ratio. The matrix elements of A_{41} and A_{42} represent bending effects at the 1505 nm wavelength which were not affected by the two-dimensional bending.

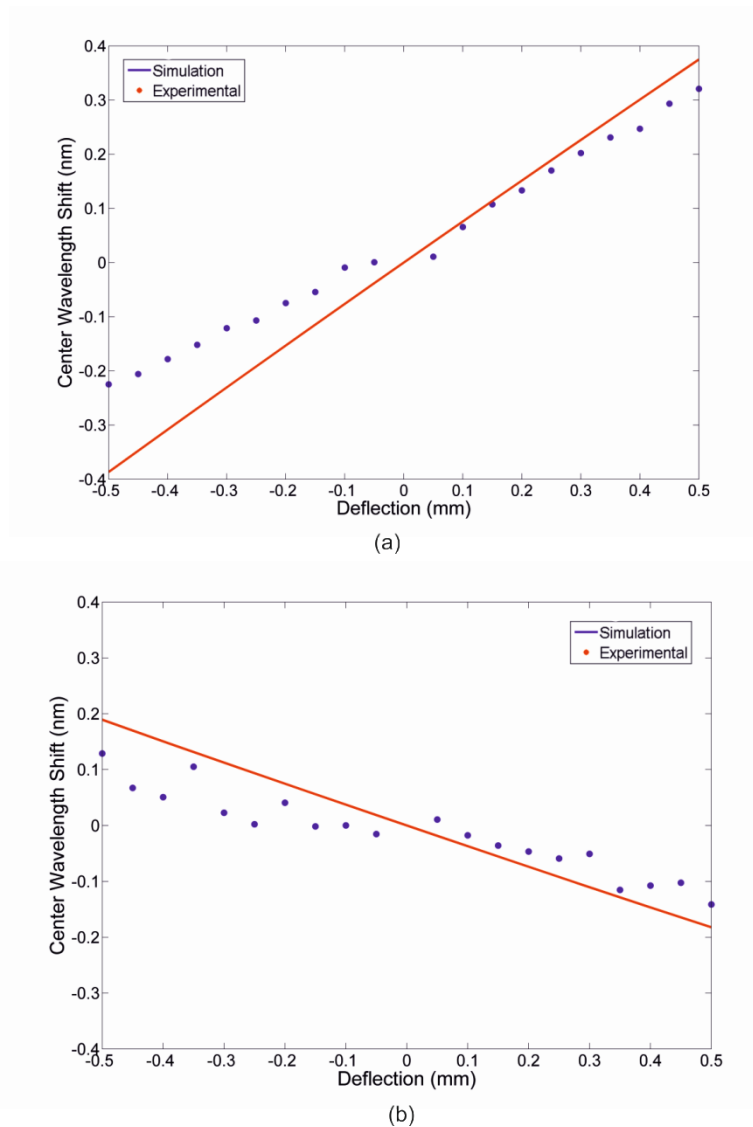


Figure 6.6.14 Centre wavelength shift against the deflection in x-axis direction for wavelength about (a) 1614 nm and (b) 1541 nm.

6.6.4.3 Simultaneous Refractive index and two-dimensional bending

The ability of the flat-fibre sensor device to sense multiple parameters simultaneously and distinguish them separately is presented in this section. The experimental work demonstrated placing refractive index oil while bending the flat-fibre substrate. This is inferred in one single monitoring by comparing the Bragg grating response about 1575 nm to the Bragg grating wavelength about 1614 nm and 1541 nm. The wavelength response for the 1614 nm and 1541 nm have been discussed in the previous section, thus only the Bragg grating wavelength about 1575 nm is concentrated in this section. The grating about 1575 nm is chosen due to the capability of the grating to react towards the external refractive index as discussed in Section 6.6.4.1.

Figure 6.6.15 (a) and (b) show the centre wavelength shift of the Bragg grating wavelength about 1575 nm in responding to the bending deflection in y-axis and x-axis, respectively. The gradient of the data when bending in y-axis and x-axis are -0.46 ± 0.01 and 0.24 ± 0.05 which represent the matrix element of A_{22} and A_{21} . For the bending in y-axis deflection, a refractive index oil of 1.45 was placed on the top of the device surface whilst bending the substrate at 0.6 mm deflection. A positive shift can be observed when placing the index oil, and as the deflection is increased up to 1.0 mm, the data seem to follow the trend of the simulated result when no index oil present as depicted in Figure 6.6.15 (a). Similar trend can be seen when placing the index oil of 1.44 on top of the flat-fibre surface whilst bending the substrate in x-axis at negative deflection of 0.25 mm as shown in Figure 6.6.15 (b). However, in this condition, the gradient of the graph is in the opposite direction and the wavelength shift due to index oil is smaller than the data shown in Figure 6.6.15 (a).

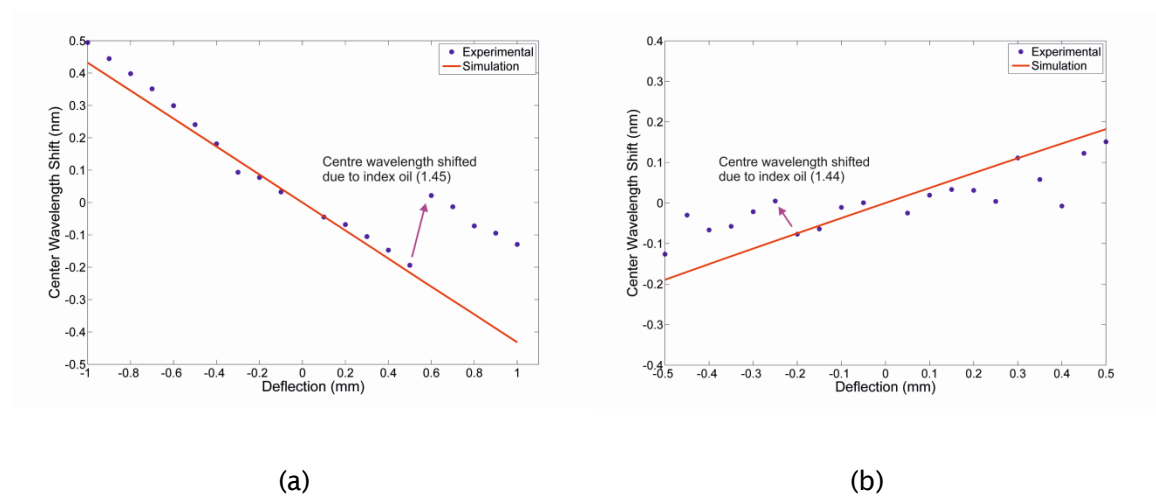


Figure 6.6.15 Centre wavelength shift against deflection in (a) y-axis and (b) x-axis for the Bragg grating at 1575 nm. A positive centre wavelength shift can be seen, indicated on the graphs, when exposing the sample to a refractive index oil.

Despite the fact that the graphs in Figure 6.6.15 demonstrate significant data in sensing two parameters of refractive index oil and two-dimensional bending, evaluating a single Bragg grating wavelength of 1575 nm is not sufficient to distinguish either the bending is in positive or negative deflection. Thus, the data shown in Figure 6.6.15 is compared to the data from Figure 6.6.13 and Figure 6.6.14 act as references. To conclude the sensing responses of the flat-fibre device to multiple parameters can be summarised using a calibrated 4×4 matrix as indicated in equation (6.14). The inverse of the matrix element, A is also given as stated in equation (6.15).

$$\begin{pmatrix} \Delta\lambda_{1614} \\ \Delta\lambda_{1575} \\ \Delta\lambda_{1541} \\ \Delta\lambda_{1505} \end{pmatrix} = \begin{pmatrix} 0.54 & -0.40 & 0.00003 & 11.7 \\ 0.24 & -0.46 & 22.56 & 8.40 \\ -0.21 & -0.41 & 0.00001 & 10.5 \\ 0.0006 & 0.0003 & 0.0003 & 5.50 \end{pmatrix} \begin{pmatrix} x \\ y \\ n \\ T \end{pmatrix} \quad (6.14)$$

$$\begin{pmatrix} x \\ y \\ n \\ T \end{pmatrix} = \begin{pmatrix} 1.3427 & 0.0000 & -1.3102 & -0.3550 \\ -0.6905 & -0.0001 & -1.7618 & 4.8323 \\ -0.0283 & 0.0443 & -0.0221 & 0.0347 \\ -0.0001 & -0.0000 & 0.0002 & 0.1816 \end{pmatrix} \begin{pmatrix} \Delta\lambda_{1614} \\ \Delta\lambda_{1575} \\ \Delta\lambda_{1541} \\ \Delta\lambda_{1505} \end{pmatrix} \quad (6.15)$$

From this matrix, the deformation of the flat-fibre substrate either in x or y axis deflection can be determined from monitoring the particular spectral Bragg grating shifts. This includes sensing a range of refractive index oils and temperature variation.

6.7 Conclusion

In conclusion, a multi-parameter sensor has been fabricated in a flat-fibre platform. The sensor has the capability of sensing different refractive index oils and two-dimensional bending in a single device using distributed Bragg gratings along the length of the flat-fibre substrate. Through evanescent field exposure, a sensitivity of 95 nm per refractive index oil was achieved. In addition, from monitoring respective Bragg gratings defined in different positions along the flat-fibre, bending in two dimensions can be distinguished. All the measurement results were summarised into a 4 x 4 matrix to determine deformation effects. This matrix represents four different parameters namely x and y axis bending, refractive index and also temperature. The work done in this chapter can be further developed by defining integrated Bragg grating waveguide such as y-splitter or x-coupler for sensing a twisting effect.

Chapter 7

Multimode Interference Device

7.1 Introduction

A multimode interference (MMI) device is an optical waveguide that supports a large number of modes within particular dimensions. In general, a self-imaging effect is used to generate multiple images of the input mode. The MMI concept has been widely implemented owing to the notable advantages of small device size, stable power splitting and a broad spectral bandwidth [111]. MMI devices have been successfully demonstrated in a wide range of applications, particularly for power splitting [112] and combining purposes [113]. These are key elements used in optical integrated devices. Conventionally, splitting or combining light using a y-splitter or x-coupler design for a large number of splitting or combining outputs will generally require long length devices and also suffer from radiation loss due to the waveguide complexity. However, in the MMI devices the structures are more compact in size because no internal bend waveguides are involved and fabrication is simpler. Therefore, the MMI structure is preferable compared to the y-splitter or x-coupler waveguides in manipulating light for multiple splitting and combining events.

Recently, they have been proposed for more advanced applications, including optical sensing and switching. *Mayeh et al* has demonstrated an optical sensor device based on a slotted MMI waveguide which offer high reliability operation [114]. It senses different refractive indices by monitoring changes in output intensity. In switching operation, the MMI concept has been used in photonic switches known as multimode interference photonic switches (MIPS) [115]. It has been reported that the fabricated MIPS

device offers better switching characteristic with lower device crosstalk and good extinction ratio. The basic principles of the MMI device where using a self-imaging concept will be given in the next section.

7.2 The Multimode Interference Device Concept

The main concept of the MMI device is a self-imaging operation by which a single transverse optical mode at the input field of the device can be reproduced as single or multiple fold images at the end facet of the MMI structure [20]. This is due to the interference of the several modes across the multimode waveguide section, forming a number of fold images at the output facet. The devices generally consist of one or more input and output access waveguides with a multimode waveguide with particular width, W and length, L between the access waveguides. The structure can be defined as $N \times M$ MMI device, where N represents the number of the input access waveguides, while M represents the number of output access waveguides. The schematic diagram of a 1×1 MMI structure is depicted in Figure 7.2.1. The 1×1 MMI structure means that there is a single input mode that can be reproduced at a certain length of the MMI device, for a particular device width. The operation characteristic of the device is dependent on the MMI dimension by which this self-imaging occurs at a specific length, L_{MMI} . This can be determined by the equation (7.1), where W is the width, n_{eff} is the effective refractive index of the waveguide, λ is the operation wavelength and M is the number of fold images at the end facet of the MMI section. For example, the length of the MMI waveguide is half of the original length (i.e. length for the 1×1 MMI device) to obtain two spot outputs (i.e. $M = 2$). This MMI operation will be explained more in the next section.

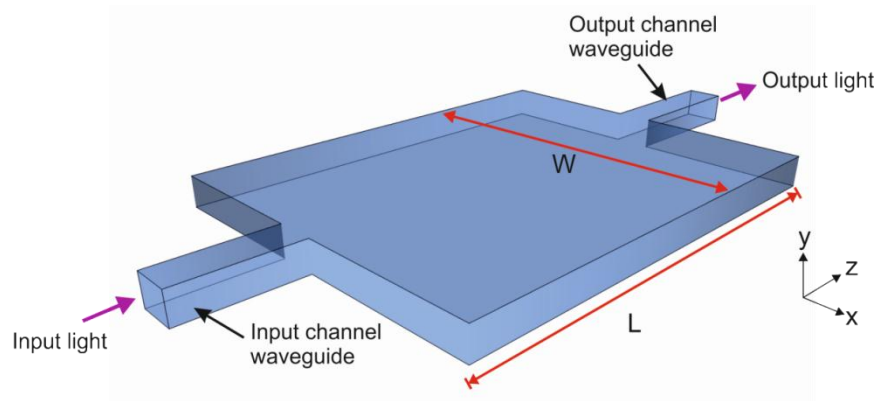


Figure 7.2.1 A principle multimode interference device with one input channel and one output channel known as 1x1 MMI device.

$$L_{MMI} = \frac{n_{eff}(W)^2}{M\lambda} \quad (7.1)$$

7.2.1 MMI Self-imaging Principle

The analysis of the self-imaging principle has been detailed by *Soldano* and *Penning* [111]. In this section, a brief explanation related to the analysis of the self-imaging principle is described. Most of the theory described in this chapter is referred from Okamoto's book and Soldano's paper [20], [111]. In the MMI device, the lateral axis of the structure is larger than the transverse axis (vertical in Figure 7.2.1). From this, it can be estimated that the transverse axis supports a single-mode in all places within the MMI central. Therefore, a two-dimensional (2D) structure is used in this analysis instead of the full three-dimensional (3D). The analysis is started by defining the propagation constant of two lowest-order modes within the structure, which will be used later in this analysis. In this analysis, only the lateral axis will be considered. From the dispersion equation stated in equation (7.2), the core index, n_c is related to the summation of the lateral wavenumber, k_{xv} , and the propagation constant, β_v , where v represents the mode numbers supported at the lateral axis.

$$k_{xv}^2 + \beta_v^2 = k_0^2 n_c^2 \quad (7.2)$$

Where,

$$k_0 = \frac{2\pi}{\lambda_0} \quad (7.3)$$

and

$$k_{xv} = \frac{(v+1)\pi}{W_{eff}} \quad (7.4)$$

It is worth noting that the lateral width of the MMI section is determined by the material of the MMI section and its surrounding. Therefore, the lateral wavenumber considers the effective width, W_{eff} of the MMI structure which correlated to the lateral penetration depth of each mode field to the MMI sidewall. This phenomenon is known as the Goos-Hänchen effect [116]. The Goos-Hänchen effect is an optical phenomenon that occurs to linearly polarized light which experiences a small shift due to reflection from an interface of two different dielectric materials. In the case of high index contrast, this effect can be ignored as the additional width is very small. Therefore, the effective width of the waveguide is assumed to be similar to the physical width of the MMI structure, therefore $W_{eff} = W$. The propagation constants β_v can be derived from equation (7.2) – (7.4) which contribute to the equation (7.5) below, where n_r and n_c are the effective refractive index of the core and cladding, respectively.

$$\beta_v = k_0 n_r - \frac{(v+1)^2 \pi \lambda_0}{4 n_r W^2} \quad (7.5)$$

The beat length of the two lowest-order modes can be defined as in equation (7.6), where β_0 is the propagation constant for the fundamental mode and β_1 for the second-order mode.

$$L_\pi = \frac{\pi}{\beta_0 - \beta_1} \simeq \frac{4 n_c W^2}{3 \lambda_0} \quad (7.6)$$

In general, the basic input field profile, $\Psi(x, z)$ located at $z = 0$ can be expressed as in equation (7.7) that is decomposed into the all modes of modal field distribution, $\psi_v(x)$.

$$\Psi(x, 0) = \sum_v c_v \psi_v(x) \quad (7.7)$$

It should be noted that equation (7.7) considers both guided and radiated modes. However, in certain conditions where the input field is narrow enough, the unguided modes are not excited, then the input field can be decomposed into the guided mode only as stated in equation (7.8), where m represents the total number of guided modes.

$$\Psi(x, 0) = \sum_{v=0}^{m-1} c_v \psi_v(x) \quad (7.8)$$

The field excitation coefficient, c_v can be written as

$$c_v = \frac{\int \Psi(x,0) \psi_v(x) dx}{\sqrt{\int \psi_v^2(x) dx}} \quad (7.9)$$

The superposition of the entire guided mode field at distance $z = L$ can then be expressed as in equation (7.10), which contributes to the output field profile, $\Psi(x, L)$.

$$\Psi(x, L) = \sum_{v=0}^{m-1} c_v \psi_v(x) \exp \left[i \frac{v(v+2)\pi}{3L\pi} L \right] \quad (7.10)$$

From the equation (7.10), it can be said that, the output image is dependent on the modal excitation c_v and the mode phase factor as depicted in equation (7.11).

$$\text{mode phase vector} = \exp \left[i \frac{v(v+2)\pi}{3L\pi} L \right] \quad (7.11)$$

However, in the next analysis onwards, only the mode phase vector is manipulated in order to simplify the analysis of an interference mechanism. In general, the interference mechanism can be categorised into two types, namely a single image and multiple image interference. By analysing equation (7.11), the output mode field can be produced as the original input mode field if the conditions are satisfied. The first condition is fulfilled when the mode phase vector is equal to one as stated in equation (7.12), whereas the second condition dictated as expressed in equation (7.13).

$$\exp \left[i \frac{v(v+2)\pi}{3L\pi} L \right] = 1 \quad (7.12)$$

$$\exp \left[i \frac{v(v+2)\pi}{3L\pi} L \right] = (-1)^v \quad (7.13)$$

In the work developed as part of this thesis, an MMI device was fabricated in flat-fibre platform by micromachining two trenches parallel to each other. This will be further described in next section.

7.3 Multimode Interference Device in Flat-fibre Platform

The material platform from which the device is made will significantly affect the performance of the MMI output. Therefore, it is important to understand the features of the material platform that is used to develop functional devices based on the multimode interference effect. In the past, MMI devices have been reported in various material platforms ranging from low to high-index-contrast platforms, for instance, silicon-on-silicon [117], polymer [118], and silicon-on-insulator [119] platforms. However, most of these platforms are either relatively expensive, have low index contrast, exhib-

it high loss, or have complex fabrication processes. In a low index contrast platform for instance silica-on-silicon, the dopant levels typically limit index contrast to less than 2%. In the context of conventional MMI devices, the flat-fibre platform would typically be considered a low-index-contrast platform. Such low-index-contrast platforms lead to lower optical confinement and, thus, reduced performance of the resulting MMI device [120]. However, it is worth noting that a low-index-contrast platform does have the benefit of providing low coupling loss, with standard silica optical fibres. This is due to better mode matching, compared to that of high-index-contrast platforms, and a comparable refractive index to fibre unlike materials such as silicon.

By understanding the benefits offered by the low- and high-index-contrast platforms, the MMI device structure in this work has combined the both platforms configurations into a single MMI device. In the past, various techniques have been used to form high-index-contrast MMI structures [121]. For example, one of the reported techniques used metal-clad sidewalls, where the waveguide surface was surrounded by a thin metal layer. This acts to increase the index contrast of the MMI device. However, this technique is limited to operating with one polarisation only [122].

In order to produce such high-index lateral confinement of the MMI device, several fabrication techniques have previously been reported. One of the techniques is by having air trenches that define the MMI section. This technique has been proposed by *Kaalund* and *Jin* which provides strong lateral confinement by the high index contrast between the core layer and the air cladding despite being in conventionally low index contrast platform [123]. They reported the MMI performance by simulations. These predictions show that by having the trenches they are able to improve the image quality of the MMI device whilst maintaining the coupling efficiency. This was followed by *Ma* and *Chin*, where they reported fabricating MMI devices using air trenches by means of a deep etching technique [124], [125]. Photolithography followed by etching is the conventional fabrication technique and has been widely used in many integrated optical applications [126]. However, these cleanroom techniques can be time consuming, and require several stages to complete a device. Also, due to the flat-fibre format, it is difficult to use lithography and etching simply because of the difficulty of spinning photoresists on such a geometry.

Consequently, in this work, the physical micromachining technique is used to form air trenches parallel to the MMI device. The technique used here offers a simple and straightforward fabrication approach where a diamond-blade dicing saw is used to physically machine a pair of trenches, as illustrated in Figure 7.3.1. These trenches form a high-index interface and thus give lateral confinement for both sides of the MMI

region. The vertical confinement is achieved by the flat-fibre core layer having a higher refractive index than the cladding and aforementioned is due to germanium doping. Particularly, the low index contrast, defined vertically, is provided by the germanium (Ge)-doped core layer ($n = 1.4623$) and is sandwiched by a top and bottom cladding layer ($n = 1.444$) of the flat-fibre. While the high index contrast is formed horizontally between air trenches and the core layer. Both conditions can be illustrated as in Figure 7.3.2. The figure illustrates the refractive index level in transverse and lateral axes of the MMI section. It shows that the index contrast between the core and the air-trenches is higher than the index contrast between the core and the cladding. In order to predict the dimension of the MMI section, BeamPROP software is used and this will be explained in the next section.

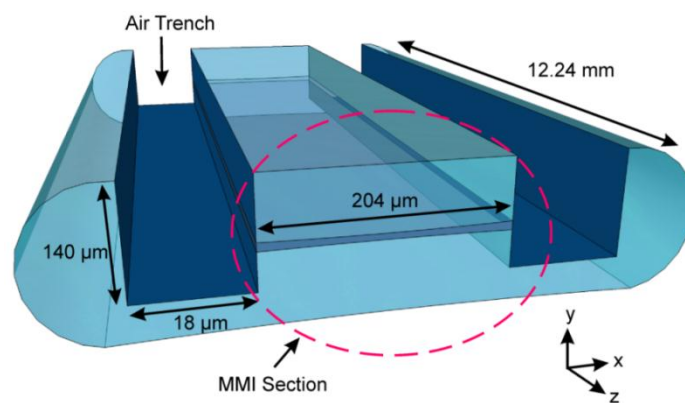


Figure 7.3.1 3D image of MMI flat-fibre device with two micromachining trenches. The MMI section is parallel to the trenches.

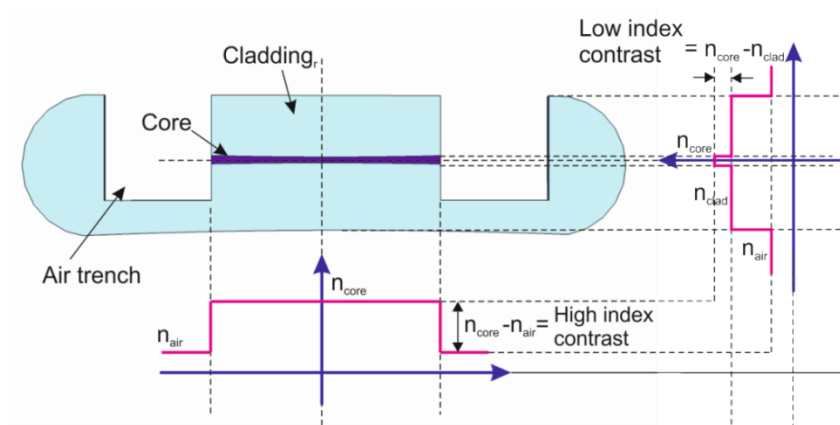


Figure 7.3.2 Illustration of high- and low-index contrast from the end facet of the flat-fibre due to air-trenches micromachining.

7.4 BeamPROP Modelling

Commercial BeamPROP software from RSoft design group is used in order to predict the dimensions of the MMI structure as well as determine the effect of certain parameters. In the BeamPROP specifications, the two dimensional modelling was chosen which only considers the lateral confinement of the MMI waveguide. As a way of demonstration, the MMI device was designed as a 1x3 splitter, where the trenches confine the light to regenerate the input mode at three individual locations at the output facet. In the modelled system, the slab waveguide mode, in the y-axis, had an effective index of 1.4592 at 1652 nm; this reduces the problem to two dimensions [20]. A simple block structure represents the MMI modelling and can be seen in Figure 7.4.1. To optimise the design, three equally spaced locations were monitored along the length of the device and do not affect its output of each successive position. This is to monitor the power travelled through the length of the MMI section.

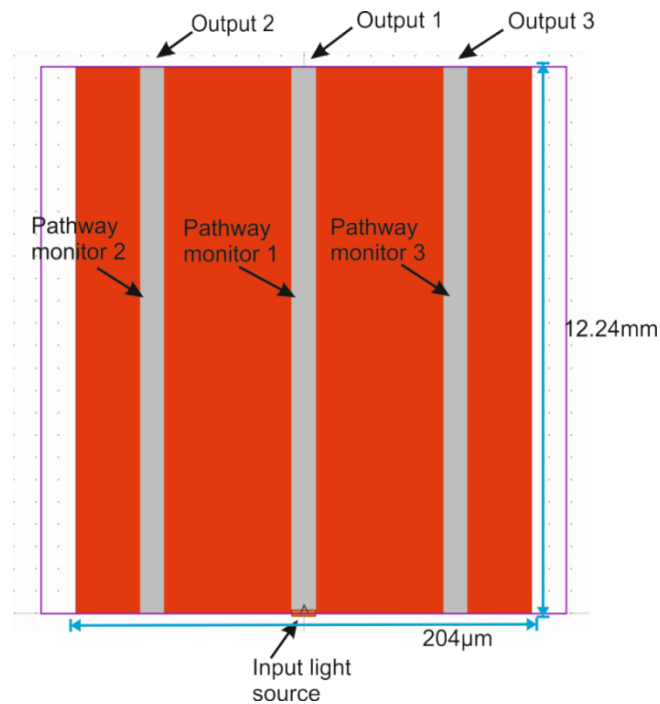
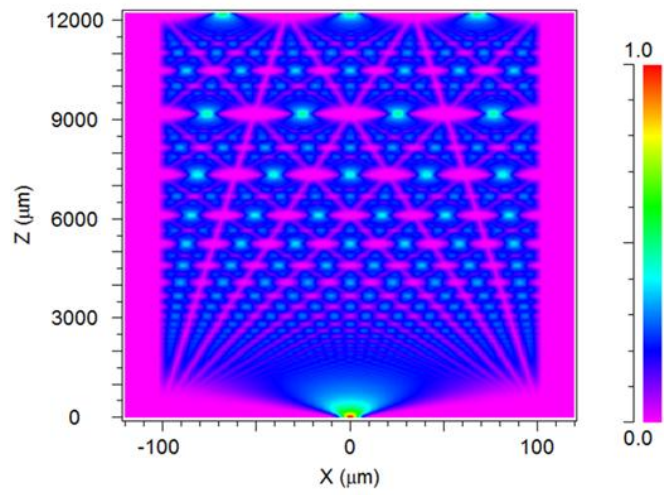
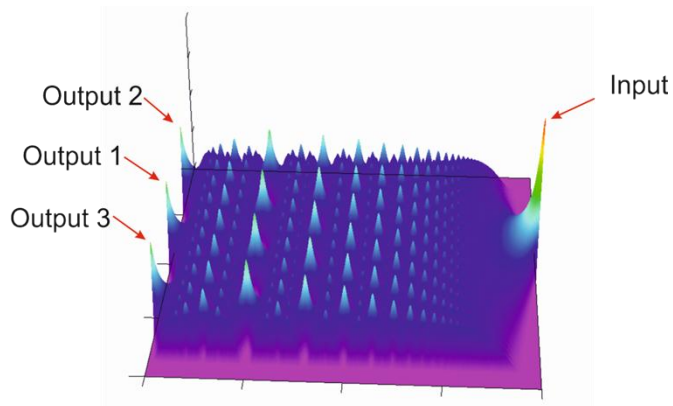


Figure 7.4.1 An MMI modelling structure built in BeamPROP RSoft software. Three pathways have been set to monitor the power that travel through the MMI section.

A Gaussian mode was selected as the launched light parameter with a mode field diameter (MFD) of $10.5 \mu\text{m}$ to represent the PM fibre used in measurement setup. The light propagation pattern throughout the MMI waveguide for the specific case of a 1×3 MMI device is shown in Figure 7.4.2, where (a) and (b) show the top-view and the 3D-image of the MMI section, respectively. Single-mode light was launched into the centre of the MMI section, and three outputs spots were produced at the output section. The wavelength of 1652 nm was implemented in the modelling. In order to compare the experimentally obtained spectral results of the MMI device, wavelength scanning was implemented in the software to observe the output power of the central peak as a function of wavelength. This will be further explained in Section 7.7. The following section discusses the fabrication of the micromachining trenches.



(a)



(b)

Figure 7.4.2 Illustration of BeamPROP modelling of the propagation light within the MMI section. (a) From top view and (b) 3D image.

7.5 Physical Micromachining of a Flat-fibre MMI device

The technique of physical micromachining is used to define the MMI section via two parallel trenches. Figure 7.5.1 shows the schematic diagram illustrating of how the micromachining cuts the MMI air trenches. The substrate is translated in the z-direction where the dicing is made to cut the core layer section laterally. The stage of the micromachining system is rotated to about 90° in order to cut the end facet of the substrate. The 1×3 MMI splitter device was fabricated in the flat-fibre platform. A $6 \mu\text{m}$ core layer thickness of a flat-fibre substrate was used which provides single vertical mode confinement. The cladding index value is known for the Suprasil F300 tube material, which yields to 1.444 refractive index. The appropriate core index is inferred from a FIMMWAVE simulation that yields the core layer refractive index of 1.4623 at 1652 nm. This value is in-line with the expected value for the core glass based upon the known doping parameters of the MCVD fibre process.

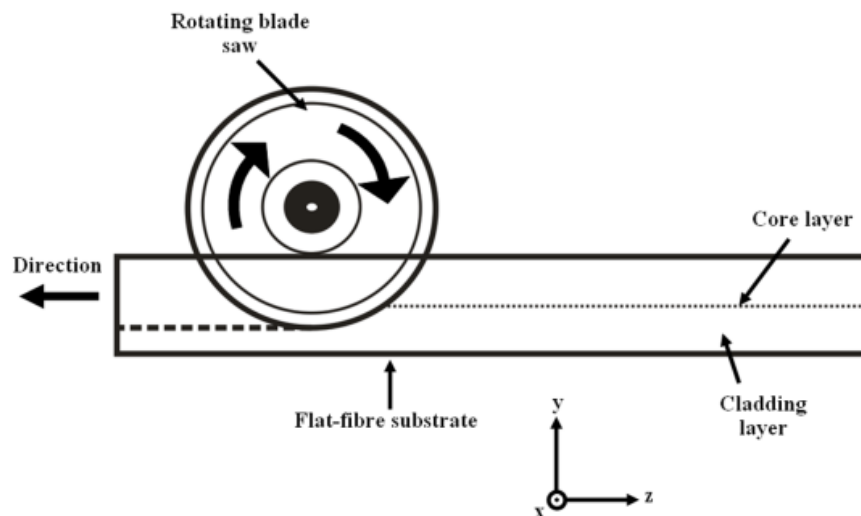


Figure 7.5.1 Dicing a trench using a rotating blade saw in opposite direction of the translation stage that the flat-fibre substrate is placed.

An ultraprecision dicing saw with a 5000 grit nickel-bonded diamond blade was used to physically cut two trenches of the MMI section. In order to reduce the total depth of the trench cuts, the overcladding of the flat-fibre substrate was firstly polished to about $100 \mu\text{m}$ of the cladding layer by using a Logitech model LP 50 polishing

machine. This allowed sawing into the core layer using the blades available. The 5000 grit blade saw type produced a trench size of 140 μm and 18 μm for the depth and width, respectively. These saw cuts define the width of the MMI device and were measured post-fabrication as 204 μm . The MMI width of 204 μm provides sufficient output channel spacing to assist in the analysis of the output via standard fibres especially during scanning an output light across the end facet of the MMI section. A future optimized device would have to consider the design constraints associated with MMI width minimization [127], [128] and the output coupling.

Before cutting the end facet of the MMI section, the BeamPROP modelling was used to predict the length of the device to achieve a 1x3 image, which was 12.54 mm. The end facet and hence the length of the device was diced by using the same dicing blade used to machine the trenches and hence had similar fabrication errors. These dimensions are optimized for the 1x3 splitting of laser light at 1652 nm. It seems that the operating wavelength is dominated by the precision of the micromachining, the width of the MMI being the most sensitive dimension. The micromachining system used in this device has a blade positional error of 2 μm and a blade width error of 2 μm . However, in high specification commercial dicing machines, these tolerances can be greatly reduced to submicrometer dimensions. Figure 7.5.2 (a) shows the end facet of the MMI section after micromachining, the trenches run parallel to the MMI section. A top view of the scanning electron microscope (SEM) image is depicted in Figure 7.5.2 (b). Although this does not provide a direct measurement of the width of the core layer, it shows that the micromachining technique yields very small wedge variation of the MMI section. Analysis via imaging white light interferometry (ZeScope made by Zemetrics) indicates width variation of less than 0.5 μm over the 12.24 mm length of the device.

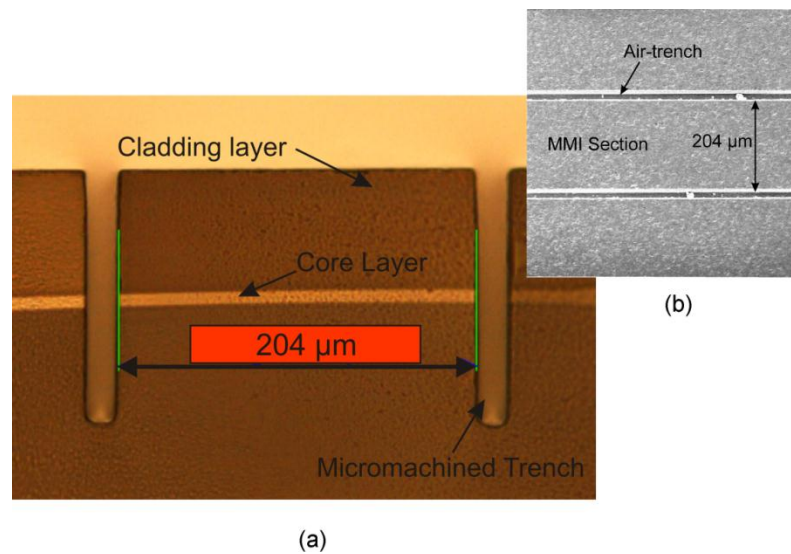


Figure 7.5.2 (a) A microscope image of the end facet of the MMI section with two trenches and (b) A top view of the SEM image showing the parallel characteristics part of the MMI length. Two trenches were cut allowing the core layer being exposed to the air, providing a high index contrast between the refractive index of the core layer and the air-trenches.

In the early stage of the fabrication, the surface roughness (R_a) of the trenches has been measured by using surface profiler of Alpha-step IQ. Three different grit sizes of blade saw type have been used, namely 400, 800 and 2000 grit size. Table 7.5.1 indicates the blade types with respect to the surface roughness. This measurement shows that the surface roughness of the MMI sidewall is strongly influenced by the dicing blade type. A blade with 2000 grit has a much smaller surface roughness, ~ 12 nm, interesting 5 times small than the 400 grit size. The blade used in fabricating the 1x3 MMI device is 5000 grit size, by which we expect to obtain an even better surface roughness than the 2000 grit blades. Recent work within the group has demonstrated a surface roughness (S_a) of 4.9 nm in a silica sample using the same technique and similar blades. Such surface roughness would significantly reduce scattering loss and thus improve the performance of the MMI device. The next section details the method used to characterise the MMI device.

Table 7.5.1 Measured surface roughness of three different grit sizes of diamond blade saw.

No.	Blade type (Grit)	Surface Roughness, R_a (nm)
1	400	60
2	800	32
3	2000	12

7.6 Characterisation Setup

A tuneable laser source with a broad spectral range of 1441 nm to 1641 nm was launched into the centre of the MMI section via a polarisation maintaining (PM) fibre. An index matching gel was applied between the PM fibre and the end facet of the MMI section as shown in Figure 7.6.1, in order to reduce coupling loss. The MMI device of the flat-fibre was characterised using the setup shown in Figure 7.6.2. The MMI sample was placed on a translation stage between the PM fibre and a 20x objective for alignment purposes. The output mode pattern was observed using a near infrared (IR) camera, where the available range of wavelength was monitored. This is done by locating the objective between the output end facet of the MMI device and the NIR camera as shown in Figure 7.6.2 (a). The performance of the MMI device was measured at 1641 nm which is close to the optimal operating wavelength of 1652 nm. This is due to the restricted tuning range of the tuneable laser.

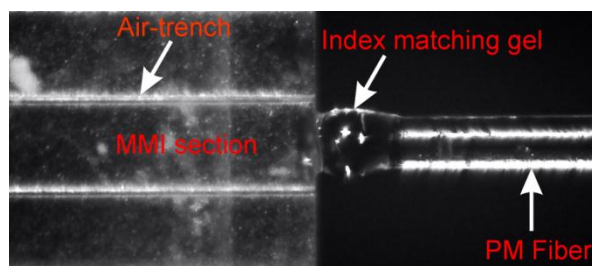


Figure 7.6.1 A butt coupling between the PM fibre and the MMI section with index matching gel.

The intensity of the output spots from the NIR camera cannot be directly measured because of the camera's low dynamic range. Thus, as an alternative method to record the device operation used a PM fibre that was directly butt coupled to the output of the MMI and translated to sample the optical intensity at the output facet, as illustrated in Figure 7.6.2 (b). The coupled power from the MMI output was measured using a power meter via a PM fibre in order to maintain the light polarisation. In addition, an SLED broadband light source (1610 nm – 1675 nm) was coupled into the device to investigate the wavelength dependence of the device. The spectrum from each output was collected with an optical fibre and analysed using an optical spectrum analyser (ANDO AQ 6317B). This configuration can be seen in Figure 7.6.2 (c). All the results achieved from these characterisation setups will be discussed in the following section, including the calculation of device excess loss and also the measurement of coupling loss.

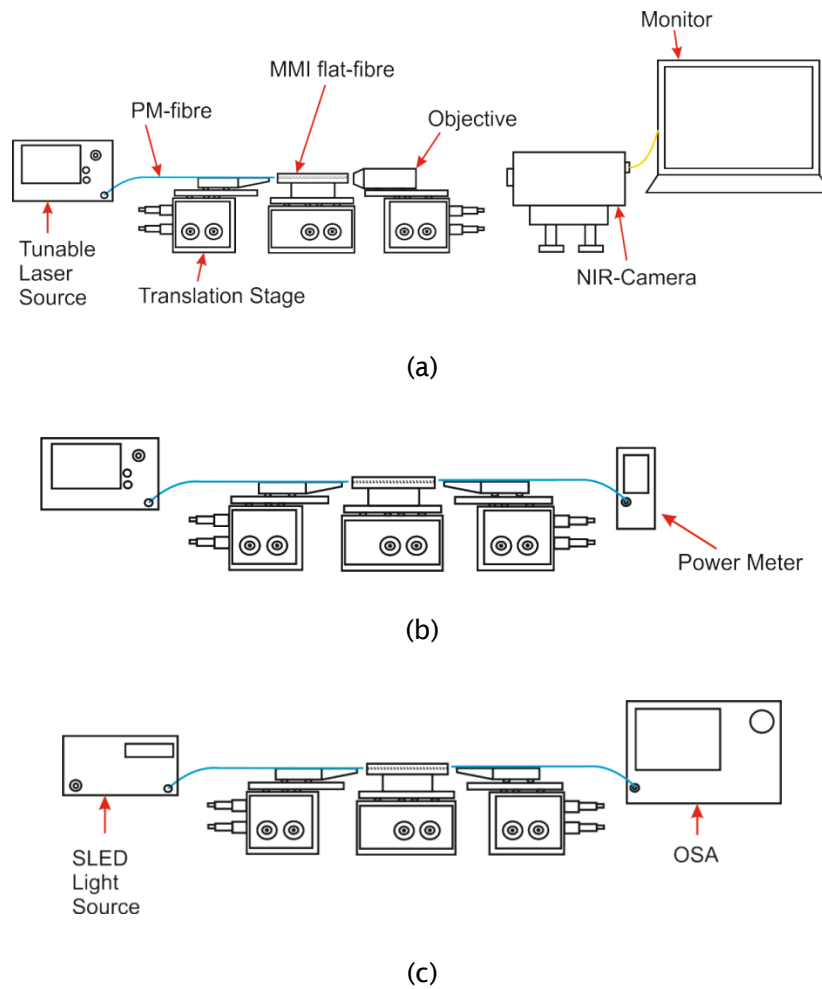


Figure 7.6.2 Characterisation setup for (a) monitoring the output mode pattern observed from monitor, (b) output power measurement by scanning the PM fibre across the MMI cross section and (c) monitoring of wavelength scanning.

7.7 Result and Discussion

In this work, the MMI device performed as a 1x3 splitter device by which one single input from a single mode fibre is split into three outputs, via the MMI. The performance of the MMI device was measured by calculating the excess loss of the device. The excess loss of the device is calculated by taking the ratio between the launched power into the sample and the sum of the three peak outputs. The modal image of the three output spots recorded by the NIR camera is shown in Figure 7.7.1. It must be noted that the intensity of each spot is not directly measured from the NIR camera image due to the low dynamic range of the camera. Therefore, the intensity of the output

modal image was measured by scanning a PM fibre and collecting the output light using a power meter as noted earlier. The output intensity distribution of the simulated and experimental data results can be seen in Figure 7.7.2. The simulation result has been convoluted with a Gaussian mode profile with mode field diameter (MFD) of $10.5\ \mu\text{m}$ to represent the PM fibre that is used for scanning the MMI output facet.



Figure 7.7.1 The modal image pattern of the 1x3 MMI device recorded by the NIR camera at 1641 nm.

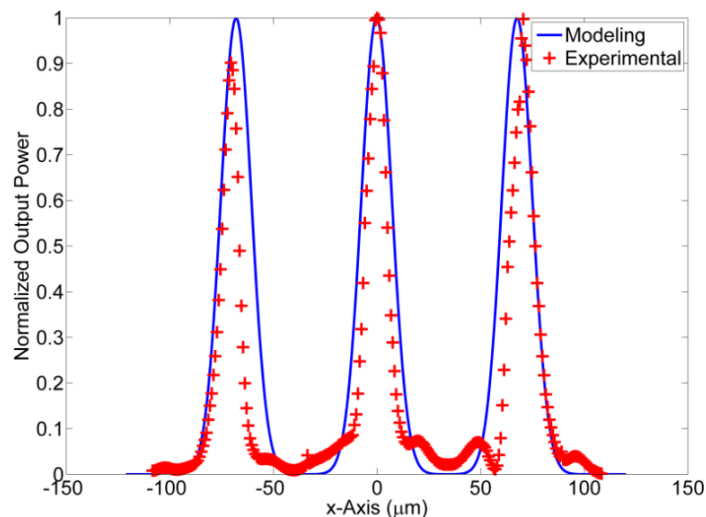


Figure 7.7.2 A distribution output power of the modal image through scanning measurement technique at the end facet of the MMI region using a PM fibre. The scanning is implemented horizontally along the width of the MMI section.

It is known that the MMI characteristic is dependent on the wavelength of the input light source. Therefore, modelling of the spectral dependence was also implemented to observe the output peak power as a function of wavelength. The insertion loss for each of the three spots was measured, as illustrated in Figure 7.7.3. It can be clearly observed that the output powers from each spot are strongly dependent on the

wavelength of the light coupled into the MMI. The pattern of the graph from the three spots is very similar particularly the optimum wavelength, i.e. lowest insertion loss. The output from spot 3 shows a small oscillation that is believed due to a slight cavity formed between the MMI device and fibre connection. From the measurement, it shows that the optimum wavelength for the device was 1652 nm with the total excess loss of 1.89 dB.

The optimum wavelength of the fabricated MMI device is not in the expected region of telecommunication wavelength (i.e. 1550 nm) mainly due to the fabrication error associated with dicing the trenches of the MMI sidewalls. It is worth noting that the most equal splitting ratio occurs at 1620 nm but this is outside the 1 dB bandwidth as described here. From the Figure 7.7.3, it is found that the bandwidth of minimum excess loss, less than 1 dB increase, spans from 1636 nm to 1673 nm corresponding to a width of 37 nm. This can be compared to recent reports of photonic-crystal-based beam splitters demonstrating a 1 dB bandwidth of 11 nm in the C-band [129]. Over this spectral bandwidth, the uniformity of the outputs is 1.24 dB which is comparable to current commercially available devices. The uniformity of the device was calculated by taking the difference between the highest and lowest insertion loss among all of the output spots.

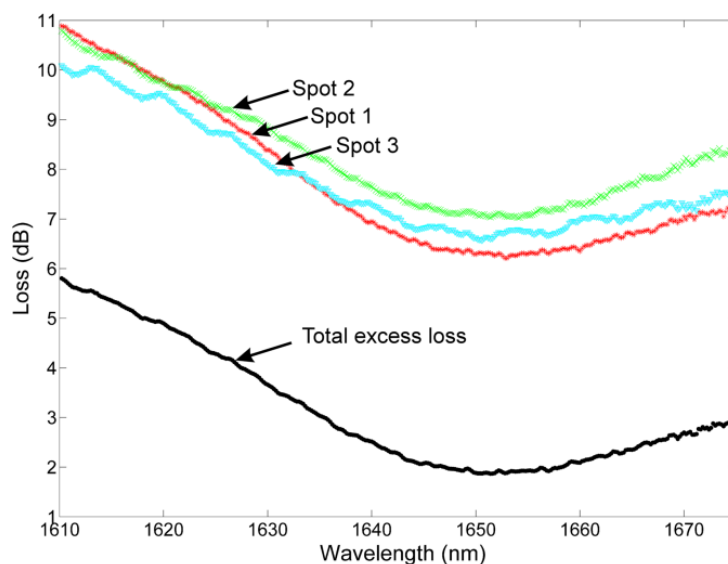


Figure 7.7.3 The insertion loss from each of the three output spots against the wavelength. The total excess loss is also calculated by summing all three output powers at each respective wavelength.

Figure 7.7.4 shows the normalised transmission from the experiment data compared to the BPM model, as a function of wavelength. The results are identical within the wavelength range of 1635 nm – 1660 nm. Beyond this spectral range, a small disagreement between the modelling and experimental result can be seen from the graph. The discrepancy between the experimental data and the model is due to the dispersion, as this was not taken into consideration when modelling the MMI device. There are three main contributions associated with the total excess loss of the MMI device namely propagation loss, coupling loss and scatter loss. These losses will be briefly discussed in the following section.

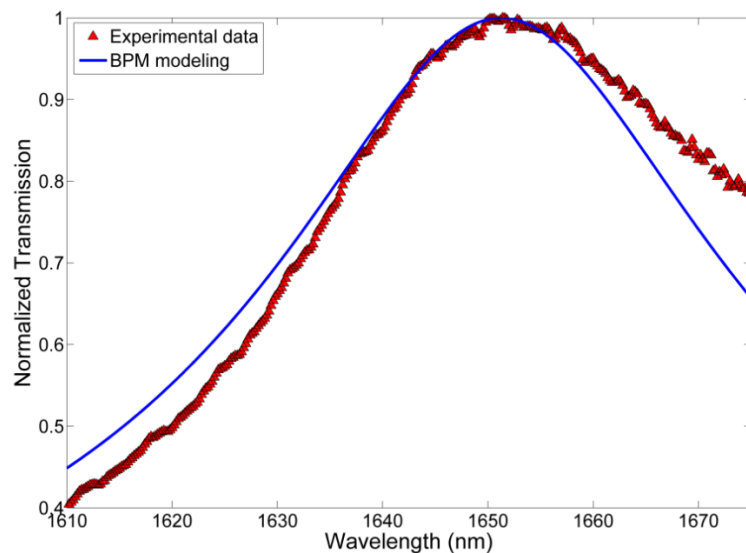


Figure 7.7.4 The solid line represents the normalised transmission from the modelling, showing good agreement to the experimental data. The optimum wavelength of the maximum point is 1652nm.

7.7.1 Propagation Loss

The propagation loss of flat-fibre has already been discussed in the Chapter 5. The value was determined using two different measurement methods in the wavelength region around 1550 nm. These were a Bragg grating loss measurement technique and a measurement using an optical backscattered reflectometer. Even though the number provided earlier was the propagation loss specifically for UV-written channel waveguides, it may be used as an estimation of the anticipated upper bound for the intrinsic

propagation loss within the flat-fibre material. This estimation of propagation loss includes the material loss and scatter loss from cladding and the core layer. It is worth noting that the scatter loss from the trench sidewalls is not included in this propagation loss, which is discussed later in the following section.

7.7.2 Scattering Loss

One of the expected loss mechanisms of the fabricated MMI device is scattering loss. By definition, scattering loss is a part of transmission loss that occurs within a waveguide due to a surface roughness of the sidewall. It has been reported that the loss in a single mode waveguide due to scattering is exponentially reduced when the waveguide width is increased [130], [125]. And is simply due to the mode interacting less with the core-cladding interface. In the case of a MMI device the situation is more complex and the loss is mode dependant, depending on the level of interaction with the sidewall.

Coupled with sidewall surface roughness, another parameter that greatly affects the scattering loss between two interfaces is the relative index contrast. Therefore, one approach in the past has been to reduce the index contrast between the core and the air trenches by putting index matching oil into the trenches. The MMI waveguide structure has high lateral index contrast between the core refractive index and air ($n = 1$), thus by putting a higher index matching oil (1.33) compared to that of air; it will ultimately decrease the index contrast between the core and thus reduce the scattering loss. However this also changes the MMI properties making it difficult to make quantitative measurements. This effect can be observed in Figure 7.7.5, where placing the index oil of 1.33 into the air trenches has changed the wavelength of the total peak power. This is expected as the index matching oil changes the effective width of the MMI device and consequently changed the length of the output spots. The peak power spots can be recovered by changing the wavelength of the input light source. To directly investigate the scattering loss in the MMI device is difficult. However, it is expected that the scattering loss of the device is small as no significant effect in terms of the device performance was observed after the index oil of 1.33 was placed within the trenches.

Finally, the coupling loss of the measurement has also been investigated and will be addressed in the following section.

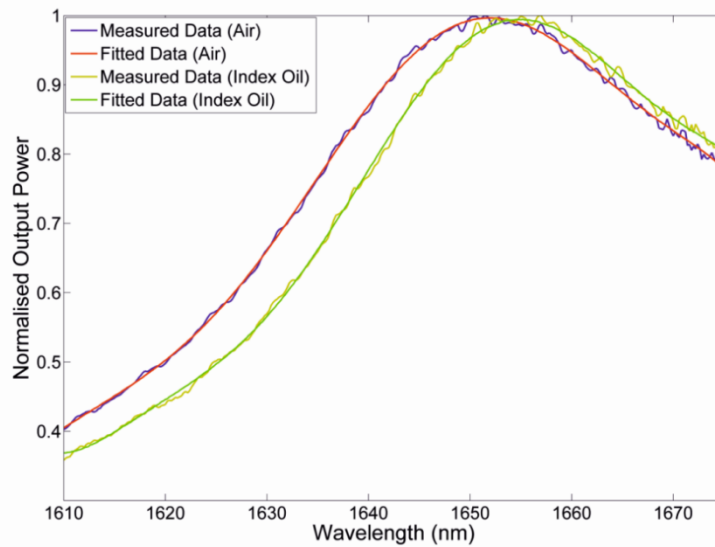


Figure 7.7.5 The normalised output power against the wavelength for trenches with and without index oil.

7.7.3 Coupling Loss

Generally, coupling loss always occurs when transferring an optical signal from into and out of a fibre. It is associated with several factors which can induce coupling loss. The majority of coupling loss originates from coupling between two different geometries, which, because they are not mode-matched results in coupling loss [131]. The factor of having different refractive index materials would also contribute to coupling loss. However, this can be reduced by putting an index matching gel between the respective interfaces. It is understood that the geometry of a PM fibre is not similar to the MMI, which means that each component will have different output mode size and thus induce a significant coupling loss between both components.

To estimate coupling losses in the MMI device, an overlap integral method has been implemented, whereby the fibre was scanned across the output facet using translation stages. To start with, two identical pieces of PM fibres were scanned in order to assess the mode field diameter (MFD) of the PM fibres and this is shown in figure 7.7.6. The MFD of the MMI device output is also measured. To simplify the mode profile analysis of output mode of the MMI device, it is assumed that all of the outputs have the same MFD value. Thus, only the mode output from spot 1 was measured vertically and horizontally in order to estimate the MFD for each axis. This measurement

has been done because of the index contrast of both axes are not the same which ultimately produced two different MFDs. These results can be seen in Figure 7.7.7 (a) and (b) for vertical and horizontal MMI output modes, respectively. Both output modes were fitted with a Gaussian mode. The measured mode profile was actually a convoluted mode profile between fibre and MMI. Therefore, these numbers have been firstly deconvoluted to obtain the actual MFD from each fibre and MMI mode profile, before the overlap integral is performed to calculate the coupling loss of the MMI device.

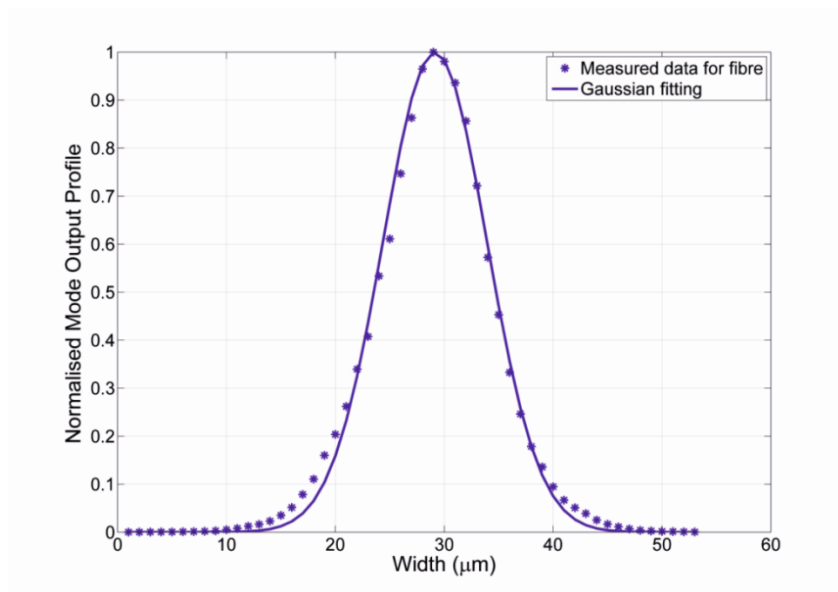


Figure 7.7.6 Normalised mode output profile for optical PM fibre. The measured data is fitted with Gaussian profile.

The measured MFD for the fibre was $6.74 \mu\text{m}$, whereas the MFD for vertical and horizontal MFD of the MMI section were $10.04 \mu\text{m}$ and $9.71 \mu\text{m}$, respectively. The fractional power coupled between two optical modes (T) can be calculated via an overlap integral and is given by equation (7.14) [16],

$$T = \left| \iint_{-\infty}^{+\infty} \psi_1 \psi_2^* dx dy \right|^2 \quad (7.14)$$

Where ψ_1 and ψ_2 represent two normalised Gaussian modes in two dimensional space (x, y) . In the simple case for two optical fibres with mode field diameters w_1 and w_2 with perfect alignment, the integral becomes,

$$T = \left(\frac{2w_1w_2}{w_1^2 + w_2^2} \right)^2 \quad (7.15)$$

In this particular work, the coupling loss was determined via a numerical overlap integral calculation. The measured MFD of the PM fibre and the MMI output mode were used in the numerical calculation and showed that the coupling loss was approximately 0.6 dB per facet providing ~1.2 dB coupling loss in total for the input and output fibre coupling to the MMI device. From this measurement, it can be observed that the excess loss of the MMI device majorly comes from coupling losses. Thus, it is important to reduce the coupling loss of the device in order to improve the MMI device performance. One way of reducing the coupling loss is to optimise the thickness of the core layer of the flat-fibre, thereby improving the modal overlap in the vertical direction. Another route is perhaps through defining UV-written channel waveguides at the input and output sections of the MMI device to provide more efficient mode conversion.

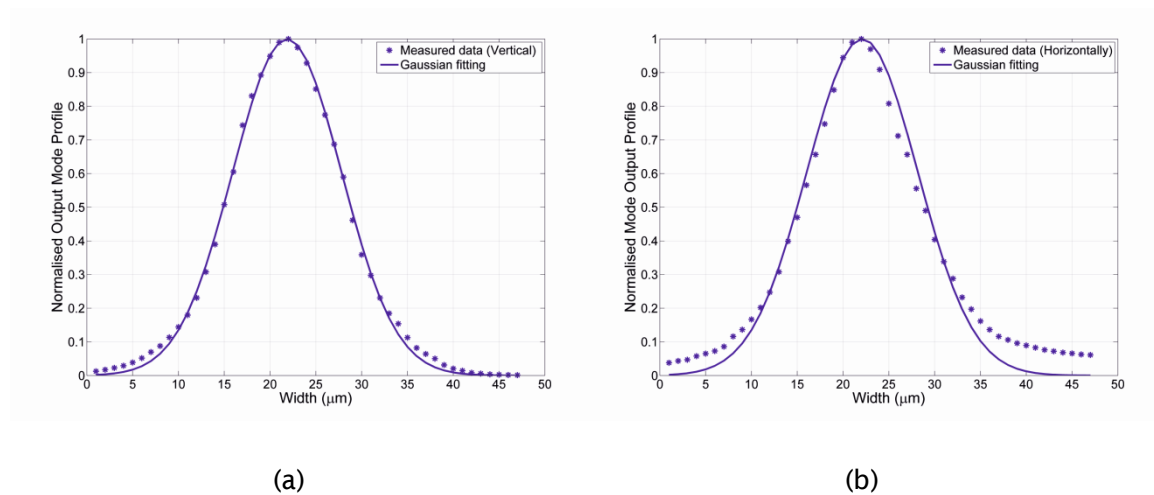


Figure 7.7.7 Normalised output mode profile from spot 1 in (a) vertical and (b) horizontal axes.

The excess loss measured here (1.89 dB) is still higher than expected from the modelling results. Removing the known losses in the system, i.e., the propagation loss

and the fibre coupling losses, an additional loss of 0.56 dB remains. This higher loss is expected to be associated with factors that the modelling does not account for, such as the scattering loss from surface roughness and a possible lack of verticality of the trench sidewalls. Another factor that can also contribute to excess loss is imperfections across the core layer (i.e. non-uniform core layer) of the MMI section as shown in Figure 4.5.3, where the effective index across the width of the core layer has residual fluctuation. From this work, this magnitude of loss is comparable to other reported work using conventional fabrication techniques [132], [133].

7.8 Conclusion

A passive multimode interference device has been successfully fabricated in a flat-fibre platform. A 1x3 splitter MMI device was achieved using particular dimensions. The basic parameters involved in producing the MMI device have been predicted using commercial BeamPROP software. The fabrication process has been described where the MMI section of the device was produced by dicing two parallel trenches. To optimise the total output power from the MMI device, a range of wavelengths have been scanned. This is due to the dependency of the MMI output power to the wavelength variation whereby the optimum output power can be achieved. Although the flat-fibre substrate is inherently a low-index-contrast platform, by using two air trenches a high-index lateral contrast can be produced to achieve better output imaging. The MMI device has 1.89 dB excess loss, which was attributed to propagation loss, coupling loss, scattering loss. To estimate all the factors that affects the performance of the MMI device, a series of experimentally investigations was undertaken. A coupling loss was measured using an overlap integral method and was found to be the main contributing factor to the excess loss. Other factors that contribute to the excess loss are due to the fabrication imperfections and scatter loss. In future work, one can think of combining a UV-writing technique and the MMI section, where the access input and output of the MMI can be defined using the UV-writing technique. This might improve the coupling loss of the device as the input and the output of the MMI section can be accessed by an optical fibre through the UV-written channel waveguides, thus improving the MMI device performance.

Chapter 8

Erbium-doped Flat-fibre

8.1 Introduction

The tremendous step forward of optical telecommunications in the mid-1990s commenced with the pioneering of the optical amplifier, whereby an optical signal could be directly amplified within an optical fibre system. In line with the optical fibre system, there is a gain medium for signal amplification. The gain medium normally contains active ions which are introduced by doping rare-earth ions into a glass host. The first demonstration of a rare-earth doped fibre amplifier employed Neodymium (Nd^{3+}) ions into a glass fibre for signal amplification [134]. The ground-breaking capability of rare-earth ions to amplify optical signals whilst exploiting other emission wavelengths has motivated numerous attempts to investigate different other types of rare-earth ions such as erbium (Er^{3+}), ytterbium (Yb^{3+}), thulium (Tm^{3+}) and more [135]. *Mears et al* first demonstrated the most significant optical fibre amplifier which is known as an erbium doped fibre amplifier (EDFA) [42]. The erbium (Er^{3+}) ion has the capability to amplify optical signals within the C-band wavelength range (~ 1550 nm) and matches the wavelength of the existing lowest loss in single mode silica optical fibre.

Since then, considerable efforts have been undertaken to develop the EDFA technology which ultimately improves the optical telecommunication system. Following this, it has been found that a silica-based material is a practical host glass to produce an EDFA. A silica-based EDFA can be directly spliced to existing telecoms optical fibres, which are also made from silica. This leads to a low coupling loss due to the low reflectivity of the joints and the matched refractive index profile. However, it must be noted

that pure silica-based host glass itself is not sufficient to produce an efficient EDFA, as in pure silica glass, a smaller amount of nonbridging Si-O groups and no network formers present lead to a rigid structure [136]. This results in difficulties in coordinating the rare-earth ion into the glass structure especially to achieve high gain power from the high doping concentration of rare-earth ions. It is therefore important to choose an appropriate host glass for the EDFA which increases the material solubility. This in turn reduces ion clustering and quenching effects within the glass structure when increasing the amount of the rare-earth ion doping [137]. In relation to that, one can think of adding other dopant compositions into the silica-based host glass such as aluminium and phosphorus to avoid clustering effects, as discussed by *Ainslie* [138]. It has been shown by *Ainslie* that no clustering effects have been observed even doping with several weight percents of rare-earth ions. These effects will be briefly explained in the next section to provide an understanding of the factors that can reduce EDFA performance. In addition, the host glass of the EDFA is also important to determine the emission and absorption cross section of the amplifier [139].

The technology of the EDFA is well-documented and has inspired the development of an erbium doped waveguide amplifier (EDWA) in a planar waveguide platform. The main reason of fabricating the EDWA is to compensate for the losses that occur in a passive integrated device (i.e. splitter) and also to provide a compact device [140]. In spite of the capability offered by the EDWA, questions have been raised about the ability of the integrated planar waveguide to support the high doping concentrations necessary due to the small length of the device (few centimetres). This issue can be overcome in a similar way to the fibre-based amplifier where doping the waveguide with numerous network formers to produce high host glass solubility. Apart from that, one way to achieve a high gain amplifier without the need to increase the erbium doped concentration is by co-doping the erbium waveguide with other rare-earth ions such as ytterbium (Yb) [141]. This method improves the pump absorption at 980 nm yielding improved optical gain. However, this is still a major challenge for the EDWA to achieve high gain power with small length and high erbium concentration. The issue has motivated the fabrication of erbium-doped flat-fibre, by which potential high doping concentration can be achieved using the flat-fibre platform due to its large cross-section and long length. Also, the potential of the flat-fibre to have low loss in a silica-based material is an advantage of the platform.

In Chapter 2, a brief description about the concept of an optical amplifier has been given. In the next section, more description about the concept of erbium-doped amplifiers and factors that can limit the efficiency of optical amplifier will be presented. This is followed by a description of the erbium-doped flat-fibre platform and also

its spectroscopy. Finally, the first demonstration of signal amplification in the erbium-doped flat-fibre platform is presented.

8.2 Erbium-Doped Waveguide Amplifier

The erbium-doped amplifier has been successfully demonstrated in many material systems [142]. In this thesis, the silica-based material system is chosen as the flat-fibre platform made from silica. In a standard optical telecommunication, a long-length of EDFA (several metres) in line with the transmission line is pumped with 980 nm to amplify a transmission signal at 1550 nm. This concept has been used in the EDWA technology, where the transmission signal can be manipulated via integrated planar system whilst amplifying it. To understand the principle of the erbium-doped amplifier, the three level energy transition of the erbium ion is described in this section, and several gain limiting factors are reviewed.

8.2.1 Energy level of Erbium doped ion

Figure 8.2.1 shows the transition energy level with respective pump wavelength [41]. The figure shows the energy levels of an erbium ion defined by the Russell-Saunders term notation which provides an abbreviated description of an atom's angular momentum. The erbium ground state is defined as $^4I_{15/2}$ where the number 4 defines the spin multiplicity, I is the total orbital angular momentum, and 15/2 gives the total angular momentum. By using a pump at a wavelength of 980 nm for instance, the erbium (Er^{3+}) ions will be excited from the ground state to the $^4I_{11/2}$ level. This occurs due to the energy from the pump light being absorbed by the erbium ions and with sufficient absorbed energy, the erbium ions are excited to the higher energy level. The excited ions will stay at this level only for a few microseconds before they decay down to the $^4I_{13/2}$ level which is known as a metastable state level without inducing any photons. The lifetime of the ions that stay at $^4I_{13/2}$ level for around 10 milliseconds. The ions decay from $^4I_{13/2}$ level to the ground state and emit light within the range of 1520 - 1570 nm. This emission is known as a spontaneous emission. The spontaneous emission is considered as noise and it can also be amplified within the active medium yielding to amplified spontaneous emission (ASE). At sufficient pump power, a population inversion can be produced where more ions are in the $^4I_{13/2}$ level compared to the ground stage. The ions that stay at the metastable level can be stimulated to the ground stage, by

sending another photon within the range of spontaneous emission wavelength. This will produce a second photon that has the same wavelength, phase and propagation direction as the transmission signal photon. The process is continuous along the active waveguide where the new photon may also stimulate other excited ions at the meta-stable level. This process is a primary stage in order to produce amplified stimulated emission. From this process, the transmission signal can be amplified and some gain can be produced depending on the erbium composition and the pump power. However, it must be noted that increasing the pump power will lead to a saturation point where all the erbium ions within the medium are excited, thus no further gain can be achieved. Increasing the erbium ion concentration in the waveguide can increase the amplifier gain, however, will also have unwanted effects which limit the amplifier gain. These effects will be described in the next section.

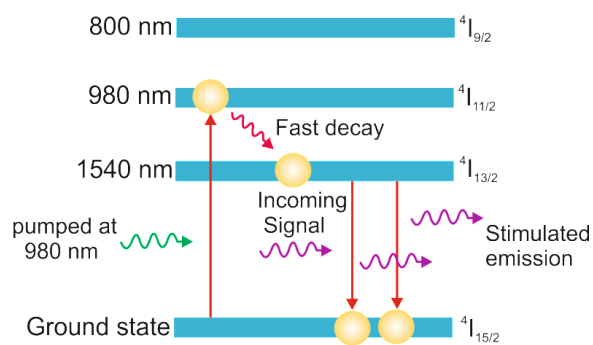


Figure 8.2.1 Illustration of a three transition energy level of an erbium-doped waveguide to produce amplified stimulated emission.

8.2.2 Limiting Factors of an Amplifier Efficiency

There are several factors that can limit amplifier gain and the most important parameter is the erbium ion concentration and length. Principally, the higher the erbium ion concentration, the higher the gain that can be obtained. However, the situation is not as simple as that due to some other associated effects that can reduce the performance of the amplifier. This is correlated to a host glass of the optical amplifier, where the solubility of the erbium to be incorporated into it must be taken into consideration. The associated effects are related to the mechanisms such as ion clustering and thermal quenching induced from ions interacting namely co-operative up-conversion and excited state absorption. Moreover, another important parameter that can limit the

performance of the amplifier is a waveguide loss. All these parameters will be described in the following sub-sections.

8.2.2.1 Host Glass

Numerous different host glasses have been employed to reduce ion clustering due to high doping concentration of erbium ions. It is understood that a fused silica is a rigid structure that has few nonbridging oxygens which causes the erbium ions to share non-bridging oxygens leading to clustering effects [143]. Therefore, adding other network formers into the silica based glass will ultimately increase the solubility of the host glass to incorporate the erbium ions composition. Dopants such as phosphorous (P), aluminium (Al) and germanium (Ge) will affect the erbium ions concentration that is allowed to be doped without inducing clustering effects. It has been found that by co-doping phosphorous into the erbium silica waveguide, it will ultimately reduce the effect of clustering even with high erbium doping concentration [144]. However, the gain spectrum is narrowed, thereby reducing the effective bandwidth. Alternatively, co-doping with aluminium reduces clustering and maintains a large gain spectrum. It has been reported that using an aluminium co-doped waveguide amplifier, net optical gain over a 41 nm wide of wavelength range with a maximum net gain of 5.4 dB at 1533 nm has been achieved [145]. Co-doping the erbium waveguide with germanium can increase the photosensitivity of the erbium doped waveguide. It has been demonstrated that doping the germanium in $\text{Er-Al}_2\text{O}_3\text{-SiO}_2$ waveguide, can provide the same emission spectrum similar to Al co-doped only [146]. The quantity of each dopant compositions of erbium, aluminium and germanium will ultimately affect the fluorescence intensity. As with phosphorus the co-doping of germanium leads to a narrower bandwidth compared with aluminium as shown in Figure 8.2.2 (taken from [139]).

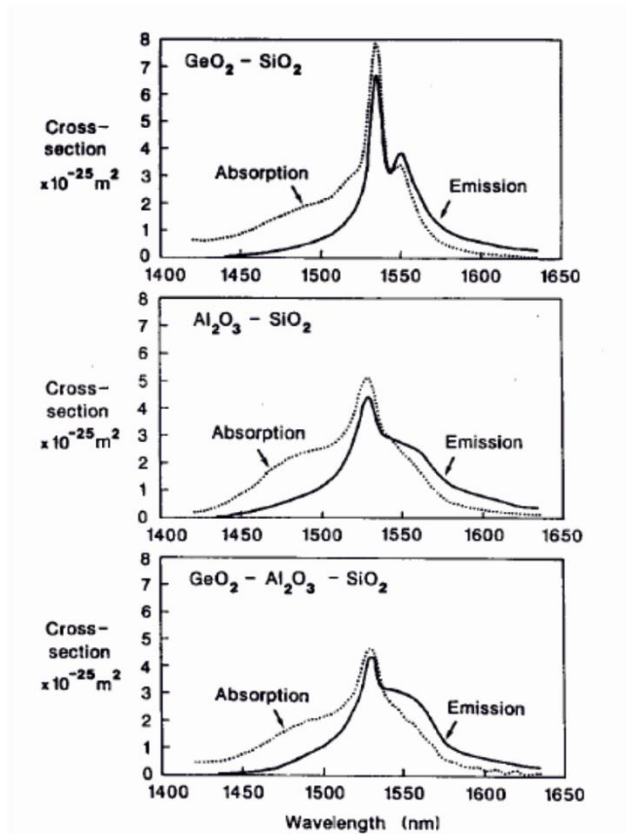


Figure 8.2.2 Cross-section data from three fibres with different host compositions, taken from [139].

8.2.2.2 Ion-ion Interactions and Excited State Absorption (ESA)

As discussed in the previous section, the host glass and doping concentration are two significant elements that must be taken into account when fabricating an erbium-doped waveguide amplifier. As a consequence, when using an inappropriate host glass, the possibility of quenching effects induced by co-operative ion interactions and excited state absorption (ESA) to occur within the active medium will increase [137]. These effects will decrease the amplifier efficiency.

In the co-operative upconversion process, two excited Er^{3+} ions can interact at the metastable level as shown in Figure 8.2.3 (a), one excited ion transfers its energy to the second excited ion and decays to the ground state, whereby the second ion is promoted to the upper state 2 as depicted in Figure 8.2.3 (b). The second ion then quickly decays back to the metastable state via nonradiative relaxation. This process

reduces the quantity of excited ions and consequently increases the required pump power to develop population inversion.

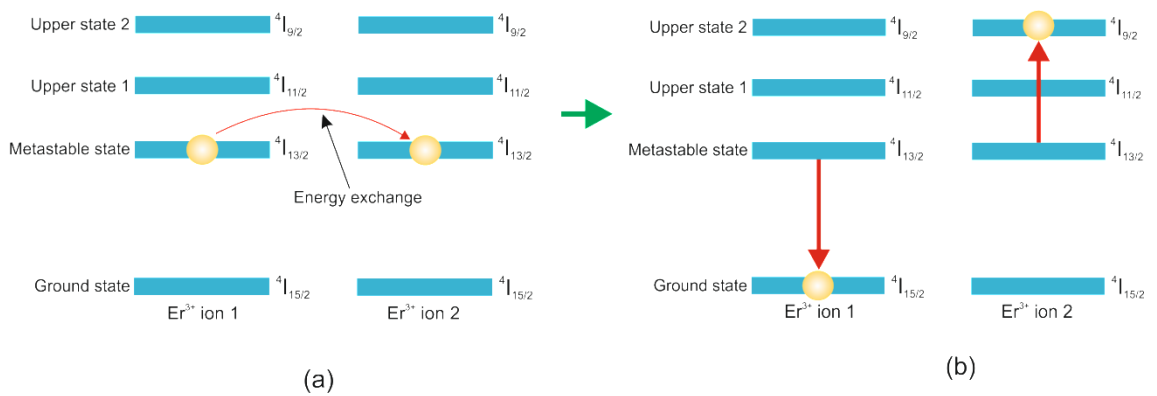


Figure 8.2.3 Illustration of co-operative upconversion process which occurs in erbium doped waveguides. (a) An energy exchange between two erbium ions and (b) shows the location of the erbium ion resulted from energy exchange process.

Another factor that can cause quenching effects is excited state absorption [142]. This process involves an ion absorption which occurs at the metastable state instead of the ground state. An excited erbium ion absorbs energy from a signal or pump photon which ultimately promotes the ion to the upper level state. This normally happens if the upper state has a long lifetime that allows the excited ion to interact with the incoming photon of the signal or pump. The excited ion at the upper level state will decay back to the metastable state with multiphonon or radiative relaxation. This affects the maximum gain and the pump efficiency of the amplifier.

8.2.2.3 Waveguide Loss

The waveguide loss can be defined as a propagation loss due to absorption and scattering of the guided light along a waveguide. The waveguide loss must be overcome in order to obtain net gain amplification by the stimulated emission process [147]. It must be noted that the pump light will also be affected by the waveguide loss as it travels through the waveguide, hence reducing the pumping efficiency. In low refractive index contrast materials for instance, some significant portion of the optical mode propagates through the undoped cladding yielding a lower gain per unit length. There-

fore, the waveguide loss is also important parameter which determines the performance of the amplifier.

The following section describes the fabrication of an erbium doped flat-fibre. A series of experimental work has been carried out to determine the physical characteristics of the erbium-doped flat-fibre platform.

8.3 Erbium-Doped Flat-Fibre

An active flat-fibre platform has been fabricated for the first time by our team, Dr. *Andrew Webb* carried out the fibre fabrication. The device employs erbium ions as the characteristics offered by this type of rare-earth ion have been well-documented. It is believed that erbium doping of the silica-based flat-fibre platform will produce similar characteristics as erbium-doped fibre amplifier (i.e. absorption spectral and fluorescence lifetime). As with the passive flat-fibre devices, a channel waveguide must be defined within the core layer for light confinement. Accordingly, similar processing has been used to the passive flat-fibre devices i.e. UV-writing to produce waveguides and Bragg gratings. A series of Bragg grating structures have been defined in order to characterise the effective index of the core layer and also the capability of the substrate to have multiplexed Bragg gratings along the substrate for future device integration. In this section, the specification of the erbium-doped flat-fibre platform and also the composition of the core layer will be given. Following this, the spectroscopy of the flat-fibre will be revealed to observe the peak absorption spectra and also the fluorescence lifetime. Finally, the first demonstration of flat-fibre amplifier will be presented and discussed at the end of this section.

8.3.1 Erbium-doped flat-fibre specification

The fabrication process and the composition of the erbium-doped flat-fibre have been described in Chapter 3. In this section, the specification of the erbium-doped flat-fibre is discussed. Figure 8.3.1 shows a microscope image of the flat-fibre cross section which indicates a core layer thickness of about 4.6 μm . The image also shows that the cladding surface of the flat-fibre platform, unlike the passive devices, is not entirely flat, however, the flatness of the core layer can be considered sufficient for channel waveguide definition. This might be proven to be a challenge when defining waveguides across the width of the device as the varying cladding thickness of the flat-fibre

could change the focus of the two-crossed UV-beams. Nevertheless, the cladding thickness along the length of the flat-fibre substrate is largely uniform. The core layer of the erbium-doped flat-fibre platform also contains aluminium and germanium dopants. The aluminium dopant was used to increase the solubility of the host glass to incorporate a higher doping concentration of erbium. This is important to reduce ion clustering and concentration quenching effects in the erbium-doped flat-fibre. In addition, the adding of germanium dopant increases the refractive index of the core layer and the photosensitivity of channel waveguide for the UV-writing process. In the following section, the spectroscopy of the erbium-doped flat-fibre namely absorption spectra and fluorescence lifetime is discussed.

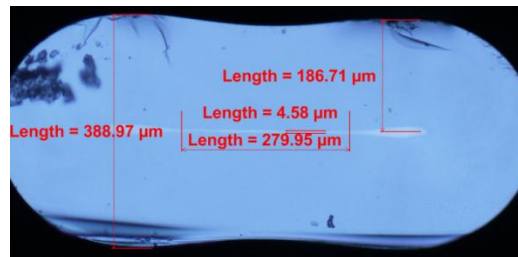


Figure 8.3.1 An image of the cross section of an erbium-doped flat-fibre platform.

8.3.2 Spectroscopy

A series of experiments have been carried out to characterise the erbium-doped flat-fibre including absorption spectra and fluorescence lifetime. The spectroscopy of the erbium-doped flat-fibre is an important measurement to understand the physical characteristics of the substrate especially in developing an amplifier. From the absorption spectra measurement, several absorption bands can be observed. These bands correspond to particular energy transitions of the active ions within the medium i.e. excitation of the erbium ions from the ground state to a higher energy level. In particular for erbium-doped waveguide, the most interesting absorption wavelength band is around 1540 nm due to the similarity of the wavelength to the standard transmission line wavelength at 1550 nm. The wavelength band around 980 nm is also interesting for developing an optical amplifier at 1540 nm.

8.3.2.1 Absorption Spectra

In this measurement, the absorption spectra of the erbium-doped flat-fibre with the substrate length of 18.8 cm are measured without defining any channel waveguides. The characterisation setup for the measurement is illustrated in Figure 8.3.2. A supercontinuum light source was launched into the erbium-doped flat-fibre via a single mode fibre. The output power from the sample was butt coupled to an optical fibre with 125 μm core diameter to collect the output light. It is understood that the large core diameter of the collecting optical fibre will also measure light that travelled through the cladding region. However, it must be noted, a pre-alignment has been done before the absorption spectra measurement, where the flat-fibre substrate is pigtailed to the single mode fibre using an UV-cure adhesive to ensure the launched light is travelled through to the core layer of the sample. Therefore, it is believed that the measured output power is largely collected from the core layer and it is sufficient to represent the absorption wavelength band occurring within the substrate. The collection fibre is directly connected to an optical spectrum analyser to observe the absorption spectra. The spectra are monitored within the wavelength range of 600 nm to 1700 nm.

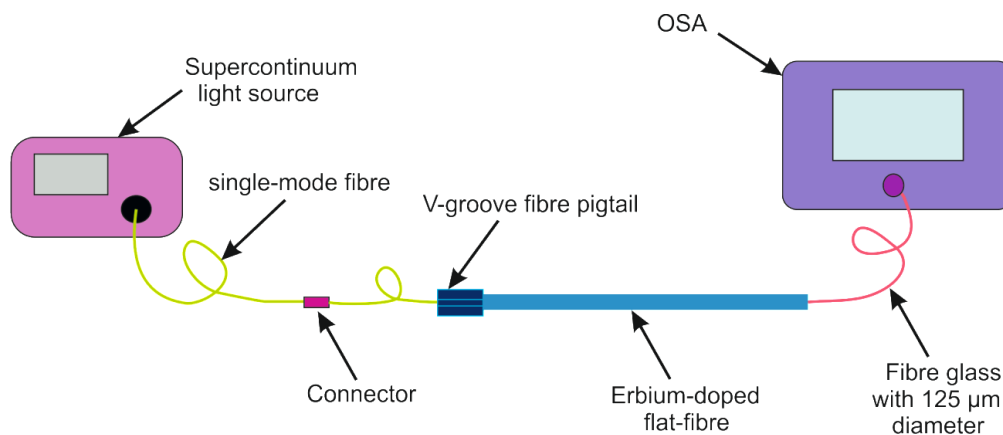


Figure 8.3.2 Characterisation setup of absorption spectra measurement for erbium-doped flat-fibre substrate.

Figure 8.3.3 shows the normalised absorption spectra of the erbium-doped flat-fibre substrate. The graph is normalised with the input power of the substrate. Three main peaks around 656 nm, 975 nm and 1525 nm can be seen in the absorption spectra. These wavelength peaks are expected from the erbium-doping. In this work only

two of the wavelength peaks are of interest namely those at a wavelength of 980 nm and 1525 nm. This is due to only those peaks will be employed in developing an erbium-doped flat-fibre amplifier. The absorption spectra indicates that the absorption loss at 976 nm is ~ 0.32 dB/cm and ~ 0.64 dB/cm at 1525 nm. Next, the fluorescence lifetime of the erbium-doped flat-fibre is measured.

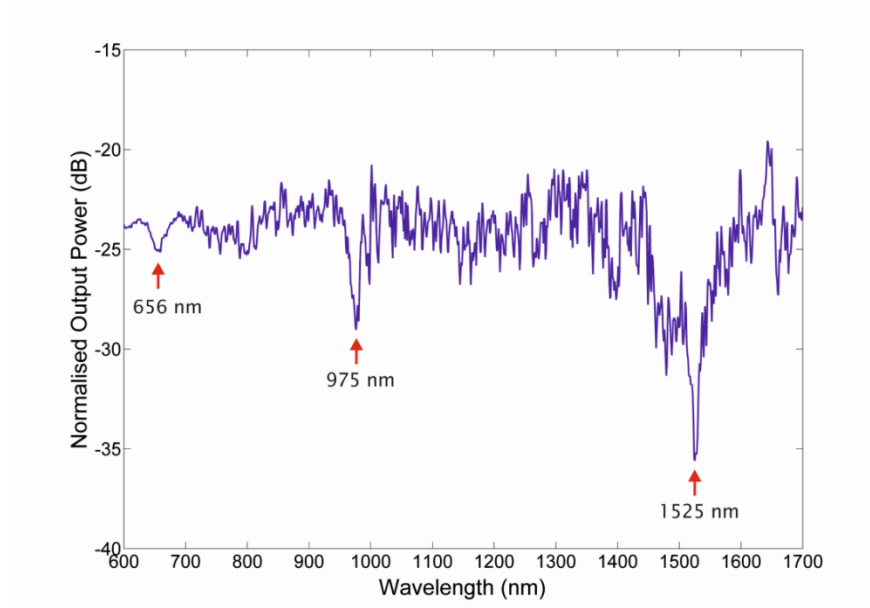


Figure 8.3.3 Absorption spectra of erbium-doped flat-fibre along 18.8 cm planar slab waveguide.

8.3.2.2 Fluorescence Lifetime

The fluorescence lifetime measurement is another significant characteristic for an erbium-doped amplifier. Launching a pump light source, at 980 nm for instance, into an erbium-doped medium results in absorption and this will excite the erbium ions into higher energy level at $^4I_{11/2}$ before fast decaying to the level of $^4I_{13/2}$. From this level, the relaxation of the excited ions down to the ground state will result in the emission of photon known as fluorescence. The lifetime of the fluorescence can be measured by modulating the pump light source using an acousto-optic modulator. Figure 8.3.4 illustrates the characterisation setup that is used to measure the fluorescence lifetime of the flat-fibre sample. A laser diode at 980 nm was used and directed to the acousto-optic modulator to modulate the laser diode controlled by a signal generator from an oscilloscope. The modulated light was focused via an objective and directed to the core

of the erbium-doped flat-fibre with the length of 80 mm. At the end of the setup, a near-IR camera has been aligned to monitor whether the light is properly launched into the core. An indium gallium arsenide (InGaAs) detector was used and placed at the top of the sample to detect emitted fluorescence light from the sample. Finally the detector is connected to the oscilloscope to monitor the lifetime of the fluorescence. A standard erbium-doped fibre was measured to validate the characterisation setup, its measured fluorescence lifetime was 8.6 ms which is comparable to the lifetime of erbium-doped fibre [137].

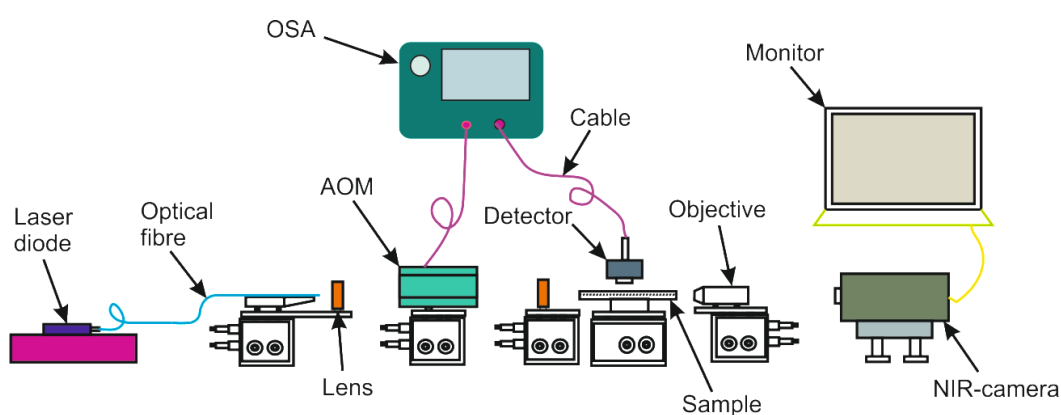


Figure 8.3.4 Characterisation of fluorescence lifetime measurement of an erbium-doped flat-fibre substrate where using laser diode as a pump light source.

By modulating the pump laser diode with amplitude modulation, the fluorescence lifetime can be measured as indicated in Figure 8.3.5. The fluorescence lifetime is defined as the time that the fluorescence light decays to e^{-1} of the starting value. In this measurement, the frequency was set as 5.2 Hz and the pulse width was 59.0 ms. The fluorescence was slowly increased until it reaches the saturation level at 0.42 V. Once the pump laser diode is off, the fluorescence light was slowly reduced. An offset about 0.2 V can be seen from the graph at the time when the pump laser is on and off. This is expected as the detector is also slightly sensitive to the optical power from the pump source. However, this will not affect the fluorescence lifetime result as this is measured at the point the fluorescence starts to decay. Figure 8.3.6 shows the fluorescence light exponentially decaying when the pump source is off. The graph has been fitted using single exponential fitting curve and yielded to the fluorescence lifetime of 9.53 ms. This number is comparable to the standard erbium-doped fibre lifetime and confirms that quenching is not significant.

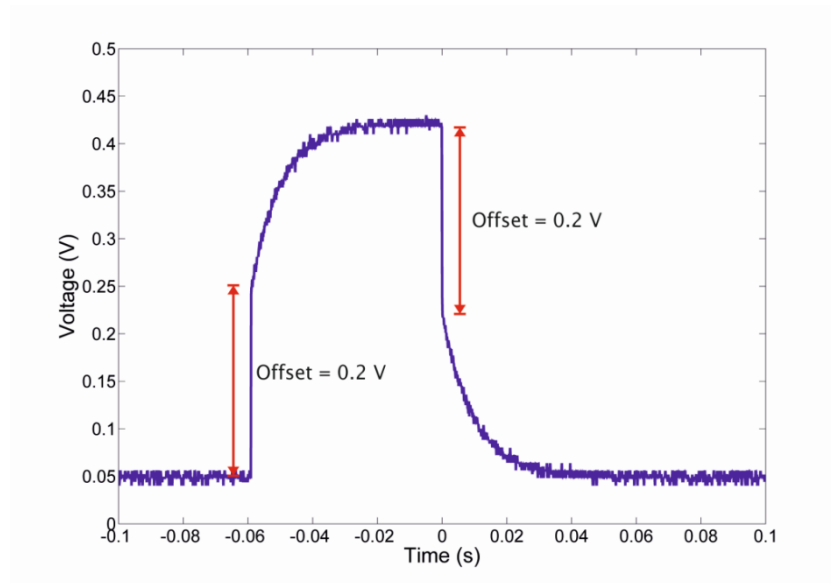


Figure 8.3.5 The fluorescence lifetime measurement showing the fluorescence exponentially decreases after the LD power laser is off.

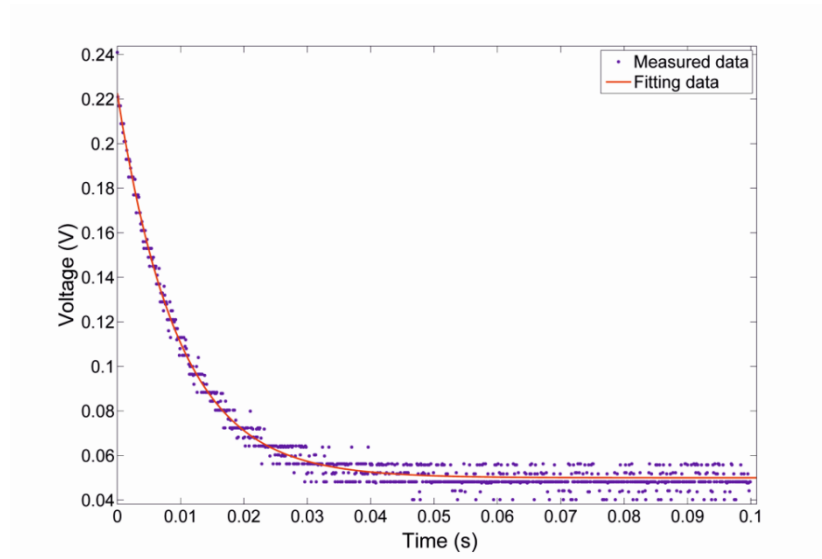


Figure 8.3.6 Fluorescence lifetime of the erbium-doped fibre where fitting with single exponential equation.

8.4 UV-Written Channel waveguide and Bragg Gratings in an Erbium-doped Flat-fibre

Similar channel waveguide development in the erbium-doped flat-fibre has been performed as that in the passive flat-fibre. Both channel waveguides and Bragg gratings structures have been defined via the direct grating writing technique. There are eleven Bragg gratings distributed along the 17 mm length of sample as illustrated in Figure 8.4.1. The Bragg grating wavelengths varied from 1250 nm to 1345 nm with a spectral separation of 10 nm. The phase modulation variant of the UV writing system was used to UV-write a channel waveguide and Bragg gratings in the erbium-doped flat-fibre. The fluence and duty cycle used in this work are 200 kJcm^{-2} and 0.8, respectively. Each grating has 1.5 mm length with no plain waveguides between the gratings. The sample is characterised using the same setup shown in Figure 3.7.1.

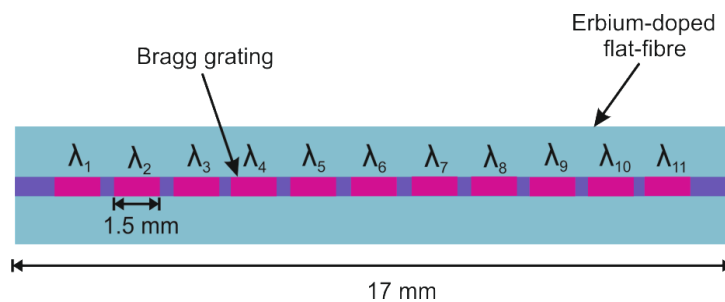


Figure 8.4.1 Schematic diagram of distributed Bragg gratings along the erbium-doped flat-fibre substrate.

The spectral reflectivity of the Bragg grating against wavelength is shown in Figure 8.4.2. To acquire this data, an unpolarised SLED light source was used and clearly shows the Bragg gratings spectra, although some of the gratings are comparably weak and is a result of the spectral property of the source. Figure 8.4.3 shows similar data with a polarised light source, although in this data the reflectivity of the Bragg gratings are weaker and some are indistinguishable. The effective refractive index for the first six distributed UV-written Bragg gratings are calculated and plotted as indicated in Figure 8.4.4. These numbers are sufficient to represent the effective index of the erbium-doped flat-fibre.

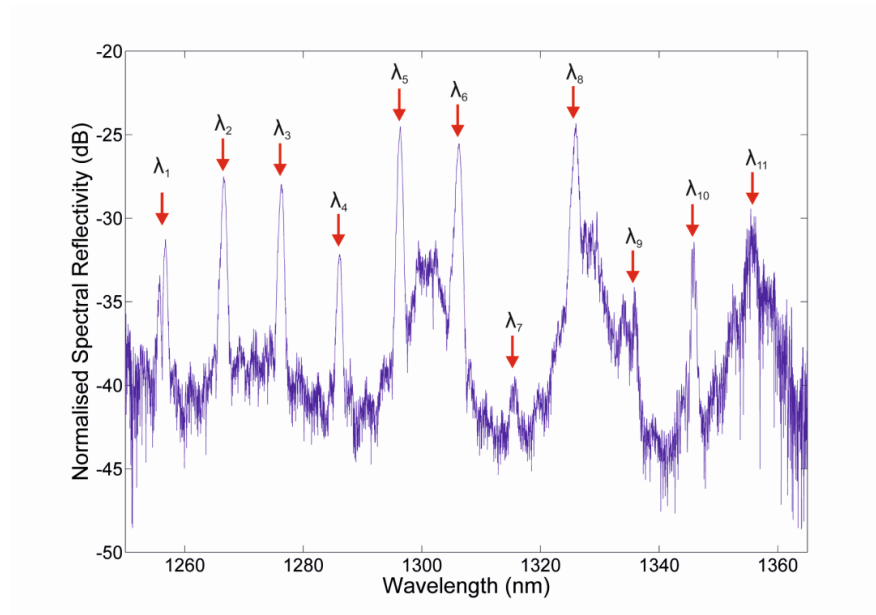


Figure 8.4.2 Normalised spectral reflectivity against wavelength for the erbium-doped flat-fibre.

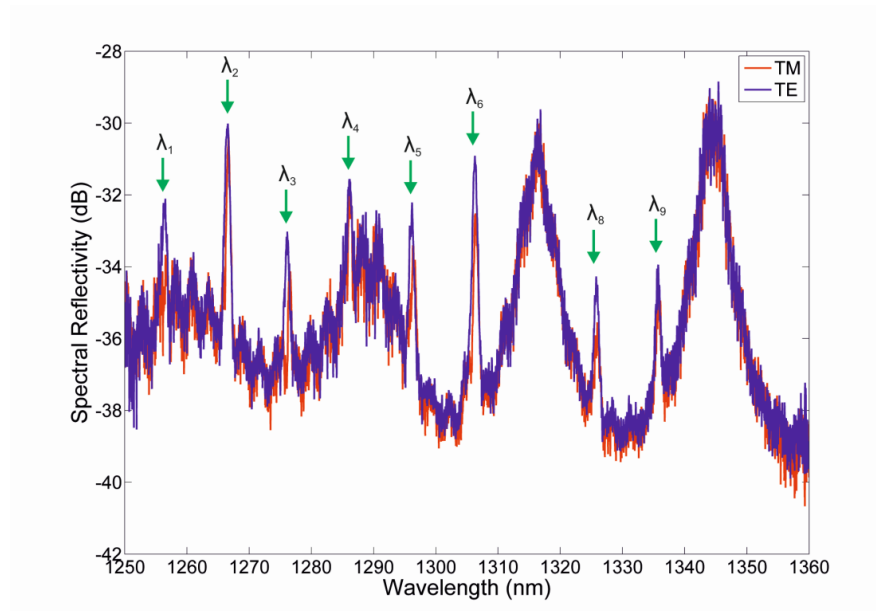


Figure 8.4.3 Spectral reflectivity against wavelength for TE and TM polarisation.

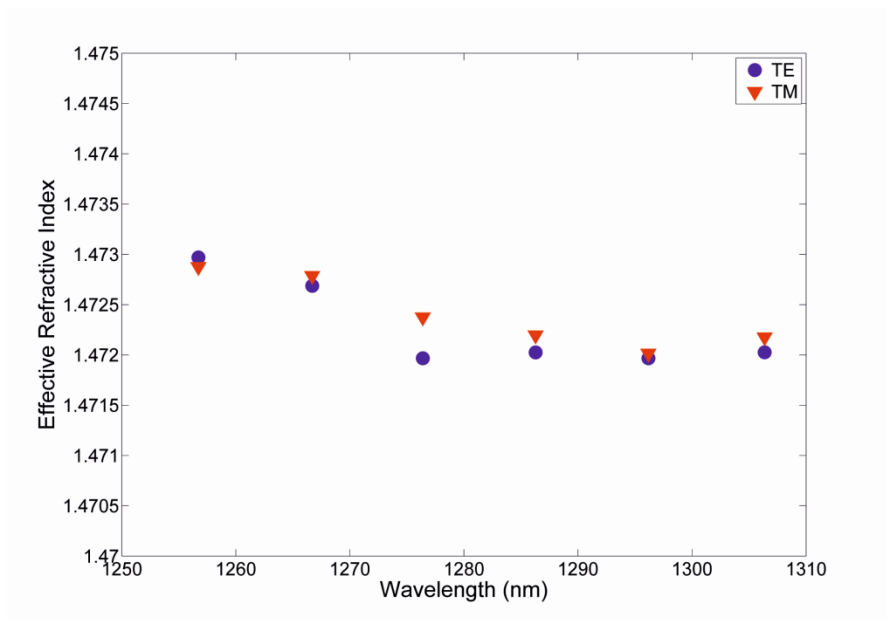


Figure 8.4.4 Effective refractive index against wavelength for TM and TE polarisation.

The propagation loss of the UV-written channel waveguide of erbium-doped flat-fibre has been measured using a Bragg grating loss measurement technique. The technique has been described in Chapter 5, where a series of Bragg gratings is used and measured the reflectivity of each Bragg grating wavelength in forward and backward directions. The sample was cut to a length of 9 mm for loss measurement purposes. This is done due to the Bragg grating loss measurement technique requires spectral reflectivity from each grating in order to measure the propagation loss. Figure 8.4.5 shows the ratio of peak power from forward, P and backward, P' direction against the grating position. From a regression data fitting, it shows that the propagation loss for the erbium-doped flat-fibre is 0.27 ± 0.14 dB/cm.

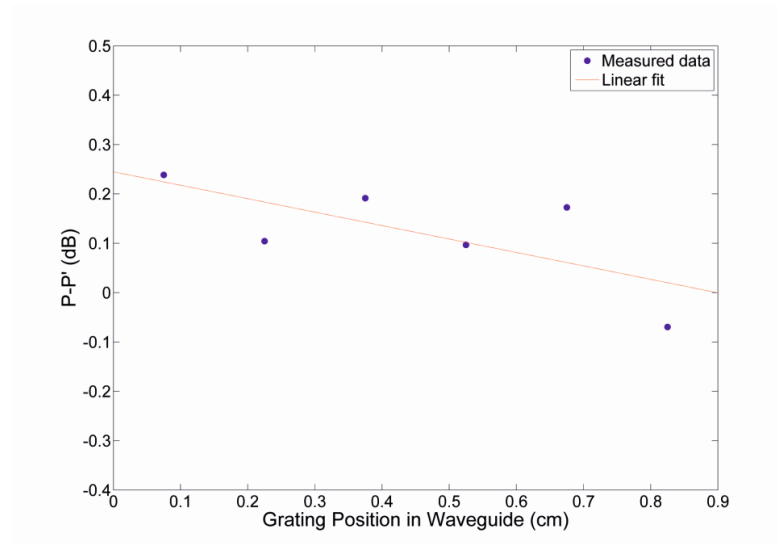


Figure 8.4.5 The ratio of peak power from forward, P and backward, P' direction against the grating position for the erbium-doped flat-fibre.

Table 8.4.1 shows a summary of the measured properties of the erbium doped flat-fibre. The table includes the erbium concentration and the birefringence of the sample. In the following section demonstrates the capability of the erbium doped flat-fibre to amplify signal when pumping the sample at particular wavelength.

Table 8.4.1 Summary of the erbium doped flat-fibre specification.

Specification	Erbium doped flat-fibre
Core layer thickness	4.6 $\mu\text{m} \pm 0.3 \mu\text{m}$
Erbium concentration	3950 ppm at 1525 nm
Erbium absorption	0.64 dB/cm at 1525 nm
Fluorescence Lifetime	9.53 ms
n_{eff} at ~ 1300 nm	1.472 for TE polarisation
Birefringence	1.3×10^{-4}
Propagation loss	0.27 ± 0.14 dB/cm

8.5 Flat-fibre Amplifier

In this section, the first demonstration of an erbium-doped flat-fibre amplifier is briefly described. A simple structure of a straight channel waveguide with the length of 30 mm was defined into the core of the flat-fibre using UV-writing technique. The fluence of the UV-written waveguide was 200 kJcm^{-2} . The sample has been hydrogen loaded for almost 2 months. As described in the previous section, signal amplification can be achieved by launching a pump light source into the active medium along with the signal data. In order to demonstrate this, the characterisation setup shown in Figure 8.5.1 was used. A laser diode (JDSU-29-7602) at 976 nm was used as a pump light source and connected to a wavelength division multiplexing (WDM) coupler to combine both the pump light and signal light obtained from a tunable light source (TLS). The TLS was connected to the WDM coupler via an isolator in order to prevent any damage due to reflected light. The output of the WDM was directed to the erbium-doped flat-fibre substrate, which was securely pigtailed to ensure the light propagated through the core layer of the substrate. An optical spectrum analyser was used to monitor the output light from the sample.

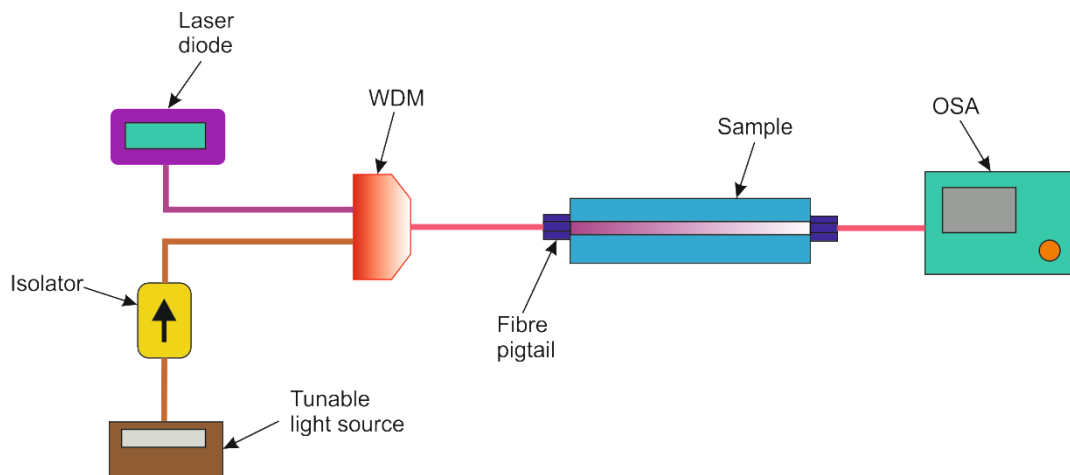


Figure 8.5.1 Characterisation setup for signal amplification, where using the wavelength division multiplexing (WDM) to couple the light from laser diode and tunable light source.

First of all, the sample was pumped with the laser diode into the flat-fibre substrate to record amplified spontaneous emission (ASE) of the flat-fibre. As shown in

Figure 8.5.2, ASE spectrum is plotted in order to decide which wavelength will have high emission peak. It was observed that the maximum peak power from the ASE was about -68.8 dBm at wavelength of 1530 nm. A considerably wide wavelength band between 1500 to 1580 nm, can be seen as a result from pumping the erbium-doped with the laser diode output power of 275 mW. The ASE power can be increased with increase in-pump power level. However, the launched output pump power was the maximum available power that can be pumped into the sample.

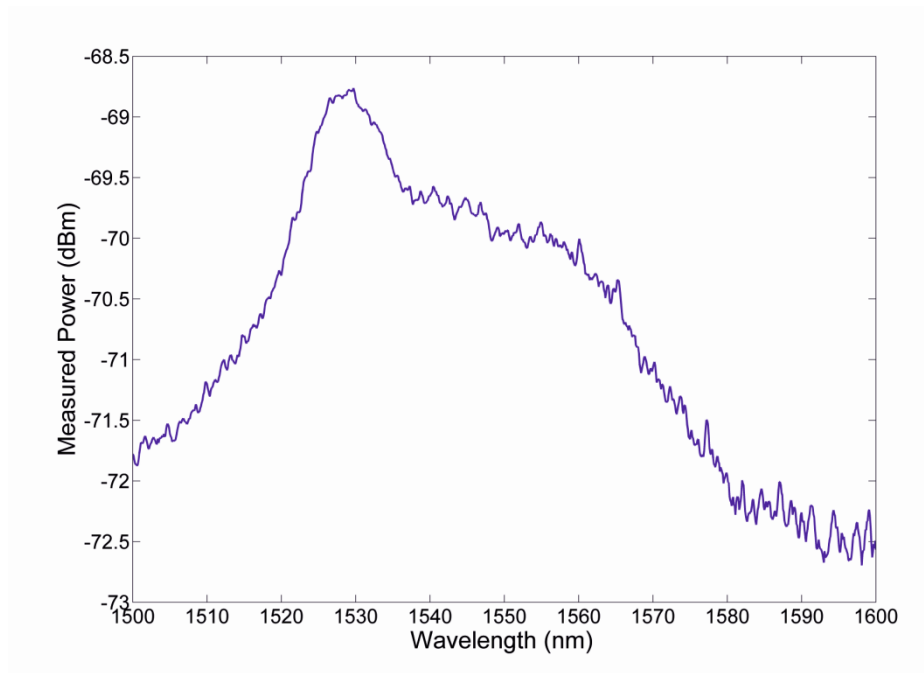


Figure 8.5.2 Amplified spontaneous emission observed from the erbium-doped flat-fibre when launching a laser diode at 980 nm.

To investigate the signal amplification in the erbium-doped flat-fibre substrate, a signal from the TLS was coupled with the pump light source via WDM to seed stimulated emission and thus amplification. In this particular measurement, input signal powers of -10 dBm and -23 dBm at signal wavelengths of 1550 nm and 1530 nm were monitored to calculate the relative gain of the erbium-doped flat-fibre. Figure 8.5.3 shows the output power against wavelength from the erbium-doped flat-fibre with and without launching the pump power into the substrate for signal wavelength and power at 1530 nm and -23 dBm, respectively. Flat-top peaks can be seen from the graph due to the resolution of the OSA which was set to 0.5 nm, a much larger resolution compared to the spectral width of the data signal from the TLS [148]. Also, it can be

observed that the ASE shifts the noise floor up by approximately 40 dB, but the relative gain is less than 1 dB, and this may be a consequence of the low absorption and the factor that no more pump power was available to increase the useful gain. The relative gain is determined by measuring the transmission spectra with the pump on and off. The experimental results are summarised in Table 8.5.1. This measurement also considers the output signal power with a wavelength at 1550 nm and 1530 nm and signal powers of -10 dBm and -23 dBm, respectively. The measured output peak power before pumping means no pump power is added to the input signal. Whilst the after pumping output peak power represents the measured output power when the pump laser diode on. The relative gain can be calculated using the equation (8.1).

$$\text{Relative Gain} = \frac{\text{Signal power (After pumping) (mW)}}{\text{Signal power (Before pumping) (mW)}} \quad (8.1)$$

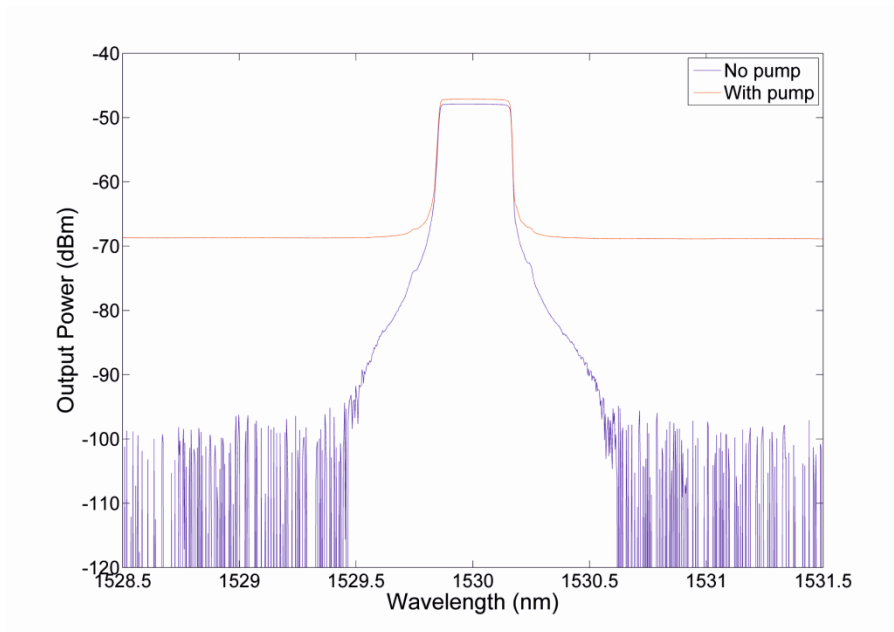


Figure 8.5.3 Output power from the erbium-doped flat-fibre substrate against wavelength with and without pump power for 1530 nm signal wavelength and signal output of -23 dBm. The resolution of the OSA was set to 0.5 nm to allow an accurate power measurement.

Table 8.5.1 Summary of the measured output power from two different signal inputs before and after pumping the erbium-doped flat-fibre.

Condition	Input signal		Before pumping	After pumping	Relative gain (dB)
	Wavelength (nm)	Power (dBm)	Output signal power (dBm)	Output signal power (dBm)	
I	1550	-10	-32.9	-32.5	0.39
II		-23	-45.8	-45.4	0.44
III	1530	-10	-35	-34.3	0.67
IV		-23	-47.9	-47.1	0.74

Table 8.5.1 shows that the highest relative gain can be achieved from Condition IV where the wavelength is 1530 nm with the signal power of -23 dB. This is expected as the wavelength at 1530 nm has higher emission peak in the ASE spectrum compared to the wavelength of 1550 nm. Also the input signal power is lower than Condition III thereby producing slightly higher gain due to gain saturation. In addition, very small output power changes can be observed before and after pumping the sample especially for signal wavelength at 1550 nm. This is anticipated as the ASE output power presents less emission at the wavelength 1550 nm compared to emission wavelength at 1530 nm.

The data shows that both signals have very small relative gains which are less than 1 dB. However, it is worth noting that from pumping the sample, the loss was reduced from 0.64 dB/cm (erbium absorption at 1525 nm) to 0.39 dB/cm which resulted in relative gain. Although, no net gain was obtained from this measurement and this has highlighted several issues which could be improved. One of the issues is probably due to high coupling losses of the fibre pigtail coupling from both sides of the sample end facets, reducing the launched pump power. Another issue comes from the UV-written channel waveguide itself which is not optimised. The fluence and duty cycle parameters of the UV-writing technique that are used in waveguide defining have not been refined. Therefore, by optimising the channel waveguide of the erbium-doped flat-fibre, the propagation loss can be reduced significantly and thus increasing the relative gain of the device. One of the challenges of working with this flat-fibre substrate was the high level of twist observed in this particular substrate which was not observed in the passive flat-fibre. This limited the length of the possible UV written devices that could be fabricated. Fabricating a new sample of erbium-doped flat-fibre

without this twist would increase the potential device length and improve the relative gain. However this preliminary experimental work shows that the erbium-doped flat fibre has potential to be used as an integrated planar amplifier.

8.6 Conclusion

An active flat-fibre platform has been fabricated for the first time with erbium as a rare-earth ion. In order to understand the physical characteristics of this active ion, the basic principle of the three level energy transitions has been described. Also, several factors that can limit the efficiency of optical amplifiers are also reviewed. The spectroscopy of the erbium-doped flat-fibre has been carried out where the absorption spectra and the fluorescence lifetime of the sample are performed. It has been found that the erbium absorption in this sample is around 0.32 dB/cm at 980 nm wavelength. In addition, a propagation loss measurement is also presented using the Bragg grating loss measurement technique. Finally, the first demonstration of signal amplification has been performed where the relative gain was 0.74 dB. The low relative gain may be attributed to poor optical coupling of the flat-fibre leading to significantly reduce the pump power. Several issues with the current device have been described and suggestions of how to improve the performance of the erbium-doped flat-fibre amplifier have been discussed.

Chapter 9

Conclusions and Future Work

9.1 Conclusions

This chapter concludes the thesis by summarising all the outcomes achieved from the developed flat-fibre optical devices. The development of the flat-fibre optical devices spanning from UV-written Bragg grating optical devices to physical micromachining devices has been presented in this thesis. These developments show the potential of flat-fibre to be a next generation planar waveguide platform in many fields such as optical telecommunication, structural health monitoring and medical instruments.

To start with, a series of direct UV-written Bragg grating flat-fibre components have been reported. The Bragg gratings provide a probe which can be used to understand the characteristics of the UV-written waveguides in the flat-fibre platform. In addition, the performance of the fabricated devices have been improved by investigating the key parameters used in the UV-writing technique, these include fluence and duty cycle. It has also demonstrated the significance of boron doping of the germanosilicate core by increasing the UV photosensitivity. To further increase the flat-fibre photosensitivity, it has been found that with appropriate processing i.e. removal of the cladding, hydrogen loading can increase the photosensitivity of the flat-fibre. This has been proven by UV-writing two different batches of flat-fibre platforms, at which one is hydrogen loaded and another one is not. This experimental series further highlighted the usefulness of UV-written Bragg gratings as a tool for loss measurement.

A novel Bragg grating loss measurement technique has been performed to measure the loss in the flat-fibre platform and has been compared to an optical backscat-

tered reflectometer. The technique uses a Bragg grating structure to define the power variation along the length of the flat-fibre. It is found that the flat-fibre has low loss propagation $\sim 0.13 \text{ dB/cm} \pm 0.03 \text{ dB/cm}$ for a straight channel waveguide. Besides this, the Bragg grating loss technique has also been further employed to optimise the design of an s-bend structure. This optimisation is useful for future fabrication of an y-splitter UV-written waveguide. This technique offers a simple and effective way to measure the device loss without the uncertainty of coupling efficiency and grating variation.

The advantage of mechanical flexibility has motivated the fabrication of an optical sensor device in the flat-fibre platform. Through polishing the surface of the flat-fibre the evanescent field of the guided mode is allowed to be exposed to a series of refractive index oils which can be used to form a refractometer. Breaking the symmetry of the flat-fibre also shifts the neutral axis of the substrate and subsequently increases the sensitivity of the flat-fibre to sense physical deflections. The distribution of multiplexed Bragg gratings along the flat-fibre sensor opens up the opportunity of the sensor device to distinguish between deflections in two dimensions. The capability of a multi-parameter sensing opens up the potential for flat-fibre to be used as a compact sensor device.

So far, all the fabricated optical devices presented in the previous paragraphs have used UV writing and Bragg grating structures either for parameter optimisation or for sensing purposes. To present the ability of the flat-fibre platform to be an optical device without using the UV-writing technique, a physical micromachining technique is used to fabricate a multimode interference (MMI) device. This device has been fabricated using high precision micromachining to cut trenches in order to produce a 1x3 MMI device. Wavelength tuning was used to optimise the output mode of the MMI device. The excess loss of the MMI was found to be 1.89 dB.

All the devices that have been described above are passive devices. In order to demonstrate an active device, an erbium-doped flat-fibre substrate was fabricated. The spectroscopy of the flat-fibre is first carried out; this includes the measurement of spectral absorption and the lifetime of the substrate. From the measurement, absorption of 0.32 dB/cm was observed at a wavelength of 980 nm and a measured fluorescence lifetime of 9.53 ms was achieved. These parameters are required in order to estimate the gain amplification of the erbium doped flat-fibre platform. The first demonstration of erbium-doped flat-fibre has been performed where the relative gain of 0.74 dB was obtained from this measurement. Several factors that cause the low internal gain have been discussed and several solutions to these factors have been suggested.

In the future this platform may form the basis of fabricating a multifunctional laser device.

It is anticipated that the flat-fibre optical device technology presented here could have applications in many novel sensing geometries, quantum information processing and even fibre to the home (FTTH) technology.

9.2 Future Work

In this section, a few suggestions of future works are suggested. This considers further works that can be carried out from the previous fabricated devices. The first to be highlighted is a physical twist and bend sensor where employing Bragg gratings in a y-splitter channel waveguide to interrogate the twist and bend parameters. This is followed by producing an MMI device using a UV-writing raster scanning technique. Last but not least is an optical hybrid device where combining a passive and active optical device in a single component.

9.2.1 Physical Twist and Bend Sensor

The flexibility and long lengths offered by the flat-fibre platform opens up the opportunity to fabricate a physical sensor that can distinguish between twisting and bending. The device would use a UV-written y-splitter design to position two interrogating Bragg gratings at asymmetric positions relative to the centre of the flat-fibre structure. One Bragg grating would be placed in each arm of the y-splitter and it is anticipated that each would give different effective index values once the substrate is twisted. In addition, in order to increase the sensitivity of the physical sensing, it is suggested to fabricate an asymmetric preform as previously discussed in Chapter 6. The characterisation setup for twisting sensor will be a challenge for this work as the other effects such as buckling and bending whilst twisting the substrate will affect the reading of the twisting sensor.

9.2.2 UV-written Multimode Interference (MMI) Device

Optical power splitting is a significant component in optical telecommunication and integrated optics. It has been found widespread applications particularly in switching, sensing and amplifying. There are several methods that have been introduced to perform power splitting such as y-splitter, x-coupler and multimode interference (MMI). However, MMI has gained more interest due to its small device size, stable power splitting and broad bandwidth. The 1×3 MMI device in flat-fibre substrate has been successfully demonstrated via micromachining two trenches parallel to the MMI section which is discussed in Chapter 7.

Other alternative technique that can be implemented to fabricate an MMI device in the flat-fibre substrate is through using a direct UV-writing technique. *Knappe et al* has demonstrated their MMI devices using the raster scanning of UV-writing technique in PECVD substrates and shown good performance. Yet, these PECVD substrates need to be loaded in hydrogen chamber for a few days to increase the photosensitivity of the samples and relatively associated with the issue of photosensitivity due to outgassing problem. In contrast, the germanium-boron-doped flat-fibre does not necessarily need to be loaded in a hydrogen chamber and can be directly written without facing any problem of photosensitivity. Accordingly, it is suggested to use a 244 nm wavelength of UV laser writing technique to fabricate the MMI devices in the flat-fibre platform. In addition, a series of Bragg grating at the input and output excess waveguides can be defined for device loss measurement. From this technique, scattering loss due to lateral surface roughness can be reduced and coupling efficiency between SMF and the access channel input UV-written waveguide of the MMI section can also be increased.

9.2.3 Optical Hybrid Device

Future work will also look to develop an active flat-fibre device using an erbium rare-earth doped flat-fibre platform to provide active capability via light amplification. This is an extension of the work presented in Chapter 8. The initial result has presented the spectroscopy of the erbium doped flat-fibre and the first demonstration of signal amplification but with very low internal gain. Thus, the following work will look at increasing doping, forming waveguides and cavities where it is hoped a flat-fibre laser will be achieved. The work can be further advanced by using the MMI concept and Bragg grating cavity in a rare-earth doped flat-fibre as illustrated in Figure 9.2.1. This leads to an opportunity for amplification or lasing in the flexible-long-length flat-fibre device. This opens up potential for a hybrid device combining passive and active components in a single chip in order to yield a more compact and cost effective optical device.

Finally, it is clear if more time were available, it should be possible to make a rare-earth doped device incorporating full coupler/gratings and featuring low losses and useful gain.

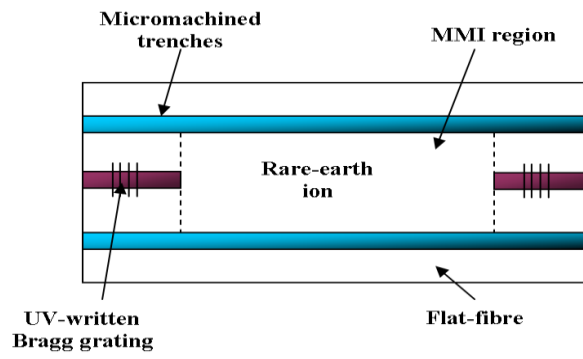


Figure 9.2.1 A schematic of flat-fibre laser using a rare-earth doped flat-fibre and MMI device combination.

Appendix A

List of Publications

S. Ambran, C. Holmes, J. C. Gates, A. S. Webb, L. G. Carpenter, F. R. M. Adikan, P. G. R. Smith, J. K. Sahu, "Fabrication of a multimode interference device in a low-loss flat-fiber platform using physical micromachining technique", *Journal of Lightwave Technology* 2012, Vol.30(17) pp.2870-2875.

S. Ambran, C. Holmes, J. C. Gates, A. S. Webb, M. F. R. Adikan, P. G. R. Smith, J. K. Sahu, 'Flat-optical fibre for a faster future', *SET for Britain 2012*, House of Commons London, 12 March 2012.

H. L. Rogers, L. G. Carpenter, **S. Ambran**, C. Sima, D. J. Wales, R. M. Parker, C. Holmes, J. C. Gates, P. G. R. Smith, "Direct grating writing: single-step Bragg grating and waveguide fabrication for telecommunications", *IONS NA-3 Stanford USA* 13-15 Oct 2011.

H. L. Rogers, L. G. Carpenter, **S. Ambran**, C. Sima, B. D. Snow, R. M. Parker, C. Holmes, J. C. Gates, P. G. R. Smith, "Direct grating writing: Single-step Bragg grating and waveguide fabrication for telecommunications and sensing applications", *IONS-9 Salamanca Spain* 7-9 Apr 2011.

S. Ambran, C. Holmes, J. C. Gates, A. S. Webb, J. K. Sahu, P. G. R. Smith, "UV-written Bragg gratings in a flat-fiber platform as a bending and twisting sensor", *CLEO/Europe-EQEC Munich* 22-26 May 2011

S. Ambran, C. Holmes, J. C. Gates, A. S. Webb, P. G. R. Smith, J. K. Sahu, "Micromachined multimode interference device in flat-fiber", *Photonics Global Conference Singapore* Dec 14 - 16 2010

H. L. Rogers, **S. Ambran**, C. Holmes, P. G. R. Smith, J. C. Gates, "In situ loss measurement of direct UV written waveguides using integrated Bragg gratings", *Optics Letters* 2010, Vol.35(17), pp.2849-2851

S. Ambran, H. L. Rogers, A. S. Webb, J. C. Gates, C. Holmes, P. G. R. Smith, J. K. Sahu, "A loss comparison of flat-fibre and silica-on-silicon direct UV written waveguides using a novel Bragg grating measurement technique", *Photon 10 Southampton*, 23-26 Aug 2010

H. L. Rogers, J. C. Gates, **S. Ambran**, P. G. R. Smith, "New technique for loss measurement of a direct UV written silica-on-silicon waveguide using integrated Bragg grating structures", *ECIO 2010 Cambridge*, 7-9 Apr 2010

S. Ambran, C. Holmes, J. C. Gates, A. S. Webb, P. A. Cooper, P. G. R. Smith, J. K. Sahu, "Refractive index and physical sensing in an optically integrated flat-fiber", (to be submitted) in *Sensors and Actuators A: Physical*, 2013.

List of References

- [1] K. Hagimoto, S. Nishi and Nakagawa, "An optical bit-rate flexible transmission system with 5 Tb/s.km capacity employing multiple in-line erbium-doped fibre amplifiers," *Journal of Lightwave Technology*, vol. 8, 1990.
- [2] G. Osborne and L. Sassoon. (2011). *The National Infrastructure Plan 2011*.
- [3] D. Yelin, B. E. Bourn, S.H. Yun and G. J. Tearney, "Double-clad fiber for endoscopy," *Optics Letters*, vol. 29, 2004.
- [4] S. E. Watkins, "Smart bridges with fibre-optic sensors," *IEEE-Instrumentation and Measurement Magazine*, vol. 6, 2003.
- [5] M. Kawachi, "Recent progress in silica-based planar lightwave circuits on silicon," *IEE Proceedings - Optoelectronics*, vol. 143, 1996.
- [6] S. E. Miller, "Integrated optics: an introduction," *Journal Bell System Technology*, vol. 48:205969, 1969.
- [7] A. Driessen, H. J. W. M. Hoekstra, F. Horst, G. J. M. Krijnen, B. J. Offrein, J. B. P. Van Schoot, P. V. Lambeck and T. J. A. Popma, "All-optical integrated optic devices: A hybrid approach," *IEE Proceedings Optoelectron*, vol. 145, 1998.
- [8] C. Sima, J. C. Gates, H. L. Rogers, P. L. Mennea, C. Holmes, M. N. Zervas and P. G. R. Smith, "Phase modulated direct UV grating writing technique for ultrawide spectrum planar Bragg grating fabrication," presented at the SPIE Photonics West, San Francisco, 2013.
- [9] T. Kominato, Y. Ohmori, H. Okazaki and M. Yasu, "Very low-loss GeO₂-doped silica waveguides fabricated by flame hydrolysis deposition method," *Electronics Letters*, vol. 26, 1990.
- [10] L. Wosinski, "Silica-on-Silicon technology for photonic integrated devices," presented at the Transparent Optical Networks, 2004, 2004.
- [11] A. S. Webb, F. R. Mahamd Adikan, J. K. Sahu, R. J. Standish, C. B. E. Gawith, J. C. Gates, P. G. R. Smith and D. N. Payne, "MCVD planar substrates for UV-written waveguide devices," *Electronics Letters*, vol. 43, 2007.
- [12] C. B. E. Gawith, A. S. Webb, F. R. M. Adikan, J. C. Gates, J. K. Sahu and P. G. R. Smith, "Flat fiber - the flexible format for distributed lab-on-a-chip," presented at the SPIE Europe Optics and Optoelectronics Conference, Prague, 2007.
- [13] G. D. Emmerson, "Novel direct UV written devices," University of Southampton 2003.
- [14] K. Pita Rajni, C. K. F. Ho, T. S. Chuan, K. C. Hin, "Photosensitivity of 20GeO₂:80SiO₂ hydrogen-loaded and non-hydrogen-loaded thin films," *Journal of Physics D: Applied Physics*, vol. 39, pp. 2504-2508, 2006.
- [15] G. D. Emmerson, S. P. Watts, C. B. E. Gawith, V. Albanis, M. Ibsen, R. B. Williams and P. G. R. Smith, "Fabrication of directly UV-written channel waveguides with simultaneously defined integral Bragg gratings," *Electronics Letters*, vol. 38, 2002.
- [16] A. Ghatak and K. Thyagarajan, *Introduction to fibre optics*: Cambridge, 1998.

- [17] G. Lifante, *Integrated photonics : Fundamental*: Wiley, 2003.
- [18] E. A. J. Marcatili, "Dielectric rectangular waveguide and directional coupler for integrated optics," *The Bell System Technical Journal*, vol. 48, 1969.
- [19] A. S. Sudbo, "Film mode matching: a versatile numerical method for vector mode field calculations in dielectric waveguides," *Pure and Applied Optics: Journal of the European Optical Society Part A*, vol. 2, 1993.
- [20] K. Okamoto, *Fundamental of optical waveguides*, 2 ed. Japan: Elsevier, 2006.
- [21] C. Sima, J. C. Gates, H. L. Rogers, P. L. Mennea, C. Holmes, M. N. Zervas and P. G. R. Smith, "Ultra-wide detuning planar Bragg grating fabrication based on direct UV grating writing with electro-optic phase modulation," *In progress of submission to the Journal Optics Express* 2013.
- [22] K. O. Hill and G. Meltz, "Fiber Bragg grating technology fundamentals and overview," *Journal of Lightwave Technology*, vol. 15, 1997.
- [23] T. Erdogan, "Fiber grating spectra," *Journal of Lightwave Technology*, vol. 15, 1997.
- [24] M. S. Ab-Rahman, H. Guna and M. H. Harun, "1xN self-made polymer optical fiber based splitter for POF-650nm-LED based application," presented at the International Conference on Electrical Engineering and informatics, Malaysia, 2009.
- [25] Y. Hibino, F. Hanawa, H. Nakagome, M. Ishii and N. Takato, "High reliability optical splitters composed of silica-based planar lightwave circuits," *Journal of Lightwave Technology*, vol. 13, 1995.
- [26] S. H. Tao, Q. Fang, J. F. Song, M. B. Yu, G. Q. Lo and D. L. kwong, "Cascade wide-angle Y-junction 1x16 optical power splitter based on silicon wire waveguides on silicon-on-insulator," *Optics Express*, vol. 16, 2008.
- [27] F. R. M. Adikan, C. B. E. Gawith, P. G. R. Smith, I. J. G. Sparrow, G. D. Emmerson, C. Riziotis and H. Ahmad, "Design and demonstration of direct UV-written small angle X couplers in silica-on-silicon for broadband operation," *Applied Optics*, vol. 45, 2006.
- [28] J. M. Hong, H. H. Ryu, S. R. Park, J. W. Jeoug, S. G. Lee, E. Lee, S. Park, D. Woo, S. Kim and B. O, "Design and fabrication of a significantly shortened multimode interference coupler for polarization splitter application," *IEEE Photonics Technology Letters*, vol. 15, 2003.
- [29] M. Olivero and M. Svalgaard, "UV-Written integrated optical 1xN splitters," *Optics Express*, vol. 14, 2006.
- [30] B. Lee, "Review of the present status of optical fiber sensors," *Optical Fiber Technology*, vol. 9, pp. 57-79, 2003.
- [31] B. Culshaw and A. Kersey, "Fiber-optic sensing: A historical perspective," *Journal of Lightwave Technology*, vol. 26, 2008.
- [32] G. Gauglitz, "Direct optical sensors: principles and selected applications," *Analytical and Bioanalytical Chemistry*, vol. 381, 2005.
- [33] J. Chen, B. Liu and H. Zhang, "Review of fibre Bragg grating sensor technology," *Front. Optoelectron. China*, vol. 4, 2011.
- [34] B. Liu, Y. Miao, H. Zhou and Q. Zhao, "Pure bending characteristic of tilted fibre Bragg grating," *Journal of Electronic Science and Technology of China*, vol. 6, 2008.

- [35] W. Liu, T. Guo, A. C. Wong, H. Tom and S. Ho, "Highly sensitive bending sensor based on Er³⁺ doped DBR fibre laser," *Optics Express*, vol. 18, 2010.
- [36] A. Iadicicco, A. Cusano and S. Campopiano, "Thinned fibre Bragg gratings as refractive index sensors," *IEEE Sensors Journal*, vol. 5, 2005.
- [37] J. Kou, M. Ding, J. Feng, Y-Lu, F. Xu and G. Brambilla, "Microfiber-based Bragg gratings for sensing applications: a review," *Sensors*, vol. 12, pp. 8861-8876, 2012.
- [38] I. J. G. Sparrow, P. G. R. Smith, G. D. Emmerson, S. P. Watts and C. Riziotis, "Planar Bragg grating sensors - fabrication and application : a review," *Journal of Sensors*, 2009.
- [39] J. Wo, G. Wang, Y. Cui, Q. Sun, R. Liang, P. P. Shum and D. Liu, "Refractive index sensor using microfiber-based Mach-Zehnder interferometer," *Optics Letters*, vol. 37, 2012.
- [40] B. H. Lee, Y. H. Kim, K. S. Park, J. B. Eom, M. J. Kim, B. S. Rho and H. Y. Choi, "Interferometric fiber optic sensors," *Sensors*, vol. 12, 2012.
- [41] M. J. F. Digonnet, *Rare-earth-doped fibre lasers and amplifiers*. New York: Marcel Dekker, 2001.
- [42] R. J. Mears, L. Reekie, I. M. Jauncy and D. N. Payne, "High gain rare-earth doped fibre amplifier at 1.54 μm ," in *OFC 87*, 1987.
- [43] F. R. M. Adikan, A. S. Webb, J. K. Sahu, J. C. Gates, C. Holmes, P. G. R. Smith and D. Payne, "Method of fabricating a planar substrate having optical waveguides," US Patent, 2010.
- [44] Y. A. Vlasov and S. J. McNab, "Losses in single-mode silicon-on-insulator strip waveguides and bends," *Optics Express*, vol. 12, 2004.
- [45] E. Ollier, "Optical MEMS devices based on moving waveguides," *IEEE Journal on Selected Topics in Quantum Electronics*, vol. 8, 2002.
- [46] P. dumais, C. L. Callender, J. P. Noad and C. J. Ledderhof, "Silica-on-Silicon optical sensor based on integrated waveguides and microchannels," *IEEE Photonics Technology Letters*, vol. 17, 2005.
- [47] M. Olivero and M. Svalgaard, "Direct UV-written broadband directional planar waveguide couplers," *Optics Express*, vol. 13, 2005.
- [48] D. L. Wood, K. L. Walker, J. B. Macchesney, J. R. Simpson and R. Csencsits, "Germanium chemistry in the MCVD process for optical fiber fabrication," *Journal of Lightwave Technology*, vol. LT-5, 1987.
- [49] L. Cognolato, "Chemical vapour deposition for optical fibre technology," *Journal of physics*, vol. 5, 1995.
- [50] S. R. Nagel, J. B. MacChesney and K. L. Walker, "An overview of the modified chemical vapor deposition (MCVD) process and performance," *IEEE Transactions on Microwave Theory and Techniques*, vol. MTT-30, 1982.
- [51] H. Murata and N. Inagaki, "Low-loss single-mode fiber development and splicing research in Japan," *IEEE Journal of Quantum Electronics*, vol. QE-17, 1981.
- [52] H. Lydtin, "PCVD: A technique suitable for large-scale fabrication of optical fibers," *Journal of Lightwave Technology*, vol. LT-4, 1986.
- [53] P. C. Schultz, "Fabrication of optical waveguides by the outside vapor deposition process," vol. 68, ed. Proceedings of the IEEE: IEEE, 1980.
- [54] R. V. Vandewoestine and A. J. Morrow, "Developments in optical waveguide fabrication by the outside vapor deposition process," *Journal of Lightwave Technology*, vol. LT-4, 1986.

- [55] K. Inada, "Recent progress in fiber fabrication techniques by vapor-phase axial deposition," *IEEE Journal of Quantum Electronics*, vol. QE-18, 1982.
- [56] S. Tomaru, M. Yasu, M. Kawachi and T. Edahiro, "VAD single mode fibre with 0.2 dB/km loss," *Electronics Letters*, vol. 17, 1981.
- [57] P. Tandon and H. Boek, "Experimental and theoretical studies of flame hydrolysis deposition process for making glasses for optical planar devices," *Journal of Non-Crystalline Solids*, vol. 317, pp. 275-289, 2003.
- [58] A. Kilian, J. Kirchhof, B. Kuhlow, G. Przyrembel and W. Wischmann, "Birefringence free planar optical waveguide made by flame hydrolysis deposition (FHD) through tailoring of the overcladding," *Journal of Lightwave Technology*, vol. 18, 2000.
- [59] Z. Le-Tian, X. Wen-Fa, W. Yuan-Da, X. Hua, L. Ai-Wu, Z. Wei and Z. Yu-Shu, "Thermal annealing of SiO₂ fabricated by flame hydrolysis deposition," *Chinese Physical Letters*, vol. 20, 2003.
- [60] H. Ou, "Different index contrast silica-on-silicon waveguides by PECVD," *Electronics Letters*, vol. 39, 2003.
- [61] M. Hoffmann, P. Kopka and E. Voges, "Low-loss fiber-matched low-temperature PECVD waveguides with small-core dimensions for optical communication systems," *IEEE Photonics Technology Letters*, vol. 9, 1997.
- [62] M. V. Bazylenko, M. Gross, P. M. Allen and P. L. Chu, "Fabrication of low-temperature PECVD channel waveguides with significantly improved loss in the 1.50 - 1.55 μm wavelength range," *IEEE Photonics Technology Letters*, vol. 7, 1995.
- [63] A. S. Webb, A. J. Boyland, R. J. Standish, S. Yoo, J. K. Sahu and D. N. Payne, "MCVD in-situ solution doping process for the fabrication of complex design large core rare-earth doped fibres," *Journal of Non-Crystalline Solids*, vol. 356, pp. 848-851, 2010.
- [64] Y. Duval, R. Kashyap and S. Fleming, "Correlation between ultraviolet-induced refractive index change and photoluminescence in Ge-doped fiber," *Applied Physics Letters*, vol. 61, 1992.
- [65] K. O. Hill, Y. Fujii, D. C. Johnson and B. S. Kawasaki, "Photosensitivity in optical fiber waveguides: Application to reflection filter fabrication," *Applied Physics Letters*, vol. 32, 1978.
- [66] M. Douay, W. X. Xie, T. Taunay, P. Bernage, P. Niay, P. Cordier, B. Poumellec, L. Dong, J. F. Bayon, H. Poignant and E. Deleuaque, "Densification involved in the UV-based photosensitivity of silica glasses and optical fibres," *Journal of Lightwave Technology*, vol. 15, 1997.
- [67] P. J. Lemiare, R. M. Atkins, V. Mizrahi and W. A. Reed, "High pressure H₂ loading as a technique for achieving ultrahigh UV photosensitivity and thermal sensitivity in GeO₂ doped optical fibres," *Electronics Letters*, vol. 29, 1993.
- [68] A. D. Heaney, T. Erdogan and N. Borrelli, "The significance of oxygen-deficient defects to the photosensitivity of hydrogen-loaded germano-silicate glass," *Journal of Applied Physics*, vol. 85, 1999.
- [69] H. I. Smith, "Fabrication techniques for surface-acoustic-wave and thin-film optical devices," *Proceeding of the IEEE*, vol. 62, 1974.
- [70] S. M. Garner, S. Lee, V. Chuyanov, A. Chen, A. Yacoubian, W. H. Steier and L. R. Dalton, "Three-dimensional integrated optics using polymers," *IEEE Journal of Quantum Electronics*, vol. 35, 1999.

- [71] C. Iliescu and F. E. H. Tay, "Wet etching of glass," presented at the Semiconductor Conference, Singapore, 2005.
- [72] K. Solehmainen, T. Aalto, J. Dekker, M. Kapulainen, M. Harjanne and K. Kukli, "Dry-etched silicon-on-insulator waveguides with low propagation and fiber-coupling losses," *Journal of Lightwave Technology*, vol. 23, 2005.
- [73] M. Svalgaard, C. V. Poulsen, A. Bjarklev and O. Poulsen, "Direct UV-Writing of buried singlemode channel waveguides in Ge-doped silica films," *electronics Letters*, vol. 30, 1994.
- [74] M. Svalgaard and M. Kristensen, "Directly UV written silica-on-silicon planar waveguides with low loss," *Electronics Letters*, vol. 33, 1997.
- [75] K. M. Davis, K. Miura, N. Sugimoto and K. Hirao, "Writing waveguides in glass with a femtosecond laser," *Optics Letters*, vol. 21, 1996.
- [76] I. Sohn, M. Lee and S. Lee, "Femtosecond laser application to PLC optical devices and packaging," *ETRI Journal*, vol. 27, 2005.
- [77] R. R. Thomson, H. T. Bookey, N. Psaila, S. Campbell, D. T. Reid, S. Shen, A. Jha and A. K. Kar, "Internal gain from an erbium-doped oxyfluoride-silicate glass waveguide fabricated using femtosecond waveguide inscription," *IEEE Photonic Technology Letter*, vol. 18, 2006.
- [78] C. Holmes, L. G. Carpenter, H. L. Rogers, J. C. Gates and P. G. R. Smith, "Physical sensitivity of silica micro-cantilevers fabricated using direct UV-writing and micromachining," *Journal of Laser Micro-Nanoengineering*, vol. 6, 2011.
- [79] Y. Qiu, Y. Sheng and C. Beaulieu, "Optimal phase mask for fibre Bragg grating fabrication," *Journal of Lightwave Technology*, vol. 17, 1999.
- [80] V. Mizrahi, P. J. Lemaire, T. Erdogan, W. A. Reed and D. J. DiGiovanni, "Ultraviolet laser fabrication of ultrastrong optical fiber gratings and of germaniadoped channel waveguides," *Applied Physics Letters*, vol. 63, 1993.
- [81] D. L. Williams, B. J. Ainslie, J. r. Armitage, R. Kashyap and R. Campbell, "Enhanced UV photosensitivity in boron codoped germanosilicate fibres," *Electronics Letters*, vol. 29, 1993.
- [82] K. S. Chiang, "Geometrical birefringence in a class of step-index fibre," *Journal of Lightwave Technology*, vol. LT-5, 1987.
- [83] M. F. Hossain, H. P. Chan, M. A. Uddin and R. K. Y. Li, "Stress-induced birefringence characteristics of polymer optical rib waveguides," *Journal of Lightwave Technology*, vol. 27, 2009.
- [84] H. L. Rogers, S. Ambran, C. Holmes, P. G. R. Smith and J. C. Gates, "In situ loss measurement of direct UV-written waveguides using integrated Bragg gratings," *Optics Letters*, vol. 35, 2010.
- [85] R. G. Hunsperger, *Integrated optics: theory and technology*, Second ed.: springer_Verlag, 1985.
- [86] R. Arsenault, D. Gregoris, S. Woolven and V. M. Ristic, "Waveguide propagation-loss measurement technique," *Optics Letters*, vol. 12, 1987.
- [87] T. A. Strasser and M. C. Gupta, "Optical loss measurement of low-loss thin-film waveguides by photographic analysis," *Applied Optics*, vol. 31, 1992.
- [88] S. Chen, Q. Yan, Q. Xu, Z. Fan and J. Liu, "Optical waveguide propagation loss measurement using multiple reflections method," *Optics Communications*, vol. 256, pp. 68-72, 2005.
- [89] Thyagarajan K Ghatak A, *Introduction to fibre optics*: Cambridge, 1998.

- [90] S. Brulisauer, D. Fluck, C. Solcia, T. Pliska and P. Gunter, "Nondestructive waveguide loss-measurement method using self-pumped phase conjugation for optimum end-fire coupling," *Optics Letters*, vol. 20, 1995.
- [91] A. Boudrioua and J. C. Loulergue, "New approach for loss measurements in optical planar waveguides," *Optics Communications*, vol. 137, pp. 37-40, 1997.
- [92] P. K. Tien and R. Ulrich, "Theory of prism-film coupler and thin-film light guides," *Journal of the Optical Society of America*, vol. 60, 1970.
- [93] Y. Zhou, M. K. Chin, K. S. Lai and C. C. K. Wong, "Low-loss measurement in partially buried optical waveguides on glass with a plastic prism," *Applied Optics*, vol. 36, 1997.
- [94] M. D. Himel and U. J. Gibson, "Measurement of planar waveguide losses using a coherent fiber bundle," *Applied Optics*, vol. 25, 1986.
- [95] B. M. Foley, P. Melman and K. T. Vo, "Novel loss measurement technique for optical waveguides by imaging of scattered light," *Electronics Letters*, vol. 28, 1992.
- [96] Y. Okamura, S. Yoshinaka and S. Yamamoto, "Measuring mode propagation losses of integrated optical waveguides: a simple method," *Applied Optics*, vol. 22.
- [97] T. Feuchter and C. Thirstrup, "High precision planar waveguide propagation loss measurement technique using a Fabry-Perot Cavity," *IEEE Photonics Technology Letters*, vol. 6, 1994.
- [98] F. R. M. Adikan, "Direct UV-written waveguide devices," PhD, Optoelectronics Research Centre, ORC, University of Southampton, Southampton, 2007.
- [99] R. T. Schermer and J. H. Cole, "Improved bend loss formula verified for optical fiber by simulation and experiment," *IEEE Journal of Quantum Electronics*, vol. 43, 2007.
- [100] V. Subramaniam, G. N. D. Brabander, D. H. Naghski and J. T. Boyd, "Measurement of mode field profiles and bend and transition losses in curved optical channel waveguides," *Journal of Lightwave Technology*, vol. 15, 1997.
- [101] P. A. S. Jorge, S. O. Silva, C. Gouveia, P. Tafulo, L. Coelho, P. Caldas, D. Viegas, G. Rego, J. M. Baptista, J. L. Santos and O. Frazao, "Fiber optic-based refractive index sensing at INESC Porto," *Sensors*, vol. 12, pp. 8371-8389, 2012.
- [102] S. J. Mihailov, "Fiber Bragg grating sensors for harsh environments," *Sensors*, vol. 12, pp. 1898-1981, 2012.
- [103] L. Jin, W. Zhang, J. Li, H. Zhang, B. Liu, Q. Tu, G. Kai and X. Dong, "Two-dimensional bend sensing with a cantilever-mounted FBG," *Measurement Science and Technology*, vol. 17, pp. 168-172, 2006.
- [104] D. C. Betz, G. Thursby and B. Culshaw, "Advanced layout of a fiber Bragg grating strain gauge rosette," *Journal of Lightwave Technology*, vol. 24, 2006.
- [105] P. M. Blanchard, J. G. Burnett, G. R. G. Erry, A. H. Greeaway, P. Harrison, B. Mangan, J. C. Knight, P. St. J. Russell, M. J. Gander, R. McBride and J. D. C. Jones, "Two-dimensional bend sensing with a single, multi-core optical fiber," *Smart Material Structure*, vol. 9, pp. 132-140, 2000.
- [106] A. Leung, P. M. Shankar and R. Mutharasan, "A review of fibre-optic biosensors," *Sensors and Actuators B*, vol. 125, pp. 688-703, 2007.

- [107] R. P. Feynman, R. B. Leighton and M. Sands, *The Feynman lectures on physics* vol. 2: Addison-Wesley, 1989.
- [108] H. Jang, M. Cho and D. Park, "Micro fluidic channel machining on fused silica glass using powder blasting," *Sensors*, vol. 8, pp. 700-710, 2008.
- [109] C. Holmes, "Direct UV written planar devices for sensing and telecommunication applications," Optoelectronics Research Centre, University of Southampton, 2009.
- [110] R. M. Parker, J. C. Gates, M. C. Gossel and P. G. R. Smith, "In vacuo measurement of the sensitivity limit of planar Bragg grating sensors for monolayer detection," *Applied Physics Letters*, vol. 95, 2009.
- [111] L. B. Soldano and E. C. M. Pennings, "Optical multi-mode interference devices based on self-imaging: Principles and applications," *Journal Lightwave Technology*, vol. 13, 1995.
- [112] J. Leuthold and C. H. Joyner, "Multimode interference couplers with tunable power splitting ratios," *Journal of Lightwave Technology*, vol. 19, 2001.
- [113] J. Leuthold, J. Eckner, E. Gamper, P. A. Besse and H. Melchior, "Multimode interference couplers for the conversion and combining of zero- and first-order modes," *Journal of Lightwave Technology*, vol. 16, 1998.
- [114] M. Mayeh, J. Viegas, P. Srivinasan, P. Marques, J. L Santos, E. G. Johnson and F. Farahi, "Design and fabrication of slotted multimode interference devices for chemical and biological sensing," *Journal of Sensors*, p. 470111, 2009.
- [115] S. Nagai, G. Morishima, H. Inayoshi and K. Utaka, "Multimode interference photonic switches (MIPS)," *Journal of Lightwave Technology*, vol. 20, 2002.
- [116] A. Rostami, "Goos-Hanchen shift description in planar optical waveguides," in *International Conference on Communication Technology Proceedings, 2003*, 2003, pp. 663-667.
- [117] C. Holmes, H. E. Major, J. C. Gates, C. B. E. gawith and P. G. R. Smith, "Period adapted Bragg mirror multimode interference device," presented at the Conference on Lasers and Electro-optics/Quantum Electronics and Laser Science Conference (CLEO/QELS), 2009.
- [118] M. H. Ibrahim, N. M. Kassim, A. B. Mohammad, M. K. Chin and S. Y. Lee, "Multimode interference optical splitter based on photodefinable bensocyclobutene (BCB 4024-40) polymer," *Optical Engineering*, vol. 46, 2007.
- [119] H. Chen and D. T. K. Tong, "Two-dimensional symmetric multimode interferences in silicon square waveguide," *IEEE Photonics Technology Letters*, vol. 17, 2005.
- [120] X. Wang and R. T. Chen, "Image enhanced polymer-based multimode interference coupler covering C and L bands using deeply etched air trenches," *Applied Physics Letters*, vol. 90, 2007.
- [121] A. M. Al-Hetar, A. B. Mohammad, A. S. M. Supaat and Z. A. Shamsan, "MMI-MZI polymer thermo-optic switch with a high refractive index contrast," *Journal of Lightwave Technology*, vol. 29, 2011.
- [122] J. Z. Huang, M. H. Hu, J. Fujita, R. Scarmozzino and R. M. Osgood, "High-performance metal-clad multimode interference devices for low-index-contrast material systems," *IEEE Photonics Technology Letters*, vol. 10, 1998.

- [123] C. J. Kaalund and Z. Jin, "Novel multimode interference devices for low index contrast materials systems featuring deeply etched air trenches," *Optics communication*, vol. 250, pp. 292-296, 2005.
- [124] Y. Ma, S. Park, L. Wang and S. T. Ho, "Ultracompact multimode interference 3-dB coupler with strong lateral confinement by deep dry etching," *IEEE Photonics Technology Letters*, vol. 12, 2000.
- [125] M. K. Chin, C. W. Lee, S. Y. Lee and S. Darmawan, "High-index-contrast waveguides and devices," *Applied Optics*, vol. 44, 2005.
- [126] V. Aimez H. S. Lim, B. S. Ooi, J. Beauvais, and J. Beerens, "A novel fabrication technique for multiple-wavelength photonic-integrated devices in InGaAs-InGaAsP laser heterostructures," *Photonics Technology Letters, IEEE*, vol. 14, 2002.
- [127] A. Hosseini, H. Subbaraman, D. Kwong, Y. Zhang and R. T. Chen, "Optimum access waveguide width for 1xN multimode interference couplers on silicon nanomembrane," *Optics Letters*, vol. 35, 2010.
- [128] M. T. Hill, X. J. M. Leijtens, G. D. Khoe and M. K. Smit, "Optimizing imbalance and loss in 2 x 2 3-dB multimode interference couplers via access waveguide width," *Journal of Lightwave Technology*, vol. 21, 2003.
- [129] M. Zhang, R. Malureanu, A. C. Kruger and M. Kristensen, "1x3 beam splitter for TE polarization based on self-imaging phenomena in photonic crystal waveguides," *Optics Express*, vol. 18, 2010.
- [130] K. K. Lee, D. R. Lim, H. Luan, A. Agarwal, J. Foresi and L. C. Kimerling, "Effect of size and roughness on light transmission in a Si/SiO₂ waveguide: Experiments and model," *Applied Physics Letters*, vol. 77, 2000.
- [131] K. Kasaya, O. Mitomi, M. Naganuma, Y. Kondo and Y. Noguchi, "A simple laterally tapered waveguide for low-loss coupling to single-mode fibres," *IEEE Photonics Technology Letters*, vol. 5, 1993.
- [132] M. Bruendel and D. G. Rabus, "1x2 and 1x3 multimode interference couplers fabricated by hot embossing and DUV-induced modification of polymers," presented at the Conference on Lasers and Electro-optics Society, 2006.
- [133] P. A. Besse, E. Gini, M. Bachmann and H. Melchior, "New 2x2 and 1x3 multimode interference couplers with free selection of power splitting ratios," *Journal of Lightwave Technology*, vol. 14, 1996.
- [134] E. Snitzer, "Proposed fibre cavities for optical masers," *Journal of physics*, vol. 32, pp. 26-39, 1961.
- [135] P. Uguhart, "Review of rare earth doped fibre lasers and amplifiers," *IEE Proceedings*, vol. 135, 1988.
- [136] E. Snitzer, "Glass lasers," *Applied optics*, vol. 5, 1966.
- [137] W. J. Miniscalco, "Erbium-doped glasses for fiber amplifiers at 1500 nm," *Journal of Lightwave Technolgy*, vol. 9, 1991.
- [138] B. J. Ainslie, "A review of the fabrication and properties of erbium-doped fibres for optical amplifiers," *Journal of Lightwave Technology*, vol. 9, 1991.
- [139] W. L. Barnes, R. I. Laming, E. J. Tarbox and P. R. Morkel, "Absorption and emission cross section of Er³⁺ doped silica fibres," *IEEE Journal of Quantum Electronics*, vol. 27, 1991.

-
- [140] D. Lowe, R. R. A. Syms and W. Huang, "Layout optimization for erbium-doped waveguide amplifiers," *Journal of Lightwave Technology*, vol. 20, 2002.
- [141] G. C. Righini, S. Pelli, M. Brenci, M. Ferrari, C. Duverger, M. Montagna and R. D. Igna, "Active optical waveguides based on Er- and Er/Yb-doped silicate glasses," *Journal of Non-Crystalline Solids*, vol. 284, pp. 223-229, 2001.
- [142] A. J. Kenyon, "Recent developments in rare-earth doped materials for optoelectronics," *Progress in Quantum Electronics*, vol. 26, pp. 225-284, 2002.
- [143] K. Arai, H. Namikawa, K. Kumata, T. Honda and Y. Ishiee, "Aluminum or phosphorus codoping effects on the fluorescence and structural properties of neodymium doped silica glass," *Journal of Applied Physics*, vol. 59, 1986.
- [144] B. C. Hwang, S. Jiang, T. Luo, J. Watson, S. Honkanen, Y. Hu, F. Smektala, J. Lucas and N. Peyghambarian, "Erbium-doped phosphate glass fibre amplifiers with gain per unit length of 2.1dB/cm," *Electronics Letters*, vol. 35, 1999.
- [145] K. Worhoff, J. D. B. Bradley, D. Geskus F. Ay, T. P. Blauwendraat and M. Pollnau, "Reliable low-cost fabrication of low-loss Al₂O₃:Er³⁺ waveguides with 5.4dB optical gain," *IEEE Journal of Quantum Electronics*, vol. 45, 2009.
- [146] Q. Xiang, Y. Zhou, B. S. Ooi, Y. L. Lam, Y. C. Chan and C. H. Kam, "Optical properties of Er³⁺-doped SiO₂-GeO₂-Al₂O₃ planar waveguide fabricated by sol-gel processes," *Thin Solid Films*, vol. 370, 2000.
- [147] P. G. Kik and A. Polman, "Erbium doped optical waveguide amplifiers on silicon," *MRS Bulletin* vol. 23, 1998.
- [148] Agilent Technologies, "Optical spectrum analysis (Application note 1550-4)," Agilent Technologies, USA2000.